ABSTRACT

Title of dissertation: EXPERIMENTAL INVESTIGATION OF A MAV-SCALE CYCLOCOPTER

Elena Shrestha
Doctor of Philosophy, 2018

Dissertation directed by: Professor Inderjit Chopra
Department of Aerospace Engineering

The development of an efficient, maneuverable, and gust tolerant hovering concept with a multi-modal locomotion capability is key to the success of micro air vehicles (MAVs) operating in multiple mission scenarios. The current research investigated performance of two unconventional cycloidal-rotor-based (cyclocopter) configurations: (1) twin-cyclocopter and (2) all-terrain cyclocopter. The twin-cyclocopter configuration used two cycloidal rotors (cyclorotors) and a smaller horizontal edgewise nose rotor to counteract the torque produced by the cyclorotors. The all-terrain cyclocopter relied on four cyclorotors oriented in an H-configuration.

Objectives of this research include the following: (1) develop control strategies to enable level forward flight of a cyclocopter purely relying on thrust vectoring, (2) identify flight dynamics model in forward flight, (3) experimentally evaluate gust tolerance strategies, and (4) determine feasibility and performance of multi-modal locomotion of the cyclocopter configuration.

The forward flight control strategy for the twin-cyclocopter used a unique

combination of independent thrust vectoring and rotational speed control of the cyclorotors. Unlike conventional rotary-winged vehicles, the cyclocopter propelled in forward flight by thrust vectoring instead of pitching the entire fuselage. While the strategy enabled the vehicle to maintain a level attitude in forward flight, it was accompanied by significant yaw-roll controls coupling and gyroscopic coupling. To understand these couplings and characterize the bare airframe dynamics, a 6-DOF flight dynamics model of the cyclocopter was extracted using a time-domain system identification technique. Decoupling methods involved simultaneously mixing roll and yaw inputs in the controller. After implementing the controls mixing strategy in the closed-loop feedback system, the cyclocopter successfully achieved level forward flight up to 5 m/s.

Thrust vectoring capability also proved critical for gust mitigation. Thrust vectoring input combined with flow feedback and position feedback improved gust tolerance up to 4 m/s for a twin-cyclocopter mounted on a 6-DOF test stand. Flow feedback relied on a dual-axis flowprobe attached to differential pressure sensors and position feedback was based on data recorded by the VICON motion capture system. The vehicle was also able to recover initial position for crosswind scenarios tested at various side-slip angles up to 30°.

Unlike existing multi-modal platforms, the all-terrain cyclocopter solely relied on its four cyclorotors as main source of propulsion, as well as wheels. Aerial and aquatic modes used aerodynamic forces generated by modulating cyclorotor rotational speeds and thrust vectors while terrestrial mode used motor torque. In aerial mode, cyclorotors operated at 1550 rpm and consumed 232 W to sustain hover. In

terrestrial mode, forward translation at 2 m/s required 28 W, which was an 88% reduction in power consumption required to hover. In aquatic mode, cyclorotors operated at 348 rpm to achieve 1.3 m/s translation and consumed 19 W, a 92% reduction in power consumption. With only a modest weight addition of 200 grams for wheels and retractable landing gear, the versatile cyclocopter platform achieved sustained hover, efficient translation and rotational maneuvers on ground, and aquatic locomotion.

EXPERIMENTAL INVESTIGATION OF A MAV-SCALE CYCLOCOPTER

by

Elena Shrestha

Dissertation submitted to the Faculty of the Graduate School of the
University of Maryland, College Park in partial fulfillment
of the requirements for the degree of
Doctor of Philosophy
2018

Advisory Committee:
Dr. Inderjit Chopra, Chair/Advisor
Dr. Anubhav Datta
Dr. James Baeder
Dr. David Akin
Dr. Nikhil Chopra

Dedication

To my family for giving me the opportunity to pursue my degree and supporting me unconditionally throughout the entire journey.

Acknowledgments

I would like to thank my advisor, Dr. Inderjit Chopra for taking the risk in hiring an inexperienced Sophomore in 2010 for the challenging cyclocopter project. The past 8 years under his supervision have molded me into a better researcher. I really appreciate the open research environment and autonomy that he provided for students in the Micro Air Vehicle (MAV) Lab.

I would also like to thank my close mentors: Dr. Derrick Yeo, Dr. Vikram Hrishikeshavan, and Dr. Moble Benedict for providing me with guidance and support throughout all the ups and downs involved in research. Dr. Yeo not only piloted the cyclocopters, he also helped guide me through the process of articulating my research ideas and provided constant moral support. Dr. Hrishikeshavan and his magical custom autopilot made it possible to scale-down and even explore different cyclocopter configurations. Finally, I am extremely grateful to Dr. Benedict for introducing me to the unforgiving (yet satisfying) world of vertical axis rotors and instilling in me the value of a strong work ethic.

I am very thankful to my committee members: Dr. Anubhav Datta, Dr. James Baeder, Dr. Dave Akin, and Dr. Nikhil Chopra for all their technical guidance and feedback on my dissertation. My sincere thanks to Dr. Datta for his continued encouragement and insightful conversations.

Throughout my graduate degree, I had the pleasure of working closely with many exceptional undergraduate research assistants, and I am very grateful to all of the students. I want to especially thank Brian Davis and Benjamin Williams for

their contributions to the development of the all-terrain cyclocopter. I hope we get an opportunity to work together again in the future.

Graduate studies would be incomplete without the friends and colleagues that make the entire experience worthwhile. Special thanks to Steven Hill for his unwavering support throughout all these years. I feel that it is necessary to dedicate another sentence to Steven. I am also very thankful to Joseph Lemich, Jonathan Chambers, James Lankford, Lex Chi, Lem Carpenter, Snehesh Shrestha, Lina Maria, Vera Klimchenko, Wanyi Ng, Michael Van Order, Angela Maki, Peter Ryseck, Eric Solomon, and all the students housed in the Manufacturing building.

Finally, I am extremely grateful to my family for their unconditional support and patience all these years. My parents, Udaya and Romee, have sacrificed so much to provide me with an opportunity to obtain my degree. I am forever indebted to them. My siblings, Urusha and Alex, have kept me grounded and provided endless emotional support.

It is impossible to acknowledge every single person, and I apologize to those I have inadvertently left out. Thank you to everyone that I have shared special memories with during my studies at the University of Maryland!

Table of Contents

List of Tables

List of Figures

List of Abbreviations

A	cyclorotor projected area
b	blade span
c	blade chord
CG	center of gravity
d_p	moment arm of propeller
d_x, d_y, d_z	moment arm of cyclorotor
D_x, D_y, D_z	X, Y, Z drag components of cyclorotor
f_s	sampling rate
F_p	Z component force from propeller
F_x, F_y, F_z	X, Y, Z lift components of cyclorotor
g	gravity
H	angular momentum of the cyclorotor
I_x, I_y, I_z	moment of inertia in body reference frame
k_d	coefficient for the drag force
K	gains used for PD controller
L, M, N	X, Y, Z component of the moment in body reference frame
m	mass
p, q, r	roll, pitch, yaw rates in body reference frame
PL	power loading
Q_{cyclo}	torque of cyclorotor
Q_{prop}	torque of propeller
R	radius
u, v, w	X, Y, Z component of velocity vector in body reference frame
γ_{abs}	absolute phase angle
γ_{hover}	hover phase angle
Φ	phase angle with respect to hover
ϕ, θ, ψ	roll, pitch, yaw Euler angles
ω	angular velocity of the cyclorotor
ρ	air density
σ	rotor solidity

BEMT	Blade Element Momentum Theory
CFD	Computation Fluid Dynamics
DARPA	Defense Advanced Research Projects Agency
FM	Figure of Merit
MAV	Micro Air Vehicle
PID	Proportional-Integral-Derivative
PIV	Particle Image Velocimetry
Re	Reynolds Number
RPM	Revolutions Per Minute
UAV	Unmanned Aerial Vehicle
VTOL	Vertical Take-off and Landing

Chapter 1: Introduction

1.1 Micro Air Vehicles

Growing interest in highly portable versatile flying platforms and recent advancements in microelectronics have led to the development of a scaled-down class of Unmanned Aerial Vehicles (UAVs) known as Micro Air Vehicles (MAVs). MAVs were formally defined as aircraft with maximum dimension of 15.24 cm (6 in) and maximum weight of 100 g (0.22 lbs) by the Defense Advanced Research Projects Agency (DARPA) in 1997 [1]. The size constraints were selected to define a robust MAV platform that is portable, operational in confined spaces, and undetectable due to its low noise signatures. In addition, the target performance set forth by DARPA included payload capacity of 20 g, endurance up to 1 hr, range of 10 km, and maximum speed between 10 to 20 m/s.

While DARPA envisioned MAVs for military applications to increase situational awareness and reduce unit exposure times, MAVs have since been widely adopted for civilian and commercial applications. Some of these applications include agricultural monitoring, search and rescue (disaster relief), package delivery, aerial photography, and infrastructure inspection (Fig. 1.1). With advent of commercial autopilot kits and accessible additive manufacturing, MAVs have also been

Figure 1.1: **Commercial applications for MAVs.**

assimilated as a recreational activity. Considering both commercial and recreational applications, the Federal Aviation Administration forecasts that the number of operating MAVs could reach 442,000 by 2021. Therefore, it is important to understand the technical barriers in designing a robust MAV platform suitable for multiple mission scenarios.

1.2 Technical Challenges

For many mission scenarios, high endurance, maneuverability, and the ability to tolerate and overcome environmental disturbances such as wind gusts are critical requirements for MAVs. Designing the next generation micro air vehicle that is also aerodynamically efficient and capable of vertical take-off and landing (VTOL), high speed forward flight, and multi-mode locomotion involves overcoming an array of technical challenges further exacerbated at the MAV-scale (Fig. 1.2).

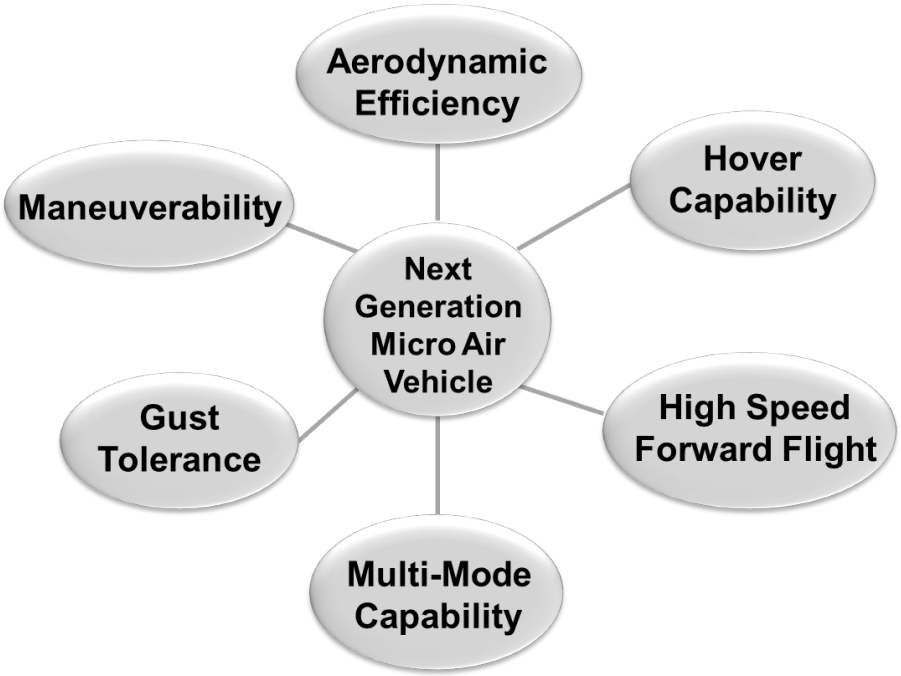

Figure 1.2: **Key design considerations for the next generation MAV.**

1.2.1 Low Reynolds Number Aerodynamics

One key challenge is understanding the governing aerodynamics of the flow regimes at which MAVs operate. Compared to their full-scale counterparts, MAVs operate at Reynolds numbers atleast two order of magnitudes lower. The Reynolds number (Re) is a non-dimensional parameter used to quantify scaling effects and is effectively a ratio of inertial forces to viscous forces that act on fluid elements in the flow:

$$Re = \frac{\rho v l}{\mu} \tag{1.1}$$

The Reynolds number is proportional to the fluid density (ρ), velocity of the object moving relative to the fluid (v), characteristic length of the object (l), and inversely proportional to the dynamic viscosity of the fluid (μ). At high Reynolds

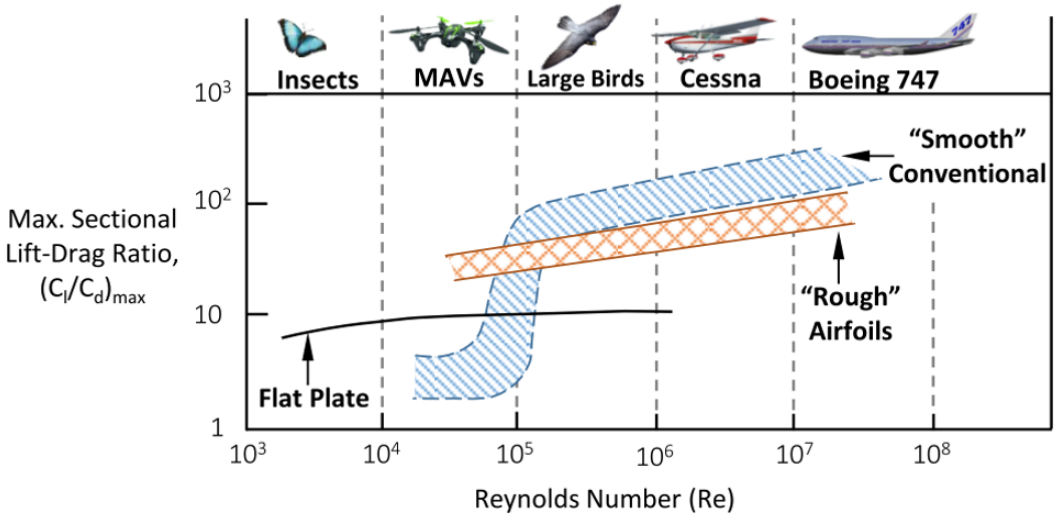

Figure 1.3: **Effect of Reynolds number on maximum sectional lift-drag ratio [2–4].**

numbers (Re $> 10^6$), inertial forces dominate and fluid momentum has a greater influence than viscous resistance. The resulting flow is mostly characterized by turbulent boundary layers. MAVs typically operate at low Reynolds number (10^4 – 10^5) because of their reduced size and low operational velocity. At low Reynolds numbers, viscous forces are dominant and the resulting flow is mostly characterized as laminar. As a result, the upper surface on the airfoil experiences large adverse pressure gradient around the leading edge. With laminar flow over the airfoil surface, the flow separates into a shear layer that reattaches as a turbulent boundary layer. The process of separation and reattachment creates a laminar separation bubble (LSB). The resulting flow is characterized by a turbulent boundary layer that remains attached throughout the surface.

The aerodynamic performance of any lifting surface is sensitive to the transition and separation of flow on the boundary layer of its airfoil section. As Reynolds

number decreases, the separated shear layer reattaches closer towards the trailing edge. Consequently, the size of both the laminar separation bubble (15%–40% chord) and thickness of the turbulent boundary layer increases, resulting in reduced maximum lift capability and increased parasitic drag [3]. At even lower Reynolds numbers (10,000 $<$ Re $<$ 50,000), the separation of shear layer occurs closer towards the trailing edge and is unable to reattach itself as a turbulent boundary layer. The phenomenon results in increased pressure drag due to the airfoil operating in trailing edge stall. Overall, flow physics lead to degraded maximum sectional lift-to-drag ratios at low Reynolds numbers (Fig. 1.3).

Figure. 1.3 shows that alternatives to conventional smooth airfoils, such as rough airfoils and flat plates, can result in increased lift-to-drag ratios at low Reynolds numbers. Early studies on low Reynolds number (20,000 $<$ Re $<$ 200,000) aerodynamics found that thin plate airfoils performed better than conventional thick cambered airfoils such as N60 [5]. In addition, a sharpened leading edge prevented flow separation and reduced viscous wake and profile losses [6, 7]. Recently, a systematic parametric study found that a 2-bladed rotor using carbon fiber blades with 1.2% thickness-to-chord ratio flat plate, 6.1% camber, large chord (21.4 mm), high taper (0.25-0.5), and negative blade twist of -10° to -20° achieved 34% increase in aerodynamic efficiency over a baseline NACA0012 rotor at Re $< 5 \times 10^4$ [4].

Overall, understanding low Reynolds number aerodynamics and its effect on MAV design is still a subject of ongoing research and one that proves critical for developing next generation platforms. While these studies focused on a conventional rotor (e.g main rotor), there is a potential to achieving higher performance with novel

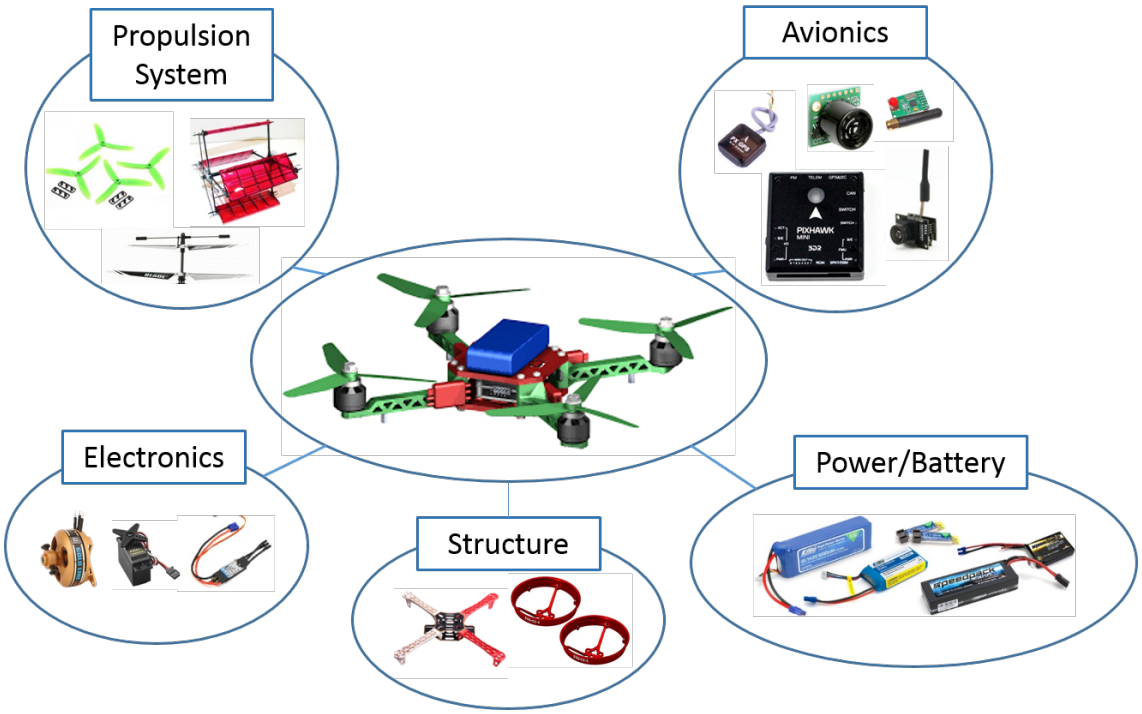

Figure 1.4: **Components required for MAVs.**

rotary-wing configurations. Such configurations are explored in this research.

1.2.2 Size, Weight,and Power (SWaP) Constraints

Aside from aerodynamic considerations, MAVs are also constrained by size, weight, and power (SWaP) requirements. Increasing endurance and range capability largely depends on efficiency of the propulsion system and the overall size and weight of the vehicle. The total mass of the vehicle should be minimized to effectively reduce power consumption. In particular, the minimum power required (ideal power) to hover for a rotary-winged platform with a single main rotor can be expressed as:

$$P = \frac{W^{3/2}}{\sqrt{2\rho A}} \tag{1.2}$$

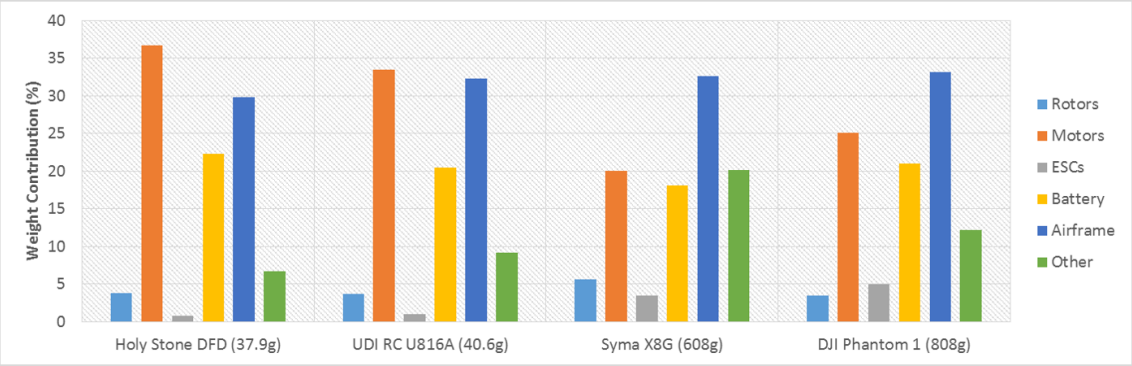

Figure 1.5: **Sub-system weights for commercial quadcopters.**

Minimum power required is dependent on vehicle weight (W), air density (ρ), and rotor area (A). As evident from the equation, power can be approximated by $W^{3/2}$ such that doubling the weight increases the power required by a factor of approximately 2.8. For a typical MAV, weight contribution can be divided into sub-systems containing propulsion, avionics, electronics, structure, and power plant (Fig. 1.4). The selection of avionics, batteries, and onboard electronics for the transmission system is severely limited by commercial availability.

Figure 1.5 presents a breakdown of sub-system contributions to total vehicle weight of commercial quadcopters [4]. Components not individually labeled (e.g avionics) are grouped together in the last category. As weight decreases by an order of magnitude, contribution of motors increases due to limited availability of commercially off-the-shelf components. Commercial availability of microelectronics plays a significant role in designing the propulsion system and even sets power requirements for MAVs. Overall, SWaP contraints require careful consideration of the MAV design in terms of mechanical complexity, commercial limitations of microelectronics, and power budget.

1.2.3 Flight Stability and Control

While reduced size and weight of MAVs provide operational benefits, the resulting low inertia coupled with limited aerodynamic damping contributes to degrading flight stability and control performance. Compared to full-scale vehicles, MAVs typically have higher thrust-to-inertia ratios that result in increased control sensitivity. The difference in flight dynamics is evident when considering scaling effects. A geometrically and dynamically scaled model can be compared with its full-scale counterpart using the following simplified relations for length (L), weight (W), and moment of inertia (I) [8, 9]:

$$L_m = L_a/N \tag{1.3}$$

$$W_m = W_a/N^3 \tag{1.4}$$

$$I_m = I_a/N^5 \tag{1.5}$$

Dynamic scaling equates the Froude number (ratio of inertia-to-gravity forces) of the model (m) to the full-scale aircraft (a). A $\frac{1}{N^{th}}$ scaled model will have $\frac{1}{N^3}$ the weight and $\frac{1}{N^5}$ the moment of inertia of its full-scale counterpart. Comparison between the Yamaha R-50 UAV and UH-1H confirmed the scaling laws [10]. Vehicle frequencies remain the same, but as the vehicle size is reduced, the subsequent decrease in weight and inertia results in increased sensitivity to control inputs. Therefore, stability augmentation is critical to achieve stable controlled flights for

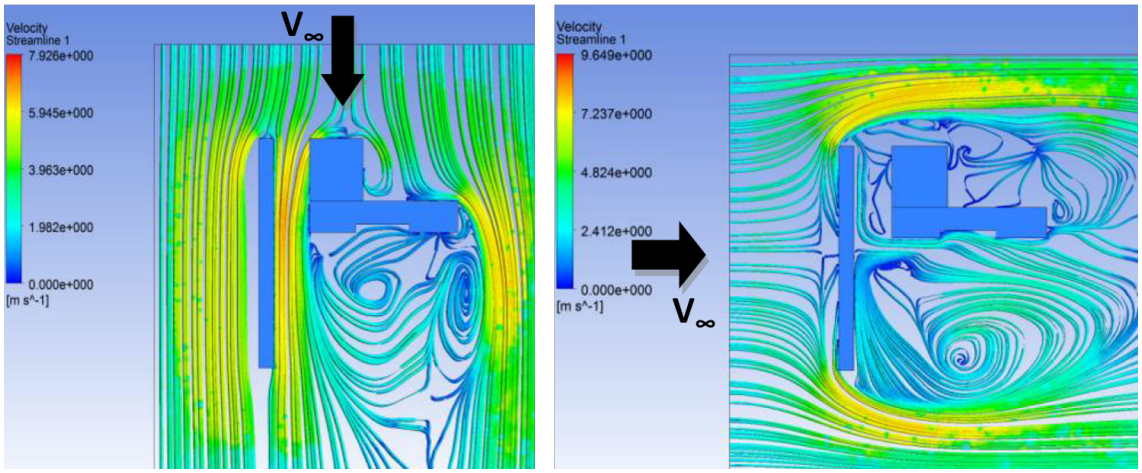

Figure 1.6: **CFD cases of wind stream-lines at 1.5 m above ground** [11].

MAVs.

Because of low inertia and operational speeds, MAVs are highly susceptible to environmental disturbances such as gusts. Flow fields in urban settings are especially prone to spatial and temporal variations arising from scattered layouts of buildings and trees (Fig. 1.6). These complex and unpredictable gusts can lead to critical perturbations in vehicle attitude, stall, and ultimate loss of control. For an edgewise gust, MAVs experience both drag force in the direction of the flow and pitching moment that rotates the vehicle away from the source. Possible methods to alleviate gust effects include increasing the vehicle's control authority and improving the closed-loop feedback system. Later sections discuss current literature in MAV gust studies and the unique control capability that increased gust tolerance capability of the unconventional MAV explored in this research.

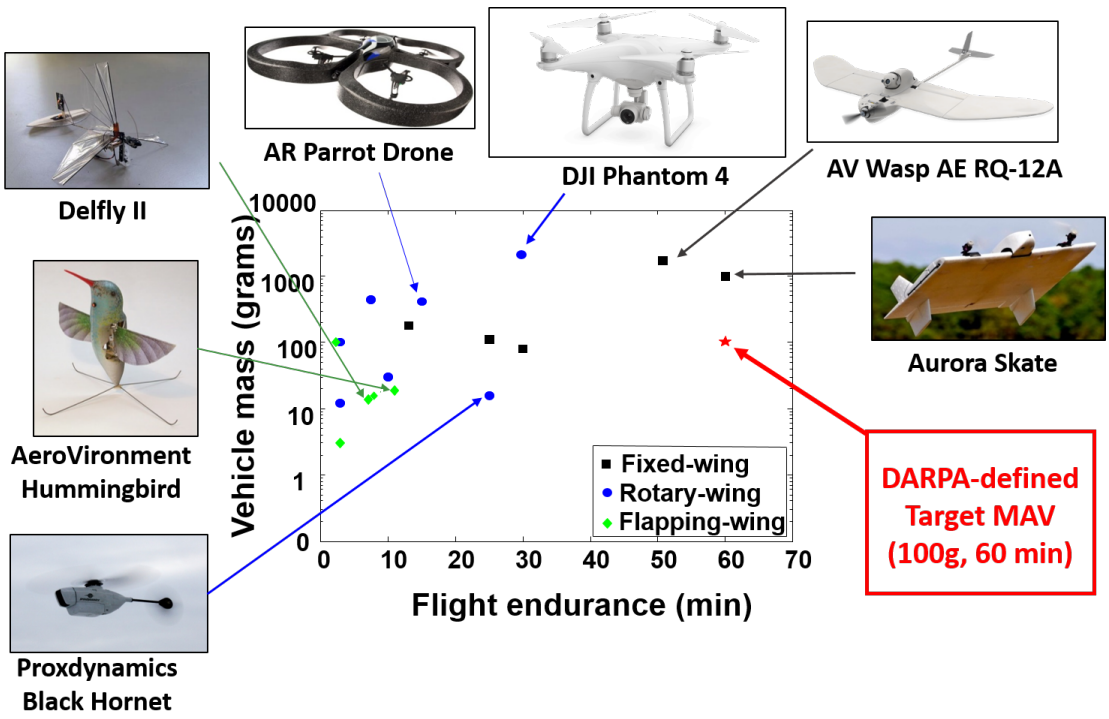

Figure 1.7: **Endurance vs. vehicle mass of current MAVs.**

1.3 Existing Micro Air Vehicle Configurations

Within the past decade, numerous successful MAVs have been developed that address many of these technical challenges. Existing vehicles can be classified into three major categories: fixed-wing, rotary-wing, and flapping-wing configurations.

1.3.1 Fixed-wing

Fixed-wing MAVs are the most prevalent due to their higher lift-to-drag ratio, mechanical simplicity, and ease of fabrication. Figure 1.7 presents flight endurance versus vehicle mass of current MAVs while highlighting the different configurations. As evident, fixed-wing MAVs typically have higher endurance than rotary-wing or flapping-wing configurations and are the closest to reach DARPA's definition of the

target MAV with weight less than 100 g and minimum endurance of 60 mins. One particular example is the AeroEnvironment Wasp AE RQ-12A that weighs 1300 grams and has an endurance up to 50 mins. The vehicle has a wing span of 102 cm (3.3 ft) and cruise speed of 10.3 m/s (23 mph). Typical cruise speed of fixed-wing MAVs range from 6 m/s to 20 m/s [12]. Although highly efficient, fixed-wing MAVs are unable to hover and are often limited to outdoor missions that require high endurance, long range, and high-speed flights.

1.3.2 Rotary-wing

Due to their hover to low-speed flight capability, rotary-wing MAVs tend to have higher mission performance in scenarios requiring indoor operation or in spatially restricted environments. Conventional rotary-wing MAVs rely on multi-rotor, single main rotor/tail rotor, or co-axial rotor designs. One of the most prominent recreational quadcopter is the DJI Phantom. The current iteration (DJI Phantom 4) weighs 1380 g, endurance up to 28 mins, and a maximum flight speed of 20 m/s. Compared to fixed-wings, rotary-wing MAVs typically have lower endurance because hovering and low-speed flight modes are states of high power consumption (Fig. 1.7). The situation is further exacerbated by the degraded performance of conventional airfoils at the low Reynolds number range (10,000 – 50,000) at which these vehicles operate. The maximum achievable figure of merit for rotary-wing MAVs is currently 0.65, compared to the 0.85 achieved by their full-scaled counterparts [13, 14].

1.3.3 Flapping-wing

Technical challenges ensuing from low Reynolds number aerodynamics, SWaP constraints, and flight stability and control have prompted for unconventional, 'out-of-the-box' MAV design solutions. One such solution is flapping-wing MAVs that are bio-inspired and categorized into avian-based and insect-based kinematics [15]. The flapping motion for avian-based platforms operate on the vertical plane and enable efficient high-speed flights. On the other hand, insect-based platforms operate on the horizontal plane using a reciprocating wing kinematics that achieve both translation and rotational motions. The reciprocating wing kinematics enable insect-based flapping-wing MAVs to hover.

While flapping-wing MAVs offer highly maneuverable and gust-tolerant solutions, existing platforms achieve low hover efficiencies. The AeroVironment Hummingbird Nano is a two-wing platform weighing 19 g with a tip-to-tip wing span of 16 cm (6.5 in). The vehicle has demonstrated continuous hover endurance of 8 mins, forward flight up to 4.9 m/s (11 mph), and tolerated gusts up to 2 m/s (5 mph) [16]. A key challenge in developing flapping-wing MAVs is that they are mechanically complex and experience heavy fatigue due to their high frequency flapping kinematics. In addition, much of the research into understanding the unsteady aerodynamics and aeroelasticity of flapping wings are still in the incipient stages. As a result, only a few flapping-wing MAVs have been successfully developed in the past decade.

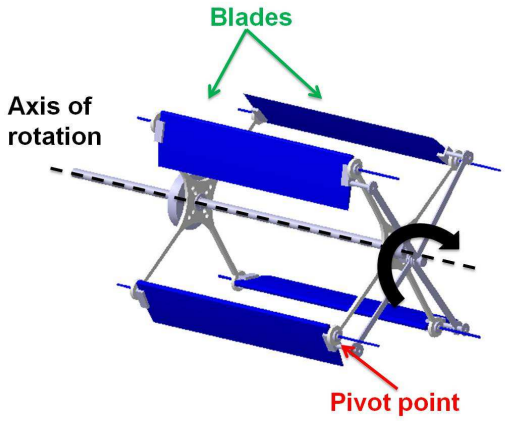

Figure 1.8: **Cyclorotor.**

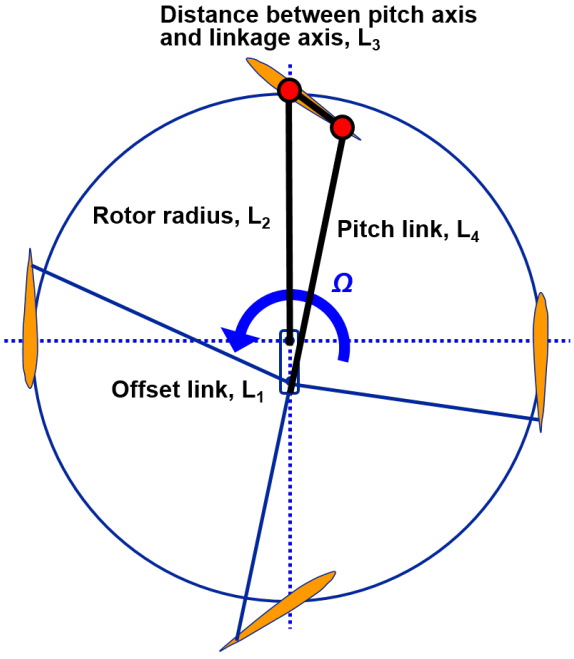

Figure 1.9: **Four-bar linkage pitching mechanism.**

1.3.4 Cycloidal Rotor Concept

Unconventional rotary-wing configurations such as the cyclocopter could be an alternate solution to developing a hover-capable, maneuverable, and gust tolerant MAV. The cyclocopter relies on cycloidal rotors (cyclorotors) as main source of propulsion. The cyclorotor is a horizontal axis propulsion system where the blades span parallel to the axis of rotation and perpendicular to direction of flight (Fig. 1.8). The unique arrangement of the cyclorotor blades with a pitching mechanism enables a passive cyclic blade pitching around the rotor azimuth. The pitching mechanism is designed such that the blades have a positive geometric angle of attack at both the top and bottom halves of the circular trajectory (Fig. 1.9), thereby producing a net resultant thrust.

Since the span-wise sections of the cyclorotor blade operate at similar aerodynamic conditions (e.g flow velocity, angle of incidence, Reynolds number, etc.), the cyclorotor can be easily optimized for maximum power loading (thrust/power). Another advantage of the cyclorotor is its thrust vectoring capability by changing the phase of cyclic pitching. Rotating the phase angle rotates the location of the maximum blade pitch angle along the rotor azimuth. As a result, both the magnitude and direction of the thrust vector can be adjusted by varying the blade pitch amplitude and phasing, respectively. The current research is focused on exploring improvements in flight performance of a cyclocopter configuration using thrust vectoring capability. Detailed information on the cyclorotor operating principles and cyclocopter vehicle development are provided in Chapter 2.

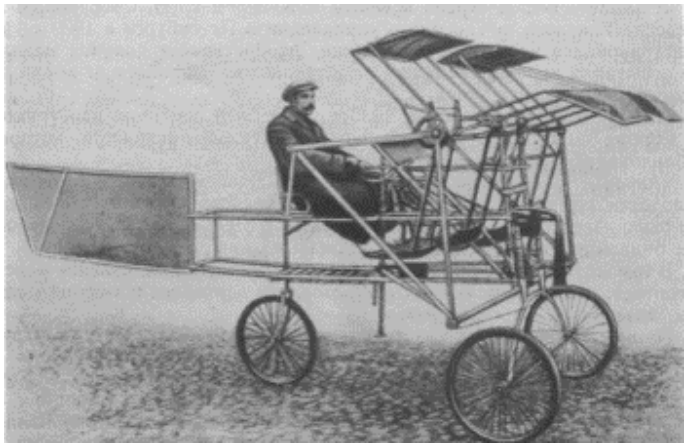

Figure 1.10: **Rendering of an early Samoliot cyclocopter concept by E.P. Sverchkov.**

1.4 Previous Studies

The following sections are categorized into literature review of (1) cyclocopter research and (2) MAV research on the experimental studies related to the current work. The latter includes studies pertaining to other rotary-wing configurations.

1.4.1 Existing Cyclocopter Research

While many breakthroughs in cyclorotor research have occurred in recent years, attempts to develop a cyclocopter date back to early 20th century (1909-1914) [17]. Numerous full-scaled models intended to seat one pilot were developed, but none of the attempts were successful in achieving flight. One of the earliest known cyclocopter was the "Samoliot" (wheel ornithopter) developed in 1909 by E. P. Sverchkov, a Russian military engineer. The manned cyclocopter was estimated to have an empty weight of 200 kg (Fig. 1.10). Another early cyclocopter was developed between 1909-1914 in France. However, the invention did not have any documentation

Figure 1.11: **Kirsten's cycloplane featured in Popular Science, model in the wind tunnel, and Kirsten-Boeing experimental test rig [18, 19].**

aside from a video of the failed flight test showing the rotors disintegrating.

In the 1920s, series of research on cycloidal propulsion systems for aerial and marine applications were published by Professor Kurt Kirsten from the University of Washington [18,19]. A collaboration with W. E. Boeing led to the development of the "Kirsten-Boeing" propeller, an early version of the cycloidal propeller (Fig. 1.11). Kirsten's idea was to equip an airship and a "cycloplane" with the propeller to provide three-dimensional control. The first model of the "cycloplane" was built with a small 26 cm (10.2 in) propeller and 15 cm (5.9 in) blade span. After wind tunnel results of the model showed satisfactory results, a larger model was built and six propellers were selected to power the USS Shenondoah airship. However, the airship crashed before the propellers were installed, which ultimately halted further development.

Kirsten also modified the propellers for maritime application and sold his patent to the Voith-Schneider Corp. Replacing the rudder, the experimental pro-

Figure 1.12: **Voith-Schneider propeller used by tugboats [20, 21].**

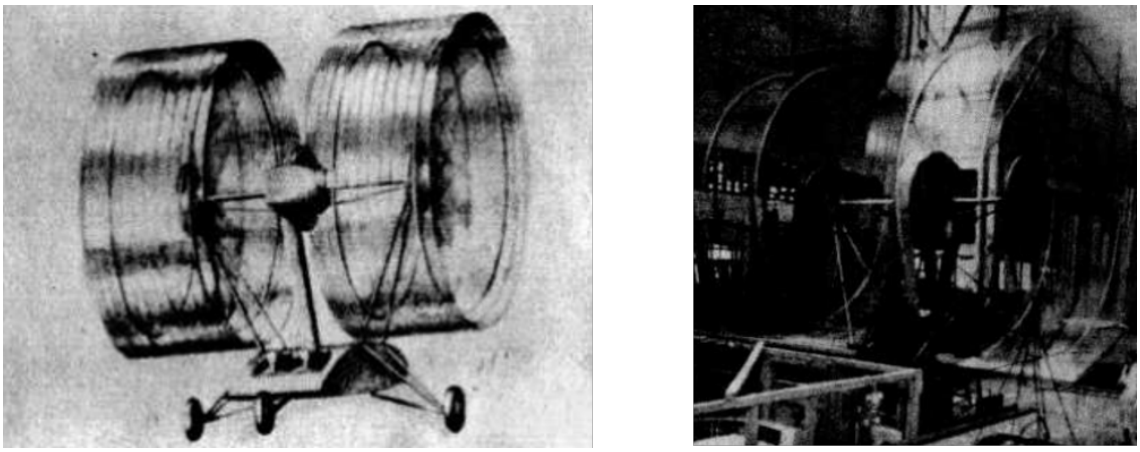

Figure 1.13: **Strandgren's cyclogyros [22].**

peller with its thrust vectoring capability could provide the necessary propulsion and control for boats. A variant of Kirsten's propeller was developed in 1931 by Ernst Schneider, an Austrian inventor [20,21]. The Voith-Schneider propeller (VSP) is still successfully being used for commercial applications (Fig. 1.12).

From 1924-1933, Swedish-French engineer Strandgren conducted series of experiments with the cyclogyro model and ultimately published the first scientific study on cycloidal rotors [22]. The publication included a simplified quasisteady aerodynamic analysis of a cyclogyro to understand how lift and propulsive thrust

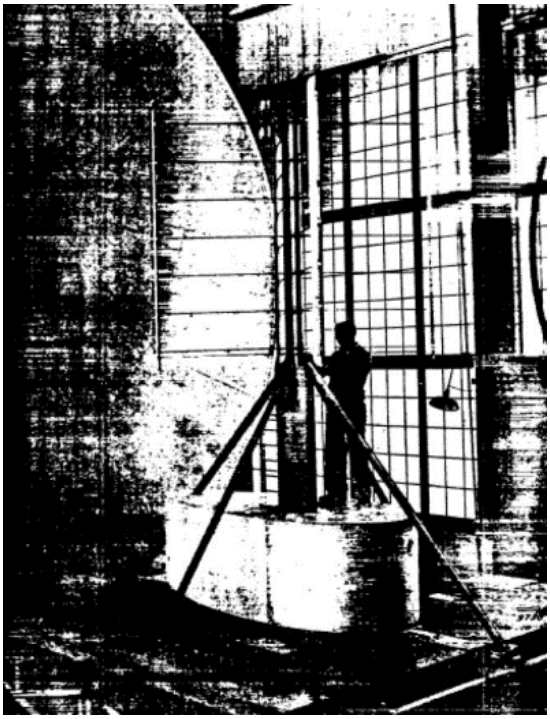

Figure 1.14: **Wheatley's experimental setup [23].**

are generated. The analysis showed that varying the amplitude and phasing of the blade pitch kinematics could change the resultant magnitude and direction of the rotor's thrust. He also explored the feasibility of the concept and built a 600 kg model (Fig. 1.13).

John B. Wheatley at the National Advisory Committee for Aeronautics (NACA) followed and continued Strandgren's analysis. In 1933, Wheatley published a simplified aerodynamic theory using blade element momentum theory (BEMT) to predict forward flight performance of the cyclogyro [23]. He also performed a case study to investigate the feasibility of a 1360 kg (3000 lbs) cyclorotor-based aircraft. In 1935, Wheatley and Windler conducted experimental studies of a cyclorotor in forward flight to compare against his analysis. The study was performed on a 4-bladed cyclorotor with a diameter and span of 2.4 m and blade chord of 0.095 m. While

Figure 1.15: **Cyclocopters developed by the Seoul National University [24–28].)**

the results qualitatively agreed with model, the relative magnitudes significantly differed because of all the simplifying assumptions used to derive the model.

With a lapse in cyclocopter research up to 1998, modern work largely focused on UAV and MAV-scale vehicle development. Advent of microelectronics, composites (e.g carbon fiber), rapid prototyping (additive manufacturing), and improved understanding of aerodynamics led to renewed interest in the cyclocopter configuration. Since 2003, many UAV-scale versions of the cyclocopter were developed at the Seoul National University in South Korea [24–28]. Work completed by Kim et. al include both computational and experimental studies in order to improve the design of a 12.8 kg quad-cyclocopter and a 110 kg twin-cyclocopter UAV (Fig. 1.15). The quad-cyclocopter used four elliptical blades with a blade span and rotor diameter of 0.5 m, NACA0018 airfoil, and operating speed of 1100 rpm. The vehicle's flight stability was augmented with a commercial attitude heading reference system (AHRS) which enabled it to demonstrate stable flight. Pilot controls included throttle, pitch, roll, and yaw, which were all achieved by modulating rotational speeds of

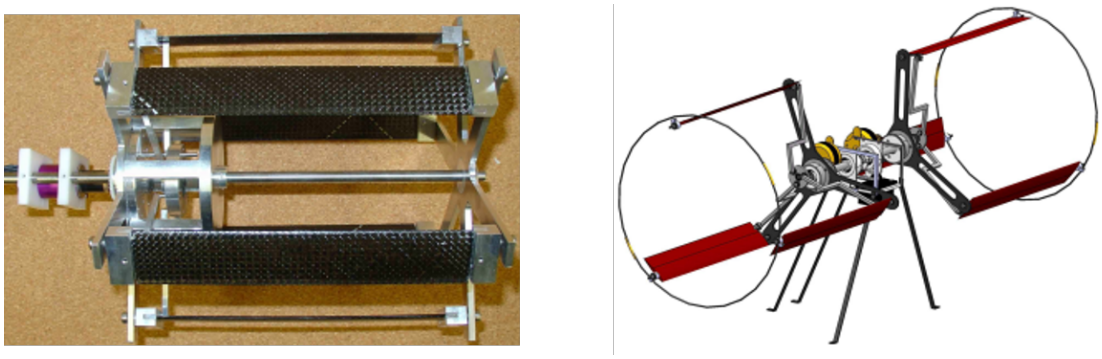

Figure 1.16: **Early twin-cyclocopter work conducted at the University of Maryland [29].**

the cyclorotors. The UAV-scale twin-cyclocopter used 4-bladed cyclorotors with 2 m diameter, blade span of 1.5 m, NACA0018 airfoil, and operating speed of 420 rpm. An additional anti-torque horizontal tail rotor with diameter of 0.574 m operated at 5320 rpm and also provided pitch control.

In 2006, Sirohi, Parsons, and Chopra conducted feasibility studies of MAV-scale cyclocopter at the University of Maryland [29, 30]. Experimental studies were conducted on a cyclorotor with a 15 cm diameter and blade blade span. The effect of rotational speed, blade pitch amplitude, and number of blades on rotor thrust and power consumption in hover were systematically studied. Analysis using a double-multiple-streamtube model was developed and compared against the experimental results. Results from the study was used as a basis for the conceptual design of a twin-cyclorotor solely using two cyclorotors (Fig. 1.16).

From 2008 to 2012, Benedict et. al performed comprehensive experimental and analytical studies on multiple MAV-scale cyclocopters at the University of Maryland [31–35]. An extensive parametric study was conducted to determine blade airfoil, rotor span, radius, rotor solidity, number of blades, blade chord length,

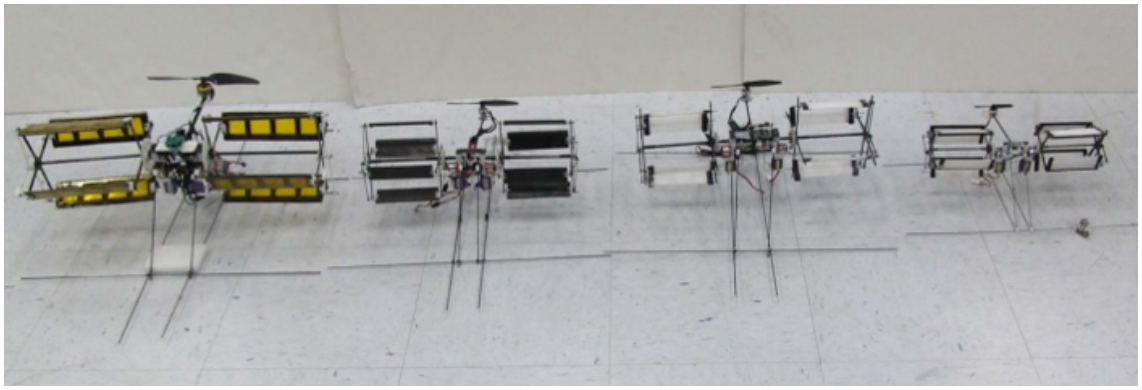

Figure 1.17: **Hover-capable cyclocopter MAVs developed at the University of Maryland.**

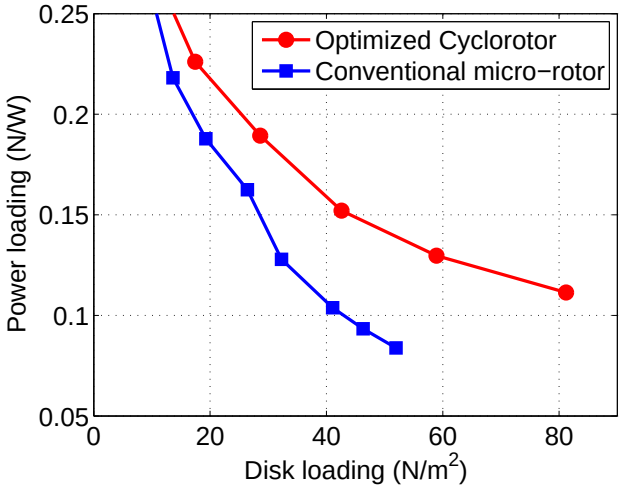

Figure 1.18: **Power loading (thrust/power) vs. disk loading (conventional micro-rotors vs. optimized cyclorotor)**

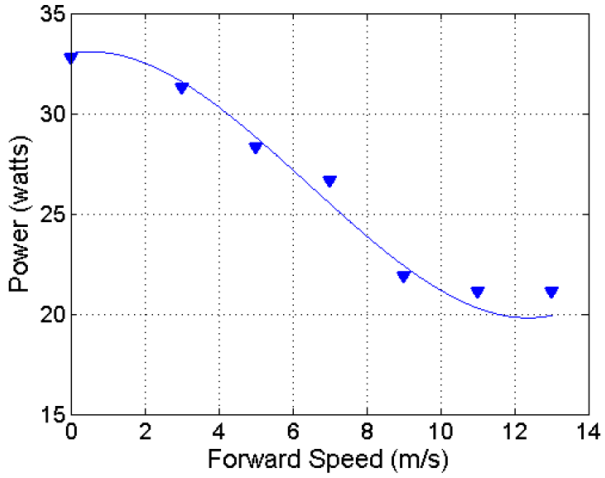

Figure 1.19: **Power versus forward speed for constant rotational speed of 1740 rpm (13.88 m/s) for level, steady flight [36, 37].**

blade planform, blade pitching amplitude, phase, and blade kinematics for an optimized cyclorotor. Compared to a conventional edge-wise rotor at the same disk loading (thrust/disk area), the optimized cyclorotor achieved higher aerodynamic power loading (Fig. 1.18). The results led to the successful development of multiple hover-capable cyclocopter MAVs (Fig.1.17). The twin-cyclocopter configuration used two cyclorotors and an additional horizontal tail rotor that counteracted the reaction torque from the cyclorotors and also provided pitch control. These vehicles ranged from 100 grams to 550 grams and relied on both rotational speed and thrust vectoring to achieve controlled hover. Since 2014, Benedict et. al continued work on the cyclocopter configuration at Texas A&M University and developed a meso-scale cyclocopter weighing only 29 grams [38].

Wind tunnel studies conducted by Jarugumilli, Benedict, and Chopra on an isolated cyclorotor have shown that an aircraft using cyclorotors could efficiently reach very high forward speeds without any lift augmenting devices/surfaces [36,37].

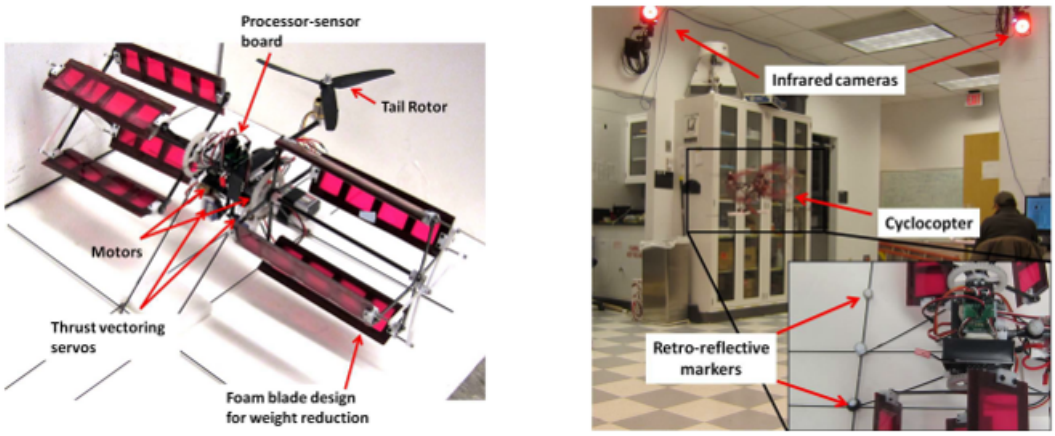

Figure 1.20: **System identification conducted on a twin-cyclocopter by the University of Maryland [39].**

It was observed that the power required for a cyclorotor to maintain a steady, level flight significantly drops with forward speed (Fig. 1.19) up to almost an advance ratio of 1, due to increased lift producing efficiency of the cyclorotors. Unlike a conventional helicopter, the forward flight of a cyclocopter would be performed purely by utilizing thrust vectoring (varying cyclic pitch phasing) instead of pitching the entire vehicle forward. Thrust vectoring enables the cyclocopter to maintain a level pitch attitude in forward flight. Unlike the transition for a tilt-rotor, transition from hover to forward flight for the cyclocopter is possible without undergoing any configuration changes. Overall, the study showed that thrust vectoring provides a mechanically simple and power efficient method of achieving forward flight.

To evaluate the vehicle's tolerance to external gust disturbances, Hrishikeshavan, Benedict, and Chopra experimentally derived a comprehensive flight dynamics model in hover using time domain system identification techniques [39]. The study was conducted using a 500 g twin-cyclocopter tested inside a motion capture system

(Fig. 1.20). It was the first vehicle performance study and system identification conducted on the cyclocopter MAV. The experiments involved series of input excitations that excited different dynamic modes. Throughout the experiments, vehicle response was recorded by both the motion capture system and onboard autopilot. The results provided insights into the existence of a destabilizing gyroscopic coupling between roll and yaw degrees of freedom, which required implementation of decoupling methods in the controls system. When compared to other rotary-based MAV platforms, the cyclocopter had higher longitudinal and lateral gust tolerances in hover (7.9 m/s and 17 m/s, respectively). The flight dynamics model from the study revealed many key insights into the vehicle's maneuverability in hover conditions and led to an improvement of the closed-loop feedback control system.

1.4.2 Gust Tolerance Studies of Rotary-wing MAVs

While flow fields in urban environments are complex and unpredictable, research studies have attempted to study the effects of gusts and turbulence on MAV performance. Galway et al. [40] modeled the effects of building wakes on a Yamaha R-50 R/C helicopter analytically using CFD and estimated that the turbulent flow fields cause up to 10° variations in attitude for wind up to 8 knots. There has also been numerous studies that took an experimental approach and either flight tested MAVs in front of a wind tunnel or a custom gust generation device. Johnson and Jacob [41] assembled a gust and shear wind tunnel using a bank of independently controlled computer fans and a flow straightener. The fan bank generated up to 5

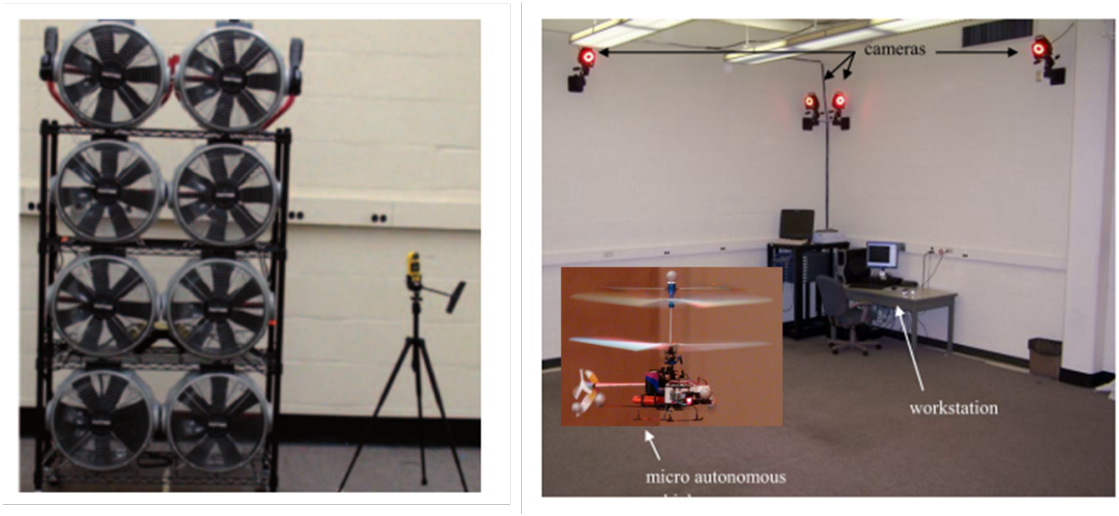

Figure 1.21: **Synthetic gust generation device and experimental setup assembled by Georgia Institute of Technology [42].**

m/s freestream velocity and a slow gust ramp input lasting 3s. The study tested a tethered R/C fixed-wing biplane MAV with a nose propeller in order to characterize its wake.

Zarovy et al. [42] assembled a gust generation system using a bank of eight rotary fans that are simultaneously controlled to achieve up to 2.6 m/s (Fig.1.21). The study specifically looked at scaling effects on disturbance rejection capability of single-main-rotor MAVs and found that the Lama 400, the largest tested R/C helicopter, was capable of withstanding 2.6 m/s gusts. In the experiments, the MAVs vertically took-off and slowly translated into the flow-field region generated by the fans. The metric used for characterizing performance is the spherical error probable (SEP) which covers 50% of the vehicles translational trajectory in gust and a smaller magnitude indicates higher gust tolerance. Similarly, Hrishikeshavan et al. used a comparable metric to study gust effects on a shrouded rotor MAV and found that the vehicle is capable of tolerating gusts up to 3 m/s [43]. The study

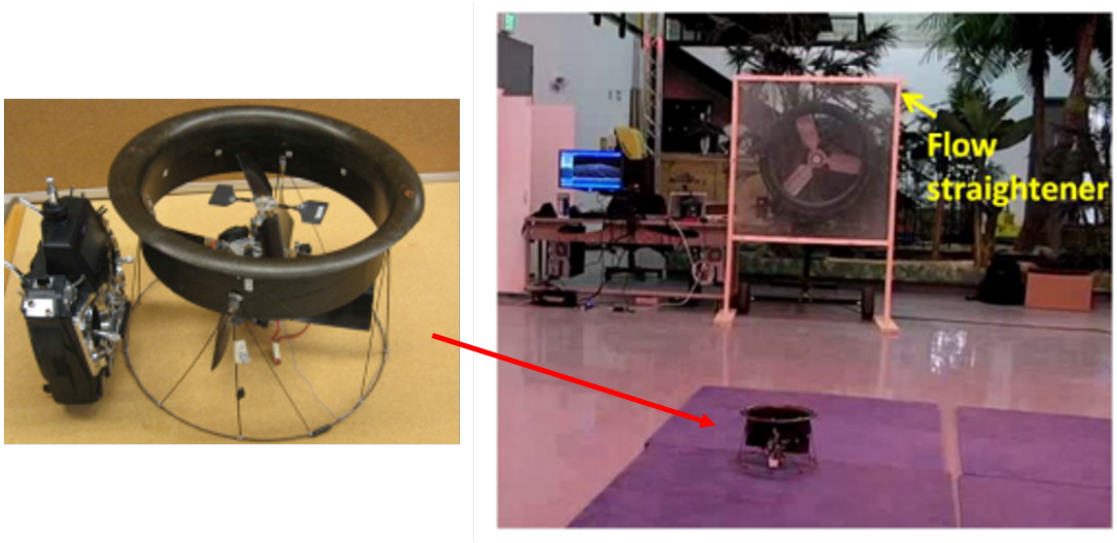

Figure 1.22: **Experimental setup for gust study of a ducted-fan MAV conducted by the University of Maryland [43].**

used the circle error probable (CEP) which restricts the radius of vehicle's trajectory within the X-Y plane. The gust generation device used a large rotary fan with a honeycomb flow-straightener to test the MAV in free flight. In addition, the vehicle was first mounted on a gimbal stand in front of an open-jet wind tunnel in order to measure the vehicle's control moments against a gust perturbation.

While there has not been any prior experimental studies investigating the response of a cyclocopter MAV to gust perturbation, Hrishikeshavan et al. conducted a maneuverability and disturbance rejection analysis using a linear 6-DOF flight dynamics model of the cyclocopter in hover [39]. As previously mentioned, the study estimated that a 550 g cyclocopter had longitudinal and lateral gust tolerances of 7.9 m/s and 17 m/s, respectively. Chapter 6 investigates the gust tolerance of the 550 g cyclocopter through wind tunnel studies and tethered flight tests using a synthetic gust generation device.

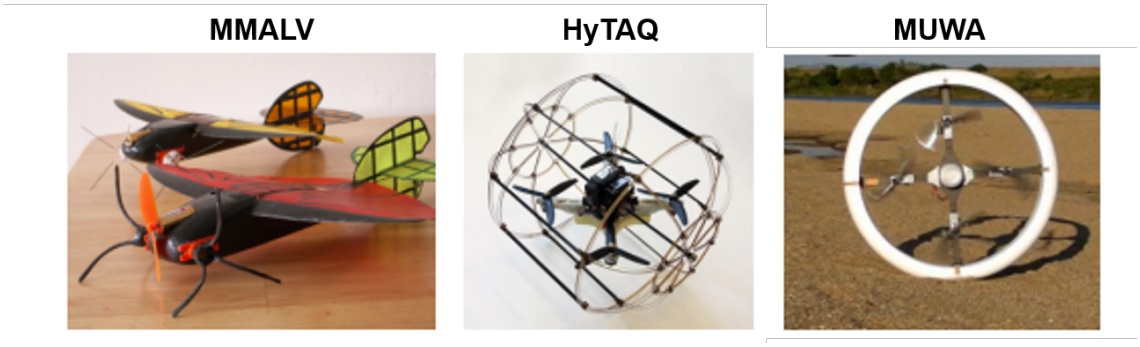

Figure 1.23: **Existing multi-modal micro air vehicles [44–46].**

1.4.3 MAVs with Multi-mode Locomotion Capability

Multi-mode mobility is prevalent in biological systems where organisms such as birds and insects efficiently switch between different modes of locomotion to conserve energy, traverse long distances, and maneuver through confined spaces. Biologically-inspired multi-modal MAV such as the Morphing Micro Air-Land Vehicle (MMALV) achieves flight using a combination of nose propeller and morphing flexible wings [44]. The MMALV weighs 120 g and has a maximum dimension of 30 cm (wingspan) 7.12. The vehicle achieves terrestrial locomotion using rotating wheel-legs (Mini-Whegs^{TM}) that are independently driven by a motor and inspired by locomotion principles of the cockroach. While the vehicle is capable of flight, it is unable to hover and requires either a 3–5 m runway or a 6 m vertical drop in order to take-off.

Rotary-winged multi-modal MAV such as the Hybrid Terrestrial and Aerial Quadrotor (HyTAQ) relies on conventional edgewise rotors with fixed-pitch propellers as main source of propulsion [45]. The 570 g platform includes a quadcopter suspended inside a rolling cage that enables terrestrial locomotion and also functions

as the landing gear 7.12. Although the multi-modal design is mechanically simple, rolling motion is attained aerodynamically using propulsive thrust from the rotors instead of directly harnessing the torque of the motors.

The Multi-field Universal Wheel for Air-land (MUWA) quadcopter is capable of aerial, terrestrial, and aquatic locomotion [46]. Rotors are independently driven by brushless motors and use variable pitch propellers that are actuated by rotary servos. Terrestrial and aquatic modes rely on the ring-shaped polystyrene foam body that operates as a mono-wheel, buoy, and landing gear. In terrestrial mode, the MUWA platform acrobatically flips onto its foam body and applies rotational control by differentially modulating torque of the four motors (Fig.7.12). For aquatic locomotion, only a fraction of the total resultant lift is applied to achieve translation since the vehicle has to pitch to generate propulsive thrust. Overall, to function in multiple modes of locomotion, the MUWA platform uses eight different actuators and an external foam body. Along with its foam outer-ring, MUWA weighs 2100 g and spans 0.91 m in diameter and 0.12 in body thickness.

1.5 Research Objective and Technical Approach

Previous work included series of experimental and analytical work on the cycloro-tor propulsion system, as well as vehicle development for both twin-cyclocopter and quad-cyclocopter configurations. However, previous studies mainly focused on demonstrating stable flight in hover and understanding flight dynamics to improve vehicle performance in that limited flight envelope. Apart from performance studies

and flow field measurements of an isolated cyclocopter in forward flight, none of the previous studies integrated thrust vectoring capability as a key control input in achieving stable level forward flight. As a result, there is a lack of understanding of cyclocopter flight dynamics in forward flight and the required control strategies to achieve level power-efficient transition from hover to level forward flight.

Moreover, the only gust tolerance study of the cyclocopter configuration was the analytical grammian-based maneuverability and disturbance rejection analysis using the experimentally derived linear 6-DOF flight dynamics model of the vehicle in hover. While the results of that study provide a foundation for gust tolerance assessment of the cyclocopter, the results still require experimental validation. In addition, previous studies focused on demonstrating controlled flight with a basic avionics package and closed-loop feedback system for flight stability and control. Additional sensors for flight performance diagnostics and a supplementary gust rejection controller could augment cyclocopter's performance against external disturbances.

Furthermore, previous studies explored ways of increasing cyclocopter's endurance through systematic aerodynamic optimization of the cyclorotors. An alternative and unconventional method of conserving energy is switching between different modes of locomotion. Such multi-mode locomotion capability has already been demonstrated for fixed-wing and rotary-wing MAVs.

With the limitations of the previous studies in mind, the key objectives of the present work include:

1. Develop control strategies required to achieve power-efficient level forward flight for the twin-cyclocopter configuration using a combination of thrust vectoring and rotational speeds of the two cyclorotors and a horizontal nose rotor.

2. System Identification of a 6-DOF flight dynamics model in forward flight and conduct performance studies in the wind tunnel in order to understand effects of cross-coupling dynamics and thrust vectoring capability on vehicle's stability and control.

3. Experimentally evaluate gust tolerance strategies based on control inputs (pitch control vs. thrust vectoring) and type of gust feedback controller (flow-based vs. position-based) to increase cyclocopter's performance against external disturbances.

4. Determine feasibility and performance of cyclocopter's multi-mode capability by demonstrating efficient aerial, terrestrial, and aquatic locomotion with seamless transition between modes. In particular, explore a quad-cyclocopter configuration unaffected by cross-coupling dynamics in hover.

1.5.1 Thesis Organization

The current chapter provided an overview of technical challenges affecting MAV design and summarized existing MAV configurations (fixed-wing, rotary-wing, flapping-wing). In addition, the chapter also presented a thorough literature review of previous work on cyclorotors and cyclocopter vehicle developement.

Chapter 2 provides a detailed overview of the twin-cyclocopter configuration developed in this research. The chapter also discusses the basic operating principle of the cyclorotor and the mechanical design of the four-bar linkage-based pitching mechanism. The aerodynamic and structural design of cyclorotor blades are also discussed, along with the resulting performance of the cyclorotor and the horizontal nose rotor.

Chapter 3 includes an extensive review of avionics including autopilots, sensors, and onboard computers for executing computationally intensive tasks such as image processing. The chapter first reviews two custom autopilots implemented on the cyclocopter and then surveys sensors and onboard computers commercially available for MAVs. These sensors are categorized for flight stability and control, flight performance diagnostics, and guidance and navigation (autonomy). Finally, the chapter concludes with an overview of the closed-loop feedback system implemented on the cyclocopter.

Chapter 4 focuses on the control strategies developed for the cyclocopter in hover and forward flight. Sources of cross-couplings across all flight modes are also discussed in details. Results from wind tunnel studies conducted using a 5-DOF experimental stand are used to develop a control strategy to achieve decoupled dynamics. Furthermore, effects of free-stream velocity, rotational speed, and phasing angle on the roll-yaw cross-couplings are closely investigated and used to determine control inputs to achieve zero pitch attitude at various airspeed.

Chapter 5 presents a 6-DOF flight dynamics model of the cyclocopter that is experimentally determined using time-domain system identification technique.

The existence of the longitudinal control derivative in translation mode is used to evaluate the control authority of thrust vectoring to command forward speed. The model is also used to identify sources of roll-yaw coupling and develop decoupling methods to achieve stable flight.

Chapter 6 examines the disturbance rejection capability of the cyclocopter through series of experiments in the wind tunnel and using a synthetic gust generation device. The results from the wind tunnel studies are used to evaluate response to gust perturbation along the longitudinal and lateral axis. The chapter also compares control authorities of pitch control versus thrust vectoring and feedback control schemes of position feedback versus flow feedback. Results of the comparative study of gust rejection strategies are provided for the 6-DOF experiments in front of a synthetic gust generation device for step gust inputs along the longitudinal axis and crosswinds.

Chapter 7 discusses design modifications to a quad-cyclocopter configuration to achieve multi-mode locomotion capability. Key structural components used to enable aerial, terrestrial, and aquatic modes are discussed. The chapter also presents the control strategies for each mode and multi-mode testing results. Results include onboard attitude data from a custom auto-pilot, power consumption for all modes, and performance in terrestrial mode evaluated using a 1-DOF test rig and VICON motion capture system.

Chapter 8 concludes this dissertation with summaries of previous chapters and suggestions of recommended future work. Overall, the chapter provides a final discussion of key contributions from this research.

Chapter 2: Vehicle Design

2.1 Overview

In order to realize improvements in aerodynamic performance, power-efficient forward flight, gust tolerance, maneuverability, and multi-mode capability, an unconventional configuration such as the cyclocopter is explored in this work. This chapter covers design and development of the cyclocopter with a focus on cyclorotor design. The key operating principle of cyclorotor and the associated mechanisms are discussed. Aerodynamic and structural variations in blade design are thoroughly explored with emphasis on weight reduction and hover performance. The chapter also summarizes parametric test results used to select the nose rotor propeller and presents scalability study on developing a meso-scale cyclorotor. Overall, this chapter discusses the development of the 550 g twin-cyclocopter that is used as the testbed and demonstrator for the remaining chapters.

2.2 Twin-Cyclocopter Configuration

The twin-cyclocopter relies on two cycloidal rotors (cyclorotors) as main source of propulsion and an additional horizontal anti-torque nose rotor. The nose rotor

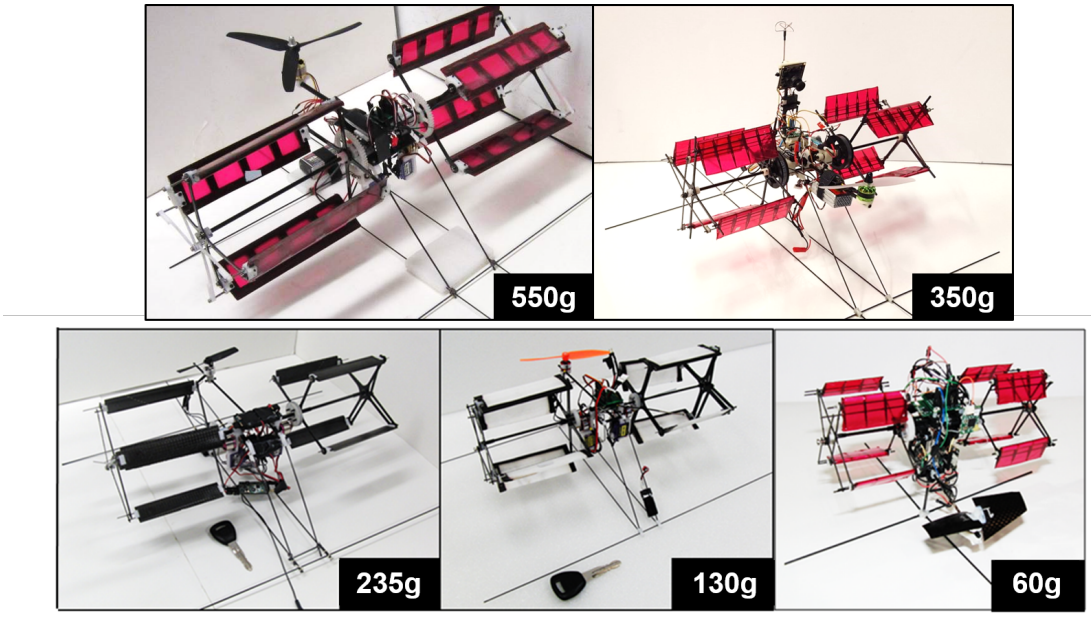

Figure 2.1: **Twin-cyclocopters developed at University of Maryland.**

counteracts the torque resulting from both cyclorotors spinning in the same direction. Anti-torque capability from the nose rotor is also augmented by increasing the horizontal offset between the rotor and vehicle's center of gravity (c.g). The offset reduces the thrust required from the nose rotor which subsequently minimizes its size. The nose rotor also provides pitch control by modulating its rotational speed. Work from this research has produced twin-cyclocopters ranging from 60 grams to 550 grams (Fig. 2.1).

The rest of the chapters will focus on the 550 g twin-cyclocopter. The vehicle has a lateral dimension of 0.381 meters (1.25 feet), longitudinal dimension of 0.457 meters (1.5 feet), and a height of 0.305 meters (1 foot) (Fig. 2.2). Each cyclorotor has a diameter of 0.152 meters (6 inches), blade span of 0.171 meters (6.75 inches), a chord of 0.051 meters (2 inches), and is independently driven by a 1400kV AXI 2204/54 out-runner motor through a 7.5:1 single-stage transmission. The horizontal

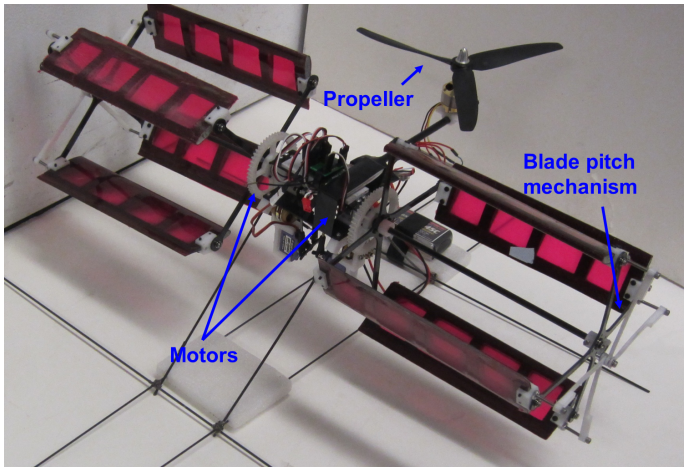

Figure 2.2: **550 g twin-cyclocopter.**

Table 2.1: Weight distribution comparison of previous generation twin-cyclocopters (60–550g).

System	60g %	130g %	235g %	550g %
Cyclorotors	23	33	34	27
Electronics	16	17	14	11
Propeller System	8	16	6	9
Battery	16	14	18	19
Structure	13	9	9	12
Transmission	12	7	17	21
Avionics	12	4	2	1
Total	**100%**	**100%**	**100%**	**100%**

nose rotor is directly driven by a 1200kV eRC BL400 brushless outrunner motor and is fitted with a 3-bladed GWS 9050 propeller. All three rotors are powered by a single 3S 11.1 volt 850 mAh Lithium-Polymer battery.

Weight distribution of various twin-cyclocopters is compared in Table 7.3. All of the vehicles are equipped with rotors individually driven by a brushless out-runner motor and two servos that rotate the thrust vectors of the cyclorotors. Additional onboard components include avionics and power supply. From the weight distribu-

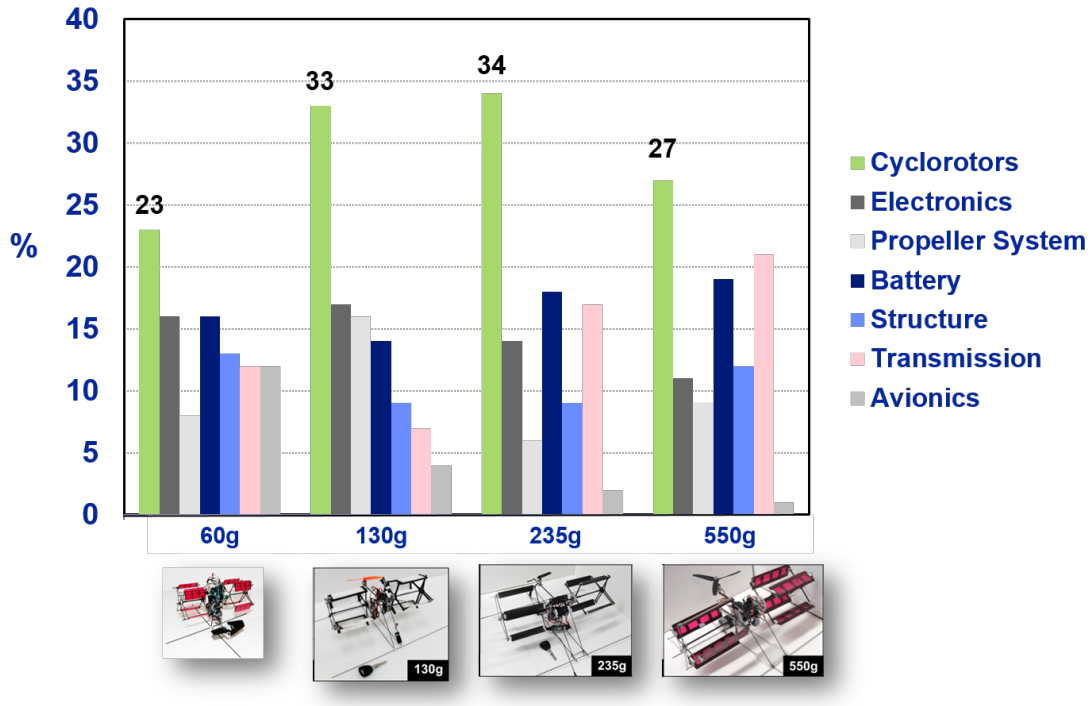

Figure 2.3: **Weight distribution of twin-cyclocopters are different scales.**

tion, it is evident that the cyclorotors make up the majority of the empty weight fraction of the vehicle. Aside from the 60g vehicle, cyclorotors consistently constitute 27–34% of the total gross weight and the range largely varies based on blade design (Fig. 2.3). Therefore, significant effort was focused on designing lightweight and structurally robust blades and pitching mechanism in order to reduce total vehicle weight and increase endurance. Another noticeable trend is that the weight contribution of the transmission system (cyclorotor motors, gears, bearings, and associated screws) increases with vehicle scale.

As expected, the weight contribution from electronics (servos, ESCs, and associated wires) increase at smaller scales. That is because the size of the selected electronics is limited by what is commercially available. A similar trend is observed

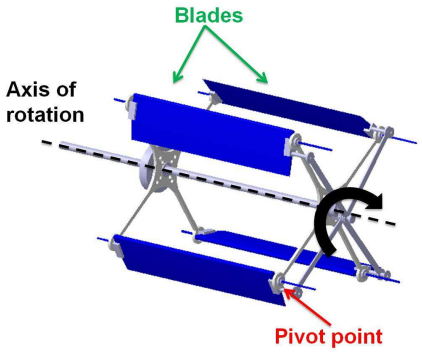

Figure 2.4: **Cyclorotor.**

in the avionics (processor, breakout board, and satellite receiver) since all of these vehicles use the lightest available onboard processor. The LiPo batteries compose 14–19% of the total vehicle weight and is also limited by commercial availability. Overall, the most significant improvements to the vehicle design can be made through the cyclorotors, which directly affects the transmission system, anti-torque propeller size, and structural weight (landing gear, fuselage, etc.).

2.3 Cyclorotor Design

The blades on the cyclorotor follow a circular trajectory about a horizontal axis of rotation (Fig. 2.4). The cyclorotor blade span is parallel to the horizontal axis and perpendicular to the direction of flight. A pitching mechanism cyclically varies individual blade pitch angle along a circular trajectory. In hover, the blades achieve a positive geometric pitch angle at both top and bottom portions of the trajectory, yielding a net resultant thrust. Both the magnitude and direction of the thrust vector can be adjusted by varying the pitch amplitude and phasing of the blade pitching kinematics.

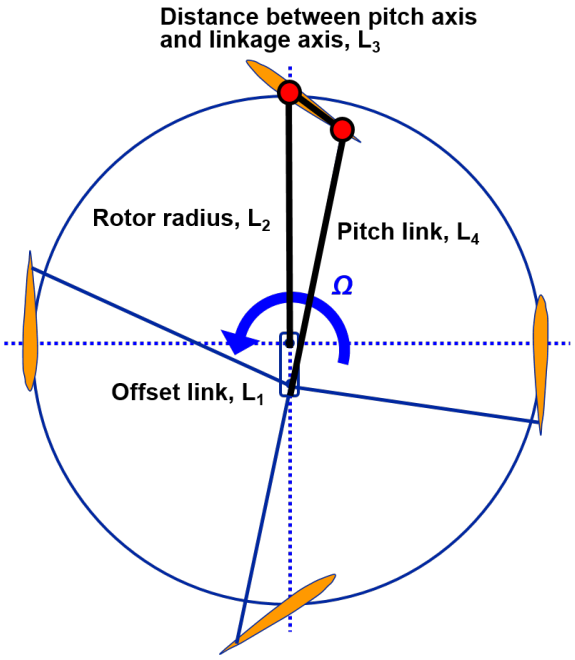

Figure 2.5: **Four-bar linkage pitching mechanism.**

Since all spanwise blade sections of the cyclorotor operate under similar aerodynamic conditions (i.e., flow velocity, angle of incidence, Reynolds number, etc.), the blades can be easily optimized to achieve best aerodynamic efficiency [31]. In addition, the uniform spanwise distribution of aerodynamic forces enables the cyclorotor to operate at lower tip speeds, thereby improving the acoustics signature. Another advantage of the cyclorotor is its unique thrust vectoring capability that is achieved by varying the phase of the cyclic pitching. By thrust vectoring instead of pitching forward, the cyclocopter can achieve level forward flight in a power efficient manner. Thrust vectoring strategy for forward flight is further discussed in Chapter 4. Effect of thrust vectoring on maneuverability and gust tolerance is also explored in Chapter 6.

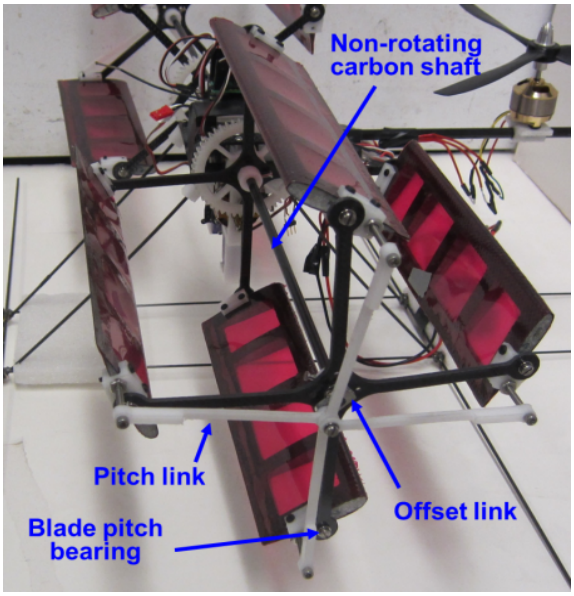

Figure 2.6: **Pitching mechanism implemented on the 550g twin-cyclocopter.**

2.3.1 Blade Pitching Mechanism

The schematic of the blade pitching mechanism is depicted in Fig. 2.5 where the four bars of the linkage system are labeled L_1, L_2, L_3 and L_4. L_1, also referred to as rotor radius, is the distance between the blade pitching axis and the horizontal axis of rotation. The pitch links (of length L_3) are connected to the end of the offset link on one end and the other end is connected to point B which is at a distance L_4 behind the pitching axis. The connections at both ends of the pitch link are through pin joints to allow the rotational degree of freedom. With this arrangement, as the rotor rotates, the blades automatically pitch cyclically, where the pitching amplitude depends on the offset length, L_2, when the other linkage lengths remains fixed. The rotation of the offset link changes the phasing of the cyclic pitching and thereby changes the direction of the thrust vector.

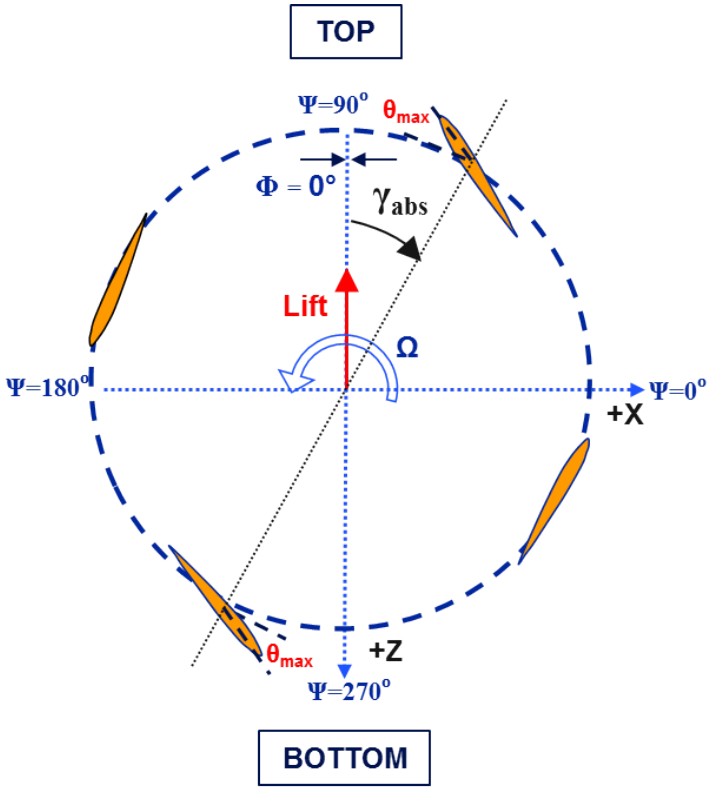

Figure 2.7: **Cyclorotor coordinate system.**

Figure 2.6 shows the actual pitching mechanism implemented on the 550g cyclorotor. The current pitching mechanism requires the offset link (L_2) to be installed at the tip of shaft in a non-rotating frame. In order to reduce mechanical complexities, the distance L_2 is kept constant. With a fixed maximum blade pitching amplitude, the magnitude of thrust is modulated during flight by varying the rotational speed.

The direction of the thrust vector can be manipulated by rotating the offset link, which changes the phasing of the harmonic pitching schedule. For the current coordinate system (Fig. 2.7), the azimuthal position of the blade (Ψ) is measured clockwise from the horizontal axis of rotation and is equivalent to zero when the blades are at the extreme left of the circular trajectory. The time-varying aero-

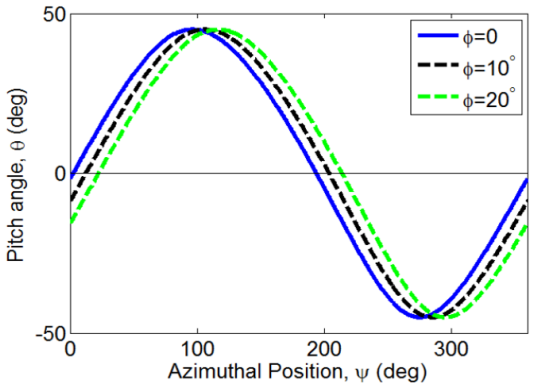

Figure 2.8: **Blade pitch angle as a function of rotor azimuth for each cyclorotor at trim.**

dynamic forces produced by the cyclorotor can be resolved into the vertical and horizontal directions with a positive x-axis extending towards the right and a positive z-axis towards the top. In the figure, the phasing angle is denoted as Φ, which is zero when aligned with the z-axis and positive with a clockwise rotation.

Even though they produce identical values of thrust at each rpm, the cyclorotors have different pitch phasings in order to counteract the clockwise reaction torque from the tail rotor (Fig. 2.8). As a result, the cyclorotor on the right has a higher phasing which tilts the thrust vector forward and produces a net counterclockwise yaw moment of the vehicle. The thrust vectoring mechanism on the cyclocopter that is used to rotate the offset link and provide a phasing input is composed of two BMS-373MG servos that are directly connected to the pitching mechanism through a 2:1 gear ratio. The setup allows for $\pm 60°$ of thrust vectoring.

The pitch links are manufactured out of Delrin acetal resin using a CNC milling machine. Compared to carbon fiber linkages used on the smaller vehicles, Delrin linkages for the 550 g cyclocopter are pliable and resistant to abrupt fractures.

Table 2.2: Cyclorotor design parameters for the 550 g cyclocopter.

Parameter	Cyclorotor
Rotor Diameter	0.152 meters (6 inches)
Blade span	0.171 meters (6.75 inches)
Blade chord	0.051 meters (2 inches)
Blade airfoil	NACA 0015
Blade pitch amplitude	$\pm 45^{\circ}$
Blade pitch axis	45% from LE

Pliability is important considering the large centrifugal loading on the blades and subsequently on the linkages which will be discussed in later sections.

2.4 Blade Design

As seen from the weight distributions, the cyclorotors compose up to 27% of the vehicle's gross weight. To reduce the empty weight fraction, the cyclorotor blades must be carefully designed to be lightweight and structurally robust. The rotor structural design must be able to withstand the dominant centrifugal force because each gram of blade weight amounts to approximately 0.4 Newton of centrifugal load on the blade. In addition, the blades also need to have high strength-to-weight ratio to minimize the bending and torsional deformations caused by the transverse centrifugal loading. The cyclorotor performance can be attributed to four main design aspects: (1) blade aerodynamic design, (2) blade structural design, (3) rotor geometry, and (4) blade kinematics.

2.4.1 Aerodynamic Design

Selection of key aerodynamic blade parameters such as blade pitching amplitude, location of pitch axis, rotor radius, blade airfoil, chord, span, and planform were based on empirical studies. The parameters of the present cyclorotor for the 550 g vehicle have been optimized through series of systematic experimental studies conducted in the past [31]. Each blade uses a NACA 0015 airfoil, a symmetric pitching amplitude of 45°, a chord/radius of 0.625, and aspect ratio of approximately 3.38. All of the design parameters of the cyclorotor are summarized in Table 2.2. Leveraging the insights gained from these studies, the present cyclorotor is designed for improved thrust-to-power ratio (power loading) in hover and power efficiency in forward flight. Emphasis was also placed on the blade and rotor structural design to reduce the overall rotor weight.

A critical parameter in cyclorotor performance regarding blade and rotor geometry is the solidity (σ):

$$\sigma = \frac{N_b c}{2\pi R} \tag{2.1}$$

The solidity is affected by the number of blades (N_b) and chord-to-radius (c/R) ratio. The radius of the cyclorotor is measured using its circular trajectory, unlike the blade span measurement used for conventional rotors. On a conventional rotor, there is an optimum solidity that is directly influenced by the total blade area ($N_b cb$) at each thrust value. However, for the cyclorotor, changing the solidity by

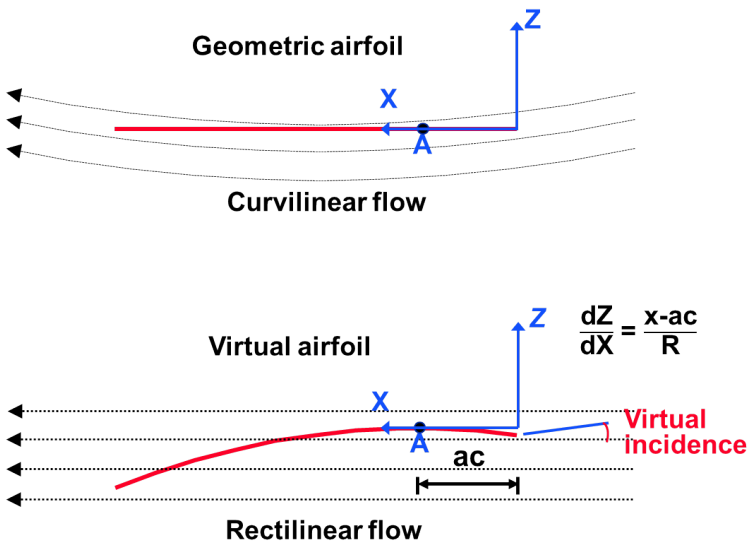

Figure 2.9: **Virtual camber and incidence in a curvilinear flow**

varying either N_b or c/R yields completely different results because of the different phenomenon involved. For a fixed c/R, changing the number of blades alters the total blade area and subsequently, the solidity, which results in a similar effect on cyclorotor performance as on the conventional rotor. For a fixed number of blades, changing c/R not only affects the blade area, but also changes the flow curvature effect on the cyclorotor [36].

The blades on the cyclorotor experience a virtual camber effect because of the curvilinear nature of the flow, which introduces a chordwise variation in velocity. Therefore, a symmetric airfoil at 0° pitch behaves as a virtually cambered airfoil at a virtual incidence (Fig. 2.9) in a rectilinear flow. The blades experience a negative virtual camber and incidence at the top of the trajectory ($C_l < 0$) and a positive camber and incidence at the bottom portion of the trajectory ($C_l > 0$). The study found that virtual camber and incidence was proportional to the chord-to-radius ratio at higher values and location of the blade pitching axis. After systematically

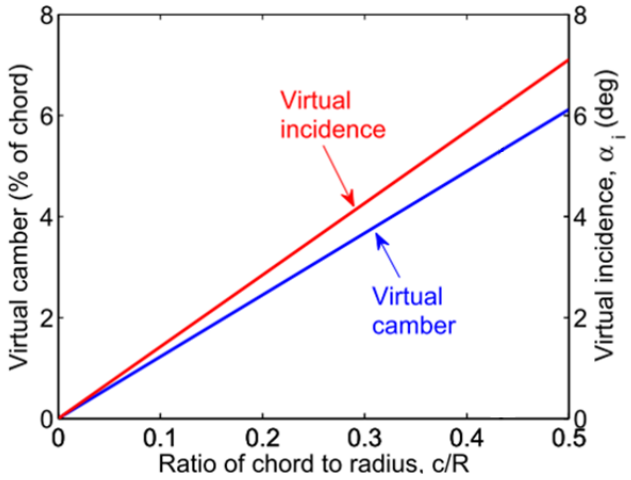

Figure 2.10: **Linear approximation to measure virtual camber and virtual incidence** [31, 47]**.**

measuring the power loading (thrust/power) with disk loading (thrust/disk area) at various solidities and at 40° pitching amplitude, the maximum performance resulted from a four-bladed rotor with a c/R ratio of approximately 0.83. While aerodynamically efficient, the c/R of 0.83 would result in heavy blades with low aspect ratios (AR) and lead to increased structural loads on the blades. However, it should be noted that power loading did not drastically change when c/R was within 0.6 to 0.8.

A linear approximation shows that the virtual camber for selected blade parameters is 3.5% of chord and virtual incidence is 5°. The pitching axis locations (x/c) of all blades were centered around the chordwise c.g. location, which resulted in x/c of 0.45. The pitching axis aligned with the chordwise location of blade c.g. in order to to reduce the pitching moments on the blade caused by the centrifugal force. In addition, it reduces the loads on the pitching mechanism and ultimately on the lightweight thrust vectoring servos with limited torque capacity (1.58 kg-cm).

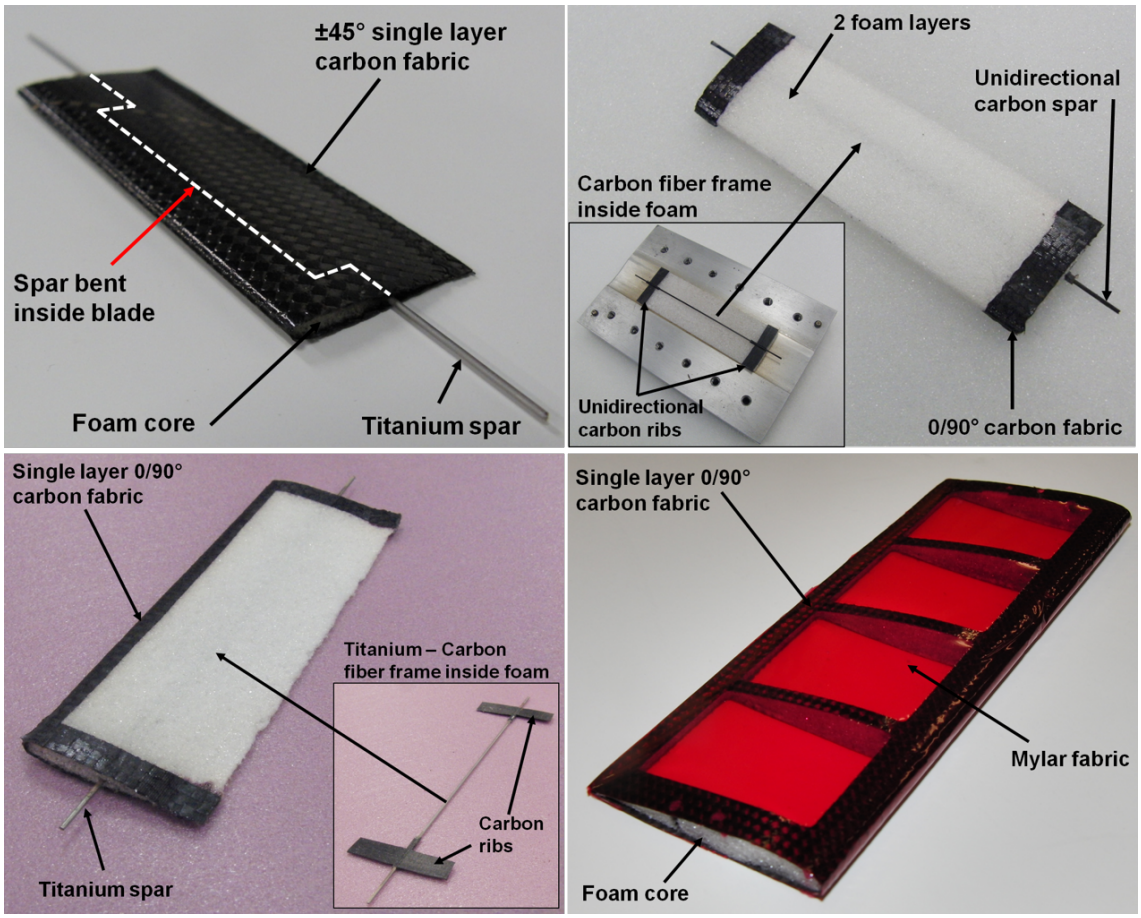

Figure 2.11: **Previous iterations of blade design.**

2.4.2 Structural Design

There have been several iterations of blade designs from the composite sandwich structure of foam wrapped with carbon fiber to multi-component rib and spar assembly (Fig. 2.11). The main purpose of the design iterations was to reduce overall blade weight while increasing bending and torsional stiffness. The blades undergo significant centrifugal loading both perpendicular and transverse along blade span. The centrifugal loading can be calculated using equation 2.2 where the force increases linearly with mass and rotor radius and quadratically with rotational speed:

$$CF = m\Omega^2 R \tag{2.2}$$

While radius and rotational speed are set by aerodynamic parameters of the blade, mass can be reduced based on improved manufacturing techniques.

2.4.2.1 Carbon Fiber Blade

The first iteration of blade design was a composite structure with rohacell foam interior wrapped with -45°/45° carbon fiber fabric. The direction of fiber and NACA 0015 profile contributed to torsional stiffness while the closed foam and carbon fiber contributed to bending stiffness. A bent titanium spar sandwiched inside the foam provided additional bending stiffness and an attachment point for blade pitching mechanism. Due to multiple components, the manufacturing process for this design was complicated and required multiple steps. Both the foam core and final carbon

fiber wrap needed to be baked at 350° for 30 minutes and 75 minutes respectively, using an aluminum mold. The blades then connected to the rotor end plates through a blade attachment adaptor held on by two screws at both spanwise boundaries of the blade. While this over-designed blade reduced structural deformations, the 10 grams blade was too heavy to use on the cyclocopter.

2.4.2.2 Exposed Foam Blade

In order to reduce the mass, the next iteration of blade design included a light-weight foam structure with a 1/16 inch titanium inner spar and strips of carbon fiber at the leading edge and spanwise bounds. The titanium spar and foam provided bending stiffness while the closed NACA 0015 profile provided torsional stiffness. Similar to the previous iteration, manufacturing was labor-intensive because of the curing process required for carbon fiber and foam. While this lightweight design provided 80% reduction in weight, the blade was too flexible and resulted in large bending deformations. In addition, the foam structure was not robust enough to survive vehicle crashes during flight testing.

2.4.2.3 Mylar Wrapped Monolithic Blade

A compromise between lightweight and stiff design was reverting back to the initial composite sandwich structure but removing multiple rectangular cross-sections to reduce weight. The cut-out blade would then be wrapped with Mylar film to maintain a closed structure. The Mylar film was 50 micron thick and provided a smooth

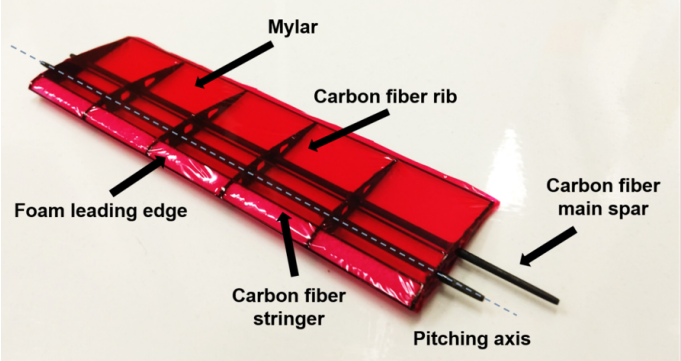

Figure 2.12: **Rib and spar blade design.**

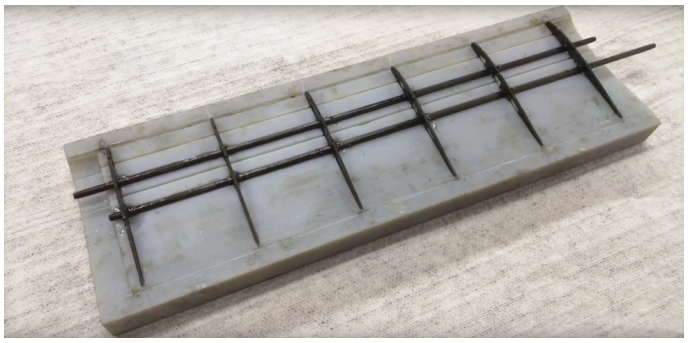

Figure 2.13: **Blade mold for constructing new blades.**

blade surface. To simplify the blade structure, the inner titanium spar was removed such that the pitching mechanism connected to the blade solely through the blade attachment. With the changes, the final blade weight was 7.4 g. The simple monolithic design also reduced probability of structural failure during flight testing. The pitching axis and linkage attachment point were on two separate delrin blade attachment pieces mounted on spanwise ends of the blade and contributed to the total blade weight. Besides the weight, a significant drawback of the design was inconsistent placement of the blade attachment pieces during the manufacturing process, which consequentially led to significant blade twist and decreased performance.

2.4.2.4 Multi-Component Rib and Spar Blade

With the advent of additive manufacturing and commercially available 3D printers, the blade design could be further improved using multi-component rib and spar structure (Fig. 2.12). The ribs are milled out carbon fiber in the NACA 0015 profile with through-holes for two 1/16 inch carbon fiber spars that attached directly to the end plates and pitching mechanism. To maintain the NACA profile, 0.1 cm diameter stringers outlined the boundaries of blade and an additional strip of foam provide a smooth leading edge shape. The multi-component blade is assembled using a 3D-printed blade mold (Fig. 2.13). Bending stiffness is provided by two carbon fiber spars and torsional stiffness is from the closed structure. Removing the need for blade attachment also improved the consistency of the blade design since the pitching axis location was determined by the spars and did not vary. This had a previously unaccounted effect of reducing blade twist at higher rotational speeds and improved cyclorotor performance. Overall, the blade only weighed 6 grams and provided high bending and torsional stiffness to mitigate effects of centrifugal loading.

2.5 Cyclorotor Performance

Various blades were tested using Nano17, a commercial force-torque sensor (Fig. 2.14) and an Ohaus Explorer precision force balance. A systematic performance sweep was conducted from 800 to 1600 rpm until the cyclorotor reached maximum power rated for the AXI motor. Figures 2.15 to 2.17 show thrust, power, and power loading

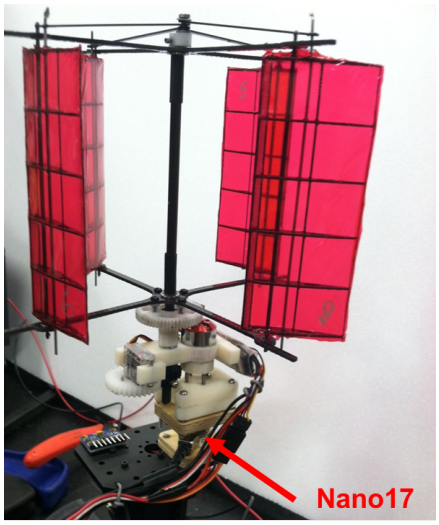

Figure 2.14: **Nano-17 (force/torque transducer) experimental setup.**

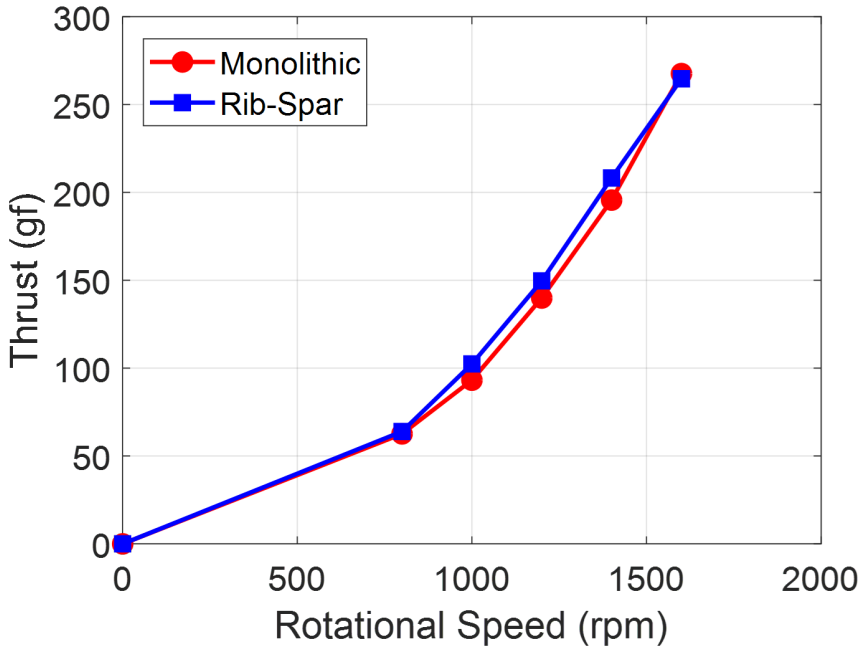

Figure 2.15: **Cyclorotor thrust vs. rotational speed**

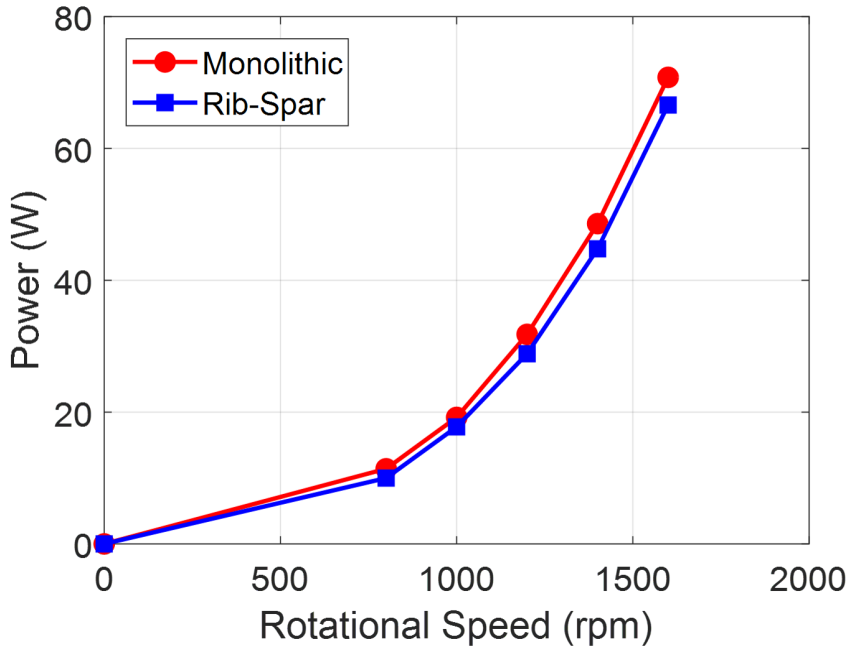

Figure 2.16: **Cyclorotor electrical power vs. thrust.**

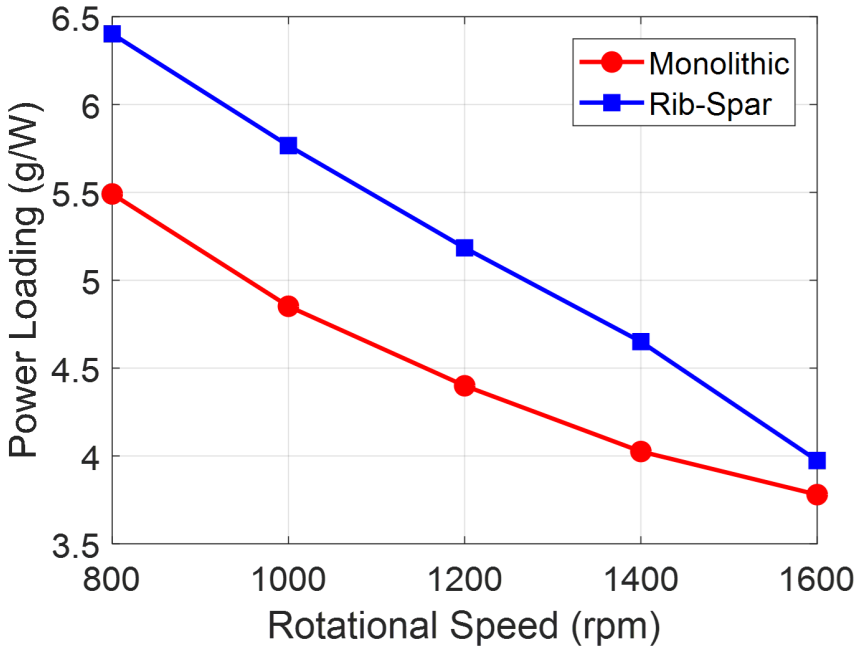

Figure 2.17: **Cyclorotor power loading vs. rotational speed.**

comparisons between the monolithic and rib-spar blade designs. Each data point is an average of multiple trials.

The aerodynamic parameters of the blade tested are summarized in Table 2.2. Both cyclorotors produced 270 grams of thrust at 1600 rpm. With each cyclorotor weighing 27 grams, the thrust-to-weight (T/W) ratio is approximately 10 at the operating rotational speed. Slight variation of power consumption was observed between the two designs. At the operational rpm, the monolithic blade design consumed 71 watts of electrical power while the rib-spar design consumed 67 watts. Because of blade construction, the monolithic design requires two 3D printed blade attachments that connect the blade to the endplates. The rib-spar design uses a carbon fiber spar inside the blade at the pitching axis to connect to the endplates. The reduction in power can be attributed to lower parasitic drag. The discrepancy in power resulted in a 18% increase in power loading from the monolithic design. Overall, both blade designs were implemented on a cyclocopter. The 550 g twin-cyclocopter uses the monolithic blade design while the quad-cyclocopter discussed in Chapter 7 uses the rib-spar design with a slight modification of the pitching axis location.

2.6 Nose Rotor

The nose rotor used on the cyclocopter was selected through series of experiments comparing power loading of commercially available propellers. The propellers are directly driven and mounted on the eRC BL400 brushless motor shaft. Five dif-

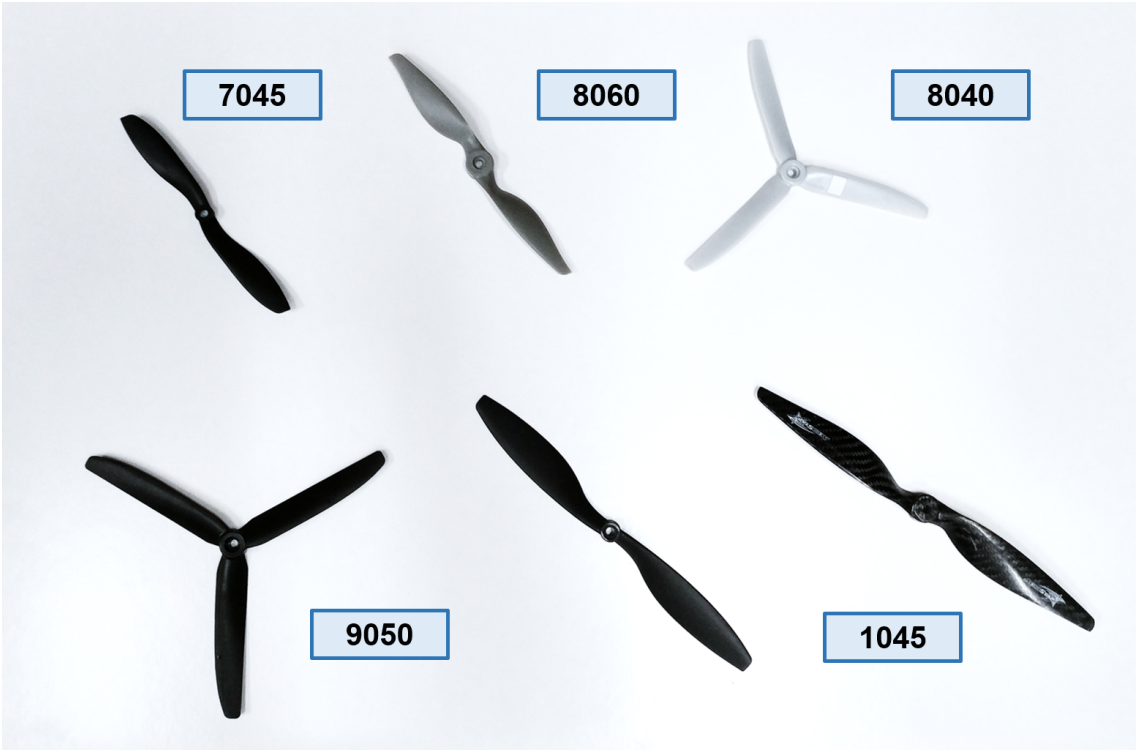

Figure 2.18: **Commercial propellers tested for the nose rotor.**

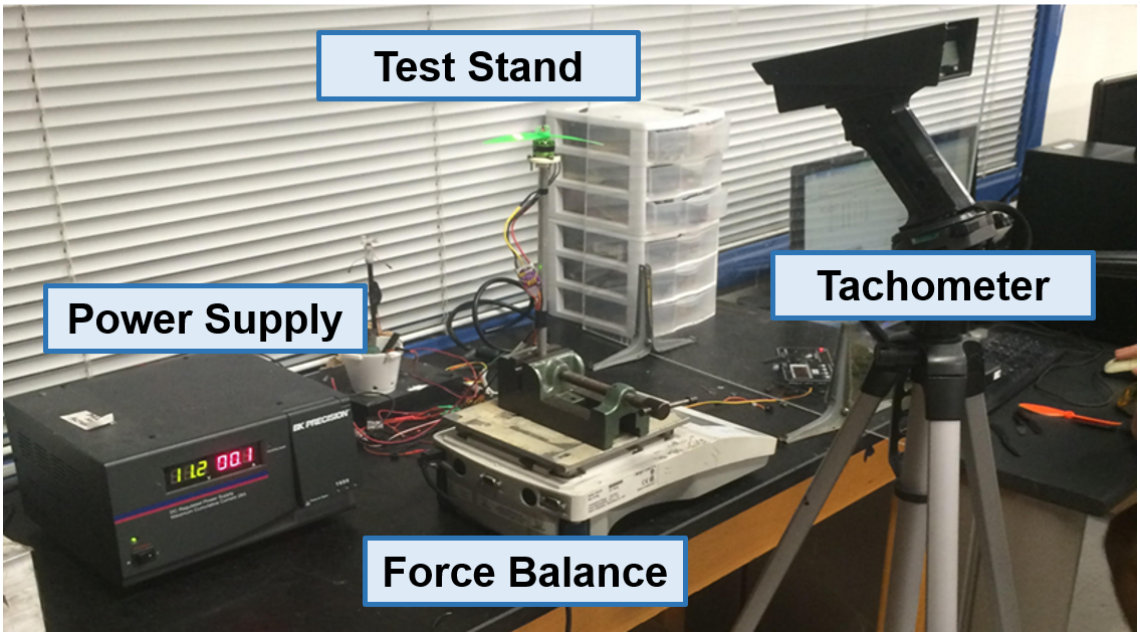

Figure 2.19: **Setup to measure thrust produced by nose rotor.**

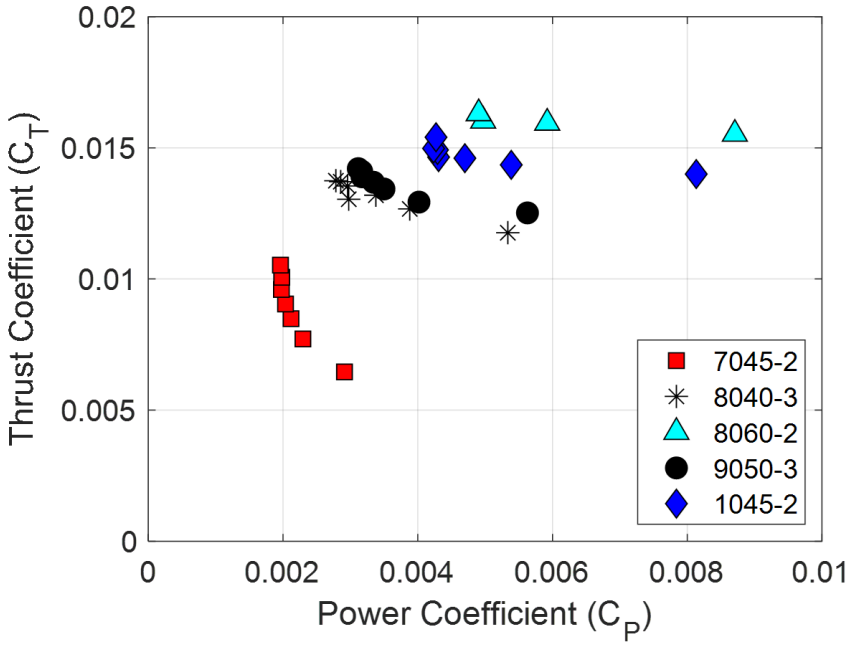

Figure 2.20: **Nose rotor C_T vs. C_P.**

ferent plastic propellers with variations in diameter, pitch, and number of blades were tested (Fig. 2.18). A 1045 carbon fiber propeller was also considered, but not included in the results because of additional mounts required to attach the propeller to the motor.

Throughout the experiment, thrust was measured using the Ohaus Explorer precision force balance (Fig. 2.19). The nose rotor was mounted on top of a stand-off tower for enough clearance to provide unobstructed airflow to the rotor. The propeller was also inverted such that downwash was directed upwards, away from the force balance, to prevent any potential ground effects. The motor was driven using AFRO 12 amps multi-rotor electronic speed controller and powered by a BK Precision DC Regulated Power Supply at 11.2 V. A reflective marker was placed on the outer casing of the motor in order to measure the operating rotational speed

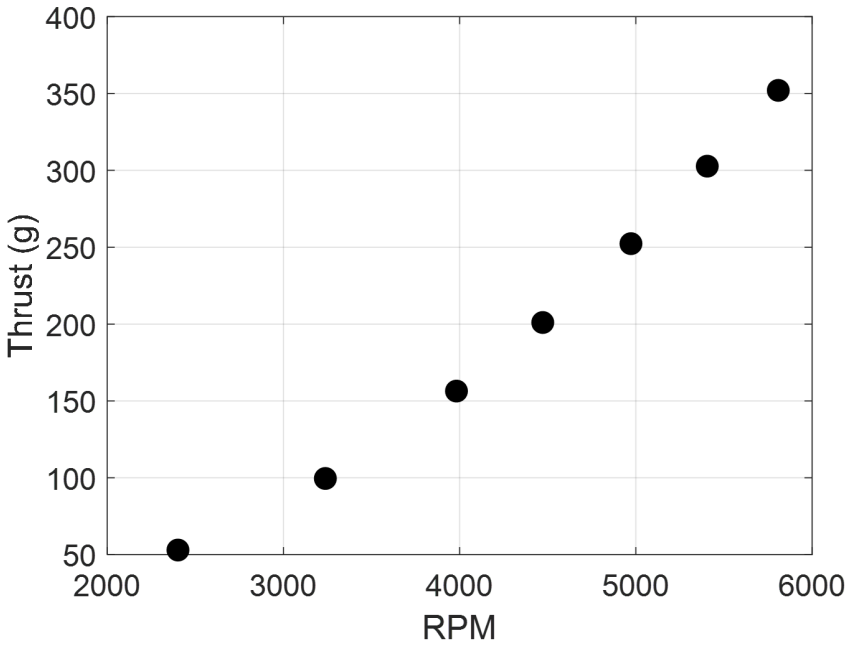

Figure 2.21: **Nose rotor thrust vs. rotational speed for 9050-3 propeller.**

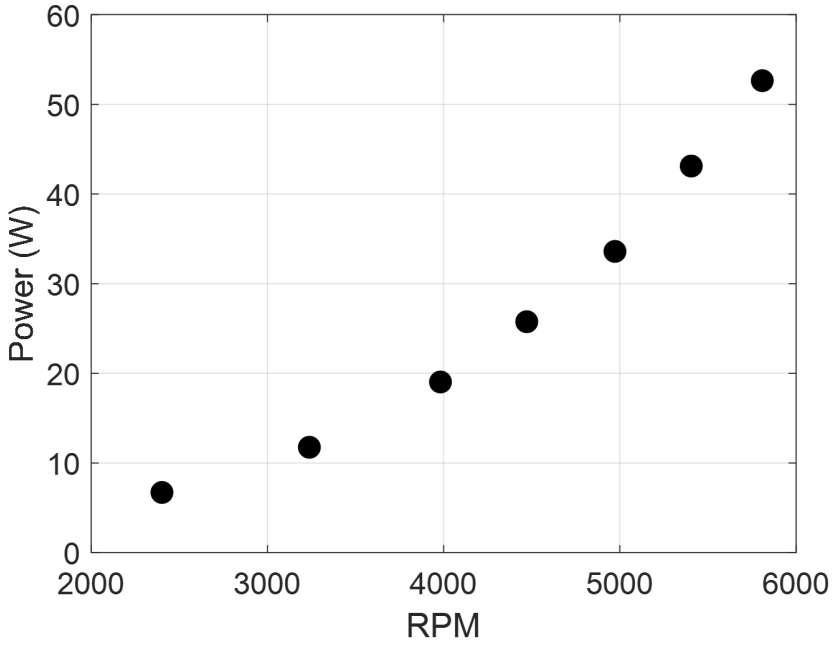

Figure 2.22: **Nose rotor electrical power vs. thrust for 9050-3 propeller.**

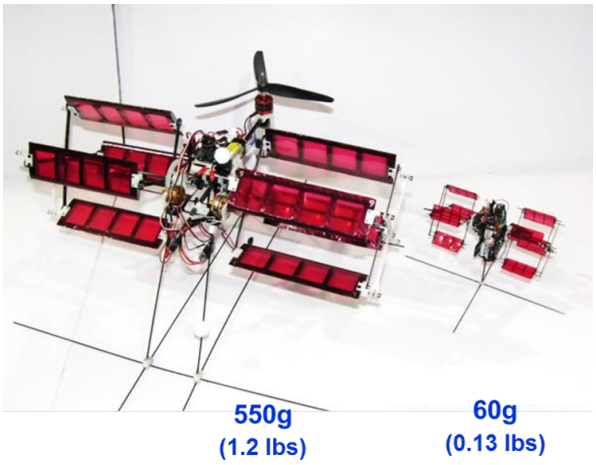

Figure 2.23: **550g and 60g twin-cyclocopters.**

using the Monarch Laser Tachometer.

Propellers were tested at various rotational speeds that produced thrust from 50 to 350 grams at increments of 50 grams. Based on C_T vs. C_P measurements, the 9050 3-bladed propeller was selected for the 550 g cyclocopter (Fig. 2.20). Figures 2.21 and 2.22 show the thrust and electrical power measurements for the selected propeller. The nominal contribution of the nose rotor is 33% of vehicle weight, but the actual thrust is dictated by the pitch trim in hover. In-flight measurement of nose rotor operating condition showed the rotational speed to be around 5000 rpm, producing 250 g to compensate for pitching moment from the cyclorotors.

2.7 Scalability

The lightweight and aerodynamically efficient multi-component rib and spar blade design made it possible to develop a 60 g meso-scale cyclocopter (Fig. 2.23). The vehicle has a lateral dimension of 0.178 meters (7 inches), longitudinal dimension of 0.127 meters (5 inches), and a height of 0.152 meters (6 inches). Each cyclorotor

Table 2.3: Blade properties (60g-scale cyclocopter).

Parameter	Blade #1	Blade #2	Blade #3
Weight (g)	0.50	1.50	0.45
Chord-to-radius (c/R)	0.57	0.47	0.47
Pitching axis (x/c)	0.25	0.50	0.25
Chord (in)	0.85	0.70	0.70
Span (in)	1.7	2.0	2.0
Virtual camber (%c)	7	5	5
Virtual incidence (deg)	8	6	6

has a diameter of 0.076 meters (3 inches), blade span of 0.043 meters (1.70 inches), a chord of 0.022 meters (0.85 inches), and uses a NACA 0015 airfoil. The blades on the cyclorotors achieve symmetric pitching with a maximum pitching amplitude of 45°.

Three different blades with the same planform area, but variations in c/R ratio, blade geometry, and structure were tested for maximum power loading. Blade #1 weighs 0.50 g, has a lower AR of 2 (c = 0.85 in, b = 1.70 in), and a higher c/R of 0.57. Blade #2 uses the initial design and weighs 1.50 g with an aspect ratio of 2.86 (c = 0.70 in, b = 2.0 in) and c/R ratio of 0.47. To observe the effects of blade structure on performance, a newly designed blade (#3) with identical blade geometry and c/R was created and weighed approximately 0.45 g. The virtual chamber for blade #1 is approximately 7% of the blade chord while 5% of chord for blades #2 and #3. In addition, blade #1 experiences an 8° virtual incidence while blades #2 and #3 experience 6° of incidence. The pitching axis location (x/c) is 0.25 for the new blade designs and x/c of 0.50 for the old design. Table 3 provides a full summary

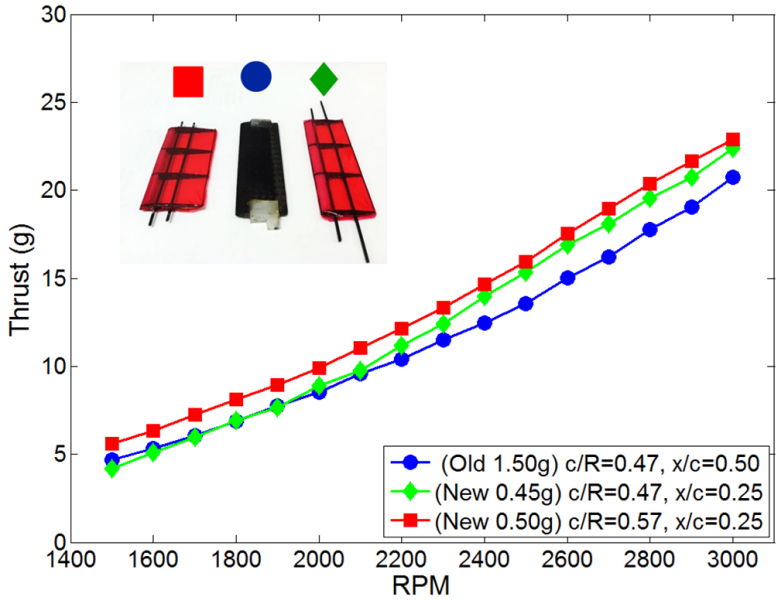

Figure 2.24: **Thrust vs. rpm for the 60g cyclorotor blades.**

of all the blade properties.

To determine the optimum blade design, both thrust and power loading were systematically measured for each blade from 1500 to 3000 rpm in increments of 100 rpm. When comparing the thrust, increased virtual chamber and incidence (blade #1) resulted in a higher thrust value at each rpm (Fig. 2.24). Interestingly, even though blades #2 and #3 had the same blade geometry, the lighter 0.45 g blade (#3) produced more thrust at higher rotational speeds. One possibility for discrepancies in rotor performance could be that blade #3 experiences a lower centrifugal loading compared to the heavier 1.50 g blade since centrifugal force varies linearly with mass and square of blade velocity (mV^2/R). However, previous studies have shown that moving the pitching axis location closer to the leading edge steadily increases the thrust produced by the cyclorotor [31]. When comparing the power loading, the

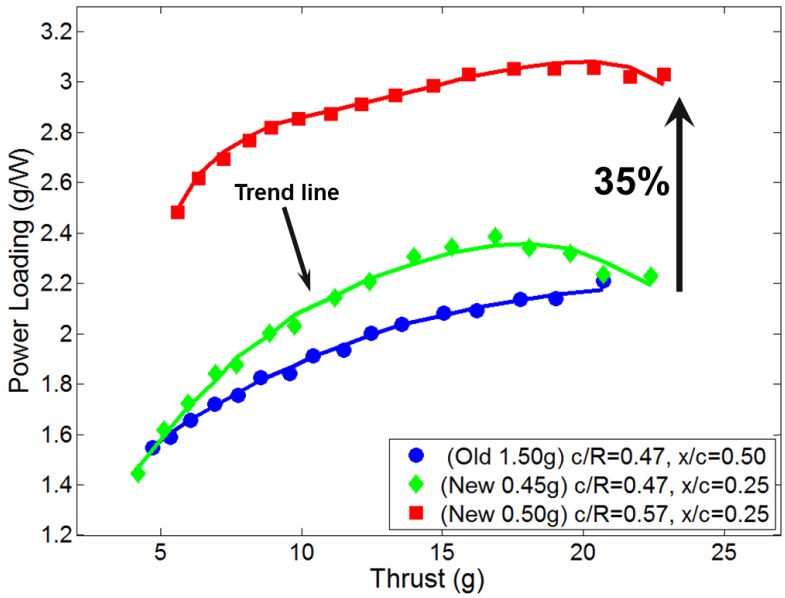

Figure 2.25: **Electrical power loading of old design vs. new blade design.**

optimum pitching axis location should be between 35% to 45% of blade chord at higher disk loadings (thrust/disk area).

A comparison of power loading (thrust/electrical power) shows an increase of up to 35% of aerodynamic efficiency from blade #2 to blade #1 (Fig. 2.25). The trend lines from these experiments agree with the previous studies on the effects of flow curvature on the cyclorotor. While increasing the c/R ratio appears to improve rotor efficiency, the overall blade geometry is also restricted by weight. There is a noticeable difference in efficiency between blades #2 and #3 caused by an increase in blade mass which proportionally leads to an increase in the centrifugal loading. However, the c/R ratio seems to have the most significant impact on cyclorotor performance.

Based on the results of the parametric study, the optimized cyclorotor on the

60 g twin-cyclocopter utilizes four 0.50 g blades with the new blade design, c/R ratio of 0.57, and pitching axis location at 25% of blade chord. Along with other structural components, the optimized cyclorotor weighs 7 g and has a thrust-to-weight (T/W) ratio of approximately 3 at the operating rotational speed of 3000 rpm (T = 23 g). This is a significant improvement to previous design iterations at the meso-scale as evidenced by thrust and power loading trends.

2.8 Summary

The 550 g twin-cyclocopter described in this chapter relied on two cyclorotors as main source of propulsion and an additional horizontal anti-torque nose rotor. The vehicle had a lateral dimension of 0.381 meters (1.25 feet), longitudinal dimension of 0.457 meters (1.5 feet), and a height of 0.305 meters (1 foot). Each cyclorotor had a diameter of 0.152 meters (6 inches), blade span of 0.171 meters (6.75 inches), and a chord of 0.051 meters (2 inches). In addition, the nose rotor used a three-bladed 9050 propeller with a 0.229 m diameter (9 inches). Each rotor was independently driven by a motor and two additional rotary servos were used to provide thrust vectoring capability for the cyclorotors.

Since the cyclorotors comprised a significant portion (23-34%) of the empty weight fraction of the vehicle, its blades were designed to be lightweight with high bending and torsional stiffness. Cyclorotors using Mylar wrapped monolithic blades and multi-Component rib-spar blades were tested. Both cyclorotors produced 270 grams of thrust at 1600 rpm, achieving a thrust-to-weight (T/W) ratio of approx-

imately 10. Slight variation of power consumption was observed between the two designs because of differences in parasitic drag due to blade construction. At the operational rpm, the monolithic blade design consumed 71 watts of electrical power while the rib-spar design consumed 67 watts, resulting in a 18% increase in power loading. Overall, both blade designs were implemented on the final cyclocopter.

Chapter 3: Avionics and Control System Development

3.1 Overview

Micro air vehicles are generally constrained by their empty weight fraction which comprises of vehicle structure, power source (e.g batteries), electronics, and onboard avionics. The previous chapter discussed the vehicle development of the cyclocopter and provided an overview of structural design, electronics, and selected LiPo batteries. In order to achieve stable flight, the vehicle must also be equipped with avionics and a closed-loop feedback system. Avionics include autopilot, sensors, and an onboard computer for executing computationally intensive tasks such as image processing. This chapter will first review two custom autopilots implemented on the cyclocopter and then survey sensors and onboard computers commercially available for MAVs.

Sensors can be categorized into three main applications: (1) flight stability and control, (2) flight performance diagnostics, and (3) guidance and navigation. Cyclocopters developed in this work relies on a combination of (1) and (2). Sensors used for flight stability and control provide measurements of vehicle attitude angle and body rates. Sensors for flight performance diagnostics provide both vehicle state (e.g RPM, altitude) and atmospheric conditions (e.g pressure, gust, temperature).

These sensors can be used to collect mission-specific atmospheric data, as well as diagnose vehicle performance issues during flight. Finally, guidance and navigation sensors enable autonomous navigation using measurements of vehicle position, velocity, attitude, and trajectory of path.

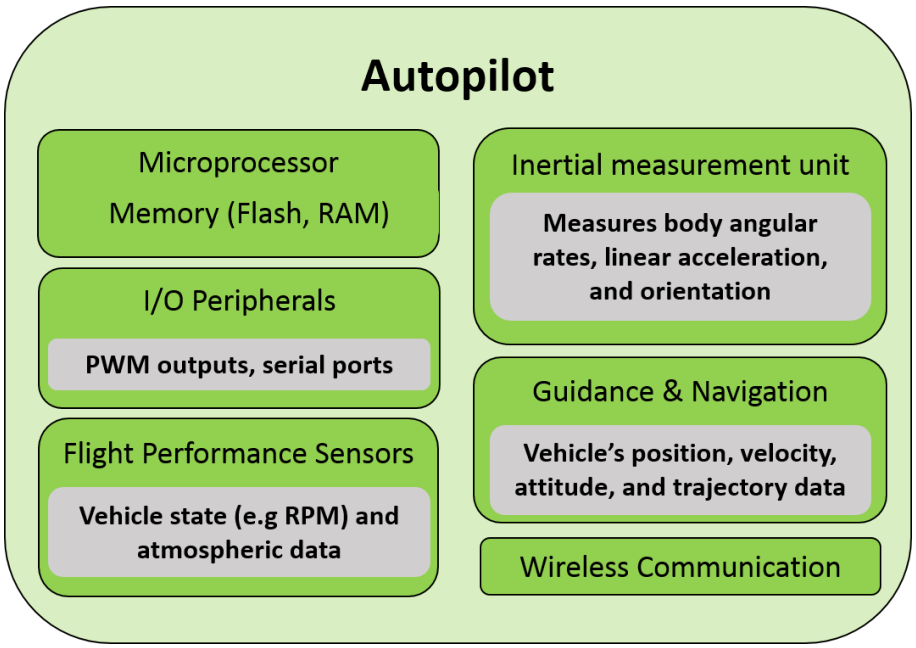

Figure 3.1: **Components of an autopilot.**

3.2 MAV-scale Autopilot

While structural components and power systems can be customized for different vehicle configurations, the choice of avionics is often limited to commercial availability. In addition, only few autopilots are open-source and permit developers to modify original source code to adapt to multiple vehicle configurations. An autopilot is generally comprised of a microprocessor with built-in memory (FLASH, RAM, etc.), input and output peripherals such as serial ports, wireless communi-

cation components, and an assortment of sensors (Fig. 3.1). The following sections compare two light-weight and open-source MAV-scale autopilots implemented on the cyclocopter. Physically, these particular autopilots are only integrated with an inertial measurement unit (IMU) onboard. However, sensors for flight performance measurement and navigation can be supplemented.

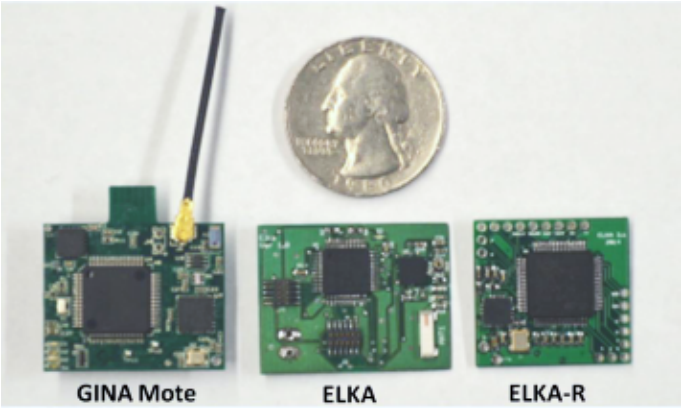

Figure 3.2: **Comparison between MAV-scale autopilot used on the cyclocopter.**

3.2.1 GINA Mote

GINA Mote is an existing autopilot weighing 1.6 grams and originally developed by the University of California, Berkeley [48]. The board is relatively small (25mm x 25mm) and houses IMU and wireless communication components (Fig. 3.2). The principal components of this board are a TI MSP430 microprocessor for onboard computation tasks, ITG3200 tri-axial gyros, KXSD9 tri-axial accelerometer, and an ATMEL radio and antenna for wireless communication. The wireless communication has a latency less than 20-30 milliseconds such that the critical inner loop feedback occurs at an update rate of 3 milliseconds.

Table 3.1: Comparison between GINA Mote, ELKA, and ELKA-R [78].

	GINA Mote	**ELKA**	**ELKA-R**
CPU	TIMSP430	ARM Cortex-M3	ARM Cortex-M4
Clock Speed (MHz)	16	72	168
Update Rate (Hz)	333	500	1000
Bits	16	32	32
Flash Memory (KB)	116	128	1024
Actuators	6	8	12
Weight (g)	1.6	1.3	1.7
Ground Control Station	Required	Optional	Optional
Breakout Board	Required	Required	Optional

The 16-bit microcontroller supports attitude stabilization at 333 Hz and was able to sufficiently stabilize the cyclocopter in hover. Due to limited flash memory (116 KB), most of the feedback control system computations were performed off-board on a nearby ground control station running LabVIEW. For example, the final actuator commands (PWM) were computed on LabVIEW after receiving vehicle attitude and body rates from the autopilot. Communication between the autopilot and remote station is achieved using a wireless IEEE 802.15.4 data link. Updates to the autopilot firmware are contributed by the original developers and others using the GINA Mote's open-source software. In addition, pilot inputs were directly transmitted to the ground control station through a serial connection via an Arduino Uno.

3.2.2 ELKA

Due to minimal updates in the past few years and inherent limitations on attitude stabilization rate and inability to perform onboard computations, the GINA Mote

was unable to sufficiently stabilize the cyclocopter beyond hover. As a result, a custom autopilot with higher computation power, flash memory, and updated sensors was developed in-house for the cyclocopter (Table 3.1).

The Embedded Lightweight Kinematic Autopilot (ELKA) weighs 1.3 grams and is powered by a single 1-cell 3.7 volt 125 mAh Li-Po battery [78]. ELKA houses a STM32 microprocessor with a 32-bit ARM Cortex-M3 core for high-end onboard computation tasks. The InvenSense MPU-9150 IMU integrated on the board includes tri-axial gyroscopes, accelerometers, and magnetometers. Wireless communications are serviced by an onboard nRF24L01 chip, a low-power 2.4 GHz RF transceiver. ELKA has a sensor update rate of 500 Hz and is capable of streaming vehicle attitude data and actuator controls data to a remote base station with a 30 milliseconds latency.

ELKA was also refined (ELKA-R) with a faster ARM Cortex-M4 processor that doubled the clock speed and update rate of the inner-loop (Table 3.1). With only an increase of 0.4 grams, ELKA-R is able to support up to 12 actuators. Unlike GINA Mote and ELKA, ELKA-R does not require an additional breakout board to connect to actuator pins. The flash memory was also increased by 8 times (1024 KB) and enabled all computations to be handled onboard. This capability provided the option of operating the cyclocopter without a ground control station for outdoor flight tests.

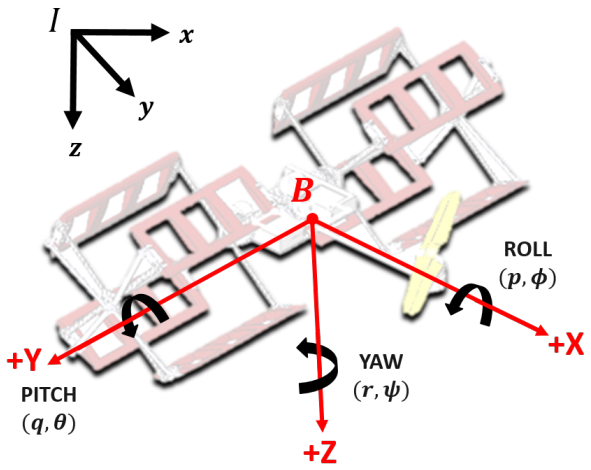

Figure 3.3: **Notation for body rates and attitude of the cyclocopter.**

3.3 Sensors for Flight Stability and Control

Without additional attitude stabilization, the cyclocopter was found to be unstable due to limited inherent aerodynamic damping [39]. At the MAV-scale, instability is further exacerbated by low vehicle inertia and faster dynamics. Artificial damping can be achieved using arrays of sensors integrated with a closed-loop feedback system. Inertial sensors used for stability augmentation include gyroscopes, accelerometers, and magnetometers. Raw measurements from these sensors are typically prone to drift and sensor noise. However, there are different filters and algorithms that are widely applied to achieve accurate estimates. The following sections provide a comprehensive overview of state measurement and attitude estimation techniques.

3.3.1 Inertial Measurement

Many of the recent advancements in development of MAVs can be attributed to microelectromechanical system (MEMS) sensors. MEMS sensors are manufactured

using a combination of semiconductor and microfabrication technologies to create a silicon substrate housing electronic and mechanical components. MEMS sensors are typically integrated into a single IMU that can measure linear acceleration along the X-Y-Z axes (a_x, a_y, a_z), angular velocities (p, q, r), and attitude (ϕ, θ, ψ). The resulting 9-DOF IMU houses tri-axial accelerometer, gyroscope, and magnetometer. As mentioned in the previous section, the IMU used on the cyclocopter is the InvenSense MPU-9150 integrated on ELKA-R.

MEMS-based accelerometer measures static acceleration due to gravity along X, Y, and Z axes in the body frame and also dynamic acceleration due to motion or vibrations. Similar to an inclinometer, the rotation angle and individual component of gravity along X, Y, and Z axes can be calculated if the sensor is tilted while stationary in space (Fig. 3.3). The actual sensing mechanism relies on micro-machined capacitive devices that compute changes in capacitance of a moving mass. The measurement is then converted to a digital signal via an analog-to-digital converter (ADC). The measured acceleration is integrated with respect to time in order to compute linear velocity and position. As a result, any constant bias error in acceleration leads to a linear error in velocity and quadratic error in position. Accelerometers are also sensitive to vibrations, especially at high frequencies.

MEMS-based gyroscope measures angular velocity of the vehicle along all axes in the body frame. When the gyroscope is rotated, a resonating mass inside displaces because of the Coriolis force. The displacement shifts the capacitance on the electrodes. Similar to accelerometers, gyroscopes output low-current electrical signals that are converted to digital signals. Due to fabrication techniques and dynamic

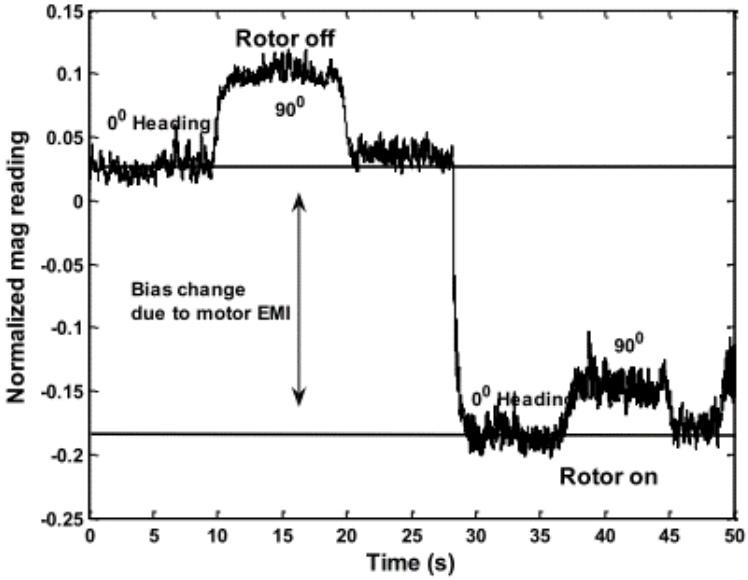

Figure 3.4: **Measurement from magnetometer showing large bias errors [50].**

physical properties of MEMS, gyroscopes experience drift and noise in measurement over time [51]. Techniques to reduce measurement errors are discussed in the later sections.

Aside from integrating gyroscope measurement along the Z-axis, vehicle's orientation can also be measured using a magnetometer. Magnetometers detect magnetic field along X, Y, and Z axes and provide relative orientation with respect to the Earth's magnetic north. The sensor outputs voltage that is proportional to the magnitude and polarity of the detected magnetic field. While magnetometers are not subject to drifts in measurement, they are affected by electromagnetic interference from motors (Fig. 3.4). Due to large bias errors, measurements from the magnetometer were not used for attitude estimation.

3.3.2 Attitude Estimation

Raw signals from tri-axial gyroscope and accelerometer implemented on the cyclocopter output linear accelerations (a_x, a_y, a_z) and angular velocities (p, q, r) in the vehicle's body frame $\mathbf{B} = (x_B, y_B, z_B)$ (Fig. 3.3). However, attitude angles (ϕ, θ, ψ) are typically provided with respect to the fixed frame or inertial frame, $\mathbf{I} = (x_I, y_I, z_I)$. Conversion between inertial and body frame is calculated using a conventional 3-2-1 rotation sequence using Euler angles $[\phi, \theta, \psi]$. The first rotation is about z_B by yaw angle (ψ), second rotation about y_B by pitch angle (θ), and finally the third rotation about z_B by roll angle (ϕ). Rotational transformation between the two frames is summarized by the following [52]:

$$[R_{BG}] = \begin{bmatrix} \cos\theta\cos\psi & \cos\theta\sin\psi & -\sin\theta \\ \sin\phi\sin\theta\cos\psi - \cos\phi\sin\psi & \sin\phi\sin\theta\sin\psi + \cos\phi\cos\psi & \sin\phi\cos\theta \\ \cos\phi\sin\theta\cos\psi + \sin\phi\sin\psi & \cos\phi\sin\theta\sin\psi - \sin\phi\cos\psi & \cos\phi\cos\theta \end{bmatrix} \tag{3.1}$$

The angular velocities are calculated using:

$$\begin{pmatrix} \dot{\phi} \\ \dot{\theta} \\ \dot{\psi} \end{pmatrix} = \begin{bmatrix} 1 & \sin\phi\tan\theta & \cos\phi\tan\theta \\ 0 & \cos\phi & -sin\phi \\ 0 & \sin\phi\sec\theta & \cos\phi\sec\theta \end{bmatrix} \begin{pmatrix} p \\ q \\ r \end{pmatrix} \tag{3.2}$$

From the transformation matrix, it is evident that singularity occurs when

$\theta = \pm 90°$. The transformation matrix is a square matrix (n) with orthonormal columns and generally referred to as the special orthogonal group ($SO(n)$). The inverse transformation (R_{GB}) can be calculated by taking a transpose of the matrix.

3.3.2.1 Quaternion Representation

One disadvantage of relying on Euler angles is existence of singularities, which can lead to gimbal lock or loss of a degree of freedom. For an aircraft, singularity at pitch attitude of 90° (nose up or nose down) is consequential. To avoid this issue, a quaternion-based attitude representation is implemented on the onboard autopilot. A quaternion is a point on the four dimensional hypersphere and is governed by the following equations where i, j, and k denote the complex numbers [54]:

$$i^2 = j^2 = k^2 = ijk = -1 \tag{3.3}$$

$$ij = k = -ji \tag{3.4}$$

$$jk = i = -kj \tag{3.5}$$

$$ki = j = -ik \tag{3.6}$$

The four parameters (q_0, q_1, q_2, q_3) represent quaternion rotation about an arbitrary axis. The parameter, q_0, is the scalar component while q_1, q_2, and q_3 are the distance along i, j and k. For a particular orientation, the relationship between the four parameters is given by:

$$q_0^2 + q_1^2 + q_2^2 + q_3^2 = 1 \tag{3.7}$$

Quaternions can be written in terms of Euler angles:

$$q_0 = \cos\frac{\psi}{2}\cos\frac{\theta}{2}\cos\frac{\phi}{2} + \sin\frac{\psi}{2}\sin\frac{\theta}{2}\sin\frac{\phi}{2} \tag{3.8}$$

$$q_1 = \cos\frac{\psi}{2}\cos\frac{\theta}{2}\sin\frac{\phi}{2} - \sin\frac{\psi}{2}\sin\frac{\theta}{2}\cos\frac{\phi}{2} \tag{3.9}$$

$$q_2 = \cos\frac{\psi}{2}\sin\frac{\theta}{2}\cos\frac{\phi}{2} + \sin\frac{\psi}{2}\cos\frac{\theta}{2}\sin\frac{\phi}{2} \tag{3.10}$$

$$q_3 = -\cos\frac{\psi}{2}\sin\frac{\theta}{2}\sin\frac{\phi}{2} + \sin\frac{\psi}{2}\cos\frac{\theta}{2}\cos\frac{\phi}{2} \tag{3.11}$$

Quaternion rates can also be expressed in terms of angular rates in the body frame:

$$\dot{q}_0 = -\frac{1}{2}(q_1 p + q_2 q + q_3 r) \tag{3.12}$$

$$\dot{q}_1 = \frac{1}{2}(q_0 p + q_2 r + q_3 q) \tag{3.13}$$

$$\dot{q}_2 = \frac{1}{2}(q_0 q + q_3 p + q_1 r) \tag{3.14}$$

$$\dot{q}_3 = \frac{1}{2}(q_0 r + q_1 q + q_2 p) \tag{3.15}$$

Conversion between quaternions and Euler angles is typically performed when selecting desired pitch, roll, or yaw angle through the ground control station. Euler angles are intuitive and easier to translate into a physical representation. However, because of the singularities, state estimation using gyroscopes and accelerometer is performed using quaternions.

3.3.2.2 Gyroscope

Angular velocities (ω) from the gyroscope in the body frame are converted to the quaternion derivative ($\dot{q}_k$) describing the rate of change between the earth (E) and body frame (B) using the following equations [53, 54]:

$$\omega = \begin{bmatrix} 0 \\ \omega_x \\ \omega_y \\ \omega_z \end{bmatrix} \tag{3.16}$$

$$\dot{q}_k = \frac{1}{2} q_{k-1} \otimes \omega_k \tag{3.17}$$

$$q_k = q_{k-1} + \dot{q}_k \triangle t \tag{3.18}$$

The quaternion derivative (Eq. 3.17) is computed at discrete time steps ($k =$

$0, 1, 2...n$). The quaternion orientation (Eq. 3.18) from the gyroscope is then estimated by integrating the quaternion derivative at the sampling period, $\triangle t$. The $\otimes$ symbol represents quaternion multiplication where:

$$q \otimes p = \begin{bmatrix} q_0p_0 - q_1p_1 - q_2p_2 - q_3p_3 \\ q_0p_1 - q_1p_0 - q_2p_3 - q_3p_2 \\ q_0p_2 - q_1p_3 - q_2p_0 - q_3p_1 \\ q_0p_3 - q_1p_2 - q_2p_1 - q_3p_0 \end{bmatrix} \tag{3.19}$$

3.3.2.3 Accelerometer

As previously mentioned, integrating gyroscope measurements leads to errors that increase over time. Correcting the gyroscope drift involves fusing sensor measurements with the accelerometer. The accelerometer measures the acceleration (a_x, a_y, a_z) in the body frame, but does not provide the rotation of the body frame relative to the earth frame. Therefore, a unique orientation is calculated by taking the shortest rotation between the gravity vector in the earth frame (g) and acceleration in the body frame (a). To avoid trigonometric functions, the rotation is calculated by minimizing an optimization function for k = 1,2...n:

$$f(q_k, g, a_k) = q_k^* \otimes g \otimes q_k - a_k \tag{3.20}$$

where q^* is the quaternion conjugate and the accelerometer measurements are:

$$a = \begin{bmatrix} 0 \\ a_x \\ a_y \\ a_z \end{bmatrix} \tag{3.21}$$

The solution to the objective function (Eq. 3.20) is found using the gradient descent algorithm. In the gradient descent algorithm, the quaternion orientation estimate ($\hat{q}_{k+1}$) is based on an initial estimate ($\hat{q}_0$) and a step-size of μ:

$$\hat{q}_{k+1} = \hat{q}_k - \mu \frac{\nabla f(q_k, g, a_k)}{\|f(q_k, g, a_k)\|} \tag{3.22}$$

The gradient of the objective function ($\nabla f(q_k, g, a_k)$) is defined in terms of its Jacobian (J) to compute the direction of error on the solution surface:

$$\nabla f(q_k, g, a_k) = J^T(q_k, g) f(q_k, g, a_k) \tag{3.23}$$

Since the gravity vector in the earth frame only has a Z component, the objective function and Jacobian can be simplified to:

$$f(q_k, a_k) = \begin{bmatrix} 2(q_2 q_4 - q_1 q_3) - a_x \\ 2(q_1 q_2 + q_3 q_4) - a_y \\ 2(\frac{1}{2} - q_2^2 - q_3^2) - a_z \end{bmatrix} \tag{3.24}$$

$$J(q_k) = \begin{bmatrix} -2q_3 & 2q_4 & -2q_1 & 2q_2 \\ 2q_2 & 2q_1 & -2q_4 & 2q_3 \\ 0 & -4q_2 & -4q_3 & 0 \end{bmatrix} \tag{3.25}$$

The optimization problem requires multiple iterations (k) for each estimated orientation and sensor measurements. However, it can also be solved through a single iteration per sample time if the convergence rate is equal to or greater than rate of change of the physical orientation.

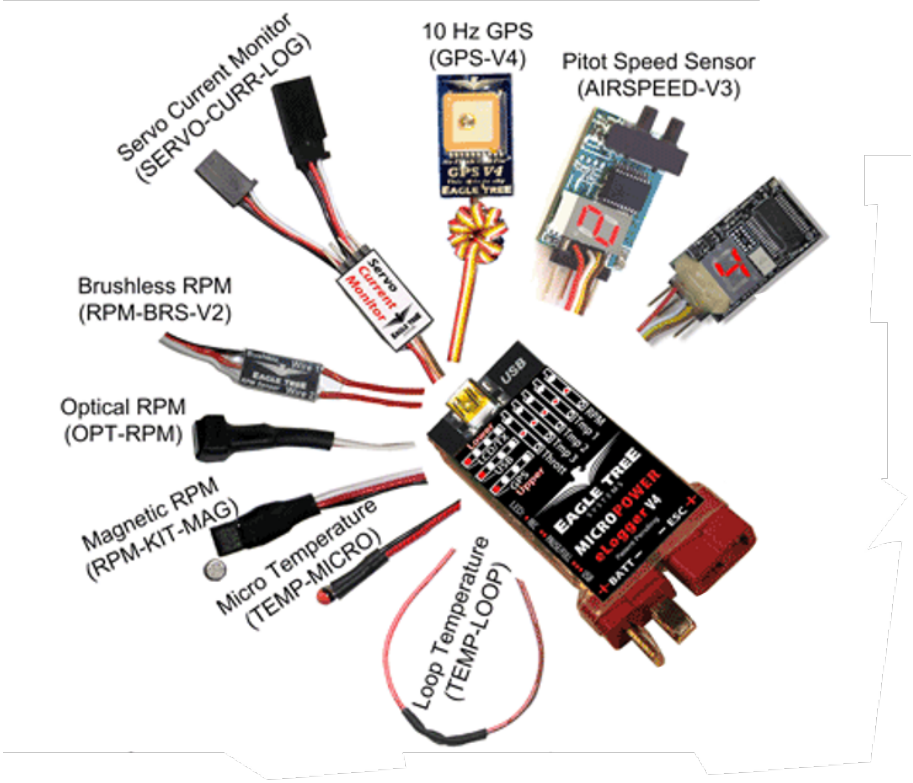

Figure 3.5: **Sensor suite for flight performance diagnostics and atmospheric measurement.**

3.4 Sensors for Flight Performance Diagnostics

Whether operating autonomously or by a pilot, vehicle's flight performance and operating conditions can be monitored using an array of sensors. Figure 3.5 shows the sensor suite integrated on a commercial data logging system. The following sections cover sensors used to measure vehicle's state and atmospheric conditions. Sensors for airspeed measurement will be covered in Chapter 6 along with a detailed overview of a custom sensor developed for the cyclocopter gust study.

3.4.1 RPM Sensors

RPM sensors that are non-contact can be categorized into electrical, magnetic, and optical sensors. Electrical RPM sensors measure back electromotive force (EMF) feedback from motors to determine approximate speed. Back EMF is commonly measured as the voltage opposing the induced current flow resulting from the movement of motor coils in the magnetic field. As motor RPM increases, back EMF also proportionally increases in order to oppose the changing magnetic field. Since back EMF is equivalent to the motor RPM and voltage constant, it can be used to directly calculate RPM. However, certain combinations of motors and electronic speed controllers (ESCs) can lead to issues with properly syncing these sensors.

Hall effect sensors operate by measuring changes in the magnetic field. The sensor is composed of a thin piece of rectangular semi-conductor (e.g gallium arsenide) that carries a continuous current. When placed within a magnetic field, electrons in the semi-conductor are influenced by the Lorentz force and deflect from

their linear path to either sides of the semi-conductor. The resulting magnetic flux creates a voltage differential called the Hall Voltage. A hall effect sensor placed near a rotating motor equipped with a small magnet on its outer casing can measure the variations in magnetic field and estimate the RPM. Existing hall effect sensors are inexpensive, compact, and highly reliable. These sensors are also able to operate under severe conditions (e.g outdoors, temperature variations, dusty setting, etc.).

Optical RPM sensors, such as tachometers, transmit infrared light beam and measure rate at which light beam is reflected. The laser beam is pulsed against a rotating element that has a reflective surface. Because of its reliance on infrared light, optical RPM sensors are limited to indoor applications. Similar mechanism is also used to measure proximity to nearest object.

3.4.2 Proximity Sensors

Proximity sensors are used to measure altitude and distance to nearest object for sense-and-avoid capabilities. These sensors are typically light-weight and low-cost since they only require a source and a receiver. Proximity sensors available for MAVs are typically for non-contact detection and emit either ultrasonic or infrared light to measure distance. A high performance ultrasonic range finder, such as the Maxbotix MB1000, has a 2.54 cm resolution, wide range from 15.24 cm to 645.16 cm, and a 20 Hz update rate. High-frequency ultrasonic pulses are transmitted back-and-forth using a single transducer in order to relay proximity information. Distance is calculated using lapsed time between sending and receiving reflections

from the sound waves. Ultrasonic range finders can be used in low lighting conditions and are unaffected by dark colors and dust. However, these sensors are not suitable for applications on soft materials (e.g carpets) since sound waves are not properly reflected.

Infrared (IR) range finders use optical sensors and estimate distance using triangulation. Sensors such as the SHARP GP2Y0A21YK operate using IR LEDs that emit a narrow light beam and measure distance between 10 cm to 80 cm. Unlike ultrasonic sensors, infrared range finders require both a transmitter and a receiver. Reflected light waves are received by a position-sensible photo detector (PSD). In addition, these sensors are restricted to indoor applications due to interference from sunlight.

3.4.3 Barometer

Another method of estimating altitude is by using a barometric pressure sensor (barometer). A barometer measures atmospheric pressure and estimates altitude based on a model relating altitude to pressure. MEMS-based barometers, such as the STMicroelectronics LPS25H, contain a suspended membrane inside a mono-silicon substrate used to measure pressure. The LPS25H is capable of acquiring high resolution measurements (± 1 Pa) with an absolute pressure range of 260 mbar to 126 0mbar. Barometers are typically calibrated to a standard atmosphere at mean sea level, which equates to pressure of 1013.25 mbars and temperature of 15° Celsius.

3.4.4 Temperature

Temperature can be monitored using a non-contact infrared sensor or a contact-based thermistor. Infrared temperature sensors convert thermal energy (0.7μm to 20μm wavelength) into electrical energy and are limited to indoor applications. Thermistor is a type of semiconductor that changes its electrical resistance based on temperature. Compared to resistance temperature detectors (RTD), thermistors provide a higher resolution because they undergo a higher resistance change per degree of temperature. Thermistor-based temperature sensors are generally used to monitor motor or battery temperature during flight.

3.5 Sensors for Guidance and Navigation (Autonomy)

The current sensor suite on the cyclocopter facilitates controlled piloted flight. For greater autonomy, the vehicle requires guidance and navigation sensors that enable localization. While inertial sensors like the accelerometer can be used to calculate displacement by numerically integrating acceleration measurements, the resulting estimate is often inaccurate and prone to drift. The following sections summarize prominent localization techniques and sensors currently employed on MAVs.

3.5.1 Global Navigation Satellite Systems (GNSS)

A common approach for outdoor navigation is to rely on real-time geo-spatial position triangulated by global navigation satellite systems (GNSS). Current GNSS systems include the Global Positioning System (GPS) by the United States, GLONASS

by Russia, Galileo by the European Union, BeiDou by China, Navigation Indian Constellation (NavIC) by India, and Quasi-Zenith Satellite System (QZSS) by Japan. These systems typically rely on medium Earth orbit (MEO) satellites that orbit at 20,000 km.

Table 3.2: Summary of popular MAV-scale commercial GPS modules.

	U-blox LEA-6H	**U-blox NEO-M8N**	**DJI D-RTK GNSS**
Compatible Board	Pixhawk/DJI NAZA	Pixhawk/DJI NAZA	DJI A3 Series
Horizontal Accuracy (m)	2.5	2.5	0.01 + 1 ppm
Vertical Accuracy (m)			0.02 + 1 ppm
Update Rate (Hz)	5	10	10
Interface	DDC, UART, USB, SPI	DDC, UART, USB, SPI	CAN, UART, USB
Min. Battery (V)	3.3	3.3	12
Weight (g)	16.8	32	139.5

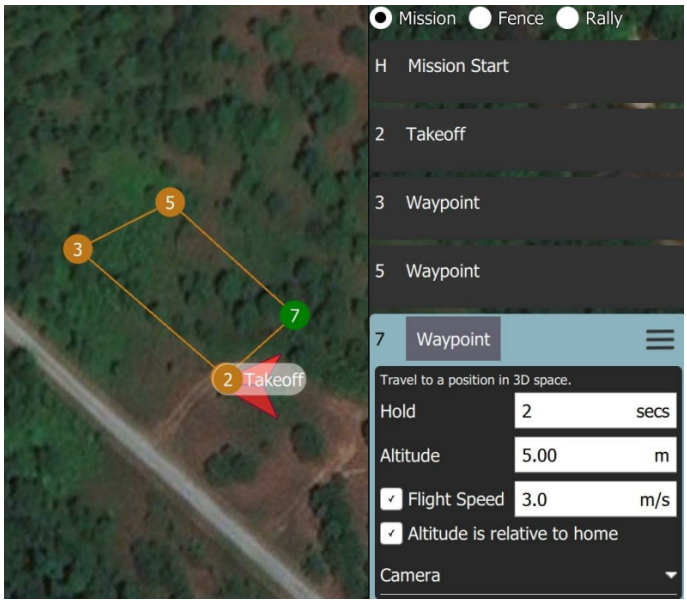

Figure 3.6: **GPS waypoint following using the Pixhawk GPS module.**

These satellites are arranged into six equally-spaced regions such that four are accessible at any location. The GPS receiver analyzes radio signals from several of these satellites and determines position, speed, and elevation using trilateration techniques. Unlike triangulation which uses angles, trilateration uses the intersection of radial distances (surface for 3-D geometry) between satellites to calculate the approximate geo-location.

Light-weight and low-cost GPS modules compatible with various flight controllers are widely available. Table 3.2 shows popular commercial GPS modules used on UAVs. These modules are capable of communicating with multiple GNSS and interfacing through various serial communication protocols. Due to FAA regulations, they are programmed to limit the maximum above ground level (AGL) altitude based on operating location.

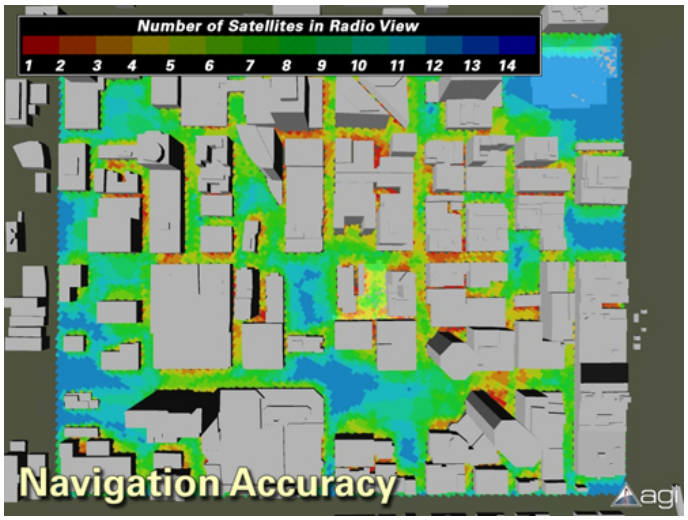

Figure 3.7: **Variation in number of reachable satellites in an urban environment.**

Figure 3.6 shows the autonomous waypoint following trajectory taken by a quadcopter equipped with Pixhawk and the u-blox LEA-6H module described in table 3.2. The u-blox GPS was tested outdoors in an open field and as a result, was able to accurately navigate the quadcopter to the selected waypoints within 2.5 meters of error. Accuracy declines when operating in urban environments composed of buildings and large structures because of propagation effects of signals diffracting off the surfaces. As a result, receivers on the GPS modules are unable to discern the different signals transmitted by satellites (Fig. 3.7). An alternative means of calculating position indoors and in urban settings is by relying on visual odometry.

3.5.2 Visual Odometry (VO)

Visual odometry (VO) is a specific form of structure from motion (SFM) technique that estimates real-time pose by identifying visual changes in captured images with

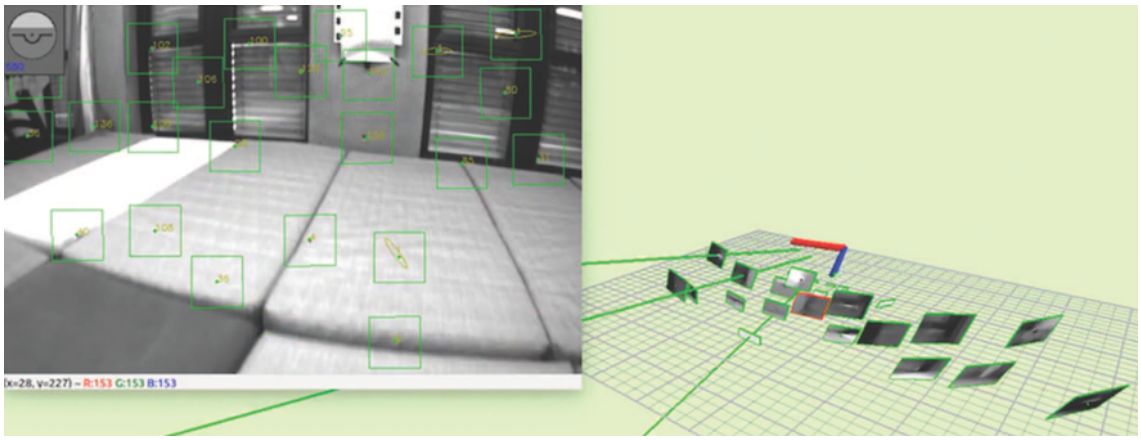

Figure 3.8: **Landmarks tracked by ROVIO to construct estimated camera poses in 3-D [57].**

respect to a reference frame [56]. VO generates a local position estimate that is incrementally updated based on detected features. Common VO methods focus on one particular technique, from feature matching or feature tracking, to optic flow. Feature tracking identifies the selected feature across all frames, whereas feature matching only uses consecutive frames. Therefore, the feature tracking technique results in lower drift in the position estimate.

Instead of using features (e.g edge, color etc.), the optic flow technique relies on spatio-temporal image gradients or pixel intensities in specific regions between consecutive frames. Traditional optic flow algorithms such as the Lucas-Kanade assume that pixels in a local neighborhood have constant intensity, spatial coherence, and undergo small motions. A least-squares fit is then applied to the neighboring pixels to obtain their 2-D velocity components (u, v) across consecutive frames.

Overall, VO can be separated into four main parts: (1) image sequence, (2) feature detection, (3) motion estimation, and (4) local bundle adjustment [56]. Motion

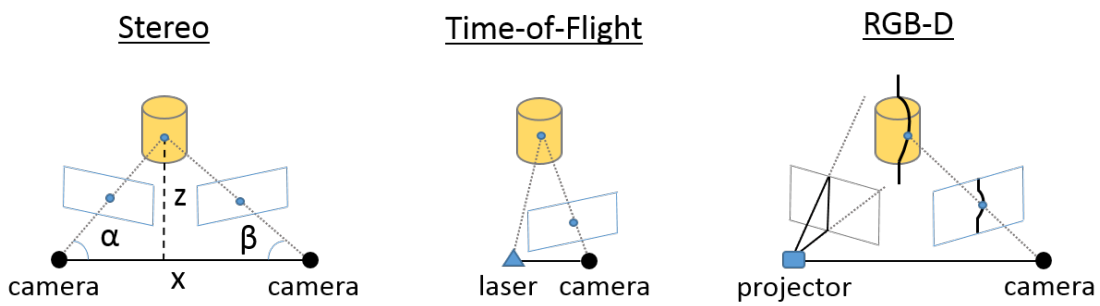

Figure 3.9: **Camera concepts used for visual odometry.**

estimation is typically performed using random sample consensus (RANSAC), an iterative method for model fitting using data set containing outliers. Using RANSAC, transformation between camera images can be recalculated using only inlier points. Local bundle adjustment is the final step and involves refining 3-D coordinates and parameters of relative motion.

Several open-source VO software frameworks are available and have been successfully demonstrated on aerial platforms [56–58]. Robust Visual Inertial Odometry (ROVIO) is a framework developed by ETH Zürich that combines visual odometry with inertial measurements using iterated extended Kalman filter (EKF). The resulting algorithm exhibits high levels of robustness and enables quick start-up by omitting initialization procedures. Figure 3.8 shows a snapshot of the monocular camera-based ROVIO extracting landmark data to construct 3-D estimated camera poses and their distance uncertainties. In terms of hardware, visual odometry can be implemented using passive, active, and event-based cameras.

Table 3.3: Comparison between types of cameras for VO.

	Advantage	**Disadvantage**
Monocular	Inexpensive and light-weight Simple calibration	No depth information
Stereo	Depth information (3-D) Observable image scale	Complex calibration Degrades to monocular (2-D) in some cases
Omni-directional	Wide field of vision (360°) Rotational invariance	Expensive and heavy Complex algorithm (synchronization)
Time-of-flight	Inexpensive and light-weight Depth information (3-D) Fast processing	Vulnerable to high ambient light Interference from other ToF devices No auto-focus capability
RGB-D	High depth image resolution Provides colored depth points Operational in low-light conditions	Expensive and heavy Low frame rate Limited to indoor applications (IR)
Event-based	Asynchronous (variable time intervals) Fast visual measurements with low latency High dynamic range Low computational cost	Requires new computer vision algorithms No intensity information Low image resolution

3.5.2.1 Passive Cameras

Passive cameras rely on an external light source (e.g sunlight) to illuminate the scene and measure naturally emitted reflections. These cameras are typically simpler in mechanical design and include monocular, stereo, and omni-directional vision technologies.

Monocular visual odometry relies on a single camera while stereo uses two or more cameras to capture multiple images of the same scene. As a result, stereo visual odometry method provides depth information. The 3-D position of an object is reconstructed using triangulation by simultaneously tracking features in successive frames captured by multiple cameras that are separated by known distances. The algorithm uses a simple pin-hole camera model (Fig. 3.9) where depth (z) is calculated using measured angles (α, β):

$$z = \frac{x}{\frac{1}{\tan\alpha} + \frac{1}{tan\beta}} \tag{3.26}$$

Complications arise when a corresponding feature or point is not identified by all cameras. If captured images lack variations in color and intensity (e.g uniformly colored wall), the stereo vision algorithm would be unable to detect features. Omni-directional cameras have a wider field of vision (up to 360°) and provides larger image frame for feature detection [59]. While they can provide a well refined 3-D model of the environment, calibrating and synchronizing multiple cameras consume high computation power. Table 3.3 provides a comparison of different types of

cameras typically used for visual odometry.

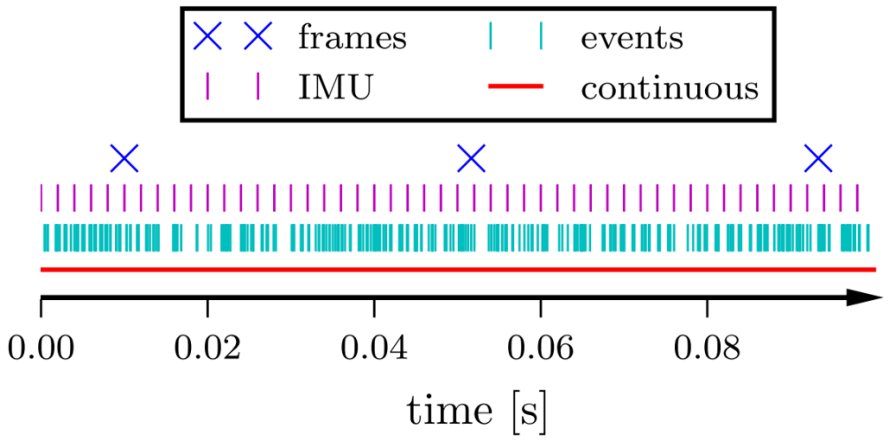

Figure 3.10: **Comparison of data transmission rate between frame-based and event-based cameras [60].**

3.5.2.2 Active Cameras

While passive cameras use natural light, active cameras illuminate the images with artificial light to measure depth. In particular, time-of-flight (ToF) cameras use a CMOS pixel array and a solid-state laser or LED in the near-infrared range [61]. The light source is pulsed as a sinusoidal electromagnetic wave with constant amplitude and frequency. Between the pulses, the reflected light is detected by an imaging sensor and converted from photonic energy to electrical current (Fig. 3.9). One disadvantage of using ToF cameras is that the reflections can be distorted by high ambient light. As a result, measurements have reduced signal-to-noise ratio, which diminishes the accuracy of depth calculation.

Instead of modulated light, RGB-depth (RBG-D) cameras, such as Microsoft's

Kinect, use an infrared structured light that operates by projecting a pattern onto the scene (Fig. 3.9) and then analyzing the pattern distortion to calculate depth [62]. Typical RGB-D cameras use a digital light processing (DLP) projector and a high resolution color camera. The resulting measurement has high depth image resolution and also colored depth points (colored point clouds). Since the structured light algorithm relies on detecting pattern disparities between frames, it operates at a lower frame rate compared to ToF sensors.

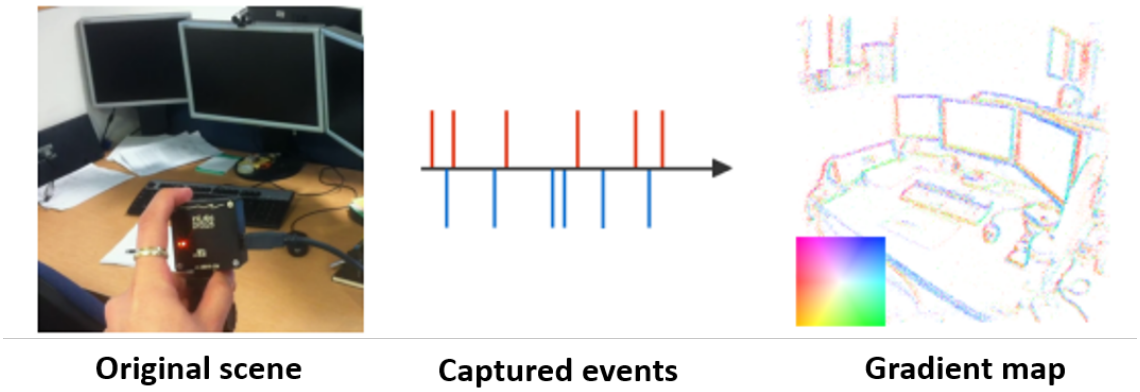

Figure 3.11: **Captured events and projected gradient map [63].**

3.5.2.3 Event-Based Cameras

A significant limitation of frame-based cameras such as ones described in previous sections is that frames are captured at fixed time intervals [64]. Each frame captures all the pixels in order to track features, which results in an inherent limitation on data rate and latency. Bio-inspired event-based cameras such as the Dynamic Vision Sensor (DVS) transmit asynchronously where each event is only registered when the sensor detects change in the image (Fig. 3.10). Instead of capturing stan-

dard intensity frames, DVS detects disparities in pixel-level brightness. In general, conventional cameras record the scene while DVS records how the scene changes. Figure 3.11 shows example of captured events and the projected gradient map of the scene. Compared to conventional cameras, event-based cameras have latency in the order of microseconds, high dynamic range (130 dB vs. 60 dB), and consume less power [60].

Since the event-based camera captures events instead of conventional frames, it requires new computer vision algorithms. In the past few years, new algorithms have been developed for visual-inertial odometry (VIO) and 3-D visual simultaneous localization and mapping (SLAM) using the DVS128 camera. Using a single event-based camera, these algorithms are able to quickly track 6-DOF camera motion and reconstruct 3-D scenes [65].

3.5.3 Simultaneous Localization and Mapping (SLAM)

While VO and VIO incrementally estimate the local pose (position and orientation) of an object using camera images, SLAM involves estimating the global pose of the vehicle on a map of the environment that is simultaneously generated. With each new measurement, the estimated pose and map of environment are incrementally updated. However, it should be noted that visual SLAM incorporates VO and VIO into the algorithm to estimate pose from matched features between images. Main components of SLAM include: (1) sensor measurement, (2) landmark/feature extraction, (3) data association, (4) state update, and (5) state prediction, where

the update and prediction steps form a closed loop [56].

Fundamentally, the concept can be defined as a probabilistic problem that is solved using Bayes' Theorem [66]. Physical implementation of SLAM requires observation and motion models to computationally calculate the probabilities. Existing statistical techniques used to approximate the SLAM solution can be categorized into filtering approaches and smoothing approaches. Filtering approaches solve SLAM real-time with each available sensor measurement and typically rely on an Extended Kalman Filter (EKF-SLAM) or a particle filter. Smoothing approaches, such as GraphSLAM and RBG-D SLAM, use least-squares error minimization to solve the full SLAM problem

Table 3.4: Existing LIDAR sensors for UAVs.

	Leddertech Vu8 (Wide)	**Velodyne VLP-16**	**Velodyne HDL-32E**
Weight (g)	129	830	1300
Range (m)	34	100	80–100
Accuracy (cm)	±5	±3	±2
Horizontal FOV (°)	100	360	360
Angular Resolution (°)	0.25	0.1–0.4	1.33
Dimensions (mm)	73(H) x 40(W) x 65(D)	103(Diam) x 72(H)	86(Diam) x 150(H)
Typical Power Consumption (W)	2	8	24
Cost (USD)	450	7999	29,900

over the entire map. These solutions rely on sensor measurements from various sources such as Light Imaging And Detection (LIDAR) scanners and cameras.

3.5.3.1 LIDAR

A LIDAR scanner operates by pulsing laser beams and analyzing the reflected light to measure traveled distance. Since the sensor uses lasers with a specific wavelength (typically 905 nm), it avoids interference from other sources [66]. Compared to cameras discussed in the previous section, LIDAR sensors have a wider field of view (FOV) and operate at high frame rates. Table 3.4 summarizes existing LIDAR sensors suitable for UAVs due to their weight and capabilities. These sensors are capable of taking high accuracy measurements ($\pm$5 cm) with considerable range of up to 100 meters. Upgrading from Leddertech Vu8 to Velodyne VLP-16 in order to acquire a full 360° FOV amounts to a significant increase in weight, quadrupled power consumption, and more than 17 times the increase in cost.

3.5.3.2 Visual SLAM (V-SLAM)

Recent advancements in CPU and GPU technologies have resulted in surge of camera-based SLAM algorithms, referred to as visual SLAM (V-SLAM). Visual SLAM has been demonstrated using monocular, stereo, omni-directional, RGB-D, and even event-based cameras. Table 3.5 compares existing V-SLAM algorithms ordered by sensor type and map density method. A sparse map density algorithm only uses a small region of pixels while a dense map algorithm uses most or all the

Table 3.5: Comparison of available visual SLAM framework [67, 68].

	PTAM	**ORB-SLAM**	**VISLAM**	**ORB-SLAM2**	**DTAM**
Sensor	Monocular	Monocular	Stereo	Monocular, Stereo, RGB-D	RGB-D
Method (Direct/Indirect)	Indirect	Indirect	N/A	Direct	Direct
Map Density	Sparse	Sparse	N/A	Semi-dense	Dense
Global Optimization	Yes	Yes	N/A	Yes	No
Loop Closure	No	Yes	N/A	Yes	No

pixels in an image frame. The resulting map from sparse methods are point clouds while dense methods provide a detailed scene. As expected, dense methods require higher computation power and typically run on GPUs. Indirect methods such as PTAM and ORB-SLAM extract features first and then use the features to localize while direct methods use pixel intensities directly instead of features. To reduce sensor drift, algorithms such as ORB-SLAM and ORB-SLAM2 employ loop closure techniques where previously detected features are used to update the current pose estimate. While most existing algorithms are open-source and developed by public institutions, emerging proprietary algorithms such as VISLAM developed by Qualcomm are becoming accessible.

3.6 MAV-Scale Onboard Computer

VIO and SLAM algorithms for autonomous navigation require computation power beyond capabilities of autopilots discussed in the previous section. MAVs must instead rely on onboard computers with dedicated processors (CPU, GPU) and adequate data processing power. A significant constraint for selecting onboard computers is limitation on weight. Table 3.6 compares commercial off-the-shelf (COTS) processors available for MAVs due to their light weight ($\leq$100g) and compact size.

3.6.1 Qualcomm Snapdragon Flight

Qualcomm Snapdragon Flight board serves as both an onboard computer and an auto-pilot because of its integrated sensors and stereo camera. The current version

Table 3.6: Comparison of available light-weight onboard computer [69].

	Snapdragon Flight	**ODROID XU-4**	**NVIDIA Jetson TX2**
Weight (g)	26	65	85
Dimensions (cm)	7.9 x 6.1 x 0.8	9.4 x 7.0 x 1.8	8.6 x 5.1 x 0.5
CPU	Krait (2.26GHz)	Exynos5422 Cortex-A15 (2GHz) + Cortex-A7 (octa-core)	ARM Cortex-A57 (2GHz) + NVIDIA Denver2 (2GHz)
GPU	Adreno 330 (578MHz)	ARM Mali-T628 MP6 (600MHz)	256-core Pascal (1300MHz)
DSP	QDSP6 V5A (801MHz)	-	-
Operating System	Linaro Linux	Linux LTS	Linux4Tegra
Integrated Sensors	Yes	No	No
Integrated Camera	Yes	No	No
Cost (USD)	400	59	500

of the board is built on the Snapdragon 801 series processor commonly found in smartphones. Weighing only 26 grams, the board is integrated with a quad-core 2.26 GHz central processing unit (CPU), a dedicated digital signal processor (DSP), and Qualcomm's 378 MHz graphics processing unit (GPU) that runs their proprietary VISLAM algorithm. VISLAM uses the 4K high-resolution Sony IMX135 forward-facing camera and the downward-facing Omnivision OV7251 optic flow camera. Additional sensors include the Telit Jupiter SE868 V2 GPS module, Invensense MPU-9250 IMU, and the Bosch BMP280 barometer. Researchers have previously demonstrated autonomous hover using the Snapdragon Flight kit interfaced with the ELKA autopilot [69, 70]. While the Snapdragon Flight 801 series was recently discontinued, a new version armed with the Snapdragon 802 series processor will be introduced in the near future.

3.6.2 ODROID XU-4

ODROID XU-4 is an inexpensive board-only alternative, equipped with two CPUs (Samsung Cortex-A15 and Cortex-A7 octa-core) and a GPU (Mali-T628 MP6). With open-source support, the board is capable of running multiple Linux operating systems such as Ubuntu 16.04, Android 4.4 Kitkat, 5.0 Lollipop, and 7.1 Nougat. ODROID also offers variety of boards with different processing power, from the Exynos5 Octa series to ESP32 series. Researchers have previously supplemented a Samsung Galaxy S5 smartphone with ODROID XU-4 to demonstrate autonomous navigation [71].

3.6.3 NVIDIA Jetson TX2

The NVIDIA Jetson TX2 is integrated with the 64-bit hex-core ARMv8 CPU complex, which is a stack of ARM Cortex-A57 (quad-core, 2GHz) and NVIDIA Denver2 CPUs. With its 256-core NVIDIA Pascal GPU and NVIDIA cuDNN and TensorRT libraries, the board supports deep neural network (DNN) architectures, recurrent neural networks (RNNs), long short-term memory networks (LSTMs), and online reinforcement learning. Aside from machine learning applications, the Jetson TX2 has been integrated with the Bebop 2 quadcopter kit to demonstrate active vision-based gap detection for quadcopters [72].

3.7 Telemetry

Whether piloted or autonomous, UAVs maintain remote communication with a nearby ground control station (GCS). Noncritical tasks with high computational costs can be processed on the GCS instead of overloading onboard avionics. In particular, missions such as surveillance and search-and-rescue especially require real-time data streams and vehicle diagnostics. Telemetry between the cyclocopter and GCS was enabled through wireless communication.

3.7.1 Wireless Communication (Wi-Fi)

Communication between ELKA and the ground control station is achieved via LabVIEW interface through a nRF wireless transceiver module (Fig. 3.12). The board receives pilot inputs through a commercial Spectrum receiver which independently

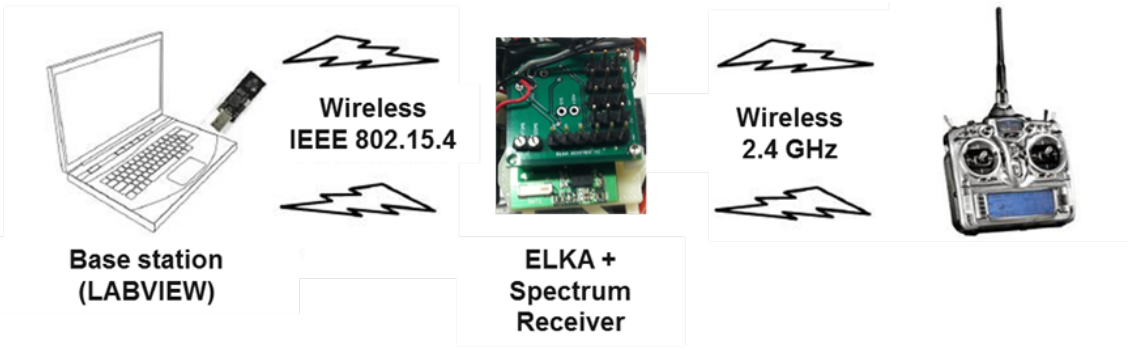

Figure 3.12: **Telemetry implemented for the cyclocopter.**

connects to the transmitter through a wireless 2.4 GHz radio link. A separate connection between the Spectrum receiver and transmitter ensures that the pilot will still have command over the vehicle if connection is lost to the ground control station.

The ground control station allows the user to modify the gains of the feedback system, change sensitivity of pilot inputs, and record attitude data transmitted by ELKA. All the data processing, feedback control calculations, and roll-yaw decoupling methods are performed onboard by ELKA. It is also able to serially connect with auxiliary sensors such as a motion capture system and simultaneously record data from all connected sensors.

High level stick inputs from the pilot are transmitted to the vehicle through the radio control (RC) transmitter and received by the satellite receiver connected to ELKA. The JR X9303 transmitter sends actuator commands via Digital Spectrum Modulation (DSM). Compared to traditional radio systems, DSM is less susceptible to radio interference or crosstalk because it does not require a crystal set to a specific frequency band and channel. Instead, DSM broadcasts signals using either

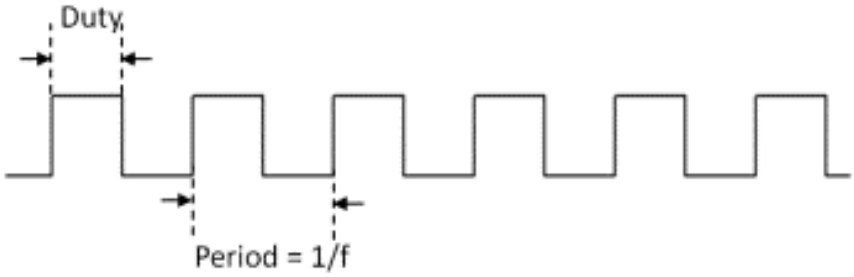

Figure 3.13: **PWM signals used by actuators (f = frequency).**

Frequency Hopping Spread Spectrum (FHSS) or Direct Sequence Spread Spectrum (DSSS). FHSS is a broadcasting method where the controller transmits narrow band signals that consistently hop between multiple frequencies within the 2.4 GHz band. DSSS is a more common method, and used by JR transmitters, where the system operates on a single frequency but on a very wide band.

The satellite receiver translates inputs from the radio controlled (RC) transmitter into pulse width modulated (PWM) signals. These inputs are in microseconds and represent the duty cycle of the PWM signal (Fig. 3.13). PWM signals range from 1000–2000 microseconds and denote the time voltage is provided to the actuator, effectively turning it on. Final inputs to the feedback control system include 5 PWM values for the three motors and two servos used by the twin-cyclocopter. The frequency of pulse can also be adjusted to match actuator requirements. Typically, motors require a higher pulse frequency (> 500 Hz) while analog servos prefer lower pulse frequency (< 100 Hz) to prevent servo noise.

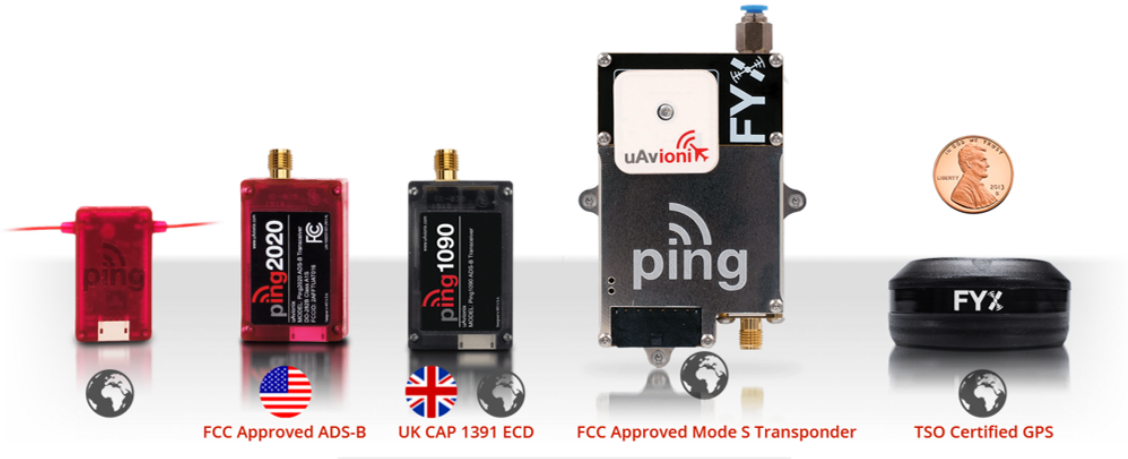

Figure 3.14: **MAV-scale ADS-B sensors developed by uAvionix.**

3.7.2 Automatic Dependent Surveillance-Broadcast (ADS-B)

Aside from communication between the UAV and its GCS, communication with neighboring aircraft is critical for safe integration of UAVs into the National Airspace System. An automatic dependent surveillance-broadcast (ADS-B) is a surveillance equipment that broadcasts the location of an aerial vehicle in real-time using a digital data link. Ground stations serve as nodes by relaying ADB-S data to vehicles in the airspace. The digital data link broadcasts in the 1090MHz band and includes flight identification number, unique aircraft code, position, altitude, rate of climb/descent, and velocity data. Recently, uAvionix released a FCC approved miniature ADS-B system for UAVs. The ping2020i is a light-weight full range ADS-B transceiver weighing at 20 grams (Fig. 3.14). Integrated with both GPS and barometer, ping2020i is capable of detecting aircraft within 100 statute mile radius.

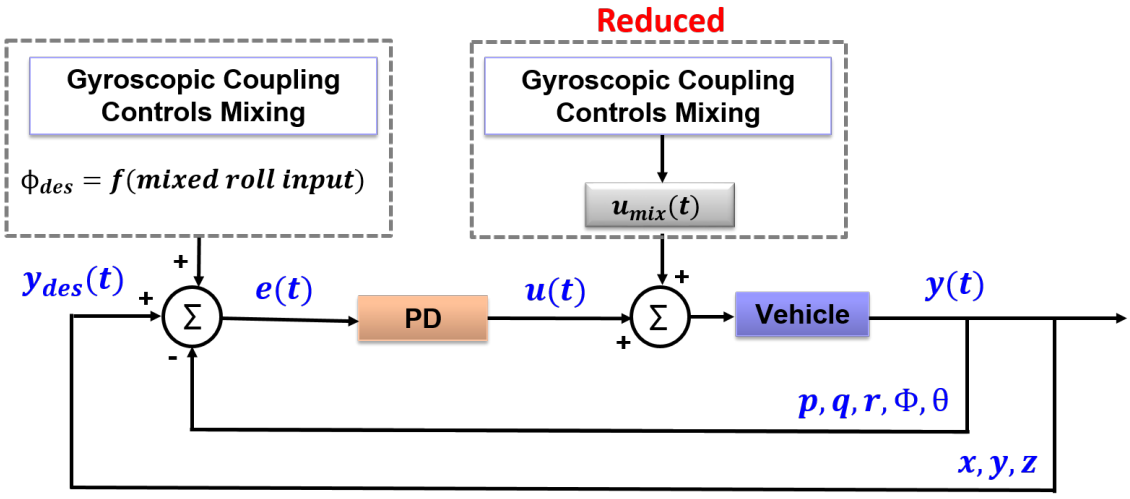

Figure 3.15: **Schematic of closed-loop feedback system with the incorporated roll-yaw decoupling strategy.**

3.8 Closed-Loop Feedback System

While the previous sections covered sensors for both piloted and autonomous navigation, the cyclocopter is primarily equipped with sensors for flight stability and control such as gyroscopes and accelerometers. Therefore, the closed-loop feedback system implemented on the vehicle is a linear single-input single-output (SISO) system divided into an inner-loop for attitude stabilization and an outer-loop for position control by a pilot (Fig. 3.15). The vehicle relies on manual control because of limitations of estimating position with the current setup of onboard sensors in an indoor setting.

Chapter 6 discusses modifications to the outer-loop to achieve autonomous navigation using external sensors. One method of estimating position and velocity is through dead-reckoning, a process of integrating accelerometer and gyroscope

measurements. Due to noise levels and biases, accuracy of the integrated data deteriorates over time. For stationary accelerometer measurements, the error in estimated position is $\alpha\sqrt{T}$ where α depends on standard deviation of the accelerometer noise and sampling frequency of data and T is the integration time [73].

As mentioned previously, alternatives to integrating inertial sensors include using cameras and estimating position through optic flow. These techniques are beyond the scope of the present study and are not considered at this time. Autonomous navigation can also be achieved using external sensors such as a motion capture system. Later chapters will discuss methodologies involved in controlling the cyclocopter using such system.

The outer-loop implemented on the vehicle updates at 45 Hz while the inner-loop updates at 1000 Hz. The outer-loop rate is limited due to the commercial transmitter. Desired states of the closed-loop feedback system include pilot commands through the RC transmitter, which associates to a desired pitch and roll Euler angles (ϕ, θ) and the angular velocities in the body frame (p, q, and r). The final control inputs to the vehicle actuators are the individual rotational speeds of the rotors and the two servo inputs for thrust vectoring.

3.8.1 Attitude Stabilization

Typical SISO systems use a proportional-integral-derivative (PID) control scheme for attitude stabilization. The proportional (P) compensator outputs a value that is a gain (K_p) multiplied by the error between the system's output and desired input.

The integral (I) compensator reduces the steady-state error of the feedback system by using the integral of error over time multiplied by a gain (K_i). Finally, the derivative (D) compensator provides damping and improves the transient response of the system by using the derivative of the error signal multiplied by a gain (K_d). The PID controller is represented by the following equation [74]:

$$u(t) = K_p e(t) + K_i \int_0^t e(\tau)d\tau + K_d \frac{de}{dt} \tag{3.27}$$

where $e(t)$ is the error between system's measured output, $\hat{y}(t)$, and desired input, $y_{des}(t)$:

$$e(t) = y_{des}(t) - \hat{y}(t) \tag{3.28}$$

Within PID, the integral controller compensates for environmental disturbances or modeling errors. It slowly reduces the steady-state errors by increasing the feedback inputs, $u(t)$. A large disturbance or immediate change in the setpoint can result in an undesirably large feedback input which can cause the system to overshoot the setpoint and destabilize the vehicle. In addition, the cyclocopter experiences inherent gyroscopic couplings along the roll-yaw axis. The gyroscopic coupling and the corresponding decoupling strategy is intensively discussed in Chapter 5. Complexities from the decoupling strategy led to selection of a PD control law for attitude stabilization of the cyclocopter.

The inner-loop can be further broken down into cascaded control loops composed of attitude and rate controllers. The inner-loop stabilizes around a desired

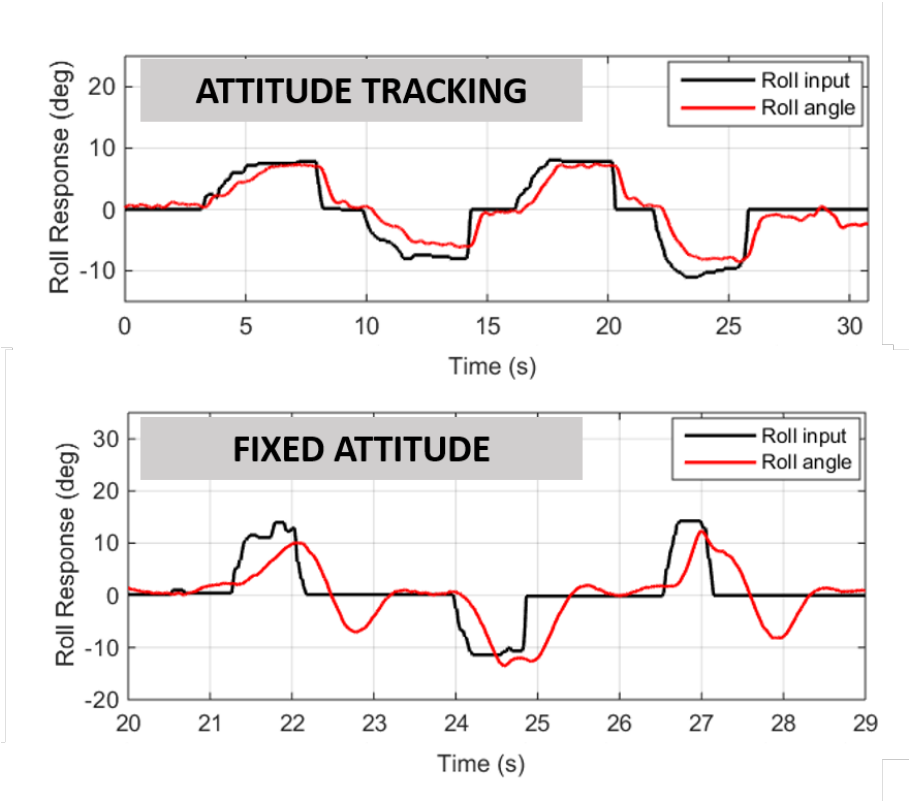

Figure 3.16: **Comparison of attitude tracking controller vs. fixed attitude controller (previous implementation).**

input commanded by the pilot. These inputs to the system are roll and pitch attitude angles (ϕ, θ). Heading angle (ψ) is provided as a feedforward term, where the final servo output is calculated based on the given pilot command and independent of the attitude controller. Both the attitude and rate controllers operate at 1000 Hz, but in the current setup, the attitude controller has a dynamic setpoint while the rate controller always stabilizes around zero angular velocities along each axis. The modification is known as derivative kick and is typically used to reduce large spikes originating from taking derivative of the setpoint.

The inner-loop control schematic achieved improved setpoint tracking (Fig. 3.16) compared to previous system [39]. The desired states (ϕ, θ, p, q, r) are dependent on

Table 3.7: Ziegler-Nichols Frequency Response Method.

Controller	K_p	T_i	T_d
P	$0.5\ K_u$	∞	0
PI	$0.4\ K_u$	$0.8\ T_u$	0
PID	$0.6\ K_u$	$0.5\ T_u$	$0.125\ T_u$

the pilot command and the mixed output from decoupling strategy. Previously, the desired states were specific to the hover condition and set to zero in order to negate any perturbation from trim. In addition, the modified controller incorporates roll-yaw decoupling scheme in the inner-loop and as a feedforward term (Fig. 3.15). The integration to the inner-loop reduced the dependence on the feedforward correction, $u_{mix}(t)$, which improved overall tracking.

3.8.2 Ziegler-Nichols PID Tuning in Hover

Equation 3.27 shows the PID controller in the time domain. However, the equation is better represented in the frequency domain (s-domain) for analysis and when designing the initial system. The PID controller in s-domain is written in terms of integration time (T_i) and derivative time (T_d):

$$u(s) = K_p(1 + \frac{1}{T_i s} + T_d s) \tag{3.29}$$

The relationship between K_d and K_i with integration and derivative times can be described by the following:

$$K_i = \frac{K_p}{T_i} \tag{3.30}$$

$$K_d = K_p T_d \tag{3.31}$$

Ziegler-Nichols is a traditional method of experimentally tuning PID gains. The tuning process involves either using open-loop step response or by characterizing frequency response of the system. The first method uses the following to determine the gains: (1) time delay between the desired step-change in output and the measured output and (2) reaction rate, which is calculated using intersection between tangent of the step response and the coordinate axes. The second method, using frequency response, is an empirical tuning process based on locating the point of intersection between the system's Nyquist curve and the negative real axis. Experimentally, this is determined by incrementally increasing the proportional gain until the system achieves sustained oscillations. Values of the gain (K_u) and period of oscillation (T_u) are then subsequently used to determine the PID gains (Table. 3.7).

Prior to free-flight tests, the Ziegler-Nichols method was used to find the proportional and derivative gains along the pitch, roll, and yaw axes through series of isolated 1-DOF and 3-DOF perturbation experiments. The vehicle was suspended by its nose rotor spar along two ball bearings encased in a 3-D printed housing for both the roll and pitch stands. The setup restricted the vehicle's rotation to $\pm 20^\circ$ either along the longitudinal or lateral axis. Afterwards, the cyclocopter was mounted on a 3-DOF gimbal stand that enabled up to $\pm 10^\circ$ of rotation along all

Table 3.8: Gains used in feedback system.

Feedback System	Gain	Value	Unit
Attitude	$K_{p\phi}$	0.4	$\frac{1}{rad}$
Attitude	$K_{p\theta}$	0.3	$\frac{1}{rad}$
Attitude	$K_{d\phi}$	0.6	$\frac{s}{rad}$
Attitude	$K_{d\psi}$	0.7	$\frac{s}{rad}$
Attitude	$K_{d\theta}$	0.7	$\frac{s}{rad}$

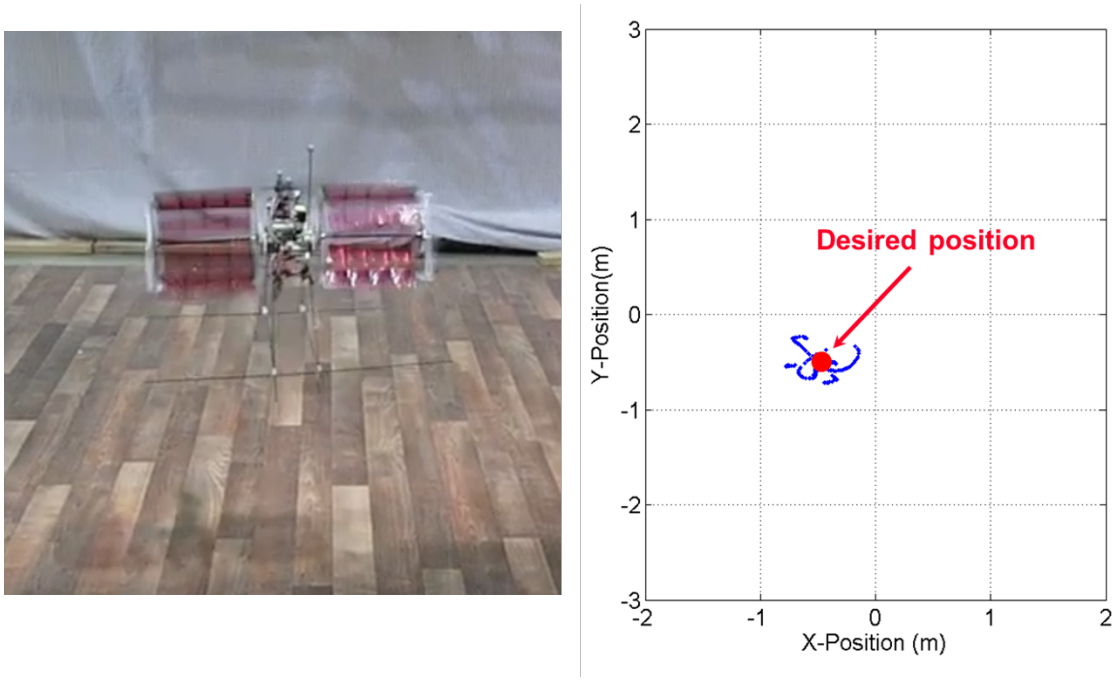

Figure 3.17: **Twin-cyclocopter in steady hover (position data on right).**

three body axes. The stand composed of a gimbal bearing attached to a 3-D printed housing, which coincided at the vehicle's center of gravity (C.G).

3.8.3 Hover Flight Tests

The gains were further fine-tuned in flight due to discrepancies between gimbal stand testing and actual flight conditions. Friction from the gimbal bearing contributed additional damping to the vehicle's dynamics, which resulted in selecting lower gains.

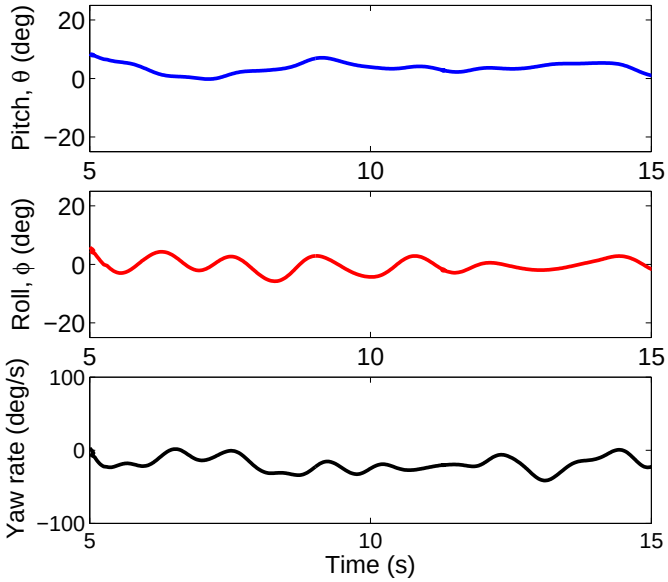

Figure 3.18: **Attitude data from ELKA during hover.**

In addition, there was a shift in C.G since the vehicle used a LiPo battery in flight instead of directly connecting to a power supply.

Flight tests were systematically conducted by first providing a pure throttle command and observing the vehicle response. The cyclocopter was found to be sensitive to ground effect. If the throttle was increased incrementally such that the cyclorotors spooled up in a slow rate, the vehicle would drift laterally and fail to gain altitude. To mitigate ground effect, throttle was increased in a step-wise manner to quickly achieve the operating RPM. Any additional forward translation out of ground effect was counteracted by either uniformly reducing the phasing of the cyclic blade pitch or varying the tail propeller RPM.

After fine-tuning the gains, the twin-cyclocopter successfully demonstrated stable piloted hover within 1 m^2 area (Fig. 3.17). Position data was taken using the VICON motion capture system. With the modified closed-loop feedback system,

onboard attitude data showed that the controller achieved satisfactory attitude angles and rates (Fig. 3.18). The next step is to explore control strategies for forward flight using the cyclocopter's thrust vectoring capability.

3.9 Summary

This chapter provided a comprehensive overview of sensors equipped on both piloted and autonomous MAVs. Due to weight restrictions, MAVs are confined to using light-weight and compact avionics consisting of autopilot, sensors, and an onboard computer. Sensors discussed in this chapter are used for flight stability and control, flight performance diagnostics, and guidance and navigation (autonomy). Sensors required for visual odometry and SLAM were also compared along with available open-source algorithms. Finally, the chapter included an introduction to closed-loop feedback system and the tuning method used for the cyclocopter.

In particular, the cyclocopter achieved stable piloted hover using a PD-based closed-loop feedback system and ELKA-R, a custom light-weight autopilot. Improvements to the inner-loop attitude stabilization resulted in improved tracking. Onboard sensors include an IMU with tri-axial gyroscopes and accelerometers. An additional pressure transducer was used to mitigate perturbation from gusts and will be discussed in a later chapter. Communication between ELKA-R and a nearby ground control station was facilitated using a nRF wireless transceiver. In addition, a 2.4 GHz radio link connected the pilot's transmitter to a Spektrum receiver onboard ELKA-R in order to maintain an independent link to the vehicle.

Chapter 4: Flight Control Strategy

4.1 Overview

The previous chapter discussed the development of twin-cyclocopter subsystems ranging from cyclorotor propulsion system to the closed-loop feedback system. In this chapter, flight control strategies for the cyclocopter are developed by using a combination of independent thrust vectoring and rotational speed control of the two cyclorotors and nose propeller. Advantages of the developed strategy include seamless transition from hover to forward flight, and capability to maintain a power-efficient level attitude in flight. Such a strategy also led to roll-yaw cross-couplings that inhibited onboard stabilization. Sources of cross-couplings across all flight modes are discussed in details. Results from wind tunnel studies conducted using a 5-DOF experimental stand were used to develop a control strategy to achieve decoupled dynamics. In addition, effects of free-stream velocity, rotational speed, and phasing angle on the roll-yaw cross-couplings were closely investigated and used to determine control inputs to achieve zero pitch attitude at various airspeed. Finally, the developed flight control strategy was successfully demonstrated up to 5 m/s.

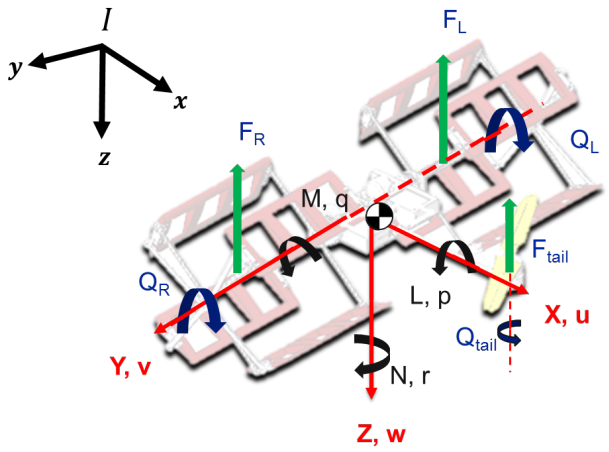

Figure 4.1: **Notation for forces and moments on the cyclocopter.**

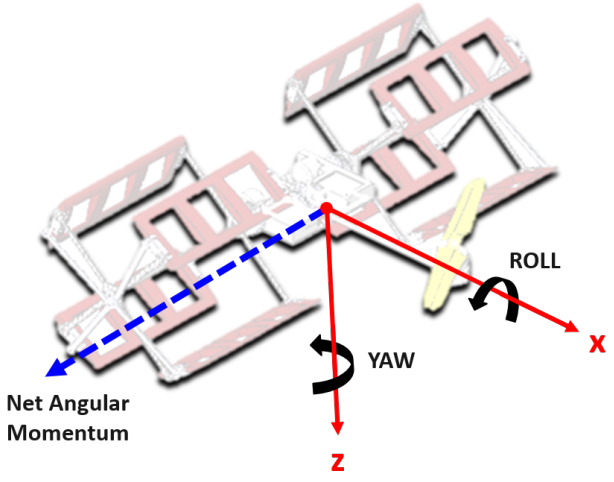

Figure 4.2: **Gyroscopic coupling due to net angular momentum.**

4.2 Rigid Body Dynamics

The first step in developing a flight control strategy is to understand the rigid body dynamics and evaluate trim equations for the forces and moments acting on the vehicle. Figure 4.1 shows the notation used for forces (X, Y, Z) and moments (L, M, N) along the vehicle's body axes. Translational velocities $[u, v, w]^T$ and angular rates $[p, q, r]^T$ are typically provided in the body frame, $\mathbf{B} = (x_B, y_B, z_B)$. However, position $[x, y, z]^T$ is typically provided with respect to the fixed frame or inertial frame, $\mathbf{I} = (x_I, y_I, z_I)$. Conversion between inertial and body frame is calculated using a conventional 3-2-1 rotation sequence using Euler angles $[\phi, \theta, \psi]$. The first rotation is about e_z by yaw angle (ψ), second rotation about e_y by pitch angle (θ), and finally the third rotation about e_x by roll angle (ϕ). Rotational transformation between the two frames is summarized by the following [52]:

$$[R_{BG}] = \begin{bmatrix} \cos\theta\cos\psi & \cos\theta\sin\psi & -\sin\theta \\ \sin\phi\sin\theta\cos\psi - \cos\phi\sin\psi & \sin\phi\sin\theta\sin\psi + \cos\phi\cos\psi & \sin\phi\cos\theta \\ \cos\phi\sin\theta\cos\psi + \sin\phi\sin\psi & \cos\phi\sin\theta\sin\psi - \sin\phi\cos\psi & \cos\phi\cos\theta \end{bmatrix} \tag{4.1}$$

Using the transformation matrix, body rates can be expressed in terms of Euler angles:

$$p = \dot{\phi} - \dot{\psi}\sin\theta \tag{4.2}$$

$$q = \dot{\theta}\cos\phi + \dot{\psi}\sin\phi\cos\theta \tag{4.3}$$

$$r = \dot{\psi}\cos\phi\cos\theta - \dot{\theta}\sin\phi \tag{4.4}$$

4.2.1 Forces and Moments

The rigid body (X, Y, Z) and moments (L, M, N) can be represented as series of ordinary differential equations as follows:

$$\sum X = m(\dot{u} + qw - rv) + mg\sin\theta + (F_L + F_R)\sin\Phi + -D_x \tag{4.5}$$

$$\sum Y = m(\dot{v} + ru - pw) - mg\sin\phi\cos\theta - D_y \tag{4.6}$$

$$\sum Z = m(\dot{w} + pv - qu) - mg\cos\phi\cos\theta - F_z + D_z \tag{4.7}$$

$$\sum L = I_{xx}\dot{p} - (I_{yy} - I_{zz})qr + (F_L - F_R)d_y + D_y d_z + H_y r \tag{4.8}$$

$$\sum M = I_{yy}\dot{q} - (I_{zz} - I_{xx})pr - (F_L + F_R)d_x + F_{tail}d_{tail} + D_x d_z - Q_{cyclo} \tag{4.9}$$

$$\sum N = I_{zz}\dot{r} - (I_{xx} - I_{yy})pq + (F_L + F_R)d_y\sin\Phi + D_y d_y - Q_{prop} - H_y p \tag{4.10}$$

In these equations, F_x, F_z, and F_{tail} are the total lift produced by the cyclorotors and propeller while F_L and F_R are the forces produced by the left and right cyclorotors (Fig 4.1). The D_x, D_y, and D_z are drag terms while the d_x, d_y, d_z, and d_{tail} terms are the moment arms. During forward flight, the forces produced by the

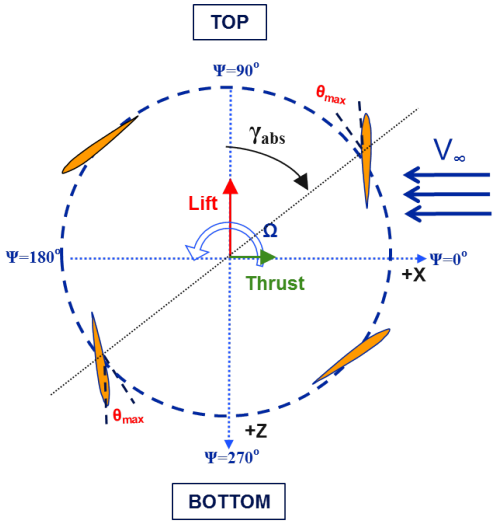

Figure 4.3: **Cyclorotor coordinates showing measurement of absolute phase angle (γ_{abs}), lift force, and propulsive force in forward flight.**

cyclorotor are influenced by its phase angle (Φ), rotational speed, and freestream velocity. The products of inertia terms (I_{xy}, I_{xz}, I_{yz}) have been removed because the cyclocopter is quasi-symmetric about the X-Y and X-Z planes.

4.2.2 Gyroscopic Coupling

The dominant gyroscopic moments produced by the cyclorotors are expressed in terms of angular momentum (H_y) in the respective axis. Angular momentum is a cross-product of rotational moment of inertia (I_r) and rotational speed (ω) of the cyclorotors. From the rigid body equations of motion, it is evident that roll and yaw dynamics are cross-coupled due the gyroscopic moment terms. The magnitude of cross-coupling increases with rotational speed, which further complicates stabilization. This inertial coupling is addressed in this chapter.

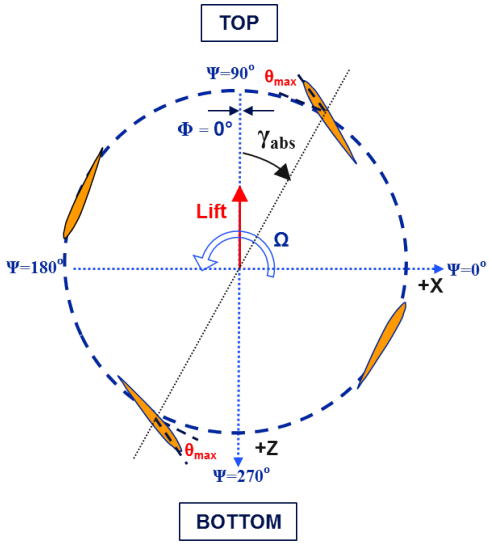

Figure 4.4: **Schematic showing hover condition with $\gamma_{abs} > 0°$ and Φ=0°.**

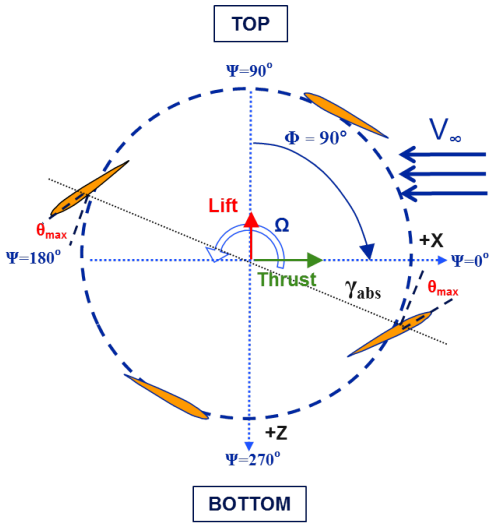

Figure 4.5: **Cyclorotor coordinates in forward flight where $\gamma_{abs} > 90°$ and Φ=90°.**

4.3 Cyclorotor Coordinate System

The coordinate system used for the cyclorotor is shown in (Fig. 4.3). The time-varying aerodynamic forces produced by the cyclorotor can be resolved into the vertical and horizontal directions. The azimuthal position of the blade (Ψ) is measured counter-clockwise from the horizontal axis of rotation and is equivalent to zero when the blades are rightmost side of the circular trajectory. The blade pitch angle (θ) is the angle between the blade chord and the line tangent to blade path. The absolute phase angle (γ_{abs}) is defined as the relative azimuthal location of the maximum blade pitch angle with respect to the -Z-axis. When $\gamma_{abs} = 0°$, the maximum blade pitch occurs at the top of the circular trajectory and when $\gamma_{abs} = +90°$, the maximum occurs $+90°$ clockwise towards the direction of incoming flow.

The lift and propulsive force components are defined as the net aerodynamic forces produced along the -Z-axis and +X-axis. For the present cyclorotor, the pitch amplitude is kept constant and the magnitude of the net resultant thrust vector is controlled by varying the cyclorotor rotational speed. The direction of the thrust vector is rotated through cyclic pitch phasing. To achieve a stable hover, the phase angle must be rotated such that the resultant thrust vector is purely vertical.

4.3.1 Forward Flight Orientation

For the remainder of the dissertation, the forward flight phase angle (Φ) of the cyclorotor, distinct from the absolute phase angle of each blade, is defined with respect to the phase in hover (γ_{hover}).

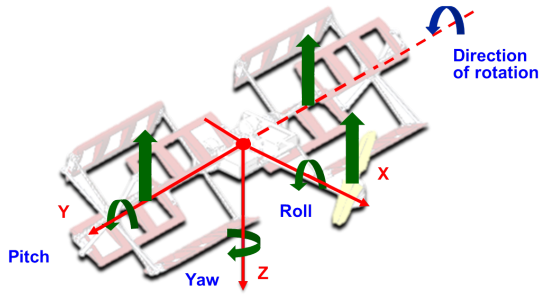

(a) Definition of pitch, roll, and yaw degrees of freedom.

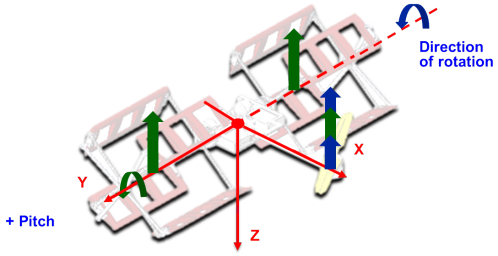

(b) Pitch control.

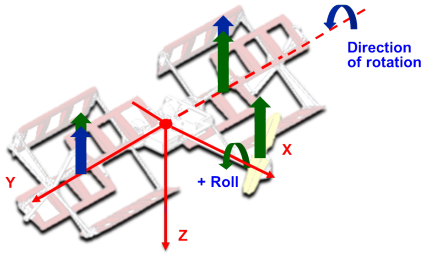

(c) Roll control.

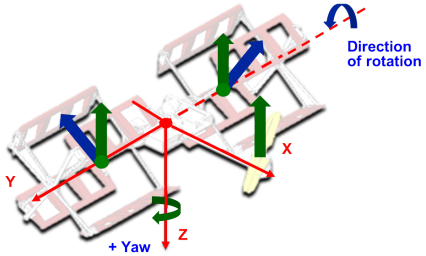

(d) Yaw control.

Figure 4.6: **Control strategy for twin-cyclocopter.**

$$\Phi = \gamma_{abs} - \gamma_{hover} \tag{4.11}$$

A forward flight phase angle of $\Phi = 0°$ corresponds to the hover condition when there is a net lift component and zero propulsive force (Fig. 4.4). As shown in (Fig. 4.5), the phase angle in forward flight is increased ($\Phi \geq 0°$) such that the blades have a non-zero pitch angle along the horizontal axis ($\Psi = 0°$ and $\Psi = 180°$). The resulting blade kinematics produces a net force vector with both a vertical lift component and a horizontal propulsive thrust component.

The phasing of cyclic blade pitch plays a significant role in trimming the cyclorotor in forward flight and this will be discussed in further detail in the next section.

4.3.2 Virtual Camber and Virtual Incidence Effect

As mentioned in chapter two, the blades on the cyclorotor experience virtual camber effect because of the curvilinear nature of the flow, which introduces a chordwise variation of velocity direction [80]. Therefore, a symmetric airfoil at 0° pitch behaves as a virtually cambered airfoil at a virtual incidence in a rectilinear flow. The blades experience a negative virtual camber and incidence at the top of the trajectory ($C_l < 0$) and a positive camber and incidence at the bottom portion of the trajectory ($C_l > 0$).

In forward flight, the advancing side of the blades are at the bottom portion of the trajectory while retreating at the top of the trajectory. The blades on the advancing side experience an increase in the net tangential velocity and a reduction in the retreating side. As a result, the blades produce a small downward lift force while operating in the upper half of the trajectory and large upwards lift force on the lower half, leading to an overall net positive lift force. Since virtual camber is influenced by the chord/radius ratio of the rotor and virtual incidence is also dependent on the chordwise location of the blade pitching axis, the magnitude of lift depend on these parameters and the direction of rotation.

While the direction of rotation is not important in hover, it is critical to the lift and thrust producing capability of the cyclorotor in forward flight. In the present vehicle, both the cyclorotors spin in the same direction along the +Y axis (Fig. 4.1), resulting in an unbalanced clockwise torque that must be counteracted by the conventional propeller. To obtain a positive resultant lift force, the cyclorotors

are mounted aft of the propeller system such that the blades are retreating at the top and advancing at the bottom of the trajectory.

4.4 Attitude Control in Hover

Figure 5.10(a) shows the definition of pitch, roll, and yaw degrees of freedom for the twin-cyclocopter. Stable hover, transition, and forward flight require a unique combination of independent rotational speed of all three motors and thrust vectoring of the cyclorotors for each mode of flight.

A positive roll is produced by increasing the rpm of the left rotor and decreasing the rpm of the right rotor (Fig. 5.10(c)). Finally, yaw is controlled through differential rotation of the two cyclorotor thrust vectors (Fig. 5.10(d)). The cyclorotors spin in the same direction along the +Y-axis so there is a net angular momentum that induces gyroscopic coupling between the roll and yaw degrees of freedom. To eliminate the gyroscopic coupling, an onboard control mixing was implemented where the roll and yaw inputs were appropriately combined to give decoupled motion. The decoupling strategy is presented with details towards the end of this chapter.

4.5 Attitude Control in Forward Flight

In forward flight, the combined forward flight phase actuation of cyclic blade pitch is used to control the forward velocity of the vehicle. Providing a cyclic pitch phasing for both cyclorotors rotates the resultant thrust vectors by the same phase angle. Essentially, an increase of the combined forward flight phase angle would

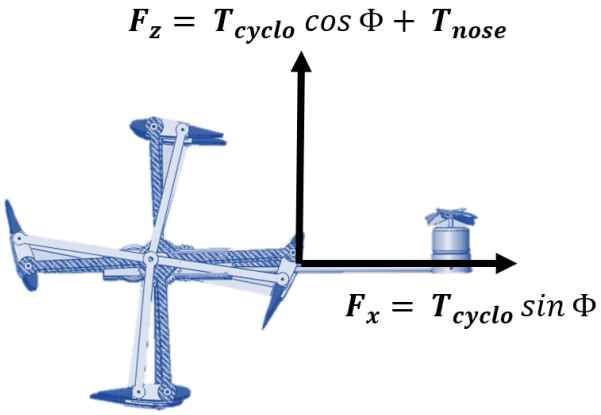

Figure 4.7: **Lift and propulsive thrust for cyclocopter in level forward flight.**

result in a higher propulsive force contribution from the cyclorotors. As in hover, pitch, roll, and yaw moments in forward flight are controlled through propeller rpm, differential cyclorotor rpm, and differential thrust vectoring, respectively. The pilot controls now include throttle (collective cyclorotor rpm), pitch (propeller rpm), roll (differential cyclorotor rpm), yaw (differential phasing), and forward velocity (collective phasing). Pitch control is available to the pilot because during flight, as the battery voltage drops, the pitch trim also changes due to discrepancies between the cyclorotors and nose rotor rotational speeds.

For the cyclocopter, transitioning from hover to forward flight does not involve any configuration changes. By slowly increasing the phase angle (Φ), the vehicle is able to steadily increase forward velocity and transition into forward flight. The rate of transition from hover to forward flight depends entirely on the phasing input (Fig. 4.7).

One of the major challenges in developing the forward flight control strategy

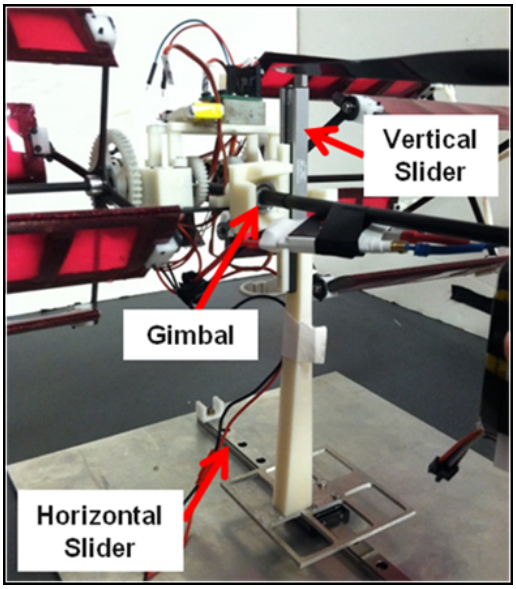

(a) 5-DOF experimental stand for wind tunnel testing.

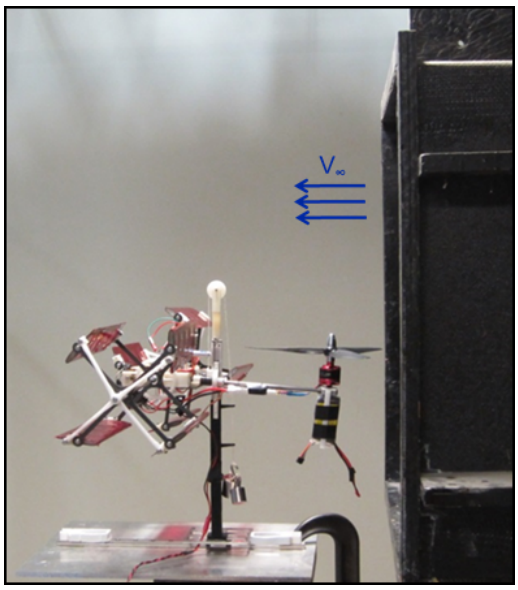

(b) Wind tunnel testing setup.

Figure 4.8: **Wind tunnel testing setup.**

is the existence of a strong coupling between the roll and yaw control that increases with the forward tilt of the thrust vector. Furthermore, this coupling is in addition to the inertial gyroscopic roll-yaw coupling that is experienced even for the hover case. Extensive wind tunnel experiments were conducted in order to understand the source of the roll-yaw control cross-coupling.

4.6 Wind Tunnel Studies

The objectives of the wind tunnel testing of the cyclocopter are as follows: (1) understand the effect of forward velocity and phase angle on vehicle dynamics, (2) systematically find the appropriate mixing ratios required to decouple the roll-yaw couplings at various operating forward velocities, and (3) quantify the control inputs required to maintain a trimmed level forward flight (total lift = weight, thrust =

drag).

One of the challenges of accurately simulating forward flight conditions in the wind tunnel was to develop an experimental setup that would enable 5-DOF motions without significantly introducing additional damping into the system. The vehicle was mounted on a spherical gimbal at CG, which allowed free rotation in pitch, roll, and yaw (Fig. 4.8(a)). The entire setup was then augmented with a horizontal and a vertical slider to enable forward translation and heave (Fig. 4.8(b)). Only the lateral translation was restricted due to the physical constraints set by the wind tunnel.

4.6.1 Methodology

The open-jet wind tunnel consists of a square test section dimensions of 0.56 meters (22 inches) in length and width. The vehicle was restricted to maximum horizontal translation from reference trim location (center of slider) of ± 0.178 meters (7 inches) and a positive heave of 0.051 meters (2 inches). Rotations about pitch, roll, and yaw were mechanically restricted to $\pm 45°$.

The variables in this experimental study were airspeed (V_∞), phase angle (Φ), and rotational speed (Ω). A systematic velocity sweep from 2 to 5 m/s was conducted at intervals of 1 m/s. At each velocity, the phase angles were varied from 0° to 50° in increments of 5°. The rotational speed was varied such that the cyclocopter always maintained a positive displacement on the vertical slider. This represents the trim condition where lift is equivalent to total vehicle weight. Throttle (collective cyclorotor rpm), pitch (propeller rpm), roll (differential cyclorotor rpm), yaw

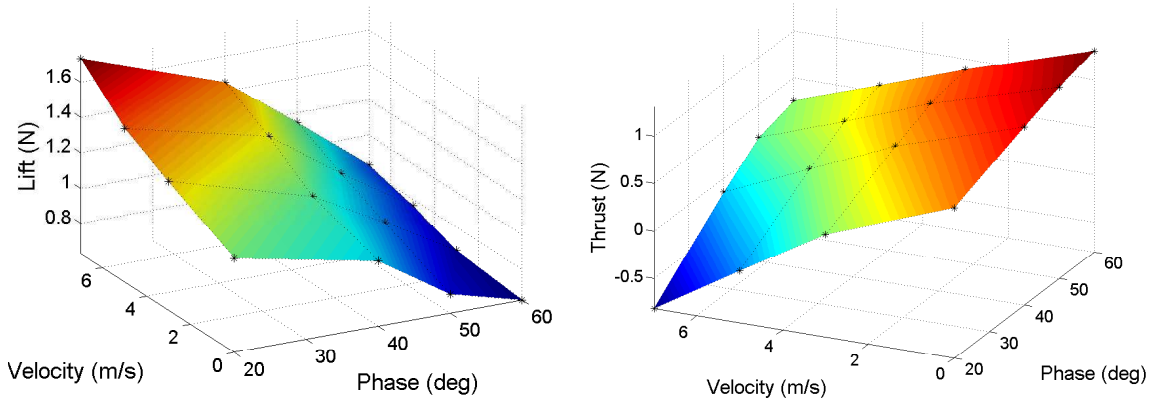

(a) Variation of lift.

(b) Variation of thrust.

Figure 4.9: **Variation of forces with velocity and phasing at 1400 RPM.**

(differential phasing), and forward velocity (collective phasing) inputs were given so that the vehicle maintained its reference trim position on the horizontal slider without pitch, roll, or yaw moments.

4.6.2 Effect of Free-Stream Velocity

An extensive wind tunnel testing was previously conducted on an isolated cyclorotor in which the effects of airspeed, phase angle, and advance ratios on lift and thrust were measured [37]. The results of the study at the constant operational speed of 1400 rpm are plotted showing the variation of lift and thrust against airspeed and phase angle (Fig. 4.9(a), 4.9(b)). Lift produced by the cyclorotor increases with free-stream velocity and decreases with phase angle while thrust inversely decreases with velocity and increases with phase angle.

A significant finding from the current experiment is that for a constant phasing, varying the free-stream velocity did not affect the magnitude of roll-yaw cross-coupling. In addition, the cyclocopter was able to maintain pitch trim within 3° for

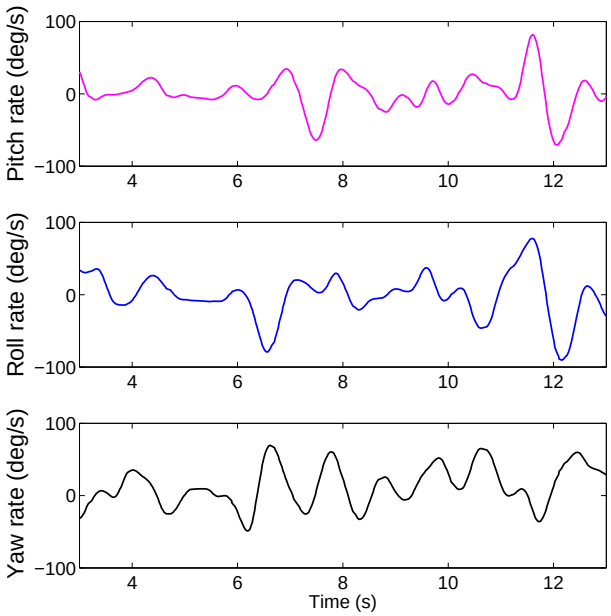

Figure 4.10: Oscillations in pitch, roll, and yaw dynamics caused by cross-coupling.

a step change in forward velocity up to 5 m/s with a PD-based feedback control system. While free-stream velocity affects the lift produced by the cyclocopter, the feedback control system is able to stabilize imbalance in the longitudinal dynamics.

4.6.3 Effect of Phasing

To understand the effect of phasing on the roll-yaw coupling, the rotational speed and airspeed are kept constant as phasing increases. In one case, the cyclorotor rotational speed is kept at a constant 1200 rpm and the airspeed is maintained at 2 m/s. Starting from Φ=0°, the phasing is incrementally increased by Φ=5°. As the phasing approaches Φ=15°, there is an observable oscillation in all three degrees of freedom (Fig. 4.6.2). Throughout the process, the feedback control system is attempting to stabilize the vehicle attitude.

Increasing the phasing, which tilts the thrust vector, results in a noticeable increase in roll-yaw coupling when at a constant forward velocity. The coupling is due to the increase in magnitude of the propulsive forces at high phase angles. Therefore, thrust vectoring has a larger impact on the roll moments and subsequently, changes in cyclorotor rotational speed have a greater influence on yaw moments. Since the roll-yaw coupling is only dependent on phase, mixing ratios for roll and yaw inputs vary only with phase angle and not forward velocity.

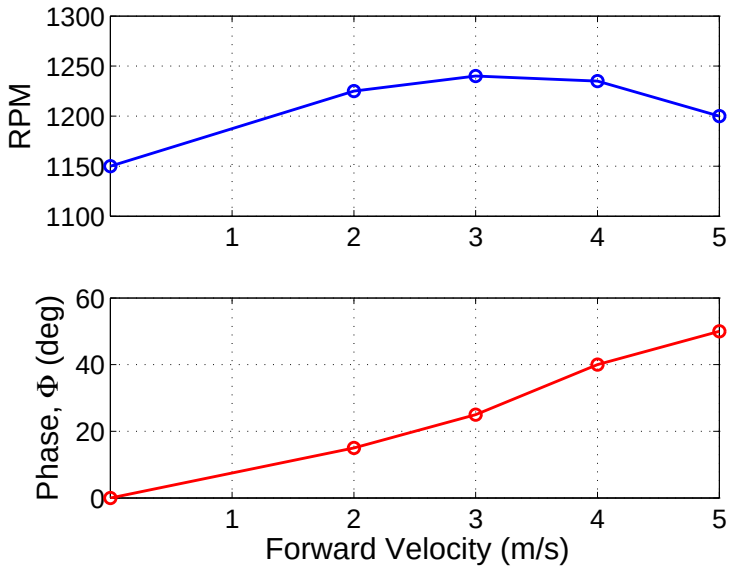

Figure 4.11: **Control inputs required to obtain trimmed free flight (lift = weight, thrust = drag).**

4.6.4 Control Inputs for Trimmed Forward Flight

A sweep of forward velocities and phasing was conducted to find the appropriate control inputs needed to achieve steady level flight (thrust = drag, lift = weight) at each velocities. At a constant forward velocity and phasing, increasing the rotational speed results in an increase of both lift and thrust and consequently, an increase

in power. Increasing phasing of the cyclorotors, while keeping both the forward velocity and rpm constant, results in an increase in thrust and a decrease in lift. Therefore, to increase steady level flight speed from a trimmed condition, both the phasing and rpm are simultaneously adjusted.

As mentioned earlier, a phase input produces a differential change in phasing of both cyclorotor thrust vectors while a throttle input uniformly adjusts the rotational speeds. Figure 4.11 shows the phasing and throttle inputs required to maintain vehicle trim (lift = weight, thrust = drag) at different freestream velocities. As the forward velocity increases, the required phasing increases almost linearly. The required rotational speed of the cyclorotor also increases until 3 m/s and then decreases at higher airspeed. Further experiments will be conducted in the future to measure vehicle performance past 5 m/s. Overall, the insights gained from the wind tunnel experiments show that the forward flight control strategy and feedback control system is suitable for free flight testing.

4.7 Roll-Yaw Decoupling Strategy

Decoupling the roll and yaw degrees of freedom in forward flight involves mixing the roll and yaw inputs of both the pilot and the feedback system. The finalized forward flight control strategy is depicted in (Fig. 4.12). A positive roll (right) input results in an increase in rpm of the left rotor and a decrease in the right rotor. At higher phases, this also leads to positive yaw (clockwise). If the positive roll input is accompanied by a negative yaw (counterclockwise), it would negate the effects of

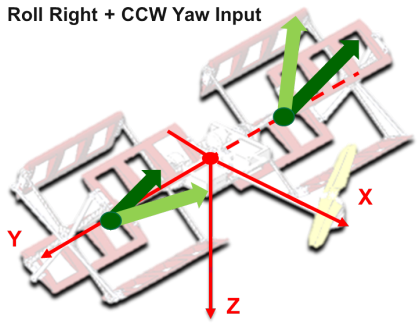

(a) Mixed roll right and counterclockwise yaw input.

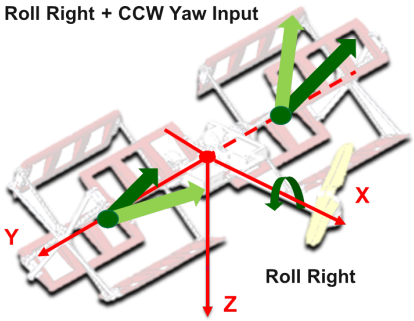

(b) Pure roll right response.

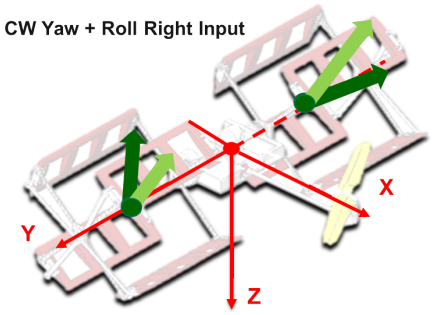

(c) Mixed clockwise yaw and roll right input.

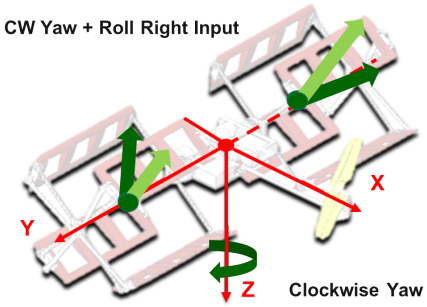

(d) Pure clockwise yaw response.

Figure 4.12: **Controls mixing for forward flight.**

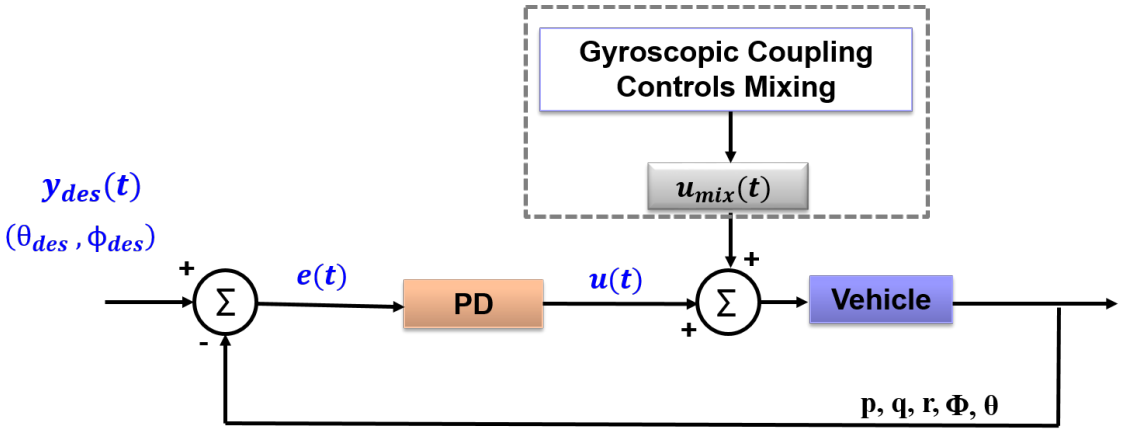

Figure 4.13: **Closed-loop feedback system with feedforward mixing of control inputs.**

the rpm on yaw and result in a pure roll output. Likewise, a positive yaw input would be paired with a negative roll input to accomplish a pure yaw output.

Both the gyroscopic and control couplings induced the same positive roll response for a positive yaw input. However, for a positive roll input, gyroscopic coupling induced a negative yaw (counterclockwise) response while the control coupling led to a positive yaw (clockwise) response. Therefore, decoupling strategy uses eight different mixing gains (a, b). The mixing scheme for gyroscopic coupling is:

$$\delta_{\phi_a} = [a_{\phi_{lat}}\delta_{lat} + a_{\phi_{ped}}\delta_{ped}] \tag{4.12}$$

$$\delta_{\psi_a} = [a_{\psi_{lat}}\delta_{lat} + a_{\psi_{ped}}\delta_{ped}] \tag{4.13}$$

The mixing ratios $a_{\phi_{lat}}$, $a_{\phi_{ped}}$, $a_{\psi_{lat}}$ and $a_{\psi_{ped}}$ were determined using a gimbal stand at the operational rpm. For a given roll or yaw input, the ratios were incrementally increased until the vehicle showed a decoupled response. The mixing scheme for controls coupling is as follows:

$$\delta_{\phi_b} = [b_{\phi_{lat}}\delta_{lat} + b_{\phi_{ped}}\delta_{ped}]sin\Phi \tag{4.14}$$

$$\delta_{\psi_b} = [b_{\psi_{lat}}\delta_{lat} + b_{\psi_{ped}}\delta_{ped}]sin\Phi \tag{4.15}$$

The mixing ratios $b_{\phi_{lat}}$, $b_{\phi_{ped}}$, $b_{\psi_{lat}}$ and $b_{\psi_{ped}}$ were identified in the wind tunnel. The mixing ratios were iterated until the vehicle dynamics were decoupled at each phasing input. The mixed inputs are combined with the output of the PD controller and sent to the vehicle (Fig. 4.13).

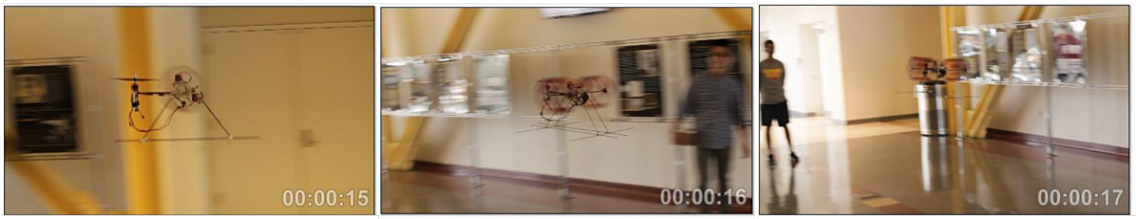

Figure 4.14: **First successful forward flight of a twin-cyclocopter (V = 3 m/s).**

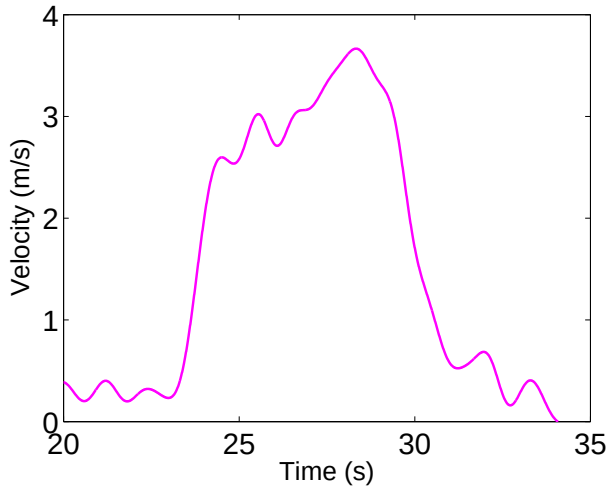

Figure 4.15: **Airspeed data taken shows forward velocity of 3.5 m/s.**

4.7.1 Controller Design

4.8 Forward Flight Test Results

During the flight tests, the proportional and derivative gains were tuned using the Ziegler-Nichols approach. The gains that offered acceptable stiffness and damping to reject external disturbance with minimal oscillations were selected. Gains and control inputs for trimmed flight varied slightly from the ones obtained through wind tunnel testing because the cyclocopter was previously constrained in a gimbal

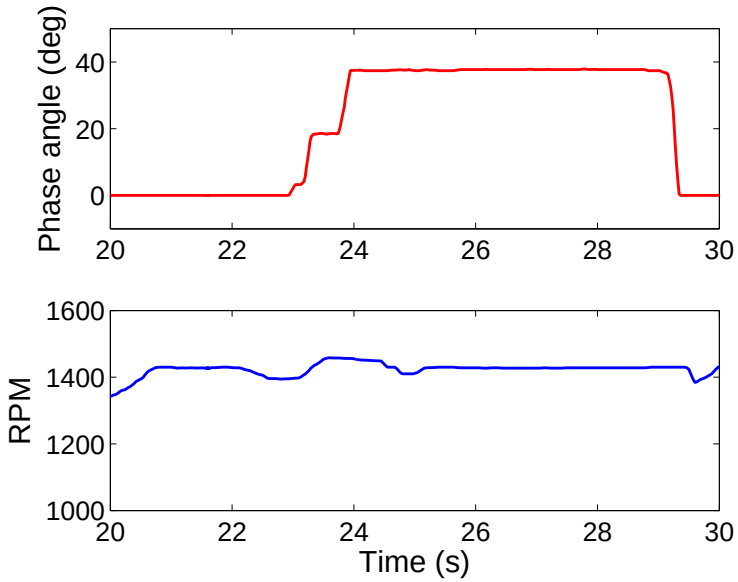

Figure 4.16: **Phase angle ($\Phi = 35°$) and rotational speed (1400 RPM) during forward flight at 3.5 m/s.**

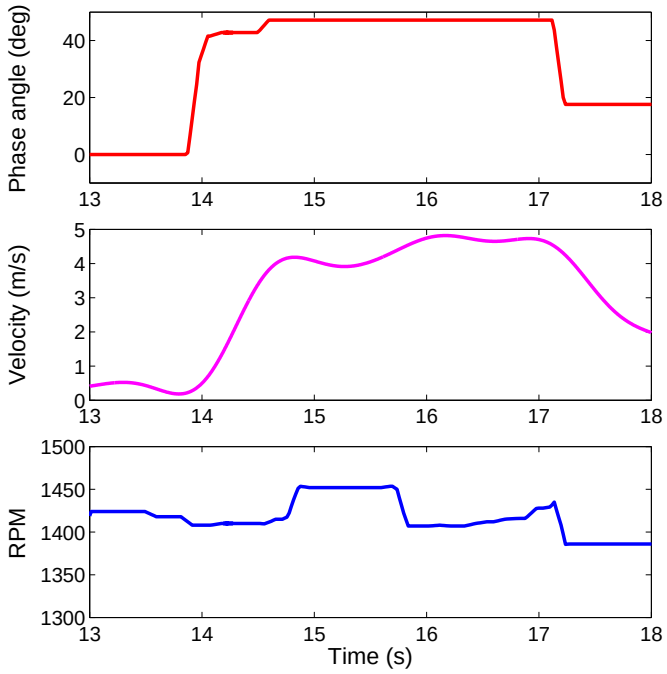

Figure 4.17: **Control inputs at 5 m/s.**

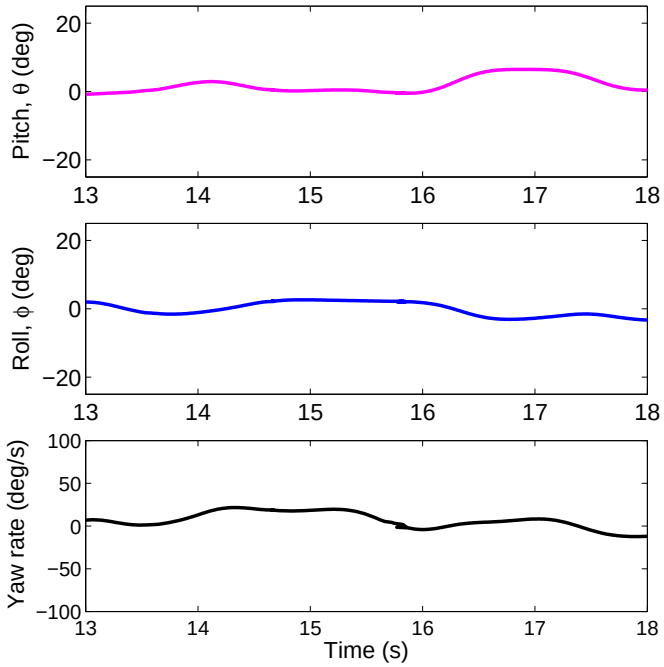

Figure 4.18: **Attitude data at 5 m/s.**

setup that provided additional damping in pitch, roll, and yaw. Additional variation was caused by shifts in the moments of inertia because the cyclocopter is equipped with a single 3S 11.1 volt 850 mAh Lithium-Polymer battery weighing 75 grams.

Flight tests were systematically conducted by first providing a pure throttle command and observing the vehicle response. Any forward translation was counteracted by either reducing the phasing of the cyclic blade pitch or varying the propeller rpm. After trimming the cyclocopter, level forward flight is then initiated solely through thrust vectoring of the cyclorotors.

The present vehicle successfully demonstrated steady level forward flight up to a maximum of 5 m/s forward velocity. Figure 4.14 shows level flight achieved at 3 m/s. As seen from figures 4.17 and 4.18, a satisfactory level forward flight was

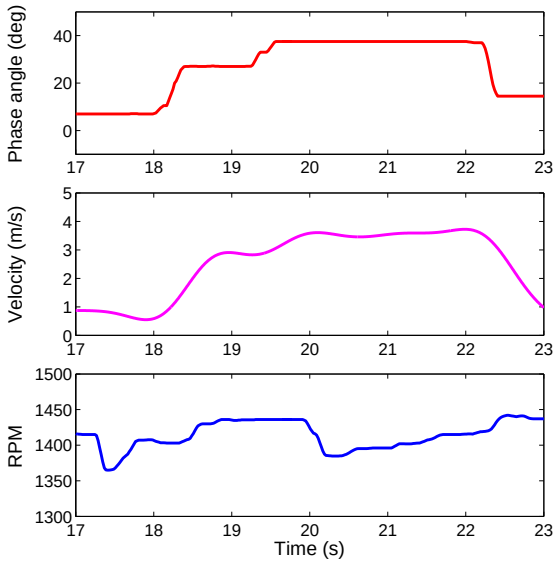

(a) **Control inputs and velocity.**

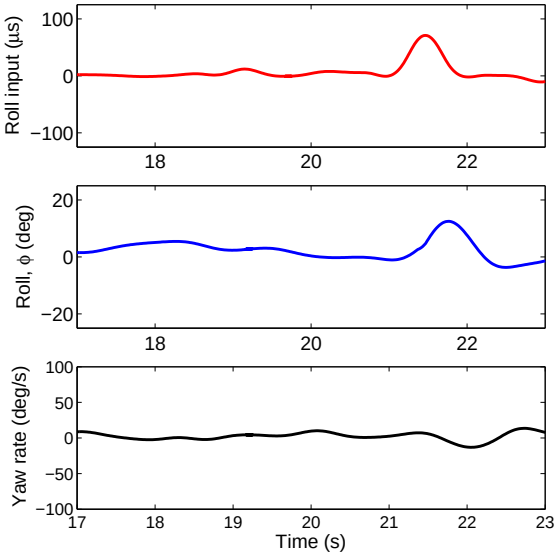

(b) **Decoupled roll right response for a roll input.**

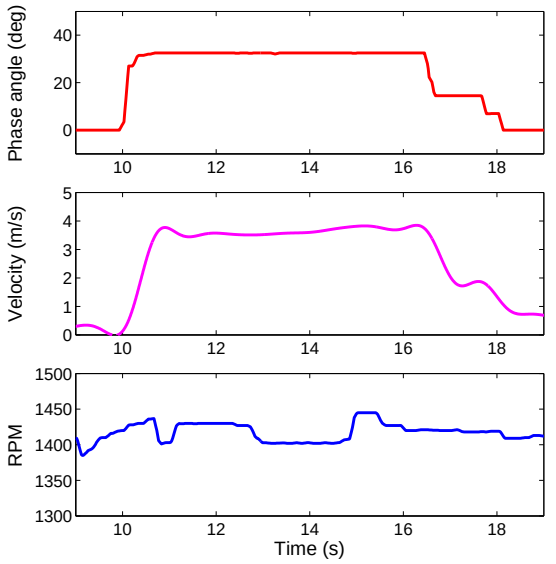

(c) **Control inputs and velocity.**

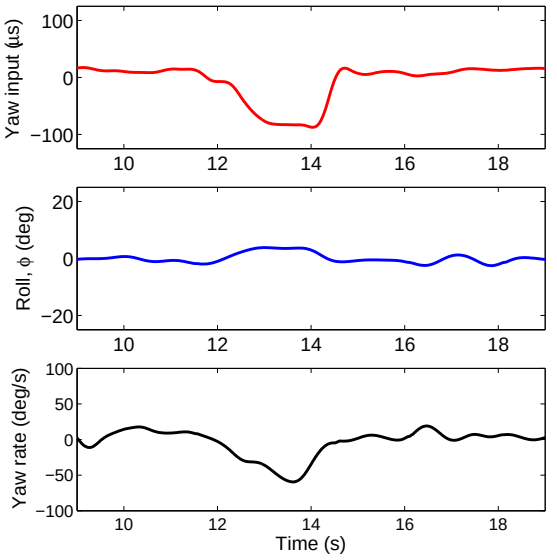

(d) **Decoupled counterclockwise yaw response for a yaw input.**

Figure 4.19: **Attitude data at 3.5 m/s.**

obtained with the pitch and roll angles held close to zero and minimum offsets in yaw rate.

Fig. 4.19 show flight test data at 3.5 m/s and $\Phi = 35°$ with the rotational speed maintained near 1400 rpm. At these control settings, roll and yaw inputs were given to demonstrate decoupled roll-yaw moments. Fig. 4.19(b) shows the vehicle response for a positive roll input (roll right) plotted against the attitude rates and roll attitude angle. The roll step input is given at time = 21 seconds. An immediate perturbation in the roll rate is observed without significant changes in the yaw rate. Interestingly, the feedback overshoots when trying to stabilize the roll moment, but quickly manages to recover the trim state. In order to get desirable performance with minimal overshoot, controller gains were fine-tuned in hover since it was found to be challenging to tune the gains in forward flight without potentially crashing the vehicle.

The mixing ratios found in the wind tunnel were again applied and tuned during free flight tests. There was a notable difference in the ratios, which can be attributed to the additional damping provided by the test stand and changes in vehicle inertia when mounting batteries. While the ratios found in the wind tunnel were similar for both roll-yaw and yaw-roll couplings, the ratios for yaw-roll coupling was much greater in flight. At higher phase angles, the yaw-roll mixing ratio was observed to be 35% higher since the vehicle is much more susceptible to yaw-roll coupling. This is due to the fact that both the gyroscopic coupling and the controls coupling induce a similar response for a yaw input, which adds the effect of the couplings, and opposite responses in roll.

The 550 gram twin-cyclocopter is currently the first forward flight capable cyclocopter in literature that has successfully used thrust vectoring to gain forward velocity instead of pitching the vehicle forward. Thrust vectoring in forward flight has unique aerodynamic advantages in that it produces both lift and thrust forces with a measured drop in required power [37]. As a result, the maximum forward flight capability can be potentially increased over a system that solely relies on tilting the vehicle to achieve translational motion.

4.9 Summary

In this chapter, the flight control strategy that enabled the cyclocopter to expand it's flight envelope to steady level attitude in power-efficient forward flight was discussed. The control strategy used a combination of independent pitch phasing and rotational speed control of the two cyclorotors, along with the propeller system, without relying on any additional control by means of a traditional empennage system. While the strategy facilitated power-efficient level forward flight, it was accompanied by a strong yaw-roll control cross-coupling. These were in addition to the gyroscopic couplings that are experienced even in hover. Existence of controls coupling in forward flight was attributed to increased magnitude of propulsive forces at high phase angles. As a result, thrust vectoring had a larger impact on roll moments and subsequently, changes in cyclorotor rotational speeds had a greater influence on yaw moments.

Decoupling the roll and yaw degrees of freedom in forward flight involved

mixing the roll and yaw inputs of both the pilot and the feedback system. Wind tunnel studies showed that the mixing ratio was dependent on phasing of the blade cyclic pitch, especially at high phase angles. If a positive roll input was accompanied by a negative yaw (counterclockwise), it would negate the effects of the rpm on yaw and result in a pure roll output. Likewise, a positive yaw input paired with a positive roll input resulted in a pure yaw output. Both the gyroscopic and control couplings induced the same positive roll response for a positive yaw input. However, for a positive roll input, gyroscopic coupling induced a negative yaw (counterclockwise) response while the control coupling led to a positive yaw (clockwise) response.

Overall, the capability to control forward flight speed using only thrust vectoring (phasing of the cyclic pitch) was successfully demonstrated up to 5 m/s. The rate of transition from hover to forward flight entirely depended on the magnitude of phasing input. Flight tests demonstrated that the cyclocopter was able to immediately halt to hover from 5 m/s flight. In addition, the cyclocopter achieved the desired airspeed within a second after a given phasing input.

Chapter 5: System Identification in Forward Flight

5.1 Overview

The previous chapter discussed the flight control strategy that enabled the cyclocopter to maintain a level attitude in forward flight. Even though such a strategy could facilitate power-efficient forward flight, it is accompanied by a strong yaw-roll cross coupling, which is in addition to the inherent gyroscopic coupling that is present in hover. To understand these couplings and characterize the bare-airframe dynamics, a 6-DOF flight dynamics model of the cyclocopter was extracted using time-domain system identification technique. The existence of the longitudinal control derivative in translation mode was used to evaluate the control authority of thrust vectoring to command forward speed. The model was also used to identify sources of roll-yaw coupling and develop decoupling methods to achieve stable flight.

5.2 Methodology

System identification is performed using the NASA Langley's System Identification Programs for Aircraft (SIDPAC) [81]. SIDPAC is a software package containing MATLAB scripts and functions of system identification tools. It is capable of per-

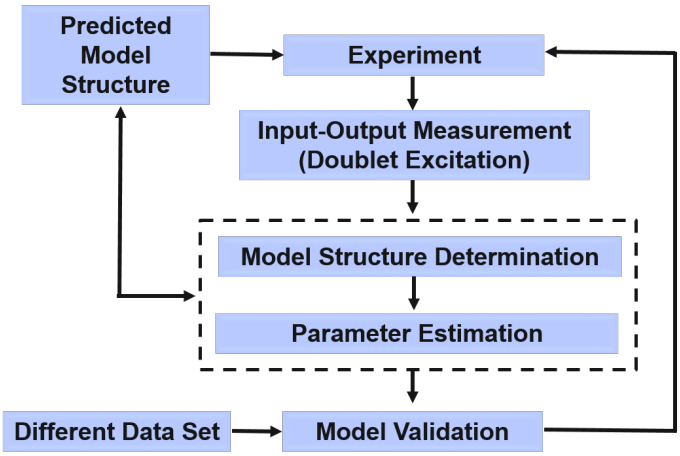

Figure 5.1: **System Identification using time-domain approach.**

forming both frequency-domain and time-domain analysis of flight data. In addition, it contains additional tools for real-time parameter estimation, model structure determination, input design, and data analysis. The first step in system identification is applying engineering simplifications and prior knowledge of the dynamic system to predict the model structure (Fig. 5.1).

5.2.1 Model Structure

As discussed in the previous chapter, a state-space model is considered in the general form:

$$\dot{x} = Ax + Bu \tag{5.1}$$

Matrix A is composed of the stability derivatives that describe the homogeneous system dynamics and matrix B contains the control derivatives. System Identification techniques provide an estimation of these stability and control derivatives. The state vector is denoted by x = [u v w p q r ϕ θ] while the input vector is denoted

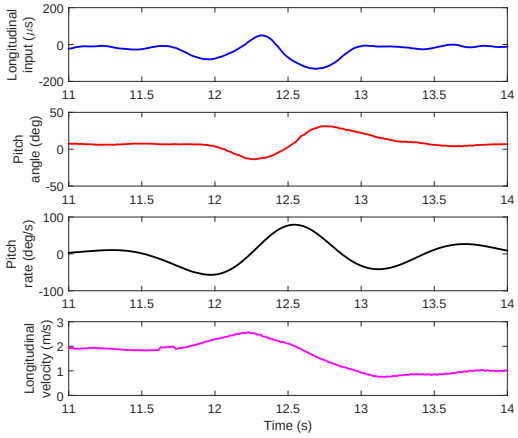

(a) Longitudinal doublet input

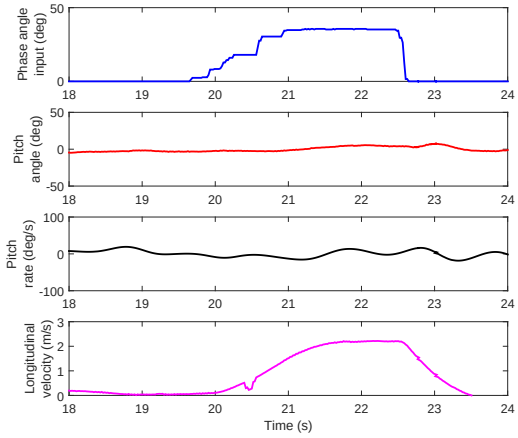

(b) Phasing input

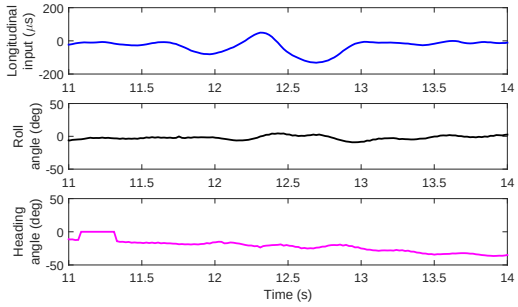

(c) Decoupled longitudinal mode

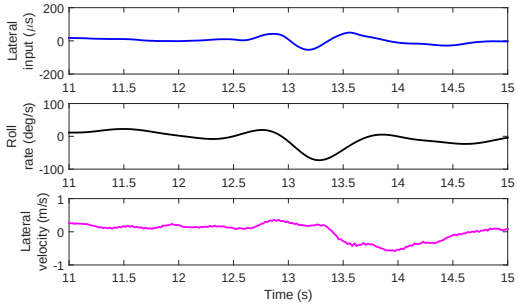

(d) Effect of δ_{lat} on lateral velocity

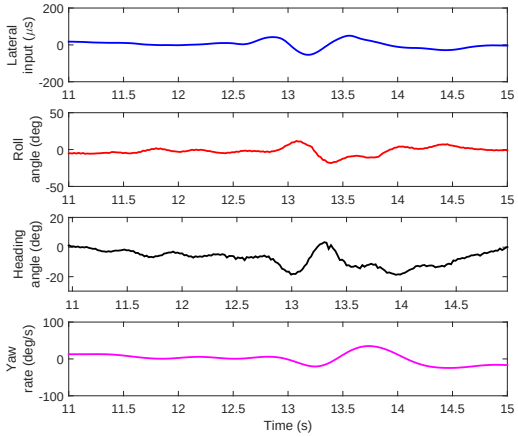

(e) Coupled response for lateral doublet input

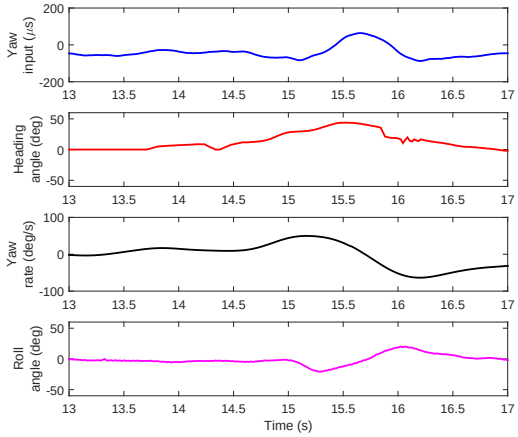

(f) Coupled response for yaw doublet input

Figure 5.2: **Time history data for pilot excitation and vehicle response.**

by u = $[\delta_{lat}\ \delta_{lon}\ \delta_{throttle}\ \delta_{ped}\ \delta_{phase}]$. States include velocities (u, v, w), angular rates (p, q, r), and Euler attitude angles $(\phi,\ \theta)$. δ_{lat} refers to the differential rpm of the

Table 5.1: Comparison between frequency-domain and time-domain methods [84].

Frequency-domain methods	**Time-domain methods**
Frequency responses (derived from time-history data)	Time-history data
Frequency sweep with long flight test records	Multistep (eg. doublets, 3-2-1-1) with shorter record lengths
Bias effects of noise eliminated from analysis	Requires noise model (e.g equation error or output error)
Direct identification of time delays	Not identified directly
No biases needed to be identified	Must be identified and can be correlated with aerodynamics parameters

two cyclorotors, δ_{lon} is the rpm control of the propeller, $\delta_{throttle}$ collectively varies rpm of all three rotors, δ_{ped} is differential thrust vectoring, and δ_{phase} is the phasing of the cyclic pitch. These inputs are in microseconds and represent the duty cycle of the PWM signal transmitted to the actuators. PWM signals range from 1000–2000 μsec. Pilot inputs are combined with initial PWM values associated with trim condition such that δ_{lat}, δ_{lon}, and $\delta_{ped} \in [-300, 300]\mu$sec, $\delta_{throttle} \in [0, 1500]\mu$sec, and $\delta_{phase} \in [0, 60]\mu$sec. For comparison with other existing flight dynamics model of MAV platforms, inputs have been scaled to $u \in [-1, 1]$. As a result, the control derivatives can be compared across vehicle platforms [82, 83].

The most significant simplification made for the model is that the cyclorotors are governed by rigid-body dynamics. In addition, the longitudinal and heave modes are independent and decoupled from the rest of the vehicle dynamics. Due to restrictions in the test volume, system identification was not performed to determine heave dynamics in forward flight.

5.2.2 Time-Domain Approach

Table 5.1 compares frequency-domain and time-domain approaches in system identification. The time-domain approach was used because of restrictions in maneuver time and limitations in performing frequency sweeps. The frequency-domain approach using spectral estimation generally requires a large amount of flight data with pilot input excitation across multiple frequency ranges. In addition, since the time-domain approach uses time-history data, the results can be directly interpreted and applied to the physical system. While the advantages of using frequency-domain methods include elimination of noise, direct identification of time delays, and applicability to unstable systems, performing Fourier transforms to acquire the initial frequency response data may introduce errors and reduce accuracy of modeling results.

Within the time-domain, there are two main parameter estimation techniques: (1) Equation-error method and (2) Output-error method. The equation-error minimizes the sum of squared differences between the measured and modeled state time derivatives while output-error minimizes the sum of weighted squared differences between measured and modeled outputs [81]. One disadvantage of the output-error method is that it involves integrating differential equations for each iteration and may lead to divergence in parameter estimation for unstable systems. The Equation-error method is used in this research because it does not require integration of the state equations and will converge to some parameter estimation. Before using the equation-error method, an initial model structure was identified using Stepwise re-

gression. Both methods are summarized in the following sections.

5.2.3 Stepwise Regression

System identification techniques used in this research results in a reduced linear regression model where one or more regressors are removed from the model [81]. The output of the linear system (y) can be represented by columns of regressors (X) that are a function of the state vectors (x) and input vectors (u), and the parameter vectors (θ) that are calculated through system identification:

$$y = \dot{x} = X(x, u)\theta \tag{5.2}$$

Measurement of the linear system is represented by the measured output (z) and random noise (v):

$$z = y + v \tag{5.3}$$

$$z = X\theta + v \tag{5.4}$$

The relevance of each candidate regressor for the reduced linear regression model is evaluated by either adding or deleting regressors one at a time. The technique of adding regressors, while starting without any in the model, is called forward selection. The technique of deleting regressors, while starting with the entire pool of candidate regressors, is called backward elimination. Stepwise regression is a computation technique that combines both forward selection and backward

elimination so that all regressors in the model are continuously re-evaluated. As a result, regressors that become redundant can be removed from the model.

The method starts by constructing a pool of candidate regressors. Adjusting for the mean value or bias (X_0), the first regressor selected is the one with the highest simple correlation with the dependent variable (z). The correlation coefficient (r_{jz}) for each regressor (ξ) is calculated using the following equation for j = 1,2,...n and N number of data points:

$$r_{jz} = \frac{\sum_{i=1}^{N}[\xi_j(i) - \bar{\xi_j}][z(i) - \bar{z}]}{\sqrt{S_{jj}S_{zz}}} \tag{5.5}$$

where S_{jj} is the centered sum of squares for the regressor (ξ_j) and S_{zz} is the centered sum of squares for the measured response (z):

$$S_{jj} = \sum_{i=1}^{N}[\xi_j(i) - \bar{\xi_j}]^2 \tag{5.6}$$

$$S_{zz} = \sum_{i=1}^{N}[z(i) - \bar{z}]^2 \tag{5.7}$$

After selecting the first regressor (ξ_1), the regressor is removed from the pool of candidate regressors and the model is used to fit the measured response through ordinary least-squares parameter estimation. The metric that quantifies the closeness of estimated model values ($\hat{y}$) to measured values (z) is called the coefficient of determination, R^2:

$$R^2 = \frac{SS_R}{SS_T} \tag{5.8}$$

where $0 \leq R^2 \leq 1$, SS_R is the regression sum of squares, and SS_T is the total sum of squares:

$$SS_R = \sum_{i=1}^{N} [y\hat{(}i) - \bar{z}]^2 \tag{5.9}$$

$$SS_T = z^T z - N\bar{z}^2 \tag{5.10}$$

Based on the equation, each new model term increases the R^2 value. If the value of R^2 changes by less than 0.05, then the regressor is deemed statistically insignificant and is omitted from the model. Additional regressors are added to the model if they satisfy the partial F statistic criterion for each estimated parameter vector ($\hat{\theta}$) for j = 1,2,...n:

$$F_p = \frac{\hat{\theta}^2}{Var(\theta_j)} \tag{5.11}$$

The F_p values indicate the significance of an individual parameter to the overall model. For a 95% confidence interval, regressors with $F_p < 20$ are removed from the model.

5.2.4 Equation-Error Method

After selecting the column of regressors (X), the model is refined using the equation-error method, which calculates the potential correlation of each regressor based on a linear least-squares formulation. The parameters (θ) are estimated by minimizing the sum of squared differences between the model and measurements in the following cost function:

$$J(\theta) = \frac{1}{2}(z - X\theta)^T(z - X\theta) \tag{5.12}$$

The best parameter estimate ($\hat{\theta}$) is one that minimizes the cost function and satisfies the following:

$$\hat{\theta} = (X^T X)^{-1} X^T z \tag{5.13}$$

The estimated linear model output ($\hat{y}$) is then calculated by:

$$\hat{y} = X\hat{\theta} = X(X^T X)^{-1} X^T z \tag{5.14}$$

The difference between the estimated value ($\hat{y}$) and measured value (z) is called the residual (v):

$$v = z - \hat{y} = z - X\hat{\theta} \tag{5.15}$$

Residuals are orthogonal to the column of regressors (X). If the columns are linearly dependent, the matrix inverse $(X^T X)^{-1}$ and the least-squares solution will not exist. Therefore, the model structure and the experiment should be carefully executed.

5.3 Experimental Setup

Characterizing the flight dynamics model using system identification techniques requires a series of pilot input excitation experiments and corresponding vehicle measurements. During the experiment, multiple lateral, longitudinal, and yaw doublet inputs were provided in separate flights. The amplitude of the doublets were selected such that the vehicle response has an acceptable signal-to-noise ratio without

causing a critical crash-inducing response. Over 60 flight tests were conducted in a 525m^3 test volume. Maneuvers were only initiated after the vehicle achieved a steady state of 2 m/s forward speed and a level attitude (zero pitch Euler angle).

Capturing pilot inputs and vehicle responses within the limited test volume was challenging as the inputs were provided only after achieving a steady cruise. Inputs were also limited to doublets instead of a frequency sweep because of: (1) limited flight testing time in the test space, (2) difficulty for the cyclocopter to maintain steady flight conditions at low frequency inputs, and (3) poor signal-to-noise ratio at lower frequencies. The following sections will provide a description of the experimental methodology and sensor instrumentation.

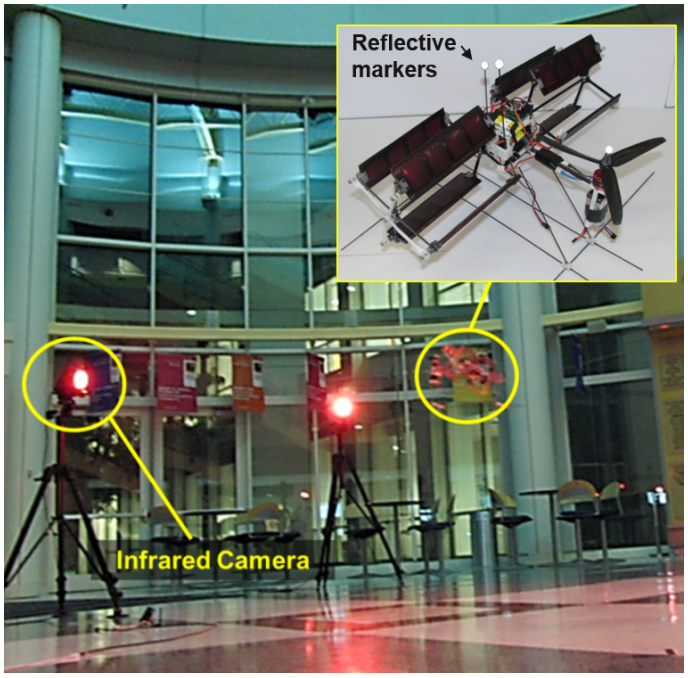

Figure 5.3: **Vicon motion capture testing setup.**

5.3.1 Data Acquisition Setup

The first step towards identifying the flight dynamics model is to systematically collect flight data. Both onboard instrumentation and external sensors are simultaneously used to collect position, velocity, and attitude data. The Vicon^{TM} Motion Capture System consists of eight high speed infrared cameras that track the retro-reflective markers placed on the vehicle (Fig. 5.3). The motion capture system triangulates the location of the markers inertially within the three-dimensional test volume. These infrared cameras capture the translational and rotational states of the vehicle at a frequency of 100 Hz.

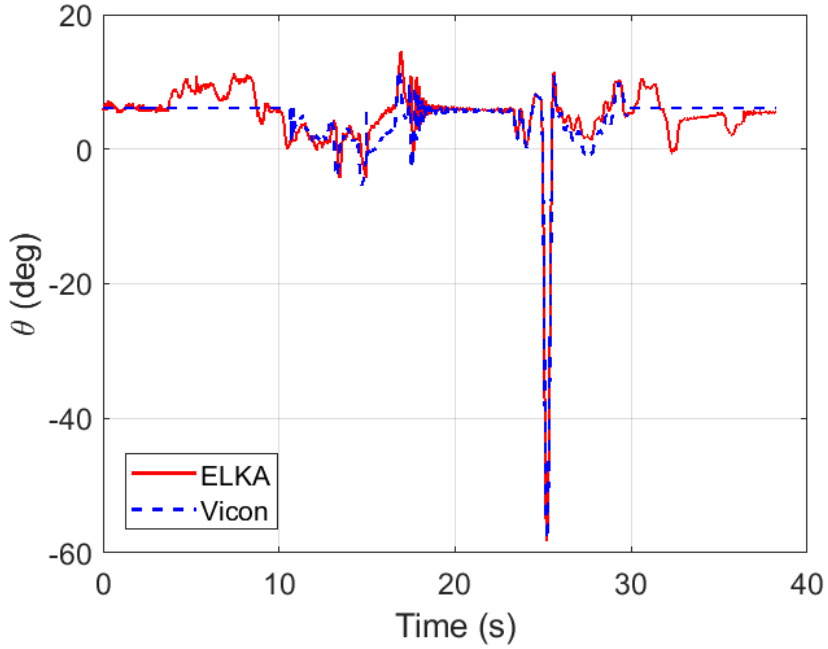

Figure 5.4: **Synchronization between ELKA and Vicon measurements using a fiducial perturbation in pitch.**

As discussed in chapter 2, the onboard instrumentation consists of ELKA, an in-house developed micro embedded processor-sensor board weighing 1.3 grams [78].

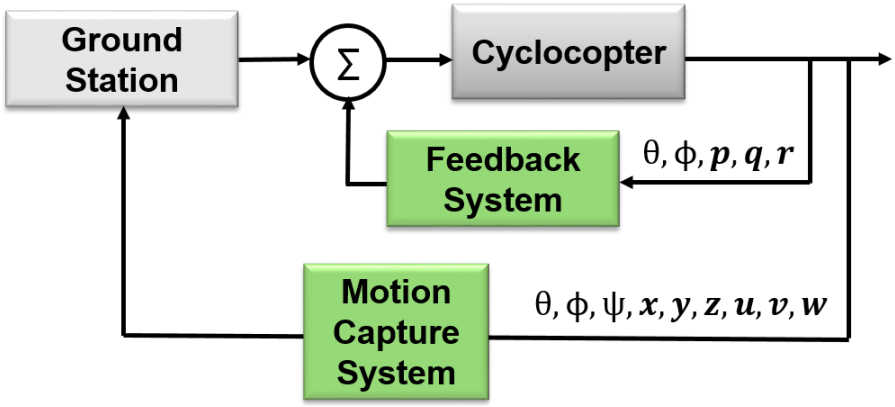

Figure 5.5: **Data flowchart between ELKA and Vicon.**

ELKA houses a STM-32 microprocessor with a 32-bit ARM Cortex M3 core for high-end onboard computation tasks and performs all the data processing, vehicle stabilization, and roll-yaw decoupling computations. The MPU-9150 IMU integrated on the board includes tri-axial gyroscopes, accelerometers, and magnetometers. Wireless communications are serviced by an onboard nRF24L01 chip, a low-power 2.4 GHz RF transceiver. ELKA has a sensor update rate of 500 Hz and is capable of streaming vehicle attitude data and actuator controls data to the base station with a latency upper bound of 30 ms. Pitch (q), roll (p), and yaw (r) attitude rates are provided by tri-axial gyroscopes and combined with accelerometer data through a gradient descent method to produce precise attitude measurements [54].

Measurements from ELKA are streamed to the ground station through a wireless IEEE 802.15.4 data link while measurements from Vicon are streamed through a network TCP/IP port. At the end of each experiment, a fiducial pitch perturbation was manually provided to the vehicle on the ground in order to synchronize the Vicon and ELKA data streams (Fig. 5.4). Both data sets were then allocated

a common time stamp after post-processing. System identification measurements include translational states (x, y, z) from Vicon and rotational states (p, q, r, θ, ϕ) from ELKA (Fig. 5.5).

5.3.2 Sampling Rate

The general rule for selecting the sampling rate is [81]:

$$f_s = 25 f_{max} \tag{5.16}$$

where f_{max} is the maximum rigid-body frequency. For the cyclocopter, the rigid-body dynamic modes occur at 4 Hz so the sampling frequency was selected as 100 Hz. As previously mentioned, the ELKA onboard processor measures the vehicle states at 500 Hz compared to 100 Hz from the Vicon motion capture system. As part of post-processing, measured states from ELKA were down-sampled in order to synchronize with Vicon measurements.

5.3.3 Bare-Airframe Dynamics

System identification is typically conducted on an open-loop system to determine the bare-airframe characteristics of a vehicle. However, since the cyclocopter is dynamically unstable, the closed-loop feedback system remained implemented with low control gains during the experiments. Furthermore, any decoupling techniques and mixing ratios were eliminated during the experiment in order to capture true vehicle dynamics in forward flight.

There are two conventional methods of extracting the bare-airframe dynamics

from a closed-loop system: (1) having a priori knowledge of control law to deduce the closed-loop dynamics matrix or (2) directly measuring actuator inputs to the rotors as a result of both pilot and onboard stabilization. Since the actuator inputs were directly available from onboard measurements, the second approach was taken. Data collected from a closed-loop system could potentially introduce correlation between input excitation and output noise [84]. To circumvent this issue and improve signal-to-noise ratio, input excitations were restricted to low amplitudes.

5.3.4 Pilot Excitation

During the experiment, all decoupling methods were removed in order to observe the vehicle's inherent roll-yaw coupled responses. The longitudinal and heave modes were assumed to be independent and decoupled. In addition, the heave mode was assumed to be identical to that in hover conditions. These assumptions were validated from the flight test results (Fig. 5.6).

Flight tests were systematically conducted by first providing a pure throttle command and observing the vehicle response. Any forward translation was counteracted by either reducing the phasing of the cyclic blade pitch or varying the propeller rpm. After trimming the cyclocopter, level forward flight is then initiated solely through thrust vectoring of the cyclorotors.

All maneuver inputs were provided after the cyclocopter achieved a steady state of 2 m/s flight at a steady, level attitude (θ, ϕ, ψ=0). From the time history data, increasing the phasing to $\Phi = 45^\circ$ with a δ_{phase} step input (time = 20 seconds)

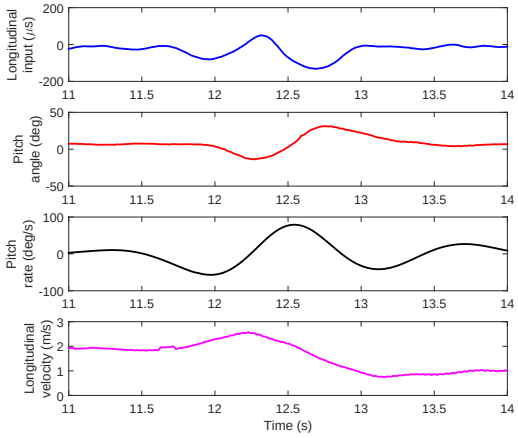

(a) Longitudinal doublet input

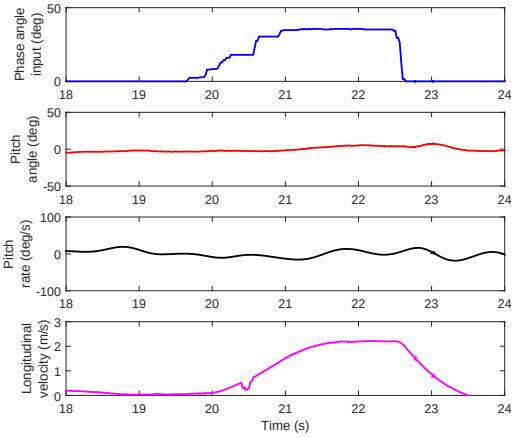

(b) Phasing input

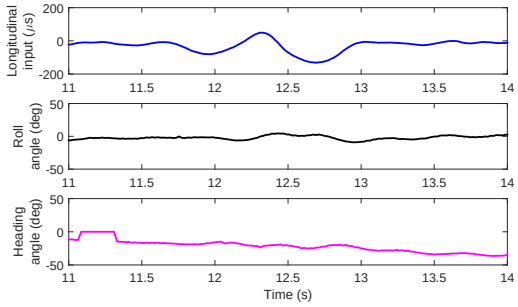

(c) Decoupled longitudinal mode

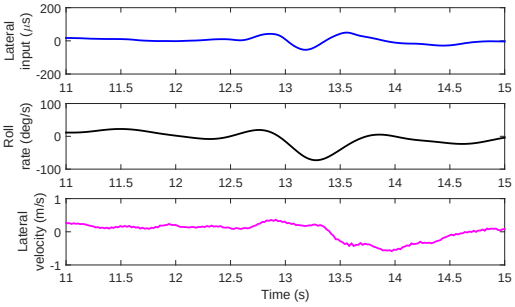

(d) Effect of δ_{lat} on lateral velocity

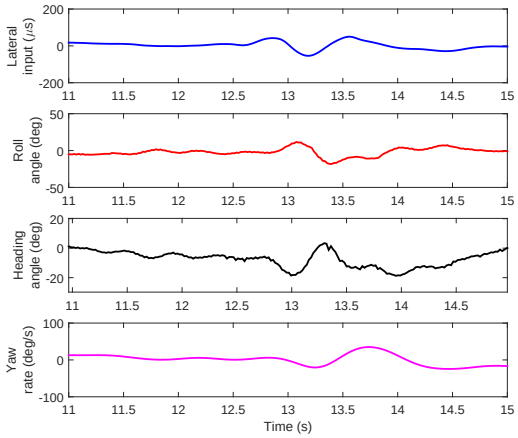

(e) Coupled response for lateral doublet input

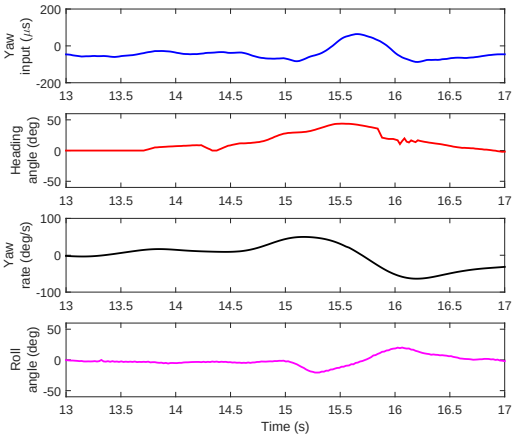

(f) Coupled response for yaw doublet input

Figure 5.6: **Time history data for pilot excitation and vehicle response.**

also causes a step change in velocity (Fig. 5.6(b)). During the acceleration phase, the initial response is large and acceleration begins to decrease with time. When

the phase input is returned, the flight speed returns to the original forward velocity at the same rate.

During the experiment, multiple lateral, longitudinal, and yaw doublet inputs were provided in separate flights. Low amplitude doublets were selected to keep resulting vehicle dynamics within the assumed linear range of operation and to achieve acceptable signal-to-noise ratio without causing a critical crash-inducing response. Higher amplitude responses generally tend to become more nonlinear, which affects the linear coherence between the input and output data.

5.3.5 Vehicle Response

Another observation from flight test results is the existence of a dominating roll-yaw coupling for both lateral and yaw inputs. The coupling also causes a secondary response from the feedback system, which leads to data collinearity. The adverse effects of data collinearity can be suppressed by omitting the secondary regressors from the regressor pool. For example, a positive roll input induces a clockwise yaw response, which leads to a counterclockwise yaw actuator input from the feedback system. Therefore, δ_{yaw} would be present in the regressor pool even though only a roll input was initially actuated. In these experiments, secondary regressors were be manually omitted to improve accuracy of parameter estimation.

Table 5.2: Parameter estimation results.

Parameter	**Value**	**F-ratio**
Longitudinal Mode		
X_u	-0.021	51
X_{phase}	1.55	125
M_u	1.97	31
M_q	0.009	22
M_{lon}	-83.1	96
Lateral and Yaw Modes		
Y_v	-0.036	68
Y_p	-0.001	115
Y_r	0.003	242
L_v	4.29	54
L_p	0.097	53
L_r	0.056	194
L_{lat}	76.4	31
L_{rud}	114	91
N_v	1.14	109
N_p	0.051	32
N_r	0.018	149
N_{lat}	-53.9	34
N_{rud}	19.5	23

$$\begin{pmatrix} \dot{u} \\ \dot{v} \\ \dot{w} \\ \dot{p} \\ \dot{q} \\ \dot{r} \\ \dot{\phi} \\ \dot{\theta} \end{pmatrix} = \begin{bmatrix} X_u & 0 & 0 & 0 & 0 & 0 & 0 & -g \\ 0 & Y_v & 0 & Y_p & 0 & Y_r & g & 0 \\ 0 & 0 & Z_w & 0 & 0 & 0 & 0 & 0 \\ 0 & L_v & 0 & L_p & 0 & L_r & 0 & 0 \\ M_u & 0 & 0 & 0 & M_q & 0 & 0 & 0 \\ 0 & N_v & 0 & N_p & 0 & N_r & 0 & 0 \\ 0 & 0 & 0 & 1 & 0 & 0 & 0 & 0 \\ 0 & 0 & 0 & 0 & 1 & 0 & 0 & 0 \end{bmatrix} \begin{pmatrix} u \\ v \\ w \\ p \\ q \\ r \\ \phi \\ \theta \end{pmatrix} + \begin{bmatrix} 0 & 0 & 0 & 0 & X_{phase} \\ 0 & 0 & 0 & 0 & 0 \\ 0 & 0 & Z_{thr} & 0 & 0 \\ L_{lat} & 0 & 0 & L_{rud} & 0 \\ 0 & M_{lon} & 0 & 0 & 0 \\ N_{lat} & 0 & 0 & N_{rud} & 0 \\ 0 & 0 & 0 & 0 & 0 \\ 0 & 0 & 0 & 0 & 0 \end{bmatrix} \begin{pmatrix} \delta_{lat} \\ \delta_{lon} \\ \delta_{throttle} \\ \delta_{yaw} \\ \delta_{phase} \end{pmatrix}$$

Figure 5.7: **Model structure for cyclocopter in forward flight.**

5.4 Results

The following sections discuss results of the system identification from Vicon experiments, including model structure determination, parameter estimation, and stability analysis.

5.4.1 Model Structure Determination

The linear model structure was first determined using stepwise regression and the corresponding stability and control derivatives were identified in the matrix form provided in Fig. 5.7. From the pool of regressors, the identified model parameters were selected based on the coefficient of determination (R^2) and F-ratio (F_p). The R^2 values exist within [0,1] and increase with the addition of regressors. If the value changes by only 0.05, then the regressor is deemed statistically insignificant and is omitted from the model. All of the identified modes had acceptable R^2 values between 0.65–0.93. The F_p values indicate the significance of an individual parameter to the overall model. For a 95% confidence interval, regressors with $F_p < 20$ were not considered. In addition, the parameters were corrected for colored residuals. Overall, the final model parameter estimates using the equation-error

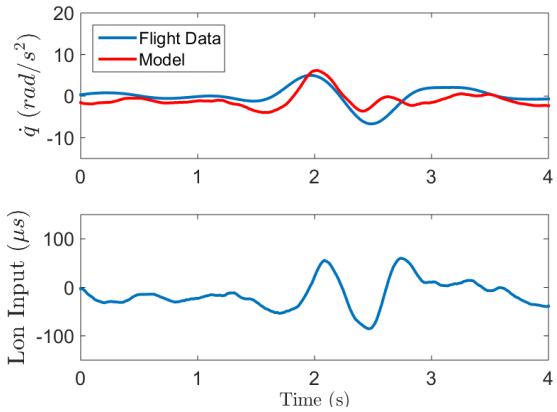

(a) Angular acceleration in pitch

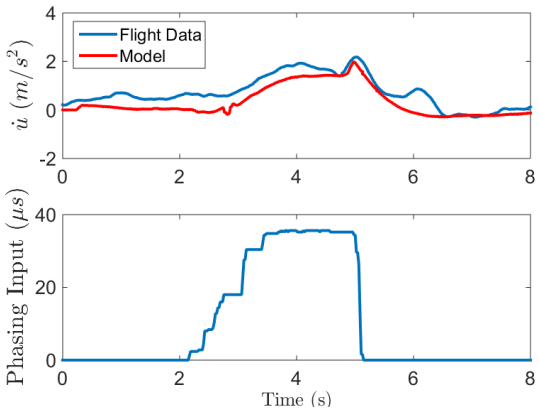

(b) Longitudinal acceleration

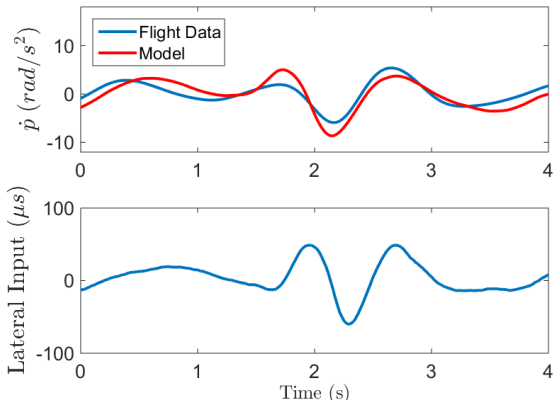

(c) Angular acceleration in roll

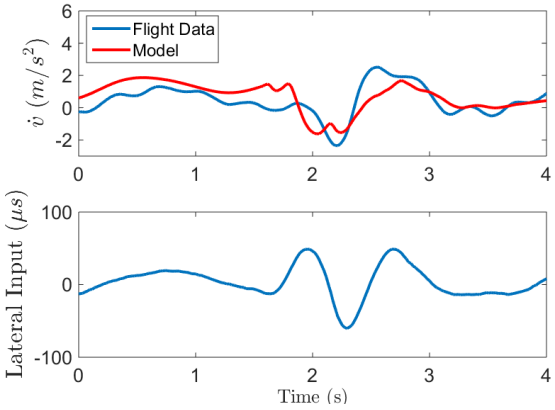

(d) Lateral acceleration

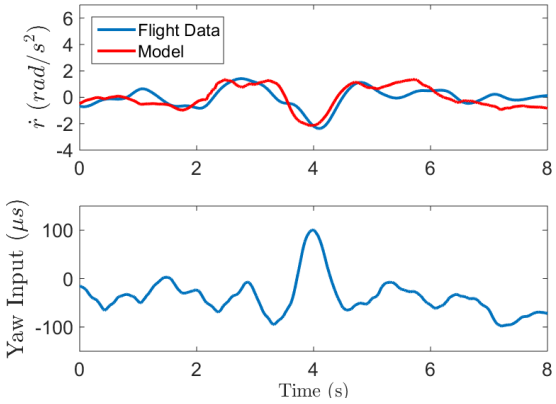

(e) Angular acceleration in yaw

Figure 5.8: **Estimated model output compared to flight data.**

method are provided in Table. 5.2.

Fig. 5.8 shows correlation between model predicted results and a different set

of flight test data. Limitations in model input and total maneuver flight time were from the restricted motion capture testing volume and length of time it took to reach the steady state. Considering these challenges, the estimated model parameters are able to adequately characterize the vehicle dynamics.

5.4.2 Longitudinal Mode

The longitudinal dynamics are identified as:

$$\begin{pmatrix} \dot{u} \\ \dot{q} \\ \dot{\theta} \end{pmatrix} = \begin{bmatrix} X_u & 0 & -g \\ M_u & 0 & 0 \\ 0 & 1 & 0 \end{bmatrix} \begin{pmatrix} u \\ q \\ \theta \end{pmatrix} + \begin{bmatrix} 0 & X_{phase} \\ M_{lon} & 0 \\ 0 & 0 \end{bmatrix} \begin{pmatrix} \delta_{lon} \\ \delta_{phase} \end{pmatrix} \tag{5.17}$$

Compared to the flight dynamics model derived in hover conditions, the only new model parameter in forward flight is the control derivative, X_{phase}. As expected, X_{phase} is positive because phasing input leads to longitudinal translation. The strength of the control derivative confirms that forward speed is highly sensitive to phasing input. Similar response was observed during flight tests. The negative longitudinal translation derivative (X_u) indicates positive aerodynamic damping. Therefore, the vehicle is able to stabilize a velocity perturbation in the longitudinal direction.

The longitudinal coupling term (M_u) is stabilizing. A perturbation increasing the longitudinal velocity will induce a nose-up pitching moment. The positive pitching moment would further decrease the forward velocity, stabilizing the cyclocopter. Likewise, a velocity perturbation from the opposite direction would cause the cyclocopter to pitch-down and increase forward speed. Compared to the other longitudinal stability derivatives, M_q is almost insignificant in magnitude and removed from the model. Therefore, the aerodynamic pitch damping is non-existent and the vehicle requires feedback damping to stabilize the pitch attitude rate.

5.4.3 Coupled Lateral-Yaw Modes

The lateral and yaw dynamics are identified as:

$$\begin{pmatrix} \dot{v} \\ \dot{p} \\ \dot{r} \\ \dot{\phi} \end{pmatrix} = \begin{bmatrix} Y_v & 0 & Y_r & g \\ L_v & L_p & L_r & 0 \\ N_v & N_p & N_r & 0 \\ 0 & 0 & 0 & 1 \end{bmatrix} \begin{pmatrix} v \\ p \\ r \\ \phi \end{pmatrix} + \begin{bmatrix} 0 & 0 \\ L_{lat} & L_{rud} \\ N_{lat} & N_{rud} \\ 0 & 0 \end{bmatrix} \begin{pmatrix} \delta_{lat} \\ \delta_{yaw} \end{pmatrix} \tag{5.18}$$

Similar to the longitudinal translation derivative, the lateral translation derivative (Y_v) is stabilizing. However, the lateral and yaw coupling terms, L_v and N_v are

destabilizing. In forward flight, a velocity perturbation would induce both roll and yaw responses. In particular, perturbation to the right induces a clockwise yaw and a roll-right moment, which would further increase the velocity. Based on Y_r, a clockwise yaw results in a translation to the right, further destabilizing the vehicle. In addition, both L_p and N_r are unstable.

The most significant observation from the model structure is the contribution of L_r and L_{rud} to the lateral state and N_p and N_{lat} to the yaw state. This is the dominating cross-coupling effect unique to the cyclocopter. The roll-yaw couplings and their respective decoupling methods are described in details in the following subsections.

5.4.3.1 Gyroscopic Coupling

As seen from the model and flight tests, the cyclocopter dynamics are dominated by gyroscopic roll-yaw cross-coupling. This coupling is caused by the unbalanced angular momentum from the cyclorotors spinning in the same direction. For a positive roll input, the vehicle responds in both roll right and counterclockwise yaw (Fig. 5.9). Likewise, for a positive yaw input, the vehicle responds in clockwise yaw and also rolls to the right.

In the present vehicle, the cross-coupling is decoupled by mixing roll and yaw inputs in the controller. To achieve a pure roll right response, a roll right input is combined with a clockwise yaw input to cancel out the inherent cross-coupling response. Likewise, for clockwise yaw, the input is appropriately combined with a

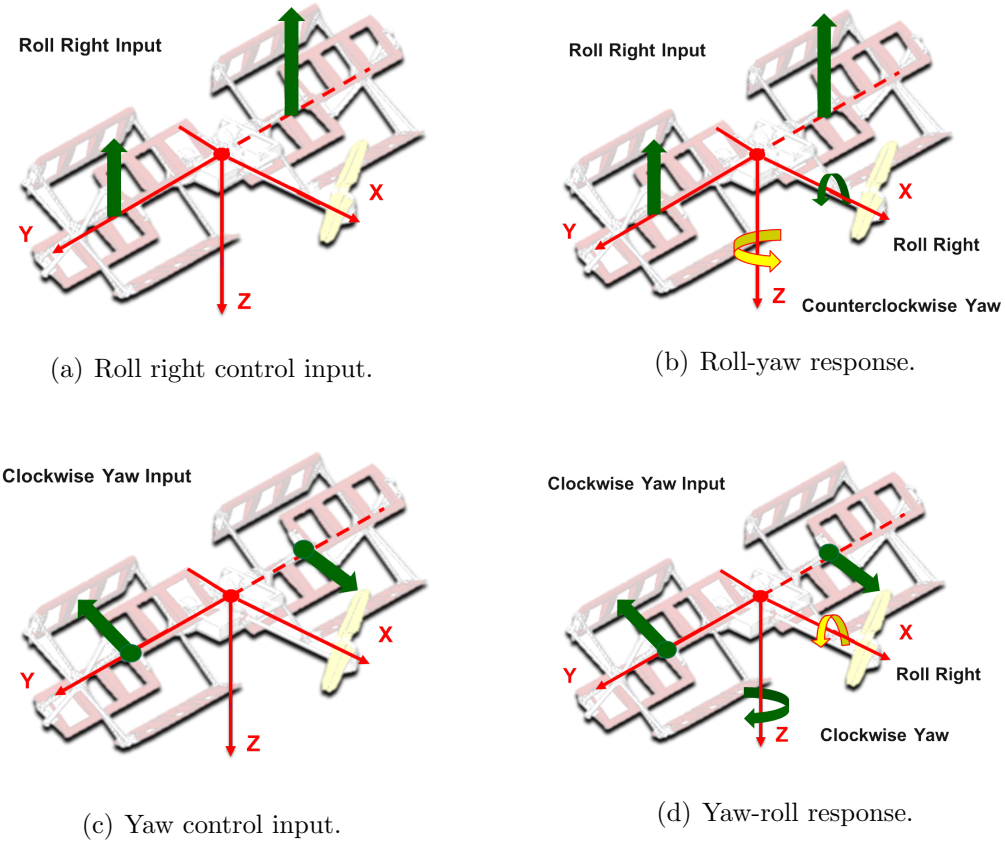

(a) Roll right control input.

(b) Roll-yaw response.

(c) Yaw control input.

(d) Yaw-roll response.

Figure 5.9: **Gyroscopic cross-coupling between roll and yaw degrees of freedom.**

roll left input. The mixing ratio is only applied to the open-loop pilot input and directly implemented on the onboard controller.

The gyroscopic mixing terms were experimentally found by suspending the cyclocopter about c.g. on a 3-DOF gimbal stand unrestrained in pitch, roll, and yaw. Starting with zero mixing, the constants for both roll and yaw inputs were slowly increased until the vehicle achieved a decoupled response. Experimental results showed a stronger coupling for a roll input, which results in higher mixing ratios. One reason for a stronger roll-yaw coupling could be that the moment of inertia about the x-axis is greater than that about the z-axis.

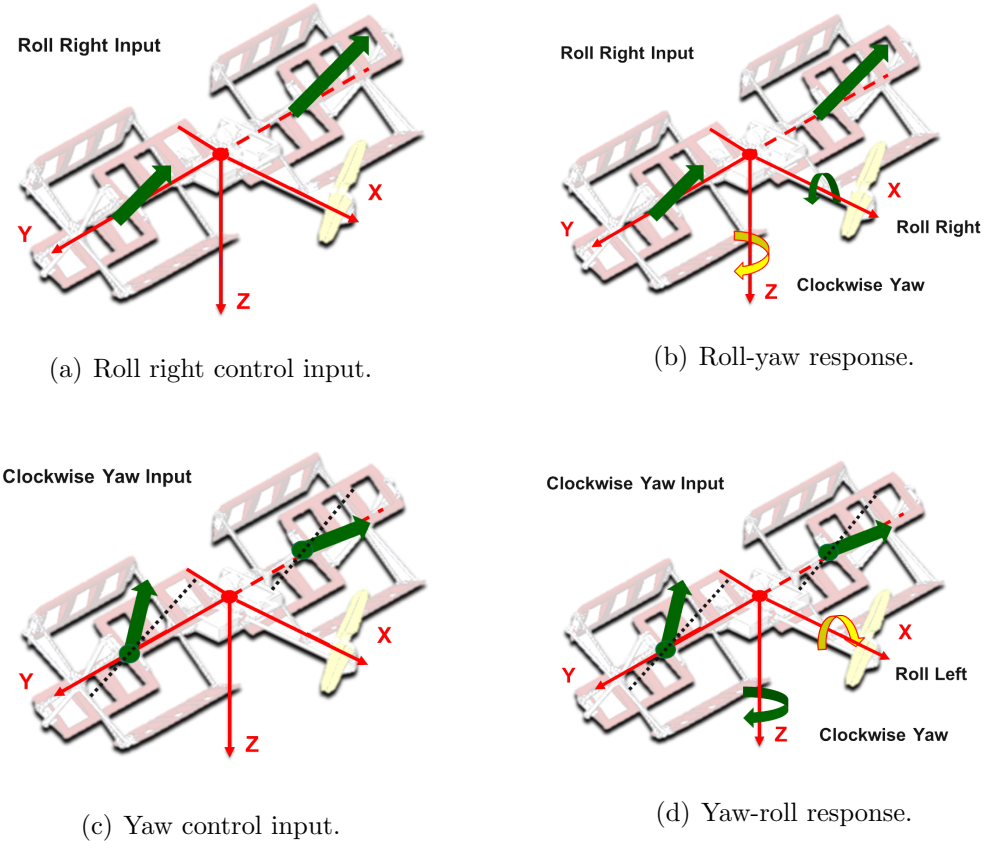

(a) Roll right control input.

(b) Roll-yaw response.

(c) Yaw control input.

(d) Yaw-roll response.

Figure 5.10: **Controls cross-coupling between roll and yaw degrees of freedom occurring at high phase angles.**

5.4.3.2 Controls Coupling

Existence of controls coupling at high phase angles is summarized in Fig. 5.10. The phenomenon can be physically explained by considering the magnitude of vertical (lift) and horizontal (thrust) forces generated by the cyclorotor at high phase angles. As the phase angle increases, the thrust vector is tilted towards the +X-axis and thus thrust increases while lift decreases. A differential change in rotational speed would have a greater effect on yaw than in roll. Likewise, thrust vectoring would effectively cause a roll response.

Table 5.3: Eigenvalue Comparison

Mode	**Eigenvalues**	
	Hover	Forward Flight
Longitudinal Translation	-3.83	-2.69
Longitudinal Rotation	1.66±3.05i	1.33±2.32i
Lateral-Yaw Translation	-2.29	0.133
	1.48	1.01
Lateral-Yaw Rotation	0.28±8.02i	-0.027±0.046i

As mentioned in section 4.7, the mixing scheme for controls coupling is as follows:

$$\delta_{\phi_b} = [b_{\phi_{lat}}\delta_{lat} + b_{\phi_{ped}}\delta_{ped}]sin\Phi \tag{5.19}$$

$$\delta_{\psi_b} = [b_{\psi_{lat}}\delta_{lat} + b_{\psi_{ped}}\delta_{ped}]sin\Phi \tag{5.20}$$

The mixing ratios were identified in the wind tunnel. In the previous experimental study, the mixing ratios were iterated until the vehicle dynamics were decoupled at each phasing input. After implementing the decoupling strategy, the vehicle was able to achieve decoupled response in forward flight.

5.4.4 Stability analysis in forward flight

The eigenvalues of the system provide a better understanding of the vehicle flight dynamics and have been summarized in Table. 5.3. The eigenvalues in hover were computed in a previous study using the same system identification techniques [39]. It is interesting to note that the eigenvalues for the longitudinal and lateral-yaw

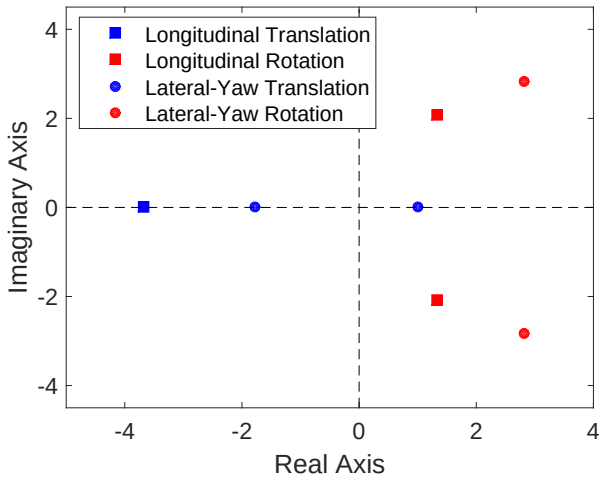

Figure 5.11: **Pole location for the cyclocopter in forward flight.**

translation modes are similar between the hover and forward flight cases.

The cyclocopter shows highly oscillatory and unstable longitudinal and lateral-yaw response in hover and forward flight. The lateral-yaw rotation mode is more unstable in forward flight possibly due to the combined roll-yaw cross-couplings previously mentioned. Unique to forward flight, the cyclocopter experiences both gyroscopic and controls coupling. Based on the locations of the system poles, the overall bare airframe dynamics of the cyclocopter is inherently unstable (Fig. 5.11). Therefore, the cyclocopter requires feedback regulation and roll-yaw controls mixing to achieve trimmed flight.

5.5 Summary

In this chapter, a flight dynamics model in forward flight was developed using system identification techniques. The 6-DOF model allowed assessment of the vehicle's susceptibility to velocity perturbation (gust) along the x-axis. The flight dynamics

model was extracted using the time-domain approach from SIDPAC system identification tools. The model was based on measurements from doublet inputs across various modes. The model structure was initially identified using stepwise regression and the parameters were estimated using the equation-error method. All maneuver inputs were provided after the cyclocopter achieved a steady state of 2 m/s flight at a steady, level attitude (θ, ϕ, ψ=0).

The existence of the control derivative, X_{phase} showed that phasing input commanded forward speed. From flight tests, it was observed that increasing the phasing with a δ_{phase} step input directly resulted in a step change in velocity. During the acceleration phase, the initial response was large and acceleration decreased with time until the vehicle reached steady state after two seconds. When the phase input was removed, the flight speed returned to the original forward velocity at the same rate. The negative longitudinal translation derivative, X_u indicated positive aerodynamic damping. Therefore, the vehicle was able to stabilize a velocity perturbation in the longitudinal direction. However, the aerodynamic pitch damping (M_q) was non-existent and the vehicle required feedback damping to stabilize the pitch attitude rate. In general, the longitudinal mode was decoupled and independent of the rest of the modes. The longitudinal coupling term, M_u was stabilizing. A perturbation that increased the longitudinal velocity would induce a nose-up pitching moment. The positive pitching moment would further decrease the forward velocity, stabilizing the cyclocopter.

The lateral translation derivative, Y_v was also stabilizing. However, the lateral and yaw coupling terms, L_v and N_v were unstable. In forward flight, a velocity per-

turbation would induce both roll and yaw responses. Based on Y_r, a clockwise yaw resulted in a translation to the right, further destabilizing the vehicle. In addition, both L_p and N_r were unstable. The model was able to validate the existence of the inherent roll-yaw coupling in forward flight, which was identified by contributions of L_r and L_{rud} to the lateral state and N_p and N_{lat} to the yaw state. These are the result of combined gyroscopic coupling and controls coupling at high phase angles. Overall, the gyroscopic coupling is caused by the unbalanced angular momentum from the cyclorotors spinning in the same direction. The controls coupling is due to the increase of magnitude of propulsive forces at high phase angles. As a result, thrust vectoring has a larger impact on the roll moments and subsequently, changes in rotor RPM have a greater influence on yaw moments.

Chapter 6: Gust Rejection Study

6.1 Overview

The previous chapter presented a linear state-space model of the cyclocopter in forward flight extracted through series of system identification experiments. The flight dynamics model showed that phasing input (thrust vectoring) had a high control authority over airspeed. In addition, a perturbation in the longitudinal velocity induced a stabilizing nose-up pitching moment. The positive pitching moment decreased the vehicle's airspeed back to desired condition. In this chapter, the disturbance rejection capability of the cyclocopter is investigated through series of experiments in the wind tunnel and using a synthetic gust generation device. The cyclocopter was first mounted on 1-DOF experimental stand in front of an open-jet wind tunnel to evaluate response to gust perturbation along the longitudinal and lateral axis. Since the cyclorotor has the unique capability of providing both lift and propulsive thrust by phasing the blade pitch cyclic, it is possible to reject gust disturbance isolated along the longitudinal axis using thrust vectoring. In addition, feedback control schemes of position feedback using a motion capture system and flow feedback using onboard flow sensing are also evaluated. Results of the comparative study of gust rejection strategies are provided for the 6-DOF experiments

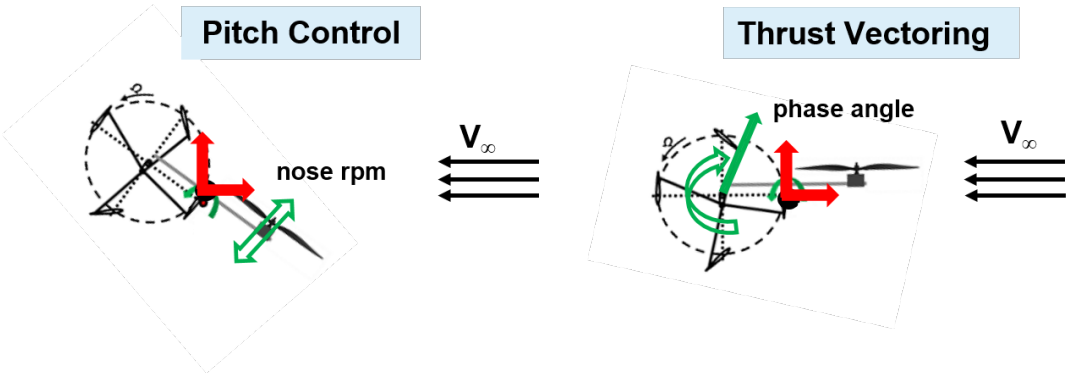

Figure 6.1: **Pitch control vs. thrust vectoring control.**

in front of a synthetic gust generation device for step gust inputs up to 4 m/s and 6 seconds in duration. Results also include performance for crosswinds up to 30 degrees from the longitudinal axis.

6.2 Gust Rejection Strategies

Due to their compact size and low inertia, MAVs are highly susceptible to gusts when operating in urban settings. For an edgewise gust, MAVs experience both drag force in the direction of the flow and pitching moment that rotates the vehicle away from the source. Possible methods to alleviate gust effects include increasing the vehicle's control authority and improving the closed-loop feedback system. The gust rejection strategies are evaluated through series of tethered experiments in the wind tunnel and in front of a custom gust generation device.

6.2.1 Control Input

Conventional rotary-winged MAVs like quadcopters rely on differential rpm to recover from gust perturbation. Through this control input, the vehicle achieves a

non-zero pitch attitude angle, thereby increasing its effective surface area and potentially reducing its gust rejection capability. For the cyclocopter configuration, there are two possible gust rejection control strategies for disturbance along the longitudinal axis: (1) pitch control by actuating nose rotor rotational speed and (2) thrust vectoring the cyclorotors (Fig. 6.1).

As introduced in previous chapters, the cyclocopter has the unique capability of thrust vectoring by phasing the blade pitch cyclic. The resulting thrust vector has both a vertical lift component and a horizontal propulsive thrust component. By vectoring the resultant thrust to increase its propulsive thrust component, the cyclocopter is able to maintain a zero pitch attitude angle in forward flight and independently translate forward and backward without adjusting the vehicle's pitch angle.

6.2.2 Feedback System

An intuitive control scheme to negate gust effects is to rely on inertial measurements coupled with closed-loop position feedback. The drag force and pitching moment experienced by the cyclocopter would affect body angular rates and displacement. Inertial measurements are then used to calculate control inputs required to recover initial position and attitude. With position feedback, the gust controller only comes into effect after the vehicle has been perturbed.

An alternative control scheme is to rely on real-time flow measurement in order to directly measure disturbances. The flow feedback controller would then predict

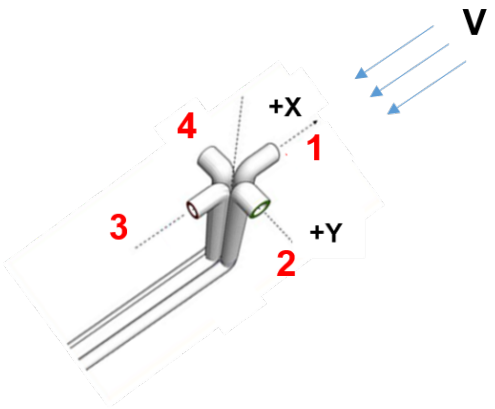

Figure 6.2: **Multi-hole flowprobe system.**

impending vehicle response and provide control inputs to negate gust effects. Unlike position feedback, flow feedback could potentially enable the vehicle to maintain its initial attitude throughout the gust perturbation. However, the control scheme is sensitive to the choice of onboard miniature flow sensor and requires a priori knowledge of control inputs suitable for measured disturbances.

6.3 Real-time Flow Measurement

A number of approaches were considered to measure freestream velocity for low operational range. A hot-wire or ultra-sonic anemometer offers high resolution and 3D measurement of velocity, but has a high weight penalty making them unsuitable for MAVs. A mechanical approach that uses miniature rotating vanes or a turbine would provide adequate resolution at low speeds, but will be mechanically complex and sensitive to vibrations observed on the cyclocopter. A pressure-probe based approach such as traditional pitot-probes could be easily implemented at the MAV-scale but are prone to poor signal-to-noise ratios at low operating airspeed.

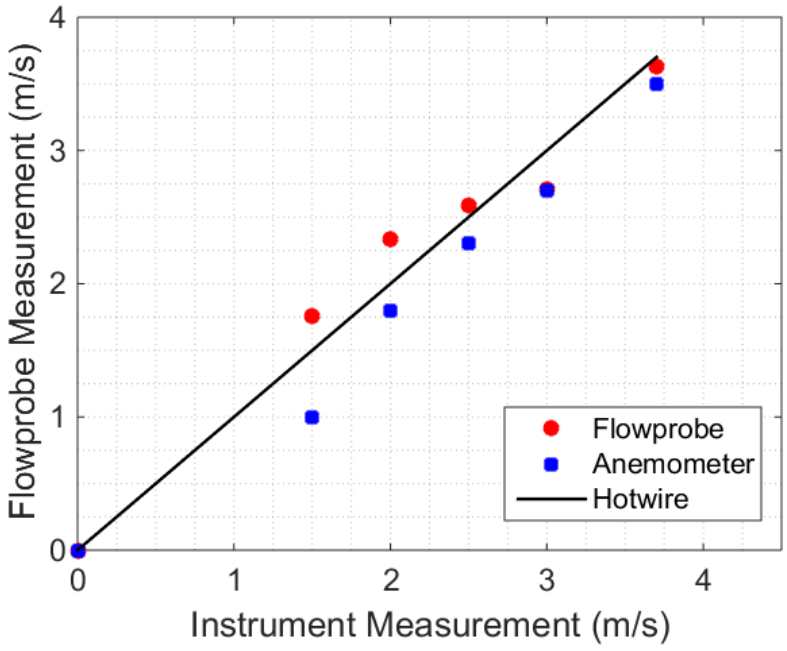

Figure 6.3: **Flowprobe calibration compared to hot-wire and rotary anemometer.**

An alternative pressure-probe based approach relies on measuring differential pressure. A traditional pitot-static probe includes a forward-facing port for total pressure and a ring of inter-connected static ports perpendicular to the flow. The dynamic pressure is measured as the difference between the total pressure and the static pressure. While this allows for a probe that is less directional, a relatively large forward velocity is needed before a clear signal is generated. The current setup uses a two-component flowprobe design with one opening facing towards the freestream and other against the flow in order to provide a differential pressure measurement. Any forward velocity causes a degree of pressure loss on the aft-facing port, enabling the probe to provide an amplified measurement of dynamic pressure with higher sensitivity at low speeds.

Freestream velocity was continuously measured throughout the experiment using an analog Honeywell HSCDRR series differential pressure sensor. The sensor measures pressure range of $\pm 249.08 Pa$ and has an input voltage of 3.33 V. The analog voltage measurements from the differential pressure sensor are converted to ADC (analog-to-digital) values on ELKA at 1000 Hz with a 32-bit resolution. Dual ports on the sensor are individually connected to an opening on the flowprobe. The pressure measurements from the sensor are converted to velocity using a scaled version of pitot static equations [85]. A multi-probe setup with flowprobes along X-Y axes (Fig 6.2) was used to enable 2D velocity measurement. The components of velocity are calculated using calibration gains (K_u, K_v, K_b), pressure measurements (X_1, X_3, Y_2, Y_4), and density (ρ):

$$u = K_u \sqrt{\frac{2K_b(X_1 - X_3)}{\rho}} \tag{6.1}$$

$$v = K_v \sqrt{\frac{2K_b(Y_2 - Y_4)}{\rho}} \tag{6.2}$$

Symmetry of the bi-directional flow probe resulted in equivalent calibration gains $(K_u = K_v)$. With this setup, the total velocity magnitude (V) and side-slip angle (β) can be calculated using:

$$V = \sqrt{u^2 + v^2} \tag{6.3}$$

$$\beta = tan^{-1} \frac{v}{V} \tag{6.4}$$

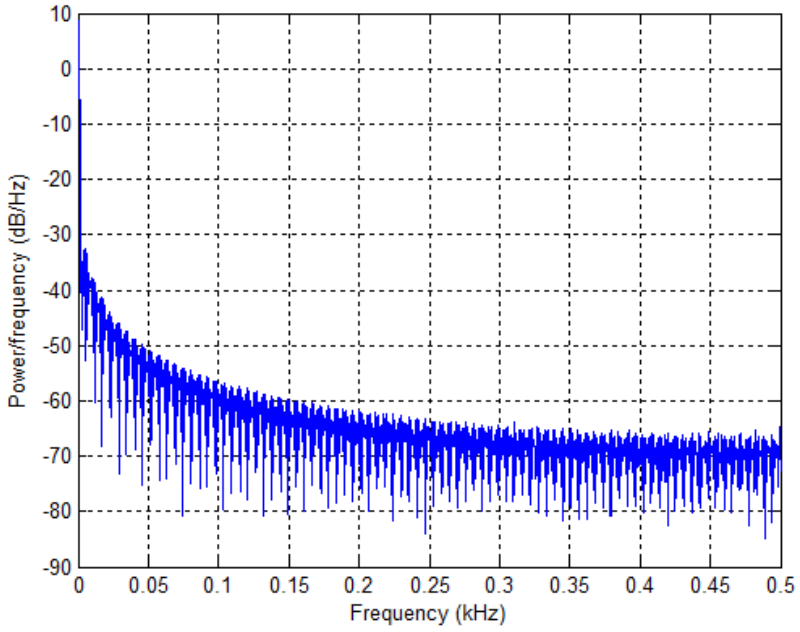

Figure 6.4: **Power spectral density estimate via Welch (contributions from the flow field).**

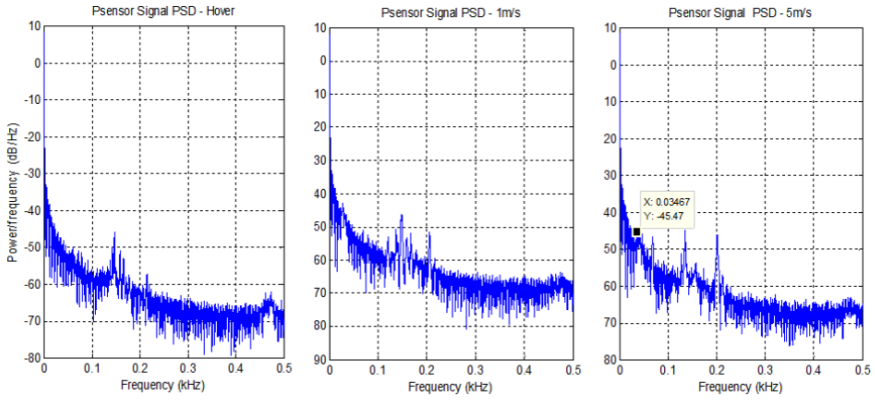

Figure 6.5: **Power spectral densities at different airspeeds (hover, 1 m/s, and 5 m/s).**

Flowprobe measurements were calibrated against measurements from both a hot-wire anemometer and rotary anemometer in the wind tunnel from 1 m/s to 8 m/s. Figure 6.3 shows velocity measurements of all three sensors. Additional calibration was experimentally performed with the probes mounted on the vehicle

to account for the flow field disturbances specific to a cyclocopter. In order to filter high frequency noise, the wind tunnel pressure data is first characterized by its power spectral density (PSD). By comparing the power spectrum with the cyclorotor powered down and with the rotors spinning, contributions from the flow field and the vehicle can be independently identified. Fig. 6.4 shows the PSD of the pressure data with the cyclorotors completely powered down. From the figure, it is evident that there are no discernible modes in the low-turbulence freestream because the flow far downstream of the wind tunnel drive system does not have any identifiable characteristic frequencies. Therefore, any observed modes in the power-on case are caused solely by the noise from the cyclorotors. The PSDs for pressure data at three different velocities are shown in Fig 6.5.

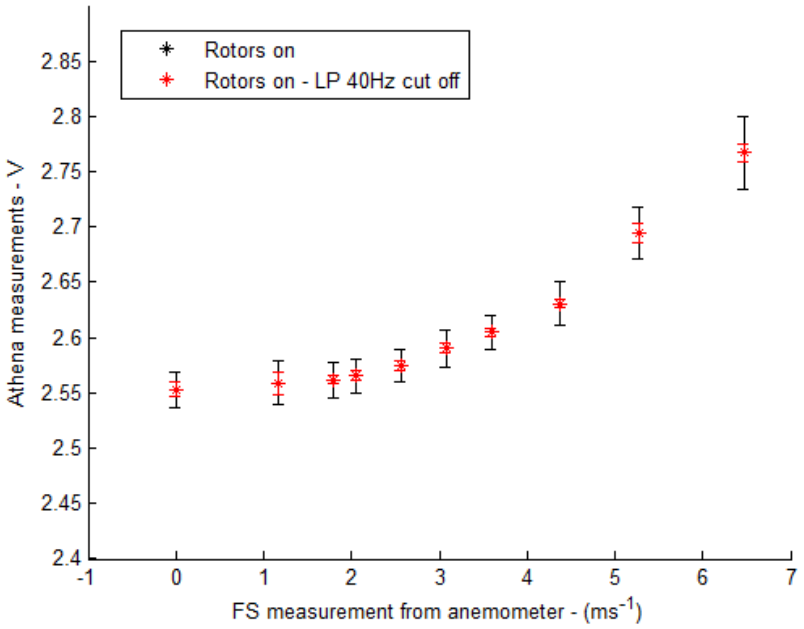

Figure 6.6: **Filtered pressure signal statistics.**

Harmonics are noted at 135 Hz and 200 Hz, which suggests that either the pres-

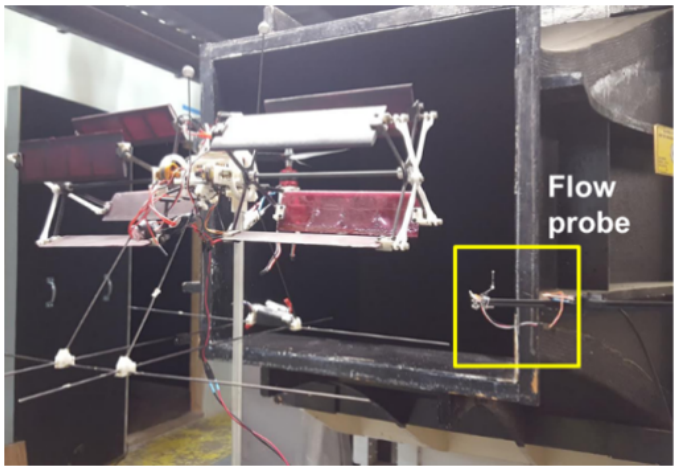

Figure 6.7: **1-DOF pitch stand.**

sure transducer measurements are being affected more by probe/vehicle structural response than actual flow or by the forward mounted propeller rotor. In addition, a harmonic near 35 Hz was noted with an incident free stream, suggesting that this might be flow field dependent. As a result, a low pass filter with a cut-off freq of 40 Hz was chosen. The filtered measurements are compared with raw measurements in Fig. 6.6.

6.4 Preliminary Wind Tunnel Studies

One method of evaluating the vehicle's control authority is by conducting tethered experiments in the open-jet wind tunnel (0.56 m $\times$ 0.56 m). The objective of the wind tunnel experiments is to determine the cyclocopter's response to an edgewise flow and identify the maximum gust perturbation along both longitudinal and lateral axis that the cyclocopter can overcome before reaching control saturation. In particular, these experiments will evaluate the effectiveness of cyclocopter's pitch

control.

6.4.1 Methodology

In order to isolate either the pitch or roll degree of freedom, the cyclocopter was mounted on a 1-DOF gimbal stand at c.g (Fig. 6.7). Rotations about pitch and roll were restricted to $\pm 8^{\circ}$. For each experiment, the control inputs are solely provided by the PD feedback control discussed in Chapter 2 to recover the desired attitude.

At the beginning of each experiment, the cyclorotors operate at 1400 rpm while the nose rotor operates at 4000 rpm. Trim values are continuously adjusted through each experiment to achieve stable hover (θ,$\phi = 0$). The inner-loop PD gains were selected to minimize settling time after a gust perturbation. While the settling time is dependent on the feedback control system, the maximum magnitude of the gust input a vehicle can tolerate before experiencing control saturation is dependent on its configuration. For each experiment, the magnitude of the gust input is varied by increments of 0.5 m/s up to 10 m/s. In addition, freestream velocity is continuously measured using the differential pressure sensor discussed in the previous section.

6.4.2 Results: Longitudinal Axis

A gust perturbation along the longitudinal axis resulted in a pitch-up moment on the cyclocopter (Fig. 6.8). The pitch-up moment may be possibly attributed to the following: (1) increase in thrust produced by the nose rotor combined with increase in pitching moment and (2) drag force on the nose rotor combined with

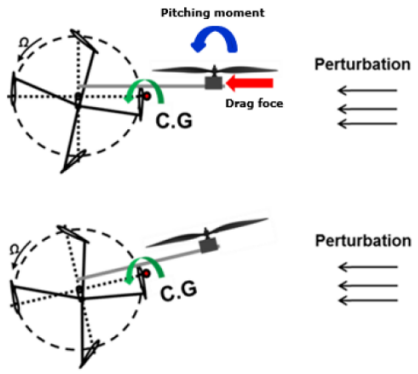

Figure 6.8: **Gust perturbation along longitudinal axis results in pitch-up moment.**

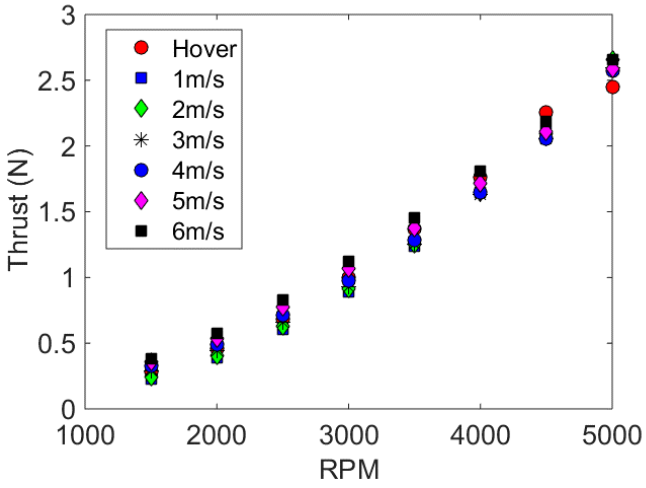

Figure 6.9: **Variation of nose rotor thrust with rotational speed at various freestream velocities.**

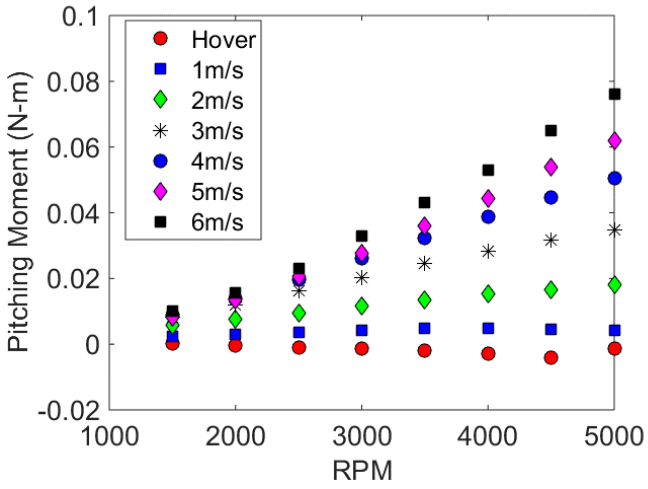

Figure 6.10: **Variation of pitching moment with rotational speed at various freestream velocities.**

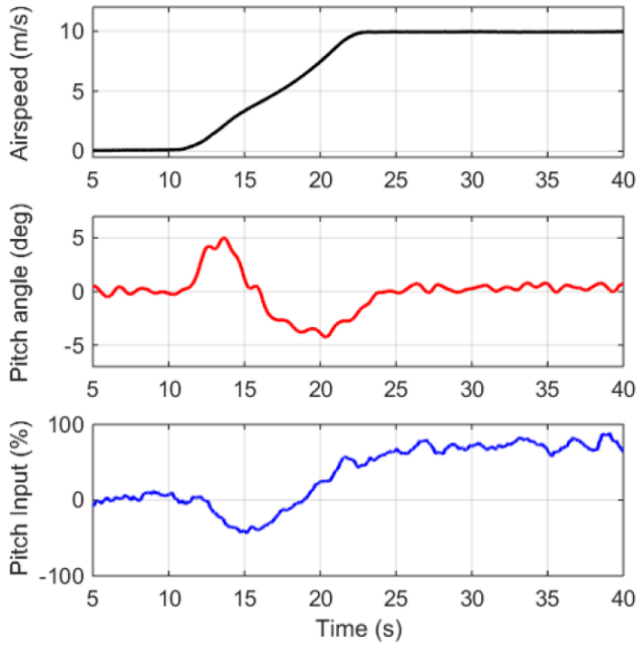

Figure 6.11: **1-DOF pitch response for 10 m/s longitudinal ramp gust perturbation.**

a low vehicle c.g. As the freestream velocity increases, the nose rotor thrust also increases at each rotational speed (Fig. 6.9). Interestingly, the pitching moment caused by blade flapping is non-negligible and also increases with freestream velocity (Fig. 6.10). Yeo et al. [85] and Hoffmann et al. [86] also observed similar trends for MAV-scale commercial propellers and accounted for blade flap in their feedback controllers. Since the nose rotor is operating at 4000 rpm, its pitching moment at higher freestream velocities will influence the cyclocopter's pitch response to a gust perturbation along the longitudinal axis.

Since the wind tunnel velocity is controlled by switching the power to the motor, the resulting gust profiles are ramp inputs. The cyclocopter was able to withstand a 10 m/s ramp gust perturbation and recover desired pitch attitude within 12 seconds before reaching control saturation (Fig. 6.11). As previously mentioned, pitch control is solely provided by regulating the rotational speed of the horizontal nose rotor. The feedback controller initially reduces the nose rotor rpm to counteract the induced pitch-up moment. However, the cyclocopter overshoots the desired pitch attitude and is pitched down towards the 10 m/s freestream. Because of the increased drag force on the vehicle, the feedback controller peaks at 90% of positive pitch input to stabilize the cyclocopter. Throughout the experiment, PD gains were consistently adjusted to reduce overshoot and settling time.

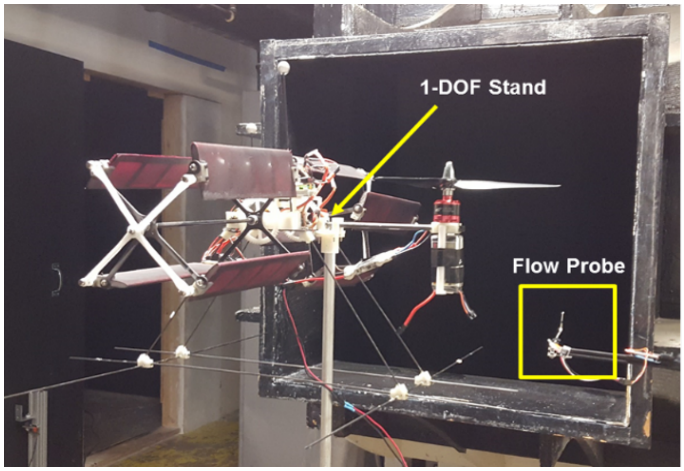

Figure 6.12: **1-DOF roll stand**

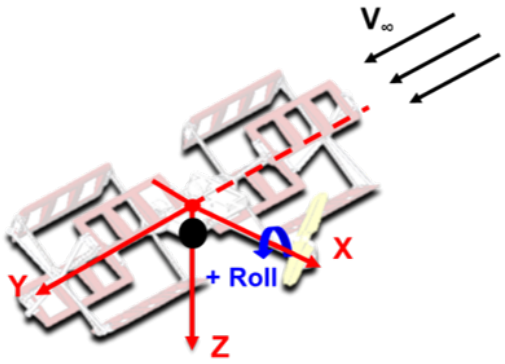

Figure 6.13: **Gust perturbation along lateral axis results in roll-right moment.**

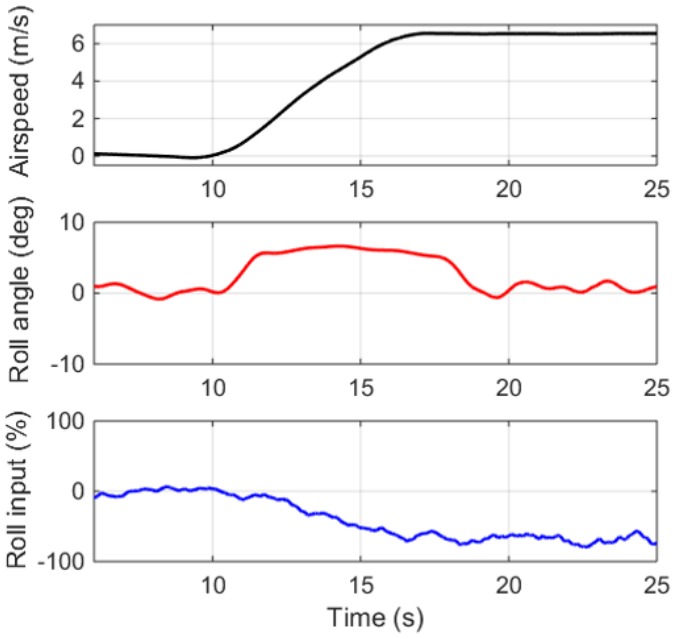

Figure 6.14: **1-DOF roll response for a 6.5 m/s lateral ramp gust perturbation.**

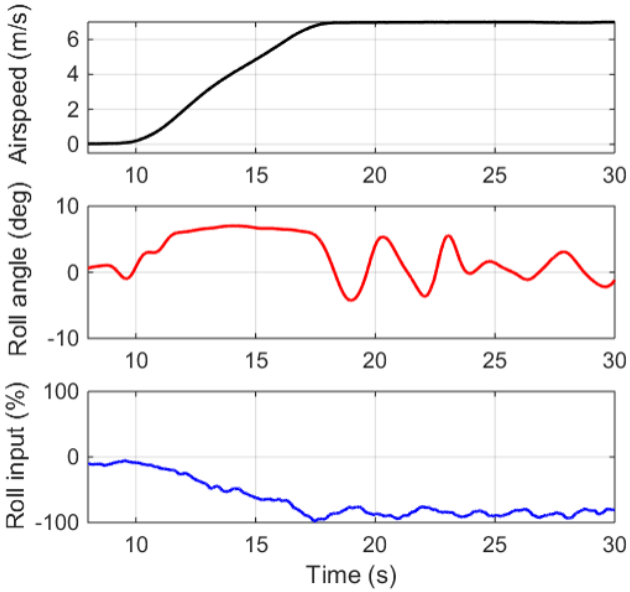

Figure 6.15: **1-DOF roll response for a 7 m/s lateral ramp gust perturbation.**

6.4.3 Results: Lateral Axis

For the 1-DOF roll experiments, the cyclocopter was positioned in front of the wind tunnel such that the freestream velocity aligned with the +Y-axis of the body frame (Figs. 6.12). With this setup, a gust perturbation along the lateral axis results in a roll-right moment (Fig. 6.13). The positive roll moment may be caused by the drag force on the cyclorotor combined with a vertical c.g offset.

The threshold for the maximum gust perturbation is much lower along the lateral axis (Fig. 6.14). The cyclocopter was able to withstand up to 6.5 m/s of gust before experiencing control saturation. The cyclocopter achieves roll control by differentially varying the rotational speed of both cyclorotors, which have a lower maximum achievable rpm compared to the nose rotor. Before applying a gust perturbation, both the cyclorotors operate near 1400 rpm while the maximum possible rotational speed is 1600 rpm. At 7 m/s, the feedback controller inputs the maximum available negative roll input which increases the operating speed of the right cyclorotor to 1600 rpm and decreases the left cyclorotor to 1200 rpm (Fig. 6.15). Similar to the 1-DOF pitch experiment, the cyclocopter overshoots the desired roll attitude and the increased drag force on the vehicle combined with control saturation leads to roll oscillation about the lateral axis (Fig. 6.15). Based on these preliminary results, the cyclocopter has a higher control authority in pitch compared to roll for gust disturbance rejection.

6.5 Tethered Experiments (6-DOF)

Preliminary wind tunnel experiments showed that a gust perturbation along the longitudinal axis leads to a pitch up moment, which consequentially results in backwards translation. Pitch control enabled the cyclocopter to recover level attitude for ramp gust profiles up to 10 m/s with a settling time of 12 seconds. However, the 1-DOF experiments do not account for translation or secondary effects on roll and yaw body rates. In addition, a slow ramp gust profile enables the controller to respond earlier at a lower gust magnitude instead of the selected magnitude.

Tethered experiments using a custom gust generation device and 6-DOF test stand were conducted to evaluate effectiveness of pitch control and thrust vectoring control for a gust along the longitudinal axis. Both position feedback and flow feedback control schemes were tested for step gust profiles with magnitudes up to 4 m/s and duration of 1, 3, and 6 seconds. The following sections provide information on the 6-DOF test stand, custom gust generation device, and the gust rejection controller.

6.5.1 Experimental Stand

In order to emulate free-flight conditions, the cyclocopter was mounted on a 6-DOF stand (Fig. 6.16) assembled using three linear ball-bearing sliders and a gimbal bearing. The gimbal mount enables up to $\pm 16^\circ$ in pitch, $\pm 20^\circ$ in roll, and $\pm 16^\circ$ in yaw while the linear sliders permit translation of 0.53 m across x-axis, 0.27 m across y-axis, and 0.15 m across z-axis. The vehicle's main mount is attached to a

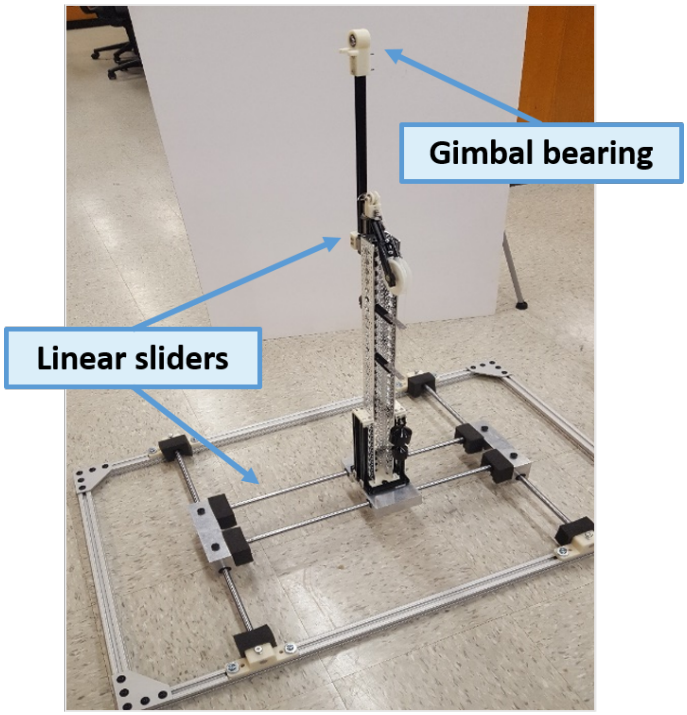

Figure 6.16: **6-DOF experimental stand.**

pulley system and a counterweight of 300 grams to offset weight of the mount. As a result, the cyclocopter is able to operate at 1400 rpm through these experiments. The coefficient of friction for the ball-bearing sliders is 0.001. However, the setup does have a considerable amount of inertia due to weight of the aluminum carriages. Therefore, experiments conducted using 6-DOF setup is to evaluate effectiveness of different gust rejection strategies.

6.5.2 Synthetic Gust Generation Device

To produce repeatable step gust perturbations, a custom gust generation setup was developed in this study (Fig. 6.17). These bladeless fans output a stream of air from small ducts outlining its boundaries. A set of three fans were grouped together and

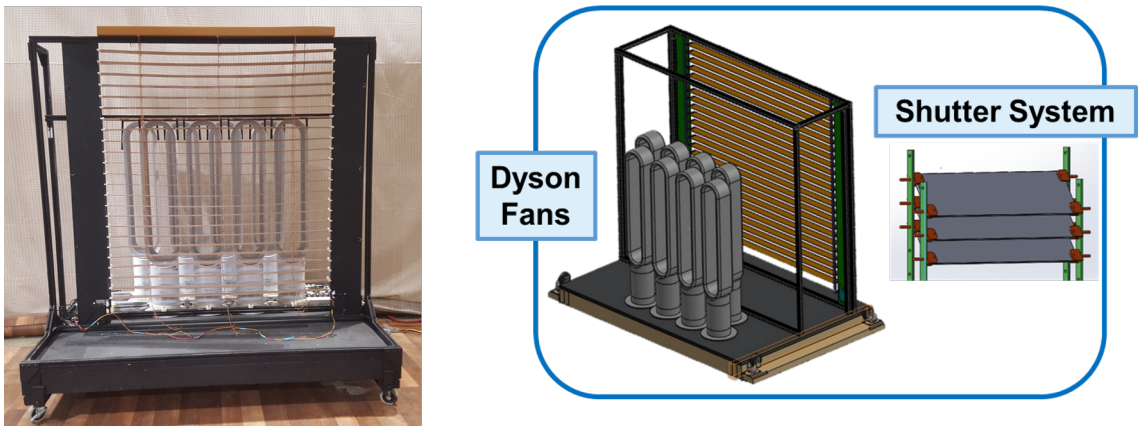

Figure 6.17: **Synthetic gust generation device with shutter system.**

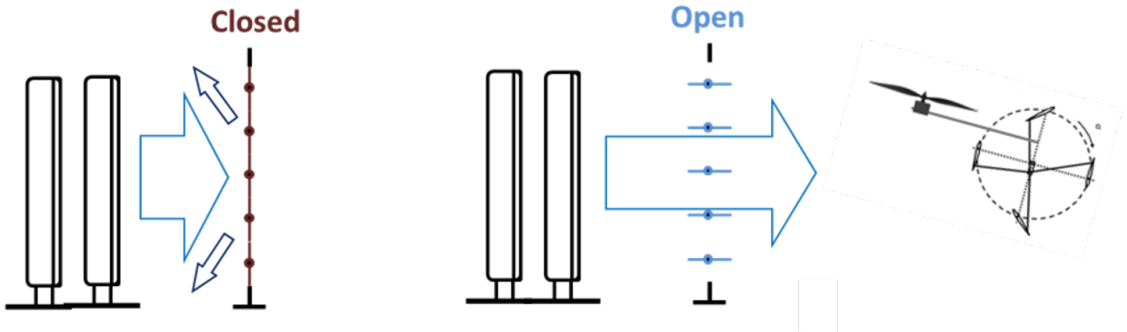

Figure 6.18: **Shutter system mechanism provides step gust inputs.**

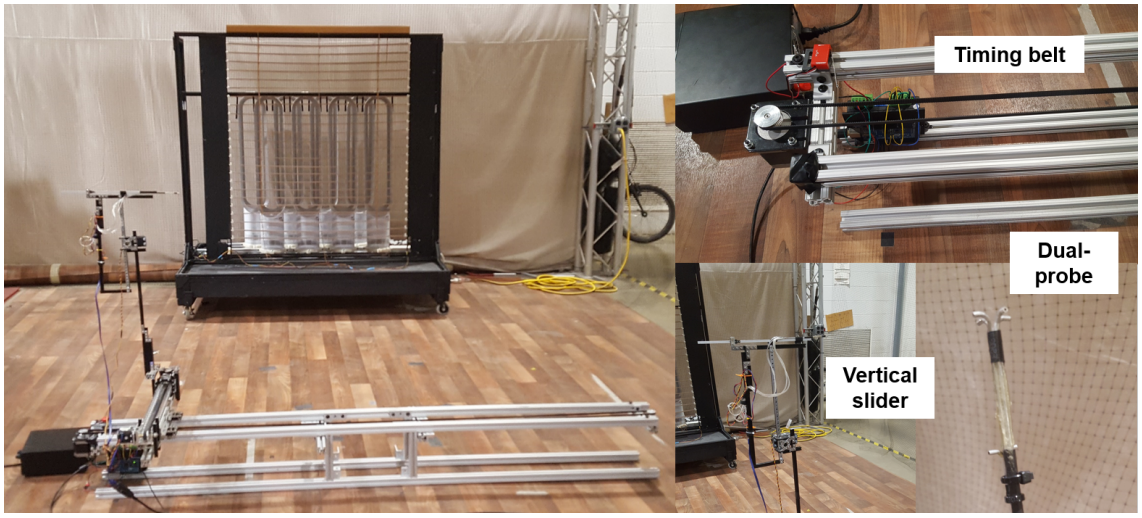

Figure 6.19: **Custom mechanism to survey flow field at 66 discrete points in test cross-section.**

placed 0.089 meters apart. Another set of fans were stacked directly behind the first row but with a 0.10 meters horizontal offset in order to augment the airflow. The setup was placed inside the testing volume (3.0 m x 2.4 m x 1.8 m) enclosed by the VICON Motion Capture System.

The fans are arranged behind a shutter system that is actuated using two Hitec HS-1000SGT rotary servos. The shutter mechanism is controlled through the ground control station and is automated to open and close for the desired duration (Fig. 6.18). With this setup, the Dyson fans are always operating in order to achieve a step gust profile instead of the ramp profile produced in the wind tunnel. Variable parameters of the gust setup include fan power, distance between adjacent fans, distance between front and back rows of fans, location of shutter system, and distance to the test area. These parameters were adjusted in order to achieve steady uniform flow throughout the test region.

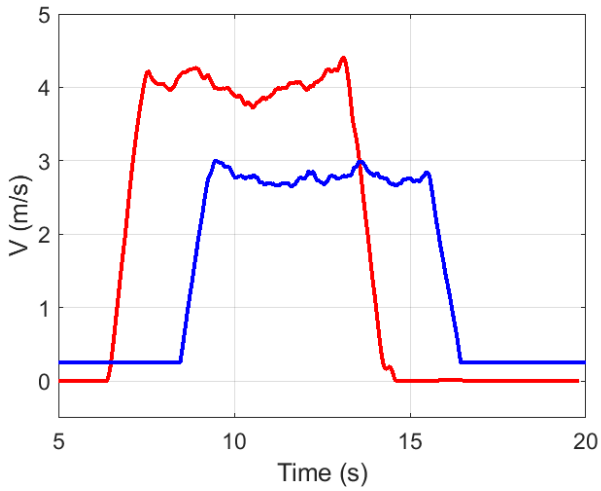

Figure 6.20: **Magnitude of step gust input for one vs. two rows of Dyson fans.**

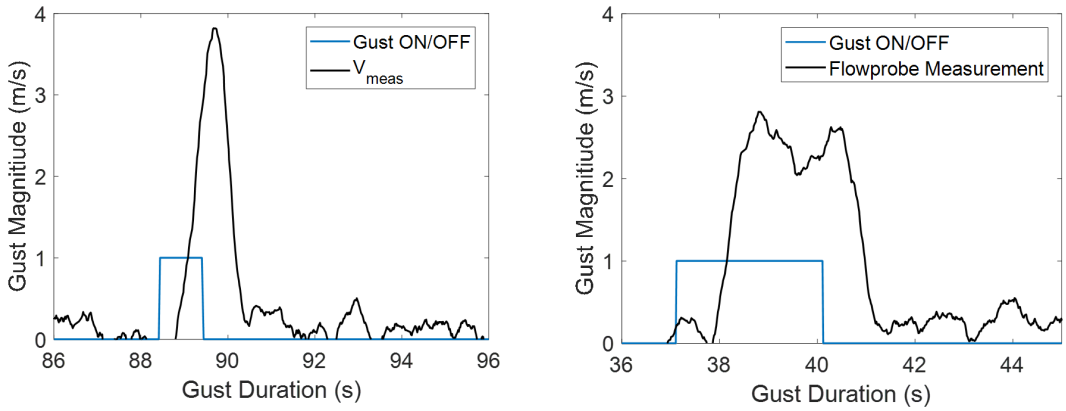

Figure 6.21: **Variations in magnitude and duration of gust profiles using the shutter mechanism.**

An important characteristic of the gust generation setup is that the flow field within the test region must have a steady unidirectional profile so that the vehicle is not subjected to additional aerodynamic effects from turbulence. A systematic flow field survey of the test region, 1.32 m from the fans, was conducted using a differential pressure sensor mounted on an automated carriage mechanism (Fig. 6.19). The survey measured the average freestream velocity at 11 points evenly distributed along the cross-stream location (0-80cm) and at 6 different flow probe heights (0-16.8cm). A sweep of the flow field shows that the mean freestream velocity is uniform across the 80 cm by 16.8 cm test region. Two rows of fans generated a maximum freestream velocity of 4 m/s with variance of 0.15 (Fig. 6.20).

$$V_{rms} = \sqrt{\sum_{i=1}^{n} \frac{V_i - \bar{V}}{n-1}} \tag{6.5}$$

$$T = \frac{V_{rms}}{\bar{V}} \times 100 \tag{6.6}$$

Using equations 6.5 and 6.6, the turbulence at the maximum generated freestream velocity is approximately 11.4%. Wind tunnels typically have a small turbulence intensity of less than 0.7% [87]. Overall, the synthetic gust generation device is capable of producing step gust inputs of 2.8 m/s and 4 m/s at various step durations. The setup can also generate sinusoidal gust profiles by actuating the shutters. Throughout the experiments, the duration of gust input was varied at 1, 3, or 6 seconds (Fig. 6.21).

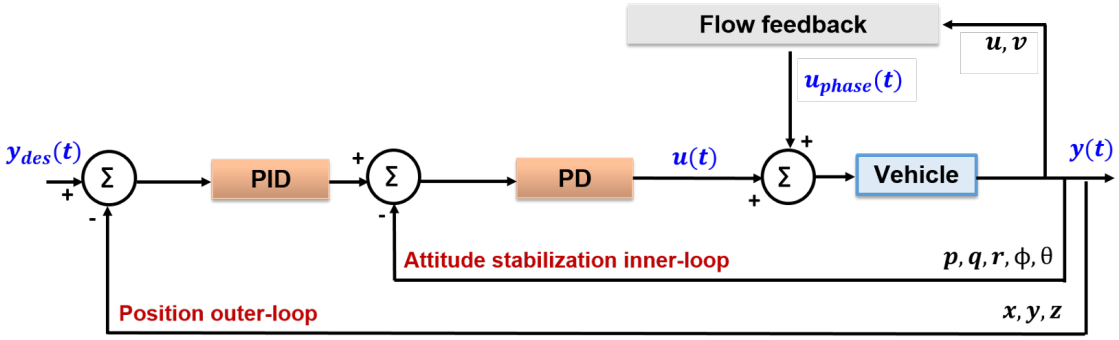

Figure 6.22: **Closed-loop feedback system with gust rejection controller.**

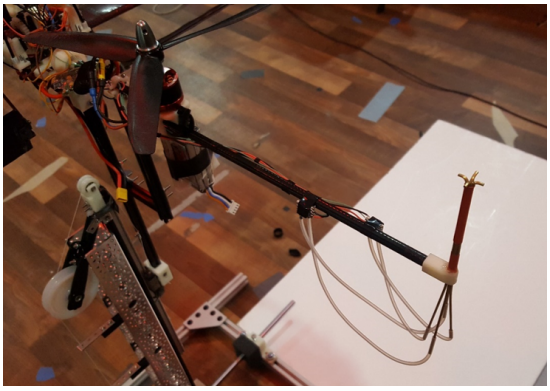

Figure 6.23: **Onboard flow sensing mounted on the cyclocopter.**

6.6 Gust Rejection Controller

The closed-loop feedback system was modified with a PID controller for autonomous position control. Position data from the VICON motion capture system were transmitted to the onboard autopilot via a LabVIEW interface on the ground control system. The position trim setpoints ($x_{des}, y_{des}, z_{des}$) were initialized at the start of each experiment. The position controller outputs desired attitude angles (ϕ, θ, ψ) and are the setpoints for the attitude stabilization inner-loop controller. The inner-loop uses a PD control scheme and modulates the rotational speeds (throttle, pitch, and roll) and differential thrust vector (yaw) inputs to the vehicle.

A gust controller with a flow feedback scheme was added to the inner-loop and only provided a collective thrust vector input to the vehicle. Unlike differential thrust vectoring, collective thrust vectoring results in forward and backward translation of the cyclocopter instead of a change in orientation. Inputs to the gust controller includes X-Y velocity components (u, v) from a miniature dual-probe flow sensor (Fig. 6.23). The appropriate phase angle control input for a given velocity was determined a priori in the wind tunnel and from forward flight experiments discussed in Chapter 4:

$$\Phi = K_{\Phi} V + \Phi_0 \tag{6.7}$$

The nominal phase angle command (Φ) is equivalent to measured velocity (V) multiplied by a gain (K_{Φ}) that was fine-tuned during these experiments. Since

the experiments were conducted in hover, the initial phase angle is zero ($\Phi_0 = 0$). However, the controller can be adapted to forward flight if the cyclocopter's flight speed is subtracted from measured velocity.

6.7 Results

While the 1-DOF wind tunnel studies explored both longitudinal and lateral gust response, 6-DOF experiments focused on longitudinal gust response in order to evaluate effectiveness of thrust vectoring control. Initial experiments assessed pitch control and thrust vectoring control against a step gust perturbation. These experiments used only position feedback as means to detect disturbances. At the beginning of each experiment, the vehicle maintained a steady hover at approximately 0.1 m longitudinal offset from the slider bounds while centered laterally. Afterwards, a step gust input was provided with magnitudes of 2.8 m/s and 4 m/s and durations of 1, 3, and 6 seconds. The selected performance metric was displacement from the desired hover position. After selecting the control input, additional experiments were conducted to specifically evaluate performance of position feedback and flow feedback controllers.

6.7.1 Pitch Control vs. Thrust Vectoring

Effectiveness of position feedback using pitch control was investigated because preliminary wind tunnel results showed that the cyclocopter is able to maintain pitch control authority in a 10 m/s gust perturbation. However, the 1-DOF experiment

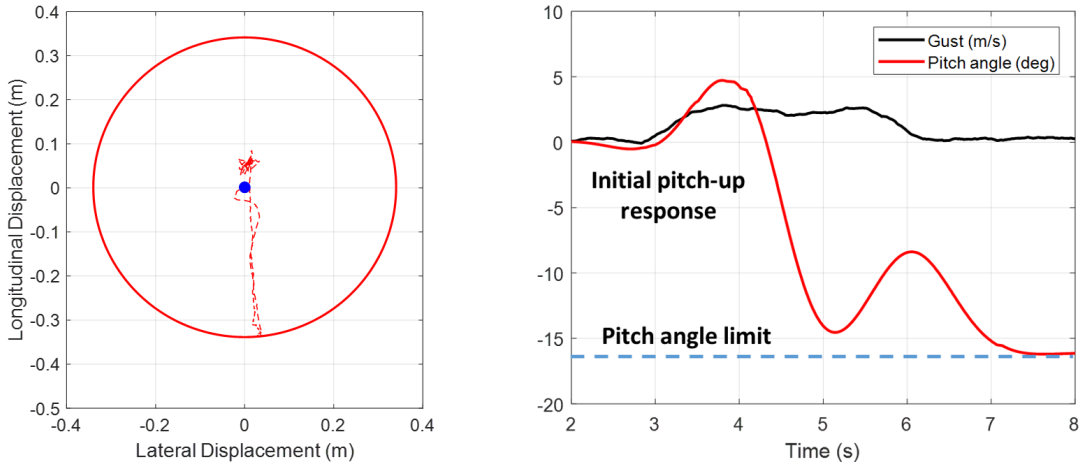

Figure 6.24: **Displacement and pitch control input for 2.8 m/s step gust.**

only assessed the vehicle's ability to recover pitch attitude and not the hover trim. For this experiment, the attitude stabilization for pitch used a PD controller and position feedback used a PID controller. Therefore, the cyclocopter will not maintain a level attitude ($\theta = 0°$) during a gust perturbation but instead use the non-zero pitch attitude to recover the trim position on the horizontal slider (thrust = drag). This control strategy is similar to how typical rotary MAVs such as quadcopters recover from gust perturbation.

Figure 6.24 shows the 6-DOF response to a 2.8 m/s gust perturbation using pitch control to recover trim. The plots display displacement along both lateral and longitudinal axis, step gust input, and the controller's response in terms of resulting pitch angle. The dashed line indicates maximum achievable pitch angle due to constraints on the gimbal stand. As evident from the figure, a step gust input causes the cyclocopter to pitch-up and subsequently translate backwards by 0.34 meters. In addition, gust along the longitudinal axis does not have a significant impact on lateral translation. The feedback controller is ultimately able to recover

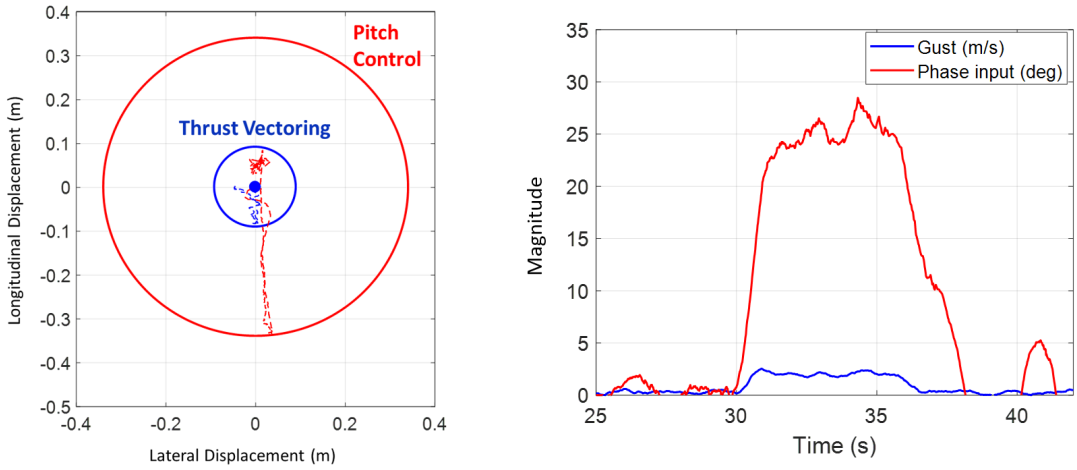

Figure 6.25: **Displacement and thrust vector input for 2.8 m/s step gust.**

desired position on the slider with a 16° pitch down attitude when operating at 1400 rpm.

Because of its thrust vectoring capability, the cyclocopter is able to provide both lift and propulsive thrust by phasing the blade pitch cyclic. Position feedback using thrust vectoring resembles the forward flight control strategy previously implemented on the vehicle. Therefore, it is entirely possible for the cyclocopter to maintain both a level attitude ($\theta = 0°$) and hover at the setpoint during a gust perturbation.

Figure 6.25 shows a comparison of the resulting displacement between pitch control and thrust vectoring. A phasing input of 26° counteracts the drag force from the 2.8 m/s gust perturbation and follows a similar step profile. Even with a phasing input, the cyclocopter still experiences a pitch-up moment, but it is stabilized by the inner-loop PD controller. The cyclocopter translates only 0.1 m along the longitudinal axis since the propulsive thrust was increased by instantaneously rotating the

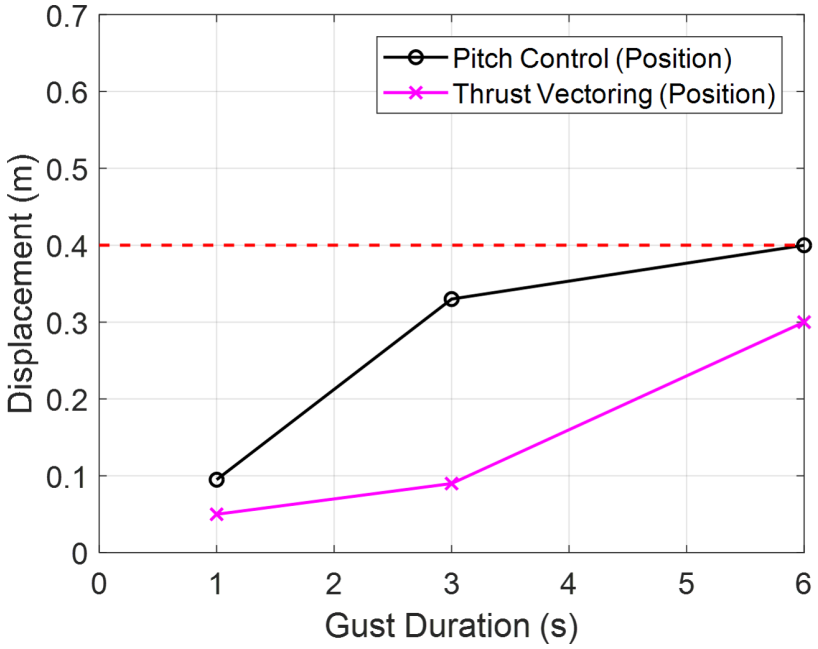

Figure 6.26: **Displacement vs. duration of gust for pitch control and thrust vectoring inputs.**

thrust vector instead of incrementally modulating the nose rotor's rotational speed.

Figure 6.26 summarizes the displacement results for both pitch control and thrust vectoring for 2.8 m/s at 1, 3, and 6 seconds durations. During the experiments, the linear slider enabled 0.53 m of translation along the perturbed axis. Accounting for the vehicles initial position, displacements of 0.4 m or above were categorized as a failed controller (i.e vehicle was not able to tolerate gust). Each data point on the graph was an averaged value of multiple trials after selecting the final gains of the position feedback controller.

Pitching forward to counteract a longitudinal gust perturbation resulted in a maximum gust tolerance of 2.8 m/s with a duration of 3 seconds. The maximum pitch attitude ($\theta = 16°$) at 1400 rpm on the 6-DOF stand did not produce adequate propulsive thrust to counteract the drag on the vehicle. While the vehicle was able to

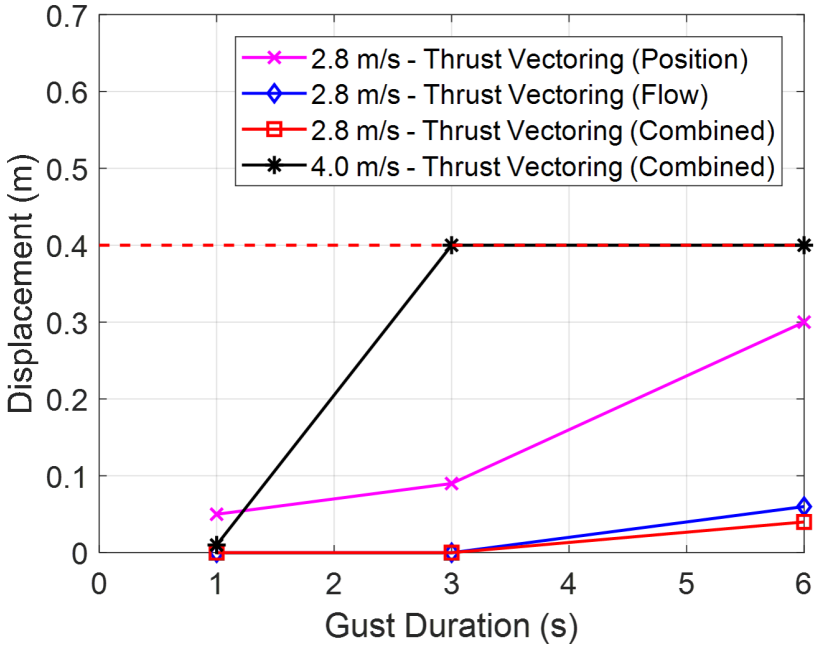

Figure 6.27: **Displacement vs. gust durations for 2.8 m/s and 4 m/s.**

output a pitching moment to overcome 10 m/s gust perturbation in pitch attitude, it was not able to recover the longitudinal translation trim using the same control strategy. Thrust vectoring resulted in reduced displacement for each gust profile and was therefore selected as the control input for the gust controller.

6.7.2 Position Feedback vs. Flow Feedback

Figure 6.27 shows resulting displacement of a gust controller using thrust vectoring control coupled with (1) position feedback, (2) flow feedback, and (3) combined position and flow feedback at both 2.8 m/s and 4 m/s step gust inputs. The results show that flow feedback is more effective than position feedback in minimizing the vehicle's response to gust. In flow feedback, the controller provides an input to negate predicted response of vehicle based on measured velocity instead of correcting

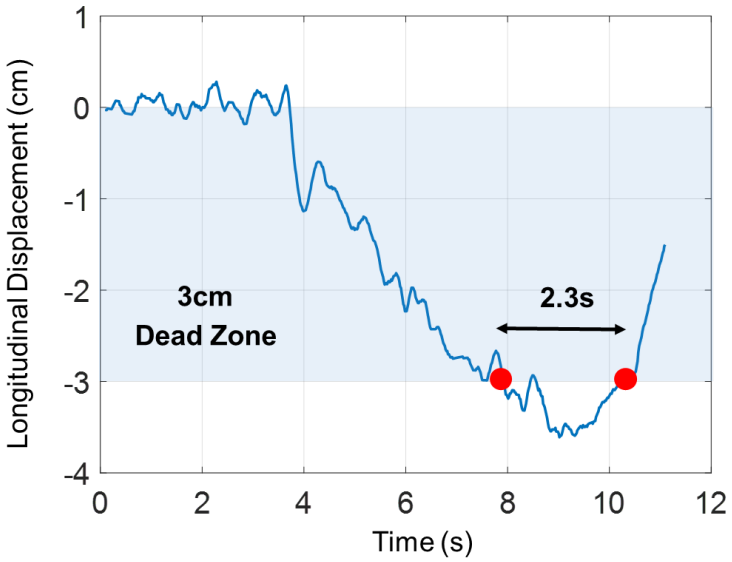

Figure 6.28: **Definition of settling time.**

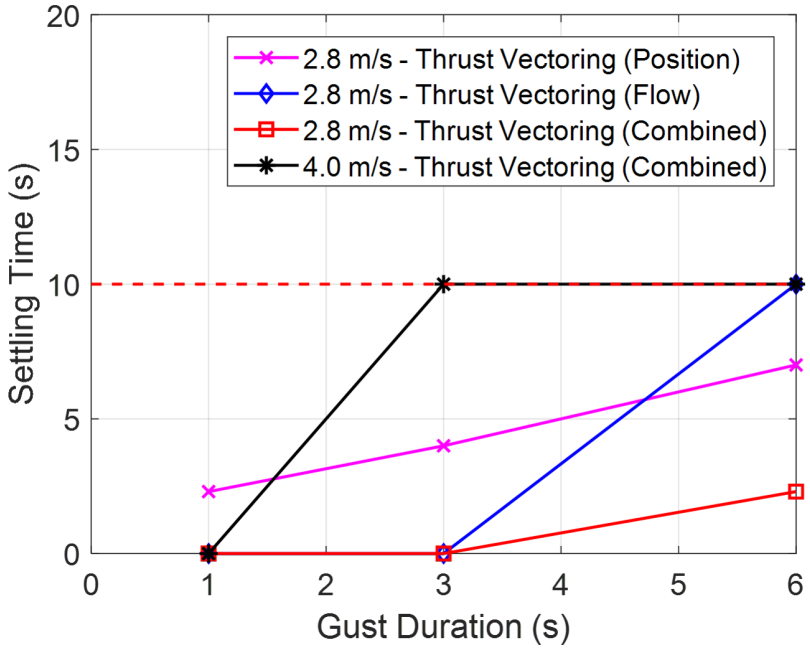

Figure 6.29: **Settling time vs. gust durations for 2.8 m/s and 4 m/s.**

after the vehicle responds to the disturbance. The combined flow feedback and position feedback controller was able to withstand 4 m/s step gust input with one second duration with only 0.01 m displacement. For 4 m/s magnitude and durations of 3 s and higher, the combined controller was unable to counteract the pitching moment due to gust and failed to recover position.

The significance of position feedback becomes evident when considering settling time. Settling time is defined as the time to recover desired position. Since the position feedback controller has a 3 cm buffer from the setpoint, settling time is only measured after the vehicle passes this point (Fig. 6.28). The buffer or dead zone prevents the gust controller from oscillating about the setpoint since the vehicle is resting on a ball bearing carriage. In addition, settling time of 10 seconds or greater was set as the time limit for the controller to recover trim. It should be noted that settling time is dependent on control system gains and is being evaluated in these experiments to highlight significance of position feedback.

Figure 6.29 shows that the combination of flow feedback and position feedback results in a lower settling time. Intuitively, the settling time result is sensible because only the position feedback controller uses displacement error in its control scheme. The intention of the flow feedback controller is to prevent any change in the vehicle's inertial state since it relies on flow measurements. If a disturbance were to effect a large displacement, the controller would not be able to recover position since the only available sensor measurement is of the flow velocity.

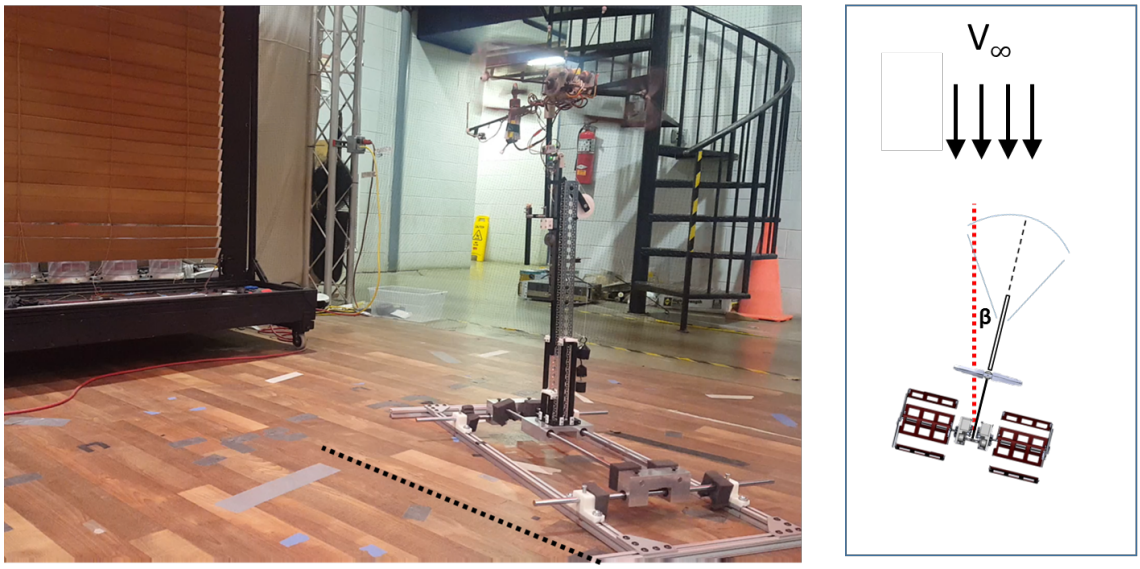

Figure 6.30: **Setup for crosswind gust scenarios ($\beta > 0$).**

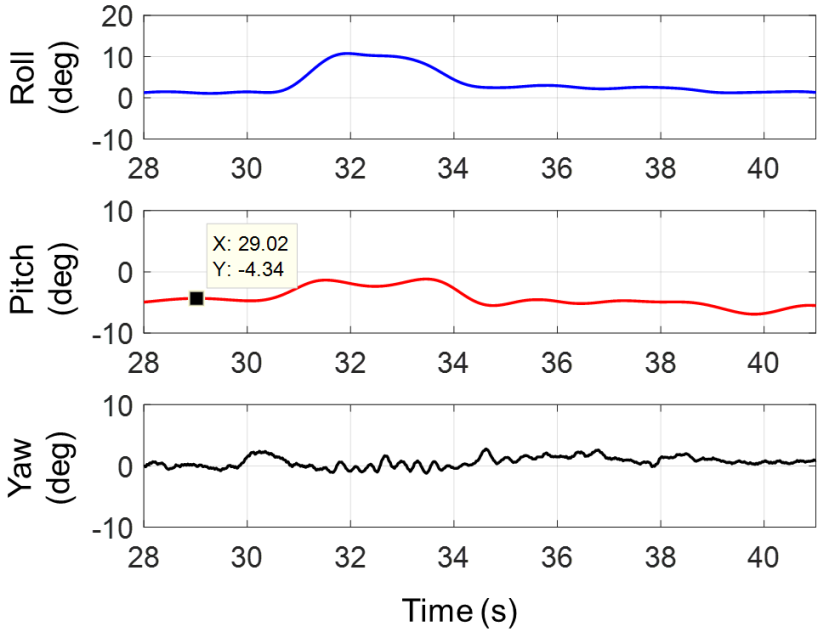

Figure 6.31: **Attitude response for step gust input at 30 degrees azimuth from longitudinal axis.**

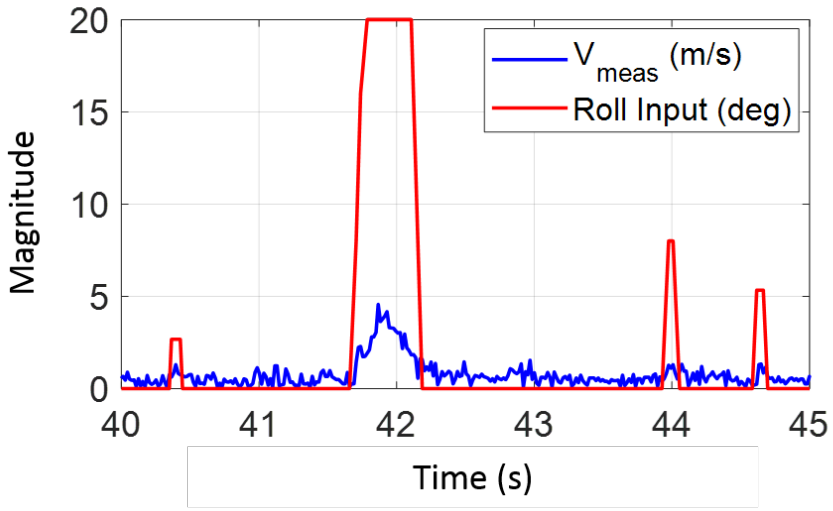

Figure 6.32: **Feedforward roll input to counteract gust effects.**

6.7.3 Crosswind Scenario

In a realistic scenario, MAVs can encounter gust perturbation from any direction in flight. Therefore, additional experiments were conducted with a gust perturbation experienced at 10, 20, and 30 degrees azimuthal variation from cyclocopters longitudinal axis (Fig. 6.30). The gust controller relied on thrust vectoring and combined flow feedback and position feedback controller in order to reduce settling time. The acceptable maximum displacement was lowered to 0.3 m to keep the vehicle within the Dyson fan test cross-section and the maximum settling time was increased to 15 seconds.

Unlike the longitudinal gust experiments where pitch response was isolated, crosswind tests affect both pitch and roll angles (Fig. 6.31). The cyclocopter responds in a roll right and pitch up reaction to a step gust perturbation. In addition

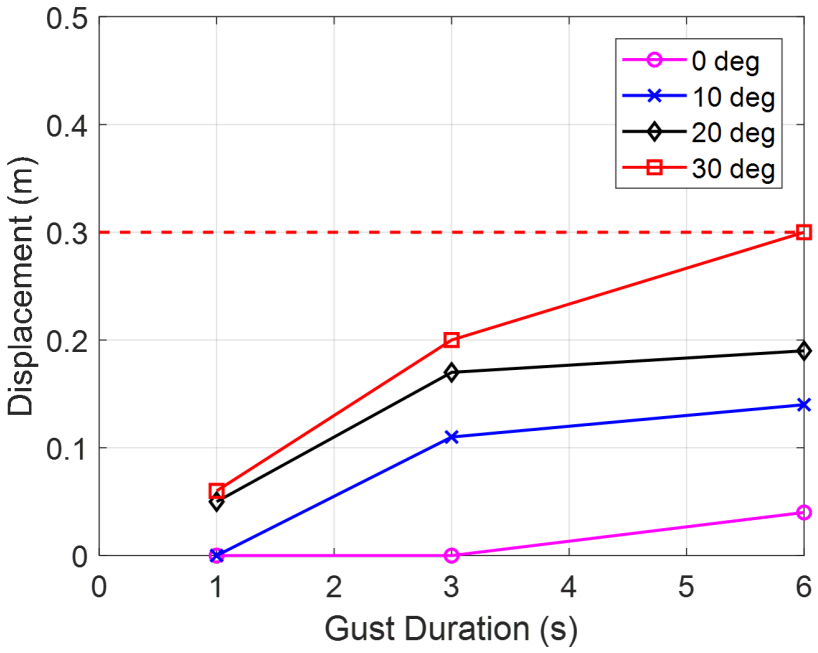

Figure 6.33: **Displacement vs. gust duration for crosswinds using combined controller.**

to the inner-loop attitude stabilization, an additional feedforward input was supplemented to the gust controller. The roll input depends on the y-component flow measurement (v_y) and uses a similar controller input calculation as discussed previously for thrust vectoring. Because the magnitude of the y-component flow measurement (v_y) is lower than the resultant velocity (V), the measurements are sensitive to noise from vibrations. Therefore the feedforward roll inputs were non-zero above a set saturation point, paralleling the step gust profiles (Fig. 6.32).

Figures 6.33 and 6.34 show that the cyclocopter was able to tolerate step gusts of 2.8 m/s in magnitude and 3 seconds duration with crosswind components at 30 degrees from the longitudinal axis. The decline in performance at higher azimuth angle can be attributed to the cyclocopter's lower control authority in roll. Similar results were observed in the 1-DOF wind tunnel experiments.

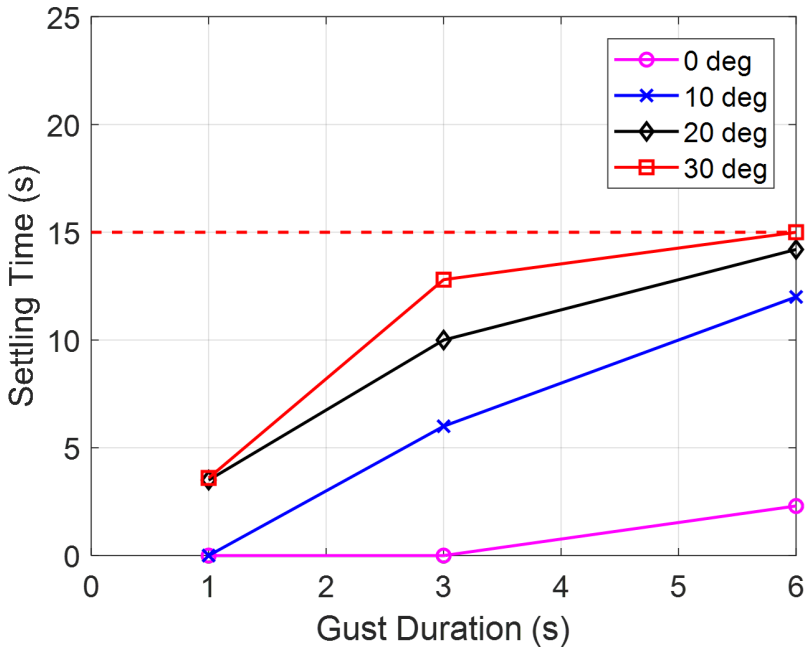

Figure 6.34: **Settling time vs. gust duration for crosswinds using combined controller.**

6.8 Summary

The gust tolerance capability of the cyclocopter was investigated through series of experiments in the wind tunnel and using a synthetic gust generation device. Both pitch control by actuating nose rotor rotational speed and thrust vectoring control were investigated. The cyclocopter was first mounted on 1-DOF experimental stand in front of an open-jet wind tunnel to evaluate response to gust perturbation along the longitudinal and lateral axis. A gust perturbation along the longitudinal axis resulted in a pitch-up moment on the cyclocopter. 1-DOF pitch stand results showed that the cyclocopter was able to withstand 10 m/s gust perturbation using pitch control. The threshold for the maximum gust perturbation was much lower along the lateral axis. 1-DOF roll stand results showed that the cyclocopter was able to

withstand up to 6.5 m/s of gust when operating at 1400 rpm before experiencing control saturation. The cyclocopter achieved roll control by differentially varying the rotational speed of both cyclorotors, which have a lower maximum achievable rpm compared to the nose rotor.

While the 1-DOF wind tunnel studies explored both longitudinal and lateral gust response, 6-DOF experiments focused on longitudinal gust response in order to evaluate effectiveness of thrust vectoring control. A synthetic gust generation device was assembled using six Dyson fans. A thorough sweep of the flow field showed that the mean freestream velocity was uniform across the 80 cm by 16.8 cm test region. The setup generated 2.8 m/s and 4 m/s gust with variance of 0.15 and a step gust profile using an automated shutter system. A gust controller with a flow feedback scheme was added to the closed-loop feedback system to augment the outer-loop PID position controller. Inputs to the gust controller included position measurements from the VICON motion capture system and flow measurements from a miniature dual-probe flow sensor.

For a step gust input along the longitudinal axis, thrust vectoring was more effective than pitch control in reducing displacement from gust. Pitch control using the position feedback controller resulted in a maximum gust tolerance of 2.8 m/s with a duration of 3 seconds while thrust vector control using the combined flow feedback and position feedback controller was able to withstand 4 m/s step gust input with one second duration with only 0.01 m displacement. The results also showed that flow feedback is more effective than position feedback in minimizing the vehicle's response to gust. While the settling time results measured effectiveness

of the gains used in the controller, the displacement results demonstrated that thrust vectoring coupled with onboard flow sensing increased gust tolerance capability of the cyclocopter.

Chapter 7: Multi-Mode Capability

7.1 Overview

The previous chapter explored potential gust tolerance benefits of the cyclocopter configuration. Another advantage is the cyclocopter's adaptability for multi-mode locomotion. Multi-mode mobility is prevalent in biological systems where organisms efficiently switch between different modes of locomotion to conserve energy, traverse long distances, and maneuver through confined spaces. Challenges include implementing unique control strategies for each mode of locomotion and overcoming the vehicle's high empty-weight fraction penalty from additional structural components required to successfully enable all three modes. The chapter initially discusses design modifications to the pitching mechanism implemented on the cyclorotor, as well as overall vehicle design specifications. Afterwards, key structural components used to enable terrestrial and aquatic modes are discussed. Finally, the developed control strategies and multi-mode testing results are presented. Results include demonstration of stable hover based on onboard attitude data from a custom auto-pilot, power consumption for all modes, and performance in terrestrial mode evaluated using a 1-DOF test rig and VICON motion capture system.

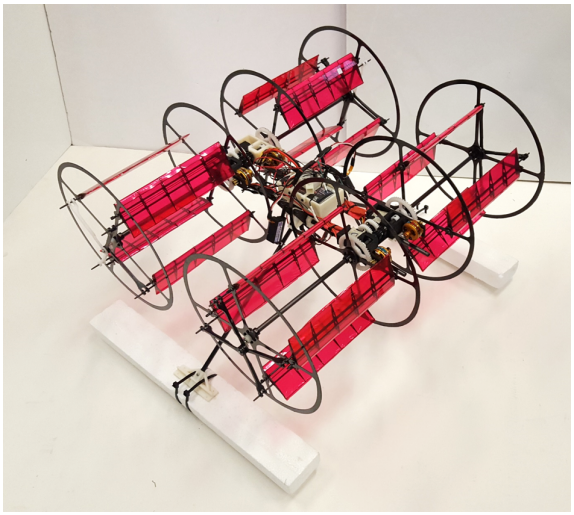

Figure 7.1: **All-terrain cyclocopter equipped with four cyclorotors.**

7.2 Vehicle Integration and Design

The all-terrain cyclocopter uses four cyclorotors configured into two pairs at the fore and aft of the vehicle (H-configuration) (Fig.7.1). Both pairs rotate in opposite directions in order to counteract the resulting torque. The vehicle spans 0.51 meters (20 inches) in width, 0.43 meters (17 inches) in length, and 0.30 meters (12 inches) in height. The all-terrain cyclocopter weighs approximately 1010 grams with the cyclorotors contributing up to 33% of the total gross take-off weight.

The cyclorotors are independently driven by a 75 W Axi out-runner motor through a 7.5:1 single-stage gear transmission. Thrust vectoring for each rotor is actuated using a rotary BMS-373MG servo that controls the blade pitching mechanism. Overall, there are eight actuators that command lift and propulsive thrust in aerial, terrestrial, and aquatic modes of locomotion. The motors are powered by a 3S 11.1V LiPo battery with 1300 mAh capacity while the servos are powered by a

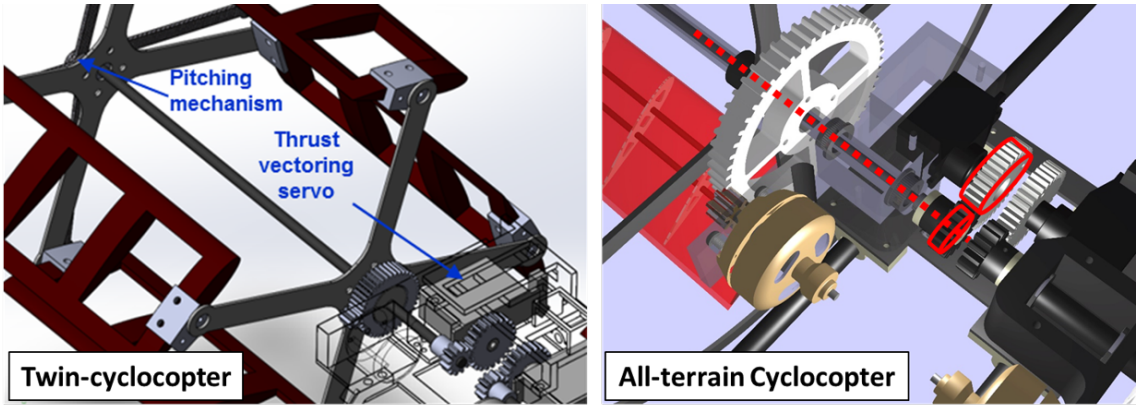

Figure 7.2: **Modified cyclorotor blade pitching mechanism for the all-terrain cyclocopter.**

single-cell 3.7 V LiPo battery with 500 mAh capacity. The following sections elaborate on cyclorotor design, additional structural components required for terrestrial and aquatic modes, and the control strategy implemented on the vehicle.

7.2.1 Cyclorotor Design

Because a cyclorotor rotates about its horizontal axis, it can be adapted into a wheel for maneuvering on ground. The vehicle can be driven directly using torque from its four motors, similar to cars with an all-wheel drive transmission. One complication with the cyclorotor design used on the twin-cyclocopter configuration is that the main rotor shaft is not connected to the gear transmission and instead connects to the blade pitching mechanism (Fig. 7.2). As a result, both endplates freely rotate and rest on ball bearings. The inner-most endplate is driven by the motor and rotates the outer endplate because of its connection through the four blades. In flight, the blade attachments points are strong enough to prevent any lag between the two endplates. In terrestrial mode, additional friction results in a noticeable lag

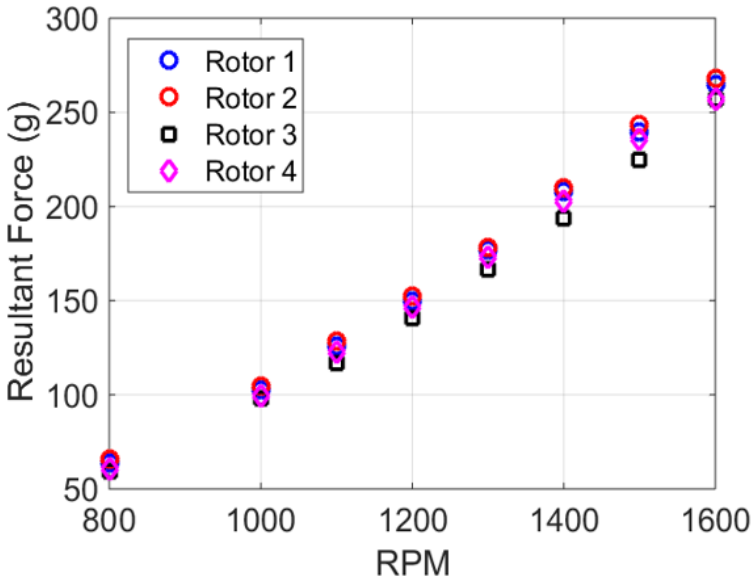

Figure 7.3: **Averaged thrust vs. RPM for cyclorotors.**

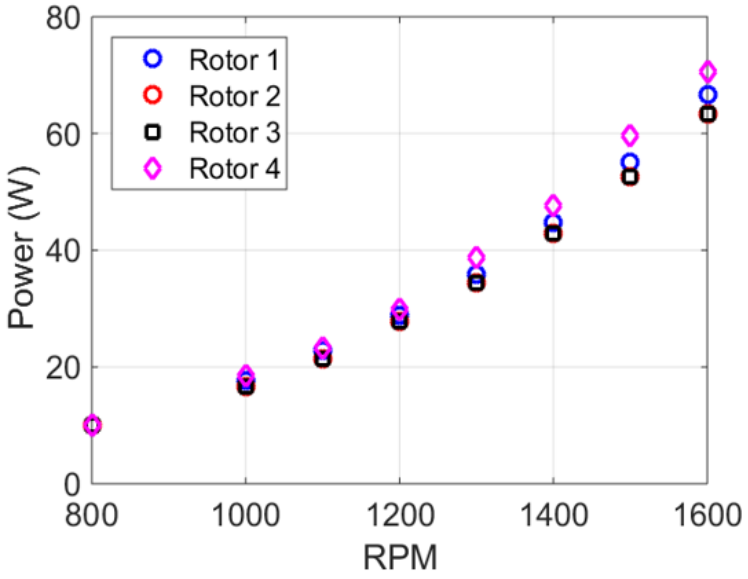

Figure 7.4: **Averaged power vs. RPM for cyclorotors.**

Table 7.1: Key cyclorotor design parameters.

Parameter	Cyclorotor
Rotor Diameter	0.152 meters (6 inches)
Blade span	0.171 meters (6.75 inches)
Blade chord	0.051 meters (2 inches)
Blade airfoil	NACA 0015
Blade pitch amplitude	$\pm 45^{\circ}$
Blade weight	5.8 grams

between the endplates, which can damage blades at the attachment points.

One solution is to combine the endplates and main shaft into one rotating body and include a separate inner-shaft that interfaces with the pitching mechanism. The all-terrain cyclocopter uses a titanium inner-shaft channeled inside the hollow carbon fiber main shaft (Fig 7.2). The titanium shaft rests on several ball bearings that enable it to freely rotate. One end of the titanium shaft is connected to the eccentric piece on the blade pitching mechanism while the other end is attached to a small spur gear. In the redesigned cyclorotor, both endplates are attached to the main shaft using a Delrin hub and are directly driven by the transmission.

As mentioned in Chapter 2, the chord/radius of 0.67 is achieved with cyclorotor radius of 0.076 m (3 in) and blade chord of 0.051 m (2 in). The blades span 0.171 m (6.75 in) and use a NACA 0015 airfoil profile and a symmetric pitching amplitude of 45°. The parameters are again summarized in Table 7.1. A linear approximation [47] shows that the virtual chamber is approximately 7% while the virtual incidence is 8°. The pitching axis locations (x/c) of the blades were centered around the chordwise center of gravity (CG) location, which resulted in x/c of 0.25. The pitching axis aligned with the chordwise location of blade CG in order to to reduce the

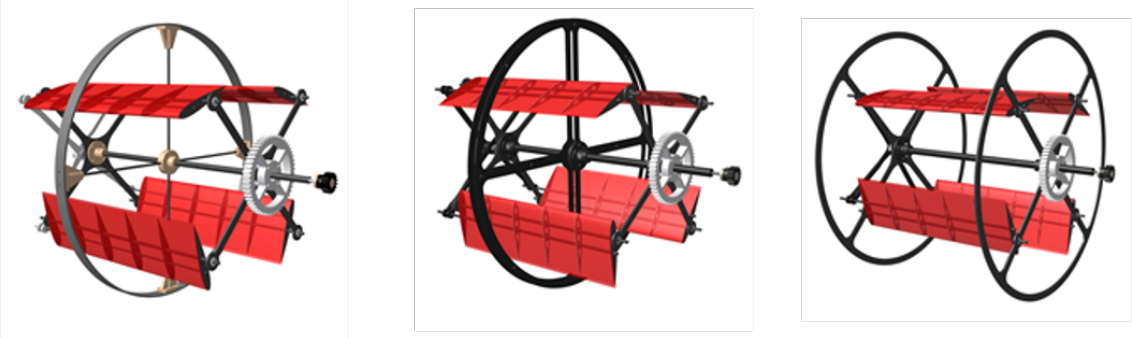

Figure 7.5: **Iterations of cyclowheel designs.**

Table 7.2: Comparison of cyclowheel designs.

Iteration	**Advantages**	**Disadvantages**
1st	Strong aluminum wheel Large surface area	Heavy (27 grams) Difficult to manufacture
2nd	Simple to manufacture	Heavy (22 grams) Reduced surface area
3rd	Lightweight (8 grams) Simple to manufacture	Reduced surface area Flexible

pitching moments on the blade caused by the centrifugal force. In addition, it reduces the loads on the pitching mechanism and ultimately on the rotary servos. Both thrust and power were systematically measured for each rotor from 800 to 1600 rpm. Figures 7.3 and 7.4 shows that each cyclorotor is able to produce 270 grams (total of 1080 grams) while drawing 65 W at the operating speed of 1600 rpm. Along with other structural components, the optimized cyclorotor weighs 83 grams and has a thrust-to-weight ratio of approximately 3.25 at 1600 rpm.

7.2.2 Cyclowheel Design

There were multiple iterations of cyclowheel design for the all-terrain cyclocopter (Fig. 7.5). The overall goal was to reduce the total cyclowheel weight and simplify the manufacturing process. Three iterations using wheel diameter of 0.23 m (9.25 in) are summarized in Table. 7.2. The initial design treated the wheel component as an independent structure attached to the main shaft. The wheel composed of a thin aluminum sheet attached to four carbon fiber spokes mounted on ABS plastic connectors. The wheel added 27 grams to the total cyclorotor weight, largely due to the 0.74 m (2.43 ft) long aluminum sheet with 0.635 cm (0.25 in) width. The weight resulted in an additional 107 grams to the overall vehicle weight. Another disadvantage of the design was the complex manufacturing process of bending the aluminum sheet in order to maintain a uniform radius.

The second iteration replaced the aluminum wheel with carbon fiber, reducing the added weight per cyclorotor to 22 grams and 88 grams to overall vehicle weight. Similar to the the first design, the wheel is still independent of the cyclorotor and is composed of two 0.79 mm (0.031 in) carbon fiber plates stacked together. The plates connect with a Delrin hub attachment on the main shaft. While it simplified the manufacturing process, the carbon fiber wheels resulted in less surface area for rubber coating. The coating improves traction and prevents the wheels from slipping on smooth surfaces.

In the final design, the wheels were efficiently integrated into the carbon fiber rotor endplates (Fig. 7.5). The diameter of the endplates was extended from 0.15

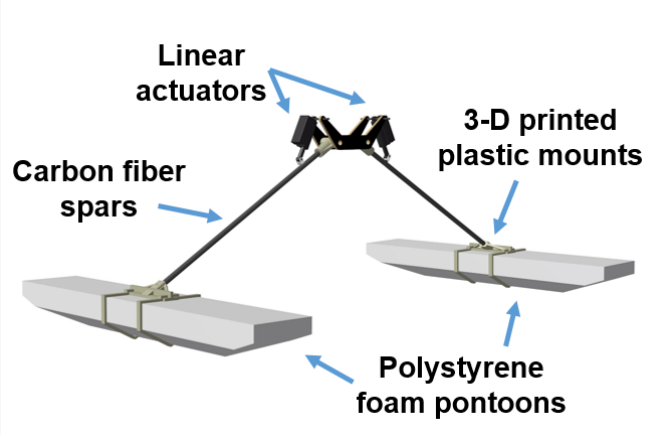

Figure 7.6: **Retractable landing gear design.**

m (6 in) to 0.23 m (9.25 in). Each cyclowheel contained two 0.8 mm (0.03 in) thick carbon fiber wheels that were rigidly attached to the main shaft. Compared to the initial design, the wheels were flexible and had reduced surface area for rubber coating. However, the integrated wheels were simple to manufacture and contributed only 8 grams to the rotor and 32 grams to the total vehicle weight.

7.2.3 Retractable Landing Gear

One of the key components of the all-terrain cyclocopter is the retractable landing gear system. Cyclorotors operate at drastically different rotational speeds for terrestrial locomotion compared to in flight. Therefore, to vertically take-off, cyclorotors need to first eliminate contact with the ground and then spool up to the operating rpm. The retractable landing gear system is driven by two Firgelli PQ-12 micro linear servos (Fig. 7.6). At full extension, the landing gear system provides up to 7 cm (2.75 in) of extension for vertical take-off and completely retracts until the wheels contact the ground. During operation, the pilot is able to retract and deploy the

Table 7.3: Weight distribution of the all-terrain cyclocopter.

System	**Weight (g)**	**% Total**
Cyclorotors	333	33
Fuselage	210	21
Transmission	152	15
Landing Gear	130	13
Batteries	115	11
Rotary Servos	45	4
Additional sensors (power logger)	20	2
Avionics	5	<1
Total	**1010 grams**	**100%**

landing gear through a switch on the transmitter. For aerial and terrestrial modes, the landing gear rests on lightweight carbon fiber spars that are attached using 3-D printed ABS mounts. Including additional carbon fiber spars along the vertical axis and carbon fiber plates used to secure the landing gear onto the vehicle's fuselage frame, the entire landing gear system weighs 100 grams.

Aquatic mode requires additional polystyrene foam pontoons mounted to the landing gear system. Pontoons provide enough buoyancy to enable the 1010 grams all-terrain cyclocopter to safely float on the surface on water. They contribute an additional 30 grams of weight to the system (total 130 grams). In order to safely operate near water, additional fuselage structures were added to shield delicate onboard electronics (avionics, battery, etc.) from exposure. Electronic speed controllers (ESCs) and connectors were also thoroughly masked with waterproof coatings.

Overall, structures required to permit terrestrial and aquatic locomotions include cyclowheels, retractable landing gear system, additional fuselage structure to

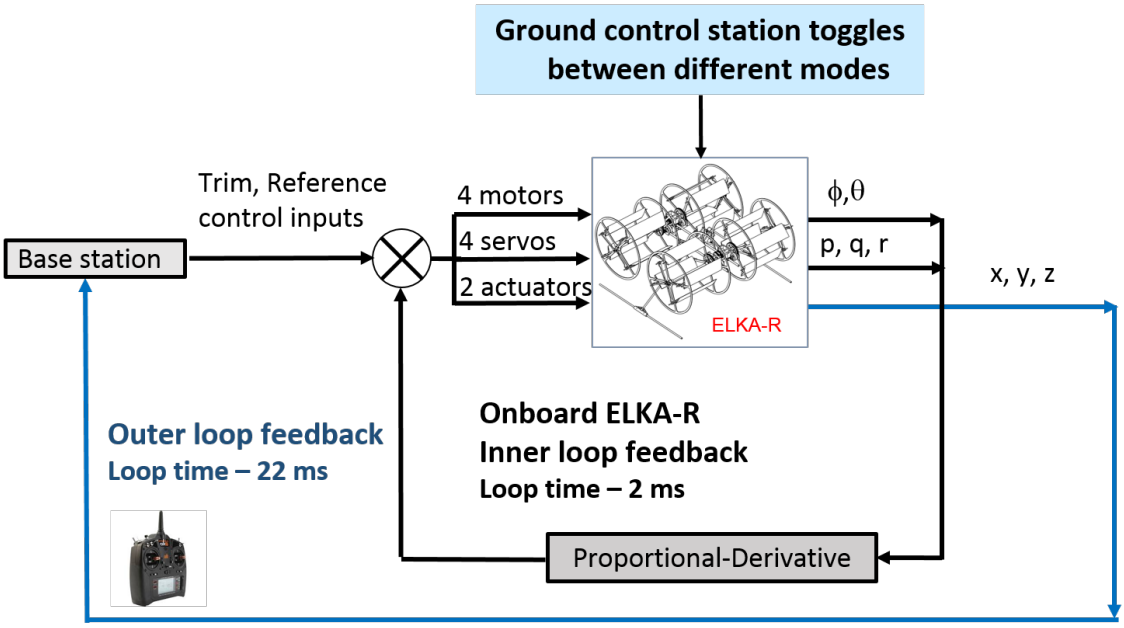

Figure 7.7: **Closed-loop feedback system for the all-terrain cyclocopter.**

shield electronics, and layers of waterproof coating for ESCs and connectors. These components contribute close to 200 grams, which account for 20% of total vehicle weight. Table 7.3 provides a weight breakdown of all the subsystems on the all-terrain cyclocopter.

7.3 Closed-loop Feedback System

The closed-loop feedback system implemented on the vehicle is similar to the scheme used by the twin-cyclocopter (Fig. 7.7). As discussed in Chapter 3, onboard attitude stabilization is implemented using ELKA-R. The inner-loop attitude stabilization uses a proportional-derivative (PD) controller, which was sufficiently able to stabilize the all-terrain cyclocopter to sustain stable hover. Inputs to the feedback are the four individual motor rotational speeds, four thrust vectoring positions of the servos,

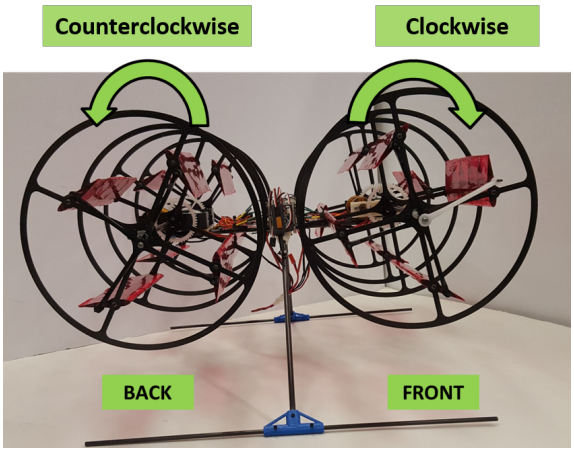

Figure 7.8: **Orientation of cyclorotors in aerial mode.**

and two inputs for the linear servos on the landing gear. The feedback states are aircraft pitch and roll Euler angles (ϕ, θ) and the attitude rates (p, q and r).

Onboard IMU data is streamed to a LabVIEW interface, which sends input to switch between different modes, permits data logging, and transmits settings for the closed-loop feedback system. All the data processing, control strategies for different locomotion modes, and feedback control calculations are performed onboard by ELKA-R. A separate connection between a commercial receiver and transmitter ensures a constant and fail-safe connection with the pilot.

7.4 Control Strategy

Aerial, terrestrial, and aquatic modes require three different control strategies that rely on combinations of motor torque and thrust vectoring. In aerial mode, cyclorotor rotational speeds and thrust vectors are individually modulated to sustain stable hover. A similar control strategy relying on aerodynamic forces generated by

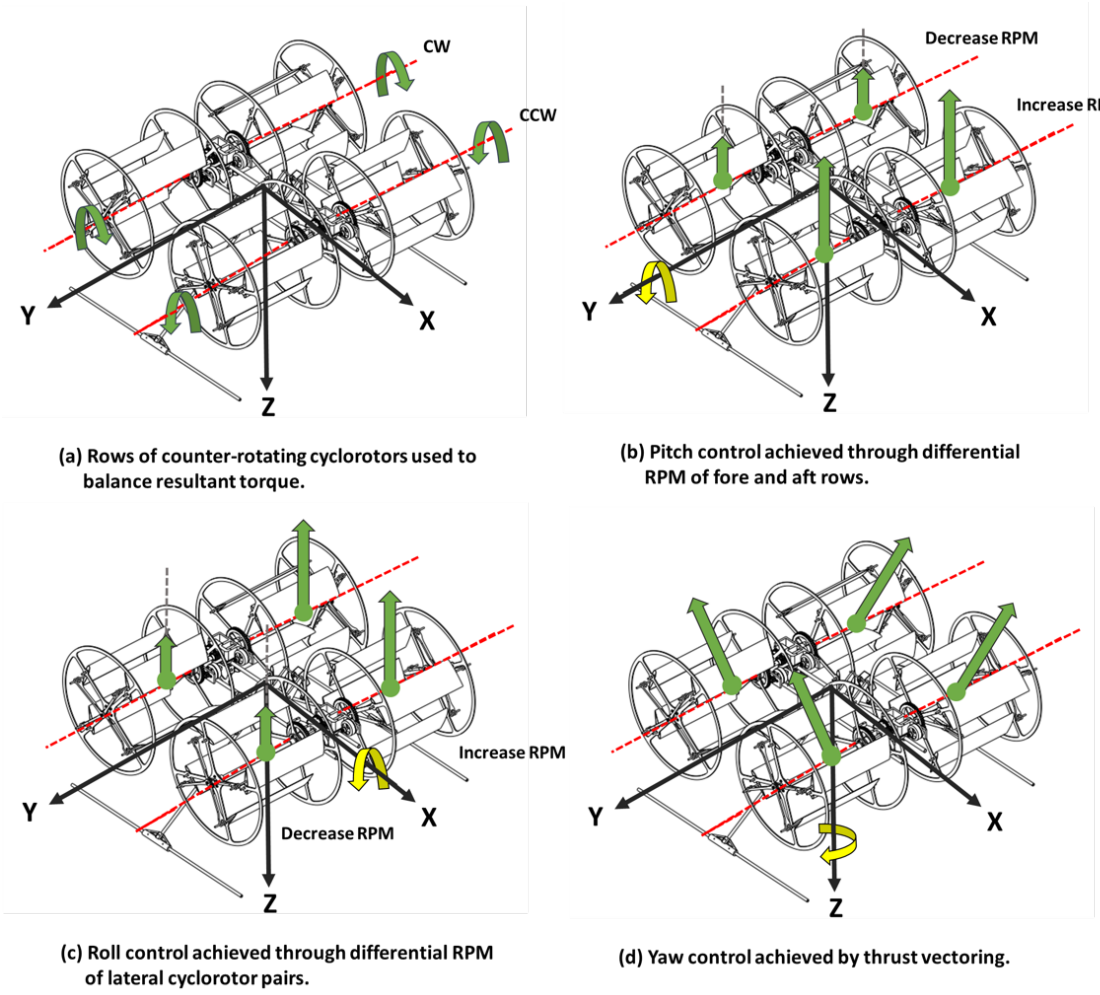

Figure 7.9: **Control strategy for aerial mode.**

cyclorotors was also implemented for aquatic locomotion while terrestrial locomotion only uses motor torque. Actuator controls mixing of all operational modes is performed onboard the flight controller while the desired mode is selected through the ground control station.

7.4.1 Aerial Mode

As previously mentioned, the fore and aft pairs of cyclorotors spin in opposite directions to counterbalance the resulting torque. On the current vehicle, cyclorotors spin outwards such that the front pair rotates clockwise along the +Y-axis while the back rotates counterclockwise (Fig. 7.8). The orientation of the rotors was selected by considering the pitch control strategy for aerial mode and the resulting torque. Figure 7.9 provides an overview of the control strategy used in hover. Pitch control is provided by modulating the rpm of the fore and aft pairs of cyclorotor 7.9(a). For a pitch down input, the rotational speed of the front rotors decreases while the back increases. The resulting torque induces a beneficial pitch down reaction moment. If the orientations were reversed, the reaction moment would oppose the initial pitching moment.

Furthermore, roll control is achieved by differentially varying rotational speeds of the side pairs 7.9(b) and yaw control is possible by differentially rotating the thrust vectors of the side pairs 7.9(c). An advantage of the quad-cyclocopter configuration over the twin-cyclocopter is decoupled dynamics. Since the angular momentum of cyclorotors are balanced, the vehicle is unaffected by gyroscopic coupling. Therefore, mixing actuator inputs between the operational modes only involves disabling the feedback control system and reversing the front pair of cyclorotors in terrestrial mode. Chapter 4 provides additional information about the roll-yaw cross coupling.

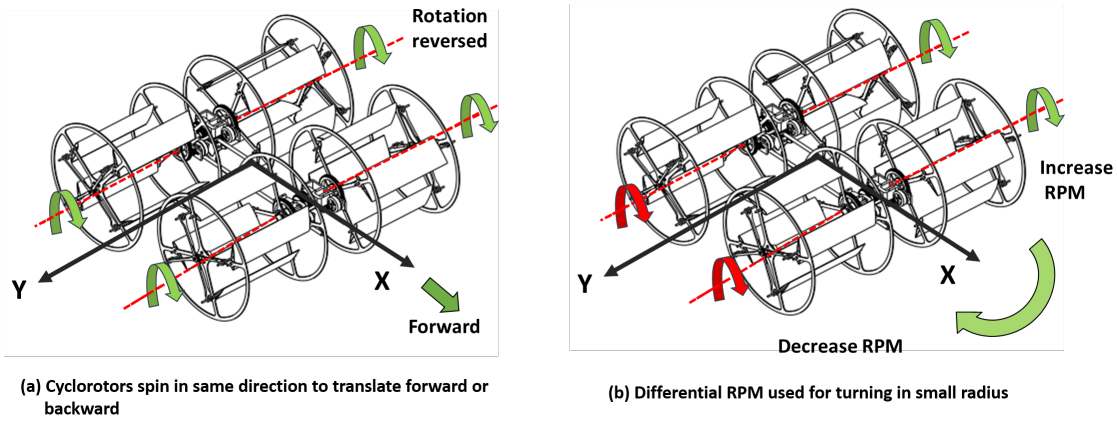

(a) Cyclorotors spin in same direction to translate forward or backward

(b) Differential RPM used for turning in small radius

Figure 7.10: **Control strategy for terrestrial mode.**

7.4.2 Terrestrial Mode

Complications of switching between aerial and terrestrial modes is that the direction of rotation of two cyclorotors must be reversed so that the rotors do not oppose the resulting translational motion. One possible solution is to simply rely on a two-wheel drive system such that only a single pair of cyclorotors would be powered. This strategy would result in unnecessary power consumption since the cyclorotors would have to operate at a higher rotational speed in order to support the other cyclorotors.

An alternative solution is using programmable electronic speed controllers (ESCs) that can electronically reverse the direction of the motors based on transmitter input. The all-terrain cyclocopter uses four Afro 12A multi-rotor ESCs re-programmed with a reversible motor setting. The direction of rotation of two cyclorotors is reversed when the throttle input is below the adjustable neutral throttle point. Since the throttle setting differs between the pairs of cyclorotors, appropriate adjustments to the transmitter throttle stick input and trim settings have been ap-

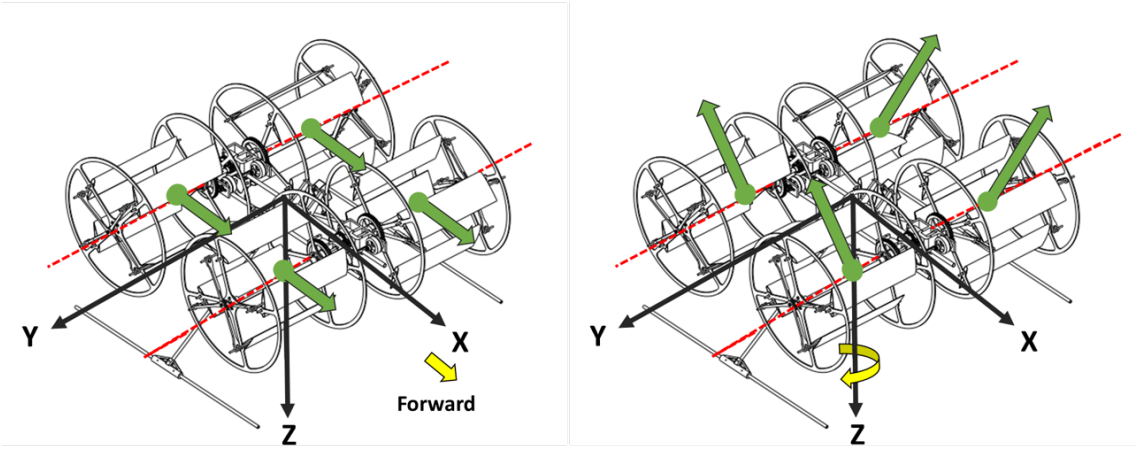

(a) Forward and backward translation via thrust vectoring. (b) Yaw control achieved by differential thrust vectoring.

Figure 7.11: **Control strategy for aquatic mode.**

plied through the flight controller so that rotors initialize and operate on the same throttle curve.

The all-terrain cyclocopter can effectively function as both two-wheel and all-wheel drive system in terrestrial mode. To translate forward, the direction of rotation of the aft pair of cyclorotors is reversed so that all cyclorotors spin clockwise about the +Y-axis (Fig. 7.10). However, backward translation is only achieved by powering the aft pair in its aerial mode configuration (counterclockwise rotation about +Y-axis). Differentially varying the rotational speeds of the side pairs enables the vehicle to turn with a small radius.

7.4.3 Aquatic Mode

In aquatic mode, the all-terrain cyclocopter relies on propulsive thrust generated by thrust vectoring the cyclorotors. For a constant throttle input, collectively thrust vectoring the cyclorotors either forward or backward results in translation in the

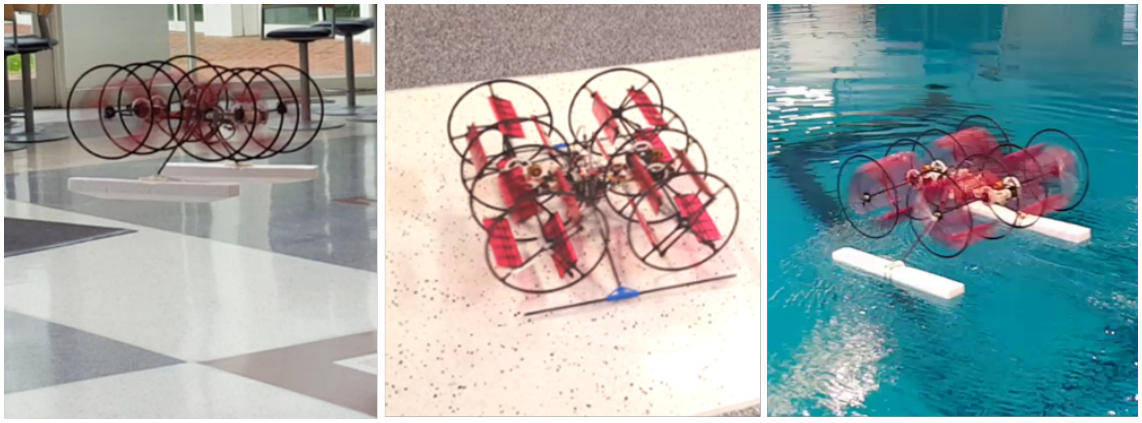

Figure 7.12: **Demonstration of aerial, terrestrial, and aquatic modes.**

Table 7.4: Performance of the all-terrain cyclocopter.

Mode	Maneuver	Speed (m/s)	Average RPM	Power Required (W)
Aerial	Hover	0	1550	232
Aquatic	Translation	1.3	348	19
Terrestrial	Translation	2	83	28

same direction (Fig. 7.11). Translational velocity can be increased by either increasing the throttle input or further rotating the thrust vector. The thrust vectors on the current vehicle can be rotated up to $\pm 60^{\circ}$ from the vertical axis. Similar to the terrestrial mode, the vehicle is unable to translate laterally and instead must change its orientation. The yaw control strategy uses differential thrust vectoring of the side pairs, which is the same strategy used in flight.

7.5 Multi-Mode Testing Results

The all-terrain cyclocopter was first systematically tested in each mode and then in hybrid aerial and terrestrial mode where the vehicle transitioned using the landing gear system. Figure 7.12 shows video stills of the vehicle successfully achieving all

three modes of locomotion. The following sections discuss performance in each mode with accompanying sensor measurements from the onboard autopilot, commercial power logger, and motion capture system. Performance results are summarized in Table 7.4.

7.5.1 Aerial Mode

Prior to flight testing, initial gains and trim settings for hover were obtained through bench-top experiments. The vehicle was mounted on a 3-DOF gimbal stand, which allowed up to $\pm 20^{\circ}$ of rotation in pitch, roll, and yaw. Gimbal testing demonstrated that the all-terrain cyclocopter's dynamics, such as gyroscopic interactions, are decoupled unlike for its twin-cyclocopter counterpart. This is due to the inherent symmetry of the vehicle about an axis parallel to the rotation axis of each cyclorotor. Therefore, no additional modifications or actuator mixing was implemented onboard the flight controller.

Flight tests were systematically conducted by first providing a pure throttle command and observing the vehicle response. Any forward translation was counteracted by either reducing the phasing of the cyclic blade pitch or varying the motor rpm. Slight inconsistencies during rotor assembly resulted in variations of operating rotational speed of the cyclorotors. Therefore, individual rpm settings were applied for each cyclorotor by adjusting pitch and roll trims. Proportional and derivative gains were fine-tuned using the Ziegler-Nichols approach. The gains that offered acceptable stiffness and damping to reject external disturbance with minimal oscil-

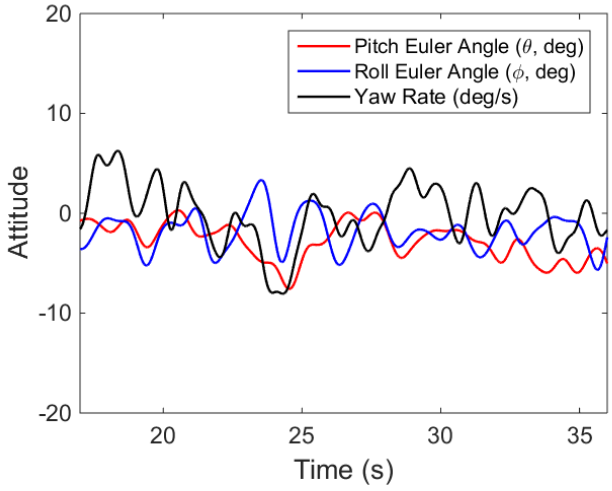

Figure 7.13: **Onboard attitude data streamed from ELKA-R during hover.**

lations were selected. Gains and control inputs for trimmed flight varied slightly from the ones obtained through gimbal testing because the gimbal setup provided additional damping along each rotation axis.

The all-terrain cyclocopter successfully demonstrated stable hover (Fig. 7.12). As seen from Fig. 7.13, a sustained hover was obtained with pitch and roll angles held close to zero with minimum fluctuations from the desired yaw rate. Power measurements recorded by a commercial Eagle Tree Systems eLogger showed that the vehicle requires 232 W to sustain hover while operating at 1550 rpm. When the vehicle is at idle, onboard microelectronics (servos, avionics, power logger, etc.) draw approximately 4.3 W (Fig. 7.14). At full extension, the landing gear system draws an additional 4 W because it supports the entire vehicle weight.

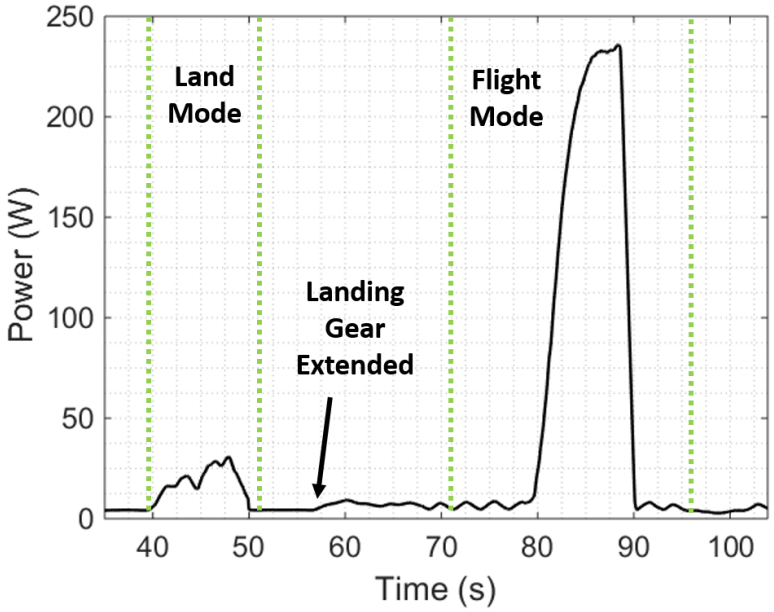

Figure 7.14: **Power required for terrestrial and aerial modes.**

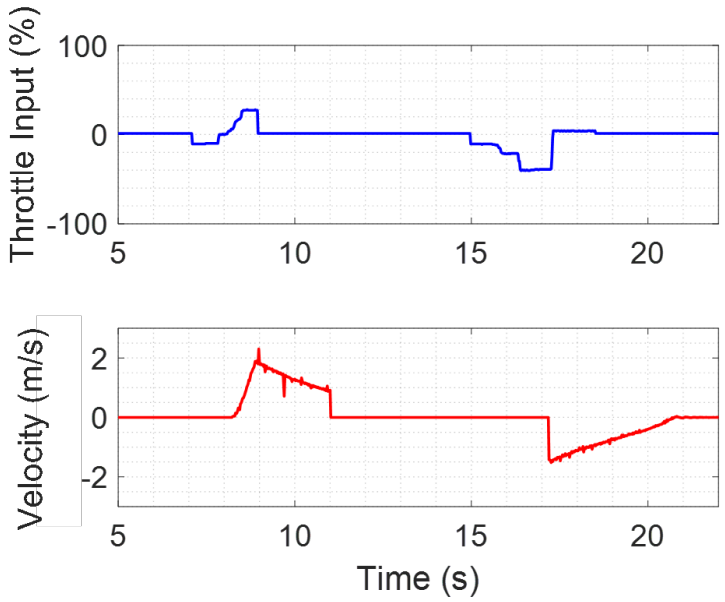

Figure 7.15: **Input required for forward and backward translation in terrestrial mode.**

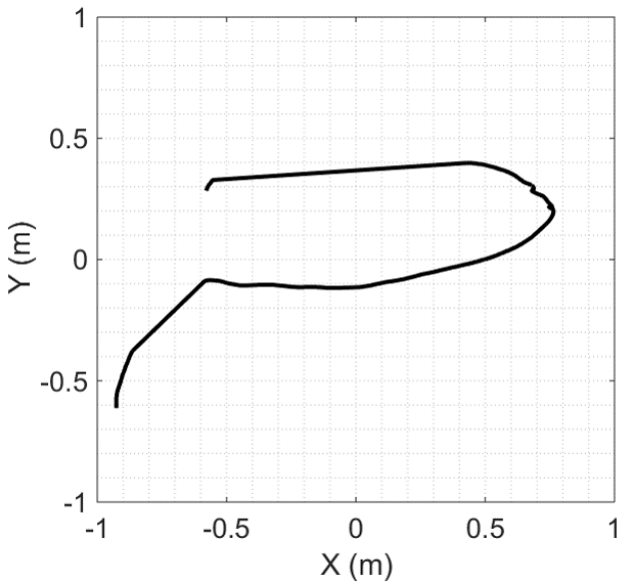

Figure 7.16: **Minimum turn radius for terrestrial locomotion.**

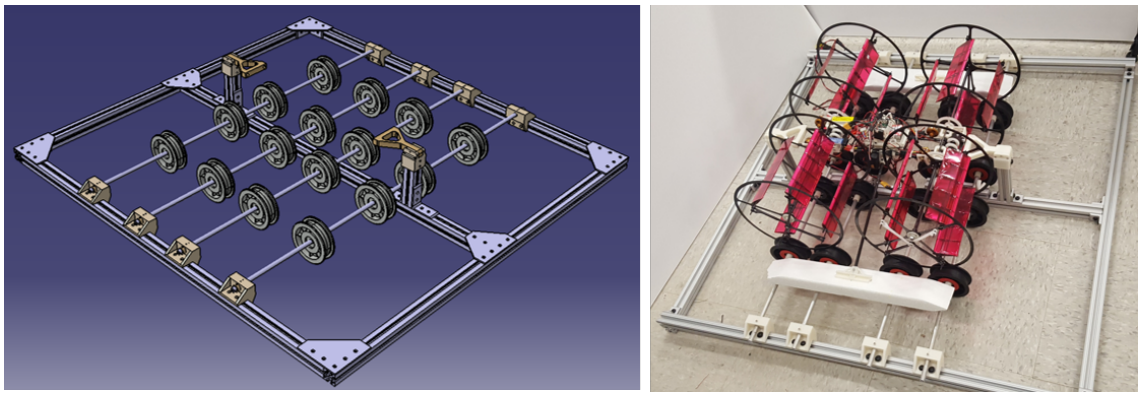

Figure 7.17: **Experimental setup to evaluate maximum ground speed.**

7.5.2 Terrestrial Mode

Switching into terrestrial or aquatic modes requires additional mode selection through the ground control station. In addition, extraction and retraction inputs for the landing gear are manually provided by the pilot either through the transmitter or the ground control station. With the current setup, seamless transition between aerial and terrestrial modes is accomplished within 5 seconds. Compared to hover, forward translation in terrestrial mode requires 28 W, which is a 88% reduction in power consumption (Fig. 7.14). Because terrestrial locomotion is directly controlled using motor torque, the vehicle is able to operate at a reduced rpm. This significant reduction in power can result in increased endurance and range.

Position and velocity measurements of terrestrial locomotion were recorded using the VICON Motion Capture System. The setup consists of eight high speed infrared cameras that track the retro-reflective markers placed on the vehicle. These infrared cameras capture the translational and rotational states of the vehicle at a frequency of 100 Hz and triangulate the location of the markers inertially within the three-dimensional test volume. A throttle stick input of 27% results in forward translation of 2 m/s (Fig. 7.15). In the rpm subfigure, negative throttle input corresponds to the reversal in cyclowheel rotation. When translating backwards, the all-terrain cyclocopter functions as a two-wheel drive system, as opposed to all-wheel drive, and only relies on the aft pair of cyclowheels. As a result, cyclowheels must operate at a higher rpm with a throttle stick input of 38% to translate backwards at 1.5 m/s. VICON experiments also shows that using differential rpm control to

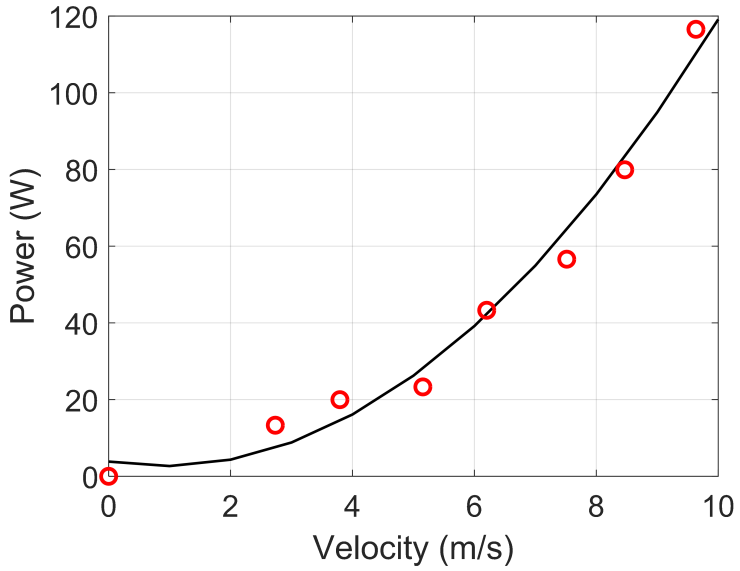

Figure 7.18: **Power vs. velocity in terrestrial mode.**

change direction of orientation results in a minimum turn radius of 0.2 m (Fig. 7.16).

An experimental setup using rotating pulleys was designed to evaluate the minimum load (no wind resistance and low friction) achievable rpm or ground speed for the all-terrain cyclocopter (Fig. 7.17). Each cyclowheel rested on four pulleys with ball bearing mounts attached to aluminum shafts. The vehicle was suspended in place using 3-D printed mounts connecting to the fore and aft spars of the fuselage. The setup enabled the vehicle to freely rotate its wheels while remaining stationary. During testing, a constant voltage of 11.1 V, equivalent to the 3S LiPo battery onboard the vehicle, was provided using an external power supply. The power supply also displayed the current drawn, which was used to calculate total power consumption. Velocity was measured using an external laser tachometer. Finally, vehicle trim was adjusted such that the cyclorotors maintained similar rotational speeds.

Under minimum load conditions (no wind resistance and low friction), the all-terrain cyclocopter demonstrated ground speed of approximately 10 m/s (22 mph) while consuming 116 W of power (Fig. 7.18). Testing on the experimental setup was limited because of significant vibrations causing the cyclowheels to lose contact with the pulleys. To prevent the vehicle from taking off, phase angles were rotated to 90 degrees so that they were parallel to the horizontal axis. At 10 m/s (22 mph), the cyclorotors operated at approximately 1000 rpm. Compared to aerial mode, the cyclowheels consumed more power (factor of 2.9) at 800 rpm because of additional friction forces from contacting the pulleys.

7.5.3 Aquatic Mode

Translational velocity in aquatic mode can be varied using the throttle input or further rotating the thrust vector to increase propulsive thrust. The vehicle was tested on calm water to demonstrate maneuvering capability. By increasing the rotational speed to 348 rpm, the vehicle achieved 1.3 m/s in forward translation. The maneuver consumed 19 W, which is only 8% of the total power required to hover.

7.6 Summary

The chapter provided an overview of the development of an all-terrain cyclocopter capable of aerial, terrestrial, and aquatic locomotion with seamless transition between the modes. Unlike existing multi-modal quadcopter platforms, the all-terrain

cyclocopter solely relied on its four cyclorotors as source of propulsion, as well as wheels. Structures required to permit terrestrial and aquatic locomotions included wheels, retractable landing gear system, additional fuselage structure to shield electronics, and layers of waterproof coating. These components contributed close to 200 grams, which accounted for 20% of total vehicle weight.

The all-terrain cyclocopter weighing 1010 grams successfully demonstrated sustained hover, translation and rotational maneuvers on ground, and aquatic locomotion. Control strategy for each mode relied on combinations of motor torque and thrust vectoring. Cyclorotor rotational speeds and thrust vectors were individually modulated to sustain stable hover. A similar control strategy relying on aerodynamic forces generated by cyclorotors was also implemented for aquatic locomotion. Because cyclorotors rotate about the horizontal axis, wheels were efficiently integrated into the carbon fiber rotor endplates and terrestrial locomotion was commanded directly by motor torque.

In aerial mode, the cyclorotors operated at 1550 rpm and consumed 232 W to sustain hover. Each optimized cyclorotor weighed 83 grams and contributed up to 33% of total gross take-off weight. At the operating rotational speed, each optimized cyclorotor produced 270 grams of lift, which resulted in thrust-to-weight ratio of approximately 3.25. Forward translation of 2 m/s in terrestrial mode required 28 W, which was a 88% reduction in power consumption required to hover. Using a pulley-based experimental setup, the cyclocopter demonstrated ground speed of 10 m/s (22 mph) under minimum load conditions (no wind resistance and low friction). Motion capture measurements also showed that using differential rpm control to change

direction of orientation resulted in a minimum turn radius of 0.2 m. Translational velocity in aquatic mode can be varied using the throttle input or further rotating the thrust vector. In aquatic mode, cyclorotors operated at 348 rpm and consumed 19 W in order to translate forward at 1.3 m/s.

Chapter 8: Conclusion and Future Work

8.1 Overview

Growing interest in highly portable versatile flying platforms and recent advancements in microelectronics led to the development of a scaled-down class of Unmanned Aerial Vehicles (UAVs) known as Micro Air Vehicles (MAVs). Applications include agricultural monitoring, search and rescue (disaster relief), package delivery, aerial photography, and infrastructure inspection. For many mission scenarios, high endurance, maneuverability, and the ability to tolerate and overcome environmental disturbances such as wind gusts are critical requirements for MAVs. Designing the next generation micro air vehicle that is also aerodynamically efficient and capable of vertical take-off and landing (VTOL), high speed forward flight, and multi-mode locomotion involves overcoming an array of technical challenges further exacerbated at the MAV-scale.

Compared to their full-scale counterparts, MAVs experience degraded performance of conventional airfoils at the low Reynolds number range (10,000 – 50,000) at which these vehicles operate. Reduced aerodynamic efficiency of blades at the MAV-scale is caused by high viscous forces, which leads to increased boundary layer thickness, increased profile drag, and large induced losses. Aside from aerodynamic

considerations, MAVs are also constrained by size, weight, and power (SWaP) requirements. Increasing endurance and range capability largely depends on efficiency of the propulsion system and the overall size and weight of the vehicle. However, selection of avionics, batteries, and onboard electronics for the transmission system is severely limited by commercial availability. While reduced size and weight of MAVs provide operational benefits, the resulting low inertia coupled with limited aerodynamic damping contributes to degrading flight stability and control performance. Compared to full-scale vehicles, MAVs typically have higher thrust-to-inertia ratios that result in increased control sensitivity. MAVs are also highly susceptible to environmental disturbances such as gusts due to their low inertia and low operational speeds.

The current research investigated performance of the twin-cyclocopter and quad-cyclocopter configurations. The twin-cyclocopter configuration used two cyclorotors and a smaller horizontal edge-wise nose rotor to counteract the torque produced by the cyclorotors. The all-terrain cyclocopter relied on four cyclorotors oriented in an H-configuration. Control strategies were developed for the twin-cyclocopter in hover and forward flight. Roll-yaw cross-couplings resulting from gyroscopic coupling and controls coupling were also discussed in details. Results from wind tunnel studies conducted using a 5-DOF experimental stand were used to develop a control strategy to achieve decoupled dynamics. Furthermore, effects of free-stream velocity, rotational speed, and phasing angle on the roll-yaw cross-couplings were closely investigated and used to determine control inputs to achieve zero pitch attitude at various airspeed. In addition, a linear 6-DOF flight dynamics

model of the twin-cyclocopter in forward flight was experimentally determined using time-domain system identification technique. The existence of the longitudinal control derivative in translation mode was used to evaluate the control authority of thrust vectoring to command forward speed. The model was also used to identify sources of roll-yaw cross-coupling.

Moreover, disturbance rejection capability of the cyclocopter was investigated through series of experiments in the wind tunnel and using a synthetic gust generation device. Disturbance rejection strategies compared control authorities of pitch control versus thrust vectoring and feedback control schemes of position feedback versus flow feedback. Furthermore, key structural components used to enable aerial, terrestrial, and aquatic modes of locomotion were explored for the all-terrain cyclocopter. Design modifications and control strategies for each mode were developed. Results included onboard attitude data from a custom auto-pilot, power consumption for all modes, and performance in terrestrial mode evaluated using a 1-DOF test rig and VICON motion capture system.

The experimental studies in forward flight, gust tolerance, and multi-mode capability provided a foundation to guide additional work towards improving cyclocopter performance across all flight modes.

8.2 Conclusions

The following are specific conclusions from this work.

8.2.1 Vehicle Development

1. The 550 g twin-cyclocopter relied on two cyclorotors as main source of propulsion and an additional horizontal anti-torque nose rotor. The vehicle had a lateral dimension of 0.381 meters (1.25 feet), longitudinal dimension of 0.457 meters (1.5 feet), and a height of 0.305 meters (1 foot). Each cyclorotor had a diameter of 0.152 meters (6 inches), blade span of 0.171 meters (6.75 inches), and a chord of 0.051 meters (2 inches). In addition, the nose rotor used a three-bladed 9050 propeller with a 0.229 m diameter (9 inches).

2. Each rotor was independently driven by a motor and two additional rotary servos were used to provide thrust vectoring capability for the cyclorotors. Thrust vectoring capability was enabled using a pitching mechanism that cyclically varied individual blade pitch angle along a circular trajectory. The direction of the thrust vector is manipulated by rotating a key component of the mechanism, which changes the phasing of the harmonic pitching schedule.

3. Since the cyclorotors comprised a significant portion (23-34%) of the empty weight fraction of the vehicle, its blades were designed to be lightweight with high bending and torsional stiffness. Selection of key aerodynamic blade parameters such as blade pitching amplitude, location of pitch axis, rotor radius, blade airfoil, chord, span, and planform were based on previous empirical studies. Each blade uses a symmetric pitching amplitude of 45°, pitch axis 45% from leading edge, rotor radius of 7.6 cm (3 in), chord/radius of 0.625, span of

17.1 cm (6.75 in), and a NACA 0015 airfoil.The direction of the thrust vector can be manipulated by rotating the offset link, which changes the phasing of the harmonic pitching schedule

4. The blades on the cyclorotor experience a virtual camber effect because of the curvilinear nature of the flow, which introduces a chordwise variation in velocity. A symmetric airfoil at 0° pitch behaves as a virtually cambered airfoil at a virtual incidence in a rectilinear flow. A linear approximation shows that the virtual camber for the selected blade parameters is 3.5% of chord and virtual incidence is 5°.

5. Cyclorotors using Mylar wrapped monolithic blades and multi-Component rib-spar blades were tested. Both cyclorotors produced 270 grams of thrust at 1600 rpm, achieving a thrust-to-weight (T/W) ratio of approximately 10. Slight variation of power consumption was observed between the two designs because of differences in parasitic drag due to blade construction. At the operational rpm, the monolithic blade design consumed 71 watts of electrical power while the rib-spar design consumed 67 watts, resulting in a 18% increase in power loading. Overall, both blade designs were implemented on the final cyclocopter.

8.2.2 Flight Control Strategy

1. Flight control strategy for the cyclocopter used a combination of independent pitch phasing and rotational speed control of the two cyclorotors, along with

the propeller system, without relying on any additional control by means of a traditional empennage system.

2. While the strategy facilitated power-efficient level forward flight, it was accompanied by a strong yaw-roll control cross-coupling. These were in addition to the gyroscopic couplings that are experienced even in hover. Existence of controls coupling in forward flight was attributed to increased magnitude of propulsive forces at high phase angles. As a result, thrust vectoring had a larger impact on roll moments and subsequently, changes in cyclorotor rotational speeds had a greater influence on yaw moments.

3. Decoupling the roll and yaw degrees of freedom in forward flight involved mixing the roll and yaw inputs of both the pilot and the feedback system. Wind tunnel studies showed that the mixing ratio was dependent on phasing of the blade cyclic pitch, especially at high phase angles. If a positive roll input was accompanied by a negative yaw (counterclockwise), it would negate the effects of the rpm on yaw and result in a pure roll output. Likewise, a positive yaw input paired with a positive roll input resulted in a pure yaw output.

4. Both the gyroscopic and control couplings induced the same positive roll response for a positive yaw input. However, for a positive roll input, gyroscopic coupling induced a negative yaw (counterclockwise) response while the control coupling led to a positive yaw (clockwise) response.

5. The capability to control forward flight speed using only thrust vectoring

(phasing of the cyclic pitch) was successfully demonstrated up to 5 m/s. The rate of transition from hover to forward flight entirely depended on the magnitude of phasing input. Flight tests demonstrated that the cyclocopter was able to immediately halt to hover from 5 m/s flight. In addition, the cyclocopter achieved the desired airspeed within a second after a given phasing input.

8.2.3 System Identification in Forward Flight

1. A linear 6-DOF flight dynamics model in forward flight was developed using system identification techniques. The flight dynamics model was extracted using the time-domain approach from SIDPAC system identification tools. The model was based on measurements from doublet inputs across various modes. The model structure was initially identified using stepwise regression and the parameters were estimated using the equation-error method. All maneuver inputs were provided after the cyclocopter achieved a steady state of 2 m/s flight at a steady, level attitude (θ, ϕ, ψ=0).

2. The existence of the control derivative, X_{phase} showed that phasing input commanded forward speed. From flight tests, it was observed that increasing the phasing with a δ_{phase} step input directly resulted in a step change in velocity. During the acceleration phase, the initial response was large and acceleration decreased with time until the vehicle reached steady state after two seconds. When the phase input was removed, the flight speed returned to the original forward velocity at the same rate.

3. The negative longitudinal translation derivative, X_u indicated positive aerodynamic damping. Therefore, the vehicle was able to stabilize a velocity perturbation in the longitudinal direction. However, the aerodynamic pitch damping (M_q) was non-existent and the vehicle required feedback damping to stabilize the pitch attitude rate. In general, the longitudinal mode was decoupled and independent of the rest of the modes.

4. The longitudinal coupling term, M_u was stabilizing. A perturbation that increased the longitudinal velocity would induce a nose-up pitching moment. The positive pitching moment would further decrease the forward velocity, stabilizing the cyclocopter.

5. The lateral translation derivative, Y_v was also stabilizing. However, the lateral and yaw coupling terms, L_v and N_v were unstable. In forward flight, a velocity perturbation would induce both roll and yaw responses. Based on Y_r, a clockwise yaw resulted in a translation to the right, further destabilizing the vehicle. In addition, both L_p and N_r were unstable.

6. The model was able to validate the existence of the inherent roll-yaw coupling in forward flight, which was identified by contributions of L_r and L_{rud} to the lateral state and N_p and N_{lat} to the yaw state. These are the result of combined gyroscopic coupling and controls coupling at high phase angles.

7. The gyroscopic coupling is caused by the unbalanced angular momentum from the cyclorotors spinning in the same direction. The controls coupling is due to

the increase of magnitude of propulsive forces at high phase angles. As a result, thrust vectoring has a larger impact on the roll moments and subsequently, changes in rotor RPM have a greater influence on yaw moments.

8.2.4 Gust Rejection Study

1. The gust tolerance capability of the cyclocopter was investigated through series of experiments in the wind tunnel and using a synthetic gust generation device. Both pitch control by actuating nose rotor rotational speed and thrust vectoring control were investigated.

2. A gust perturbation along the longitudinal axis resulted in a pitch-up moment on the cyclocopter. 1-DOF pitch stand results from the wind tunnel showed that the cyclocopter was able to withstand 10 m/s gust perturbation using pitch control. The threshold for the maximum gust perturbation was much lower along the lateral axis. 1-DOF roll stand results showed that the cyclocopter was able to withstand up to 6.5 m/s of gust when operating at 1400 rpm before experiencing control saturation. The cyclocopter achieved roll control by differentially varying the rotational speed of both cyclorotors, which has a lower maximum achievable rpm compared to the nose rotor.

3. 6-DOF experiments focused on longitudinal gust response in order to evaluate effectiveness of thrust vectoring control. A synthetic gust generation device was assembled using six Dyson fans. A thorough sweep of the flow field showed that the mean freestream velocity was uniform across the 80 cm by 16.8 cm

test region. The setup generated 2.8 m/s and 4 m/s gust with variance of 0.15 and a step gust profile using an automated shutter system.

4. A gust controller with a flow feedback scheme was added to the closed-loop feedback system to augment the outer-loop PID position controller. Inputs to the gust controller included position measurements from the VICON motion capture system and flow measurements from a miniature dual-probe flow sensor.

5. For a step gust input along the longitudinal axis, thrust vectoring was more effective than pitch control in reducing displacement from gust. Pitch control using the position feedback controller resulted in a maximum gust tolerance of 2.8 m/s with a duration of 3 seconds while thrust vector control using the combined flow feedback and position feedback controller was able to withstand 4 m/s step gust input with one second duration with only 0.01 m displacement.

6. The results also showed that flow feedback is more effective than position feedback in minimizing the vehicle's response to gust. While the settling time results measured effectiveness of the gains used in the controller, the displacement results demonstrated that thrust vectoring coupled with onboard flow sensing increased gust tolerance capability of the cyclocopter.

8.2.5 Multi-Mode Capability

1. All-terrain cyclocopter capable of aerial, terrestrial, and aquatic locomotion with seamless transition between the modes was developed. Unlike existing

multi-modal quadcopter platforms, the all-terrain cyclocopter solely relied on its four cyclorotors as source of propulsion, as well as wheels.

2. Structures required to permit terrestrial and aquatic locomotions included wheels, retractable landing gear system, additional fuselage structure to shield electronics, and layers of waterproof coating. These components contributed close to 200 grams, which accounted for 20% of total vehicle weight.

3. The all-terrain cyclocopter weighing 1010 grams successfully demonstrated sustained hover, translation and rotational maneuvers on ground, and aquatic locomotion. Control strategy for each mode relied on combinations of motor torque and thrust vectoring. Cyclorotor rotational speeds and thrust vectors were individually modulated to sustain stable hover. A similar control strategy relying on aerodynamic forces generated by cyclorotors was also implemented for aquatic locomotion. Because cyclorotors rotate about the horizontal axis, wheels were efficiently integrated into the carbon fiber rotor endplates and terrestrial locomotion was commanded directly by motor torque.

4. In aerial mode, the cyclorotors operated at 1550 rpm and consumed 232 W to sustain hover. Each optimized cyclorotor weighed 83 grams and contributed up to 33% of total gross take-off weight. At the operating rotational speed, each optimized cyclorotor produced 270 grams of lift, which resulted in thrust-to-weight ratio of approximately 3.25. Forward translation of 2 m/s in terrestrial mode required 28 W, which was a 88% reduction in power consumption required to hover. In aquatic mode, cyclorotors operated at 348 rpm and

consumed 19 W in order to translate forward at 1.3 m/s.

5. Using a pulley-based experimental setup, the cyclocopter demonstrated ground speed of 10 m/s (22 mph) under minimum load conditions (no wind resistance and low friction). Motion capture measurements also showed that using differential rpm control to change direction of orientation resulted in a minimum turn radius of 0.2 m.

8.3 Recommendations for Future Work

The feasibility and performance of the cyclocopter configuration was explored in this research. However, these experimental studies only provide a foundation to guide additional work towards improving vehicle performance across all flight modes. Suggestions for future work focused on the vehicle instead of an isolated cyclorotor include:

1. **Performance Studies:** Both the twin-cyclocopter and quad-cyclocopter configurations were investigated in this work. Particularly for the quad-cyclocopter configuration, additional studies could explore changing key geometric parameters (e.g offset between the fore and aft pairs of cyclorotors) to improve performance in hover and forward flight. The study entails understanding aerodynamic performance of the cyclorotors, specifically characterizing its downwash. A possible CFD/CSD coupled study combined with PIV on cyclorotor-to-cyclorotor interaction could provide insights into the optimal geometric configuration for forward flight. Another important study is evaluating the cyclo-

copter's aeroacoustics. Previous chapters mentioned that the cyclorotor has reduced acoustic signature compared to a geometrically similar conventional rotor because of its lower operating tip speeds. However, a proper experimental validation would quantify the vehicle's acoustic signature and allow comparisons with other rotary-wing configurations.

2. **Autonomous Flight Capability:** The current work mostly focused on piloted flights and closed-loop position controller using an external motion capture system. The SISO PID controller allowed the feedback control system to be easily modified for each of the experimental studies. However, future work can focus on achieving autonomous control using a multivariable controller design combined with guidance and navigation sensors discussed in Chapter 3. Multivariable controller could provide improved performance for disturbance rejection. Instead of external position sensors, onboard sensors would allow field testing of the gust rejection controller.

3. **Non-Linear 6-DOF Flight Dynamics Model:** A relatively simple linear 6-DOF flight dynamics model in forward flight was derived in this work. An important aspect of future work should be to improve the model fidelity by including higher order effects across all flight modes. Understanding higher order effects could potentially improve the gust rejection controller, especially if these effects are included in the closed-loop feedback system.

4. **Continuation of Gust Rejection Study:** Free-flight experiments in front of the synthetic gust generation device and ultimately outdoors in realistic

conditions should be considered for future work. In conjunction with the previous suggestion, the effects of gust loads can be incorporated into the flight dynamics model and would require an aerodynamic model of the cyclorotor. Moreover, systematic gust trade studies can be conducted with varying gust profiles (magnitude, duration), turbulence levels, shape (e.g sinusoidal), and frequencies. Performance could also be compared against other rotary-wing configurations.

Bibliography

[1] McMichael, J.M, and Francis, USAF (Ret.), C. M. S., "Micro Air Vehicles: Toward a New Dimension in Flight," U.S Department of Defense Weapon Systems Technology Information Analysis Center (WSTIAC) Newsletter, Vol. 1, No. 1-3, August 7, 1997.

[2] McMasters, J. H., Henderson, M. L., "Low Speed Single-Element Airfoil Synthesis," NASA Langley Research Center, The Science and Technology of Low Speed and Motorless Flight, Hampton, VA, March 29-30, 1979.

[3] Mueller, T., J., "Aerodynamic Measurements at Low Reynolds Numbers for Fixed Wing Micro-Air Vehicles," RTO AVT/VKI Special Course on Development and Operation of UAVs for Military and Civil Applications, VKI, Belgium, September 13-17, 1999.

[4] Winslow, J., "Understanding of Low Reynolds Number Aerodynamics and Design of Micro Rotary-wing Air Vehicles," M.Sc Thesis, Department of Aerospace Engineering, University of Maryland, College Park, 2016.

[5] Schmitz, F. W., "Aerodynamik des Flugmodell," C. J. E. Volckmann Nachf. E. Wette, Berlin-Charlottenburg, 1942.

[6] Laitone, E.V., "Wind Tunnel Tests of Wings at Reynolds Numbers Below 70000," Experiments in Fluids Vol. 23, 1997, pp 405-409.

[7] Ramasamy, M., Johnson, B., and Leishman, J. G., "Understanding the Aerodynamic Efficiency of a Hovering Micro-Rotor," Journal of American Helicopter Society, Vol. 53, No. 4, October 2008, pp. 412428.

[8] Burk, S. M., Wilson, C. F, Jr., "Radio-Controlled Model Design and Testing Techniques for Stall/Spin Evaluation of General-Aviation Aircraft." SAE National Business Aircraft Meeting, 1975.

[9] Mettler, B., Identication Modeling and Characteristics of Small Scale Rotorcraft, Kluwer Academic Publishers, 2003.

[10] Mettler, B., Tischler, M., and Kanade, T., "System Identification of Small-Size Unmanned Helicopter Dynamics," Proceedings of the American Helicopter Society 55th Forum, Montreal, Quebec, Canada, May 25–27, 1999.

[11] Fadl, M., and Karadelis, J., "CFD Simulation for Wind Comfort and Safety in Urban Area: A Case Study of Coventry University Central Campus," *International Journal of Architecture, Engineering and Construction*, Vol. 2, (2), June 2006, pp. 131–143.

[12] Hassanalian, M., and Abdelkefi, A., "Classifications, Applications, and Design Challenges of Drones: A Review," *Progress in Aerospace Sciences*, May 2017.

[13] Pines, D., and Bohorquez, F., "Challenges Facing Future Micro-Air-Vehicle Development," *Journal of Aircraft*, Vol. 43, (2), March/April 2006, pp. 290–305.

[14] Leishman, J.G., Principles of Helicopter Aerodynamics (Cambridge Univ. Press, New York, 2000).

[15] Shyy, W., Lian, Y., Tang, J., Viieru, D., and Liu, H., Aerodynamics of Low Reynolds Number Flyers, Cambridge University Press, New York, NY, 2008.

[16] Keennon, M., Klingebiel, K., Won, H., and Andriukov, A., "Development of the Nano Hummingbird: A Tailless Flapping Wing Micro Air Vehicle," 50th AIAA Aerospace Sciences Meeting, , Nashville, TN, January 912, 2012.

[17] Shavrov, V., History of Aircraft Construction in the USSR to 1938, Mashinostroenie (Moscow), Vol. 1, pp. 3940, 1985.

[18] Sachse, H., "Kirsten-Boeing Propeller," Technical Memorandum 351, National Advisory Committee for Aeronautics, January 1926.

[19] Kirsten, F. K., "Cycloidal Propulsion Applied to Aircraft," Transactions of the American Society of Mechanical Engineers, Vol. 50, (12), 1928, pp 2547.

[20] Schneider, E., "Blade Wheel Propeller Particularly for Watercraft," Patent 2,291,062, 28 July 1942.

[21] Bartels, Jens-Erk, and Dirk Jrgens, The Voith Schneider Propeller: Current applications and new developments, Technical report, Voith Turbo Marine GmbH, 2006.

[22] Strandgren, C. B., "The Theory of the Strandgren Cyclogiro," NACA Technical Report Vol. 41, No. 7, Washington D.C., July 1933.

[23] Wheatley, J., "Simplied Aerodynamic Analysis of the Cyclogiro Rotating Wing System," Technical Report 467, National Advisory Committee for Aeronautics, August 1933.

[24] Kim, S., Yun, C., Kim, D., Yoon, Y., and Park, I., "Design and Performance Tests of Cycloidal Propulsion Systems," Paper AIAA-2003-1786, 44th AIAA/ASME/ASCE/AHS/ASC Structures, Structural Dynamics, and Materials Conference, Norfolk, Virginia, April 710, 2003.

[25] Yun, C. Y., Park, I. K., Hwang, I. S., and Kim, S. J., "Thrust Control Mechanism of VTOL UAV Cyclocopter with Cycloidal Blades System," *Journal of Intelligent Material Systems and Structures*, Vol. 16, No. 1112, December 2005, pp. 937943.

[26] Yun, C. Y., Park, I. K., Lee, H. Y., Jung, J. S., Hwang, I. S., and Kim, S. J., "Design of a New Unmanned Aerial Vehicle Cyclocopter," *Journal of American Helicopter Society*, Vol. 52, (1), January 2007, pp. 2435.

[27] Hwang, I. S., Min, S. Y., Lee, C. H., and Kim, S. J., "Development of a Four-Rotor Cyclocopter," *Journal of Aircraft*, Vol. 45, (6), December 2008, pp.2151–2157.

[28] Min., S. Y., Lee. C. H., Sung, M. H., Kim, Y. S., Hur, C. M., and Kim, S. J., "Experimental Study of a Quadrotor Cyclocopter," Proceedings of the 69th American Helicopter Society Annual Forum, Phoenix, AZ, May 21–23, 2013.

[29] Sirohi, J., Parsons, E., and Chopra, I., "Hover Performance of a Cycloidal Rotor for a Micro Air Vehicle," Journal of American Helicopter Society, Vol. 52, (3), July 2007, pp. 263-279.

[30] Parsons, E., "Investigation and Characterization of a Cycloidal Rotor for Application to a Micro-Air Vehicle," M.S. Thesis, University of Maryland, College Park, MD, 2005.

[31] Benedict, M., "Fundamental Understanding of the Cycloidal-Rotor Concept for Micro Air Vehicle Applications," Ph.D. Thesis, University of Maryland, College Park, MD December 2010.

[32] Benedict M., Ramasamy, M., and Chopra, I., "Improving the Aerodynamic Performance of Micro-Air-Vehicle-Scale Cycloidal Rotor: An Experimental Approach," *Journal of Aircraft*, Vol. 47, No. 4, July–August 2010, pp. 1117–1125.

[33] Benedict, M., Jarugumilli, T., and Chopra, I., "Experimental Optimization of MAV-Scale Cycloidal Rotor Performance," *Journal of the American Helicopter Society*, Vol. 56, No. 2, April 2011, pp. 1–11.

[34] Benedict, M., Gupta, R., and Chopra, I., "Design, Development, and Open-Loop Flight Testing of a Twin-Rotor Cyclocopter Micro Air Vehicle," *Journal of the American Helicopter Society*, Vol. 58, No. 4, October 2013, pp. 1–10.

[35] Benedict, M., Shrestha, E., Hrishikeshavan, V., and Chopra, I., "Development of Micro Twin-Rotor Cyclocopters Capable of Autonomous Hover," *Journal of Aircraft*, Vol. 51, (2), March–April 2014, pp.672-676.

[36] Benedict, M., Jarugumilli, T., and Chopra, I., "Effect of Rotor Geometry and Blade Kinematics on Cycloidal Rotor Hover Performance," *Journal of Aircraft*, Vol. 50, No. 5, 2013, pp. 1340–1352.

[37] Jarugumilli, T., Benedict, M. and Chopra, I., "Wind Tunnel Studies on a Micro Air Vehicle-Scale Cycloidal Rotor," *Journal of the American Helicopter Society*, Vol. 59, No. 2, April 2014, pp. 02208 (1–10).

[38] Runco, C., Benedict, M., and Coleman, D., "Design and Development of a Meso-Scale Cyclocopter," AIAA SciTech Forum, (AIAA 2016-1255).

[39] Hrishikeshavan, V., Benedict, M., and Chopra, I., "Identification of Flight Dynamics of a Cylcocopter Micro Air Vehicle in Hover," *Journal of Aircraft*, Vol. 52, No. 1 (2015), pp. 116-129.

[40] Galway, D., Etele, J., and Fusina, G., "Modeling of Urban Wind Field Effects on Unmanned Rotorcraft Flight," *Journal of Aircraft*, Vol. 48, No. 5, 2011.

[41] Johnson, E. and Jacob, J., "Development and Testing of a Gust and Shear Tunnel for NAVs and MAVs," 47th AIAA Aerospace Sciences Meeting Including The New Horizons Forum and Aerospace Exposition, January 2009.

[42] Zarovy, S., Costello, M., and Mehta, A., "Experimental method for studying gust effects on micro rotorcraft," *Journal of Aerospace Engineering*, Vol. 227, No. 4, April 2013, pp. 703-703.

[43] Hrishikeshavan, V. and Chopra, I., "Performance, Flight Testing of Shrouded Rotor Micro Air Vehicle in Edgewise Gusts," *Journal of Aircraft*, Vol. 49, No. 1, Jan. 2012, pp. 193–205.

[44] Boria F., Bachmann J., Ifju P., Quinn R., Vaidyanathan R., Perry C., and Wagener J., "A sensor platform capable of aerial and terrestrial locomotion," IEEE/RSJ International Conference on Intelligent Robots and Systems, 2005, Edmonton, Canada.

[45] Kalantari A. and Spenko M., "Design and Experimental Validation of HyTAQ, a Hybrid Terrestrial and Aerial Quadrotor," Proceedings of the IEEE International Conference on Robotics and Automation, 2013, Karlsruhe, Germany.

[46] Kawasaki K., Zhao M., Okada K., Inaba M., "MUWA: Multi-field universal wheel for air-land vehicle with quad variable-pitch propellers," Proceedings of the 26th IEEE/RSJ International Conference on Intelligent Robots and Systems: New Horizon, 2013, Tokyo, Japan.

[47] Migliore, P.G., Wolfe, W.P., and Fanuccif, J.B., "Flow Curvature Effects on Darrieus Turbine Blade Aerodynamics," Journal of Energy, Vol. 4, (2), 1980, pp. 49–55.

[48] Mehta, A., and Pister, K. "WARPWING: a complete open source control platform for miniature robots," Proceedings of IEEE/ RSJ International Conference on Intelligent Robots and Systems (IROS), Taipei, Taiwan, October 2010.

[49] Hrishikeshavan V., and Chopra I., "Refined lightweight inertial navigation system for micro air vehicle applications," American Helicopter Society International 6th International Specialists' Meeting On Unmanned Rotorcraft System, 2015, pp. 200–210.

[50] Hrishikeshavan, V. "Experimental Investigation of a Shrouded Rotor Micro Air Vehicle in Hover and in Edgewise Gusts," Ph.D Thesis, Department of Aerospace Engineering, University of Maryland, College Park, 2011.

[51] Diao, Z., Quan, H., Lan, L., and Han, Y., "Analysis and Compensation of MEMS Gyroscope Drift," Proceedings of the 7th International Conference on Sensing Technology, 2013.

[52] Kasdin, J., and Paley, D. *Engineering Dynamics: A Comprehensive Introduction*. Princeton University Press, 2011.

[53] Kuipers, J. B. *Quaternions and Rotation Sequences: A Primer with Applications to Orbits, Aerospace and Virtual Reality*. Princeton University Press, 1999.

[54] Madgwick, SO. *An efficient orientation filter for inertial and inertial-magnetic sensor arrays*. UK: Internal report and University of Bristol, 2010.

[55] Thong, Y., Woolfson, M., Crowe, J., Hayes-Gill, B., and Challis, R., "Dependence of inertial measurements of distance on accelerometer noise," *Measurement Science Technology*, Vol. 13, pp. 1163–1172, 2002.

[56] Yousif, K., Bab-Hadiahsar, A., and Hoseinnezhad, R., "An Overview to Visual Odometry and Visual SLAM: Applications to Mobile Robotics," *Intelligent Industrial Systems*, Vol. 1, No. 4, 2015, pp. 289-311.

[57] Sa et. al, "Build Your Own Visual-Inertial Drone: A Cost-Effective and Open-Source Autonomous Drone," *IEEE Robotics and Automation Magazine*, Vol. 25, No. 1, March 2018, pp. 89–103.

[58] Delmerico, J., and Scaramuzza, D., "A Benchmark Comparison of Monocular Visual-Inertial Odometry Algorithms for Flying Robots," Proceedings of IEEE International Conference on Robotics and Automation (ICRA), May 2018.

[59] Aqel, M., Marhaban, M., Saripan, I., and Ismail, N., "Review of visual odometry: types, approaches, challenges, and applications," *SpringerPlus*, Vol. 5, No. 1, 2016, pp. 1897.

[60] Mueggler, E., Gallego, G., Rebecq, H., and Scaramuzza, D., "Continuous-Time Visual-Inertial Odometry for Event Cameras," Proceedings of IEEE Transactions on Robotics and Automation, June 2018.

[61] Li, L., "Time-of-Flight Camera - An Introduction," Sensing Solutions, May 2014.

[62] Aleny, G., Foix, S., and Torras, C., "Using ToF and RGBD Cameras for 3D Robot Perception and Manipulation in Human Environments," *Intelligent Service Robotics*, Vol. 7, 2014, pp. 211–220.

[63] Kim, H., Handa, A., Benosman, R., Ieng, S., and Davison, A., "Simultaneous Mosaicing and Tracking with an Event Camera," Proceedings of the British Machine Vision Conference, BMVA Press, September 2014.

[64] Everding, L., and Conradt, J., "Low-Latency Line Tracking Using Event-Based Dynamic Vision Sensors," *Frontiers in Neurobotics*, Vol. 12, No. 4, 2018.

[65] Pijnaker Hordijk B.J., Scheper K.Y.W., de Croon GCHE., "Vertical Landing for Micro Air Vehicles using Event-based Optical Flow. J Field Robotics," 2017;00:1-22. https://doi.org/10.1002/rob.21764.

[66] Coppejans, H., and Myburgh, H., "A Primer on Autonomous Aerial Vehicle Design," *Sensors*, Vol. 15, 2018, pp. 30033–30061.

[67] Taketomi, T., Uchiyama, H., and Ikeda, S., "Visual SLAM algorithms: a survey from 2010 to 2016," *IPSJ Transactions on Computer Vision and Applications*, 2017, pp. 9–16. https://doi.org/10.1186/s41074-017-0027-2.

[68] Gaoussou, H., and Dewei, P., "Evaluation of the Visual Odometry Methods for Semi-Dense Real-Time," *Advanced Computing: An International Journal (ACIJ)*, Vol. 9, No. 2, March 2018, pp. 1–14.

[69] Solomon, E., Hrishikeshavan, V., and Chopra, I., "Autonomous Quadrotor Control and Navigation with Snapdragon Flight," Proceedings of the American Helicopter Society 74th Annual Forum, Phoenix, AZ, May 14–17, 2018.

[70] Solomon, E., Vorwald, C., Hrishikeshavan, V., and Chopra, I., "Visual Odometry Onboard a Micro Air Vehicle Using Snapdragon Flight," Proceedings of 7th American Helicopter Society Technical Meeting on VTOL Unmanned Aircraft Systems and Autonomy, Mesa, AZ, Jan 24–26, 2017.

[71] Loianno, G., Mulgaonkar, Y., Brunner, C., Ahuja, D., Ramanandan, A., Murali, C., Diaz, S., Kumar, V., "Smarpthones power ying robots," IEEE/RSJ International Conference on Intelligent Robots and Systems (IROS), September 2015, pp. 1256-1263.

[72] Sanket, N., Singh, C., Ganguly, K., Fermuller, C., and Aloimonos, Y., "GapFlyt: Active Vision Based Minimalist Structure-less Gap Detection For Quadrotor Flight," Published in IEEE Robotics and Autonomation Letters, 2018.

[73] Thong, Y., Woolfson, M., Crowe, J., Hayes-Gill, B., and Challis, R., "Dependence of Inertial Measurements of Distance on Accelerometer Noise," *Measurement Science Technology*, Vol. 13, pp. 1163–1172, 2002.

[74] Astrom, K., and Murray, R., "Feedback Systems: An Introduction for Scientists and Engineers," Princeton, NJ, 2008.

[75] Pamadi, B. *Performance, Stability, Dynamics, and Control of Airplanes.* American Institute of Aeronautics and Astronautics, 1998.

[76] Benedict, M., Jarugumilli, T., Lakashminaryayan, V. and Chopra, I., "Effect of Flow Curvature on Forward Flight Performance of a Micro-Air-Vehicle-Scale Cycloidal-Rotor," *AIAA Journal*, Vol. 52, No. 6, June 2014, pp. 1159-1169.

[77] Zachary, H., A., Benedict, M., Hrishikeshavan, V., and Chopra, I., "Design, Development, and Flight Test of a Small-Scale Cyclogyro UAV Utilizing a Novel Cam-Based Passive Blade Pitching Mechanism," *International Journal of Micro Air Vehicles*, Vol. 5, No. 2, June 2013, pp. 145–162.

[78] Petricca, L., Hrishikeshavan, V., Ohlckers, P., Chopra, I., "Design, fabrication and test of an embedded lightweight kinematic autopilot (ELKA)," *International Journal of Intelligent Unmanned Systems*, Vol. 2 (2014), pp.140–150.

[79] Yeo, D., Atkins, E., Bernal, L., and Shyy, W., "Fixed-Wing Unmanned Aircraft In-Flight Pitch and Yaw Control Moment Sensing," *Journal of Aircraft*, Vol. 52, No. 2 (2015), pp. 403–420.

[80] Benedict, M., Jarugumilli, T., Lakashminaryayan, V. and Chopra, I., "Effect of Flow Curvature on Forward Flight Performance of a Micro-Air-Vehicle-Scale Cycloidal-Rotor," *AIAA Journal*, Vol. 52, No. 6, June 2014, pp. 1159-1169.

[81] Klein, V., and Morelli, E., *Aircraft System Identication: Theory and Practice.* AIAA Education Series, Reston, Virginia, 2006.

[82] Conroy, J., Humbert, J., and Pines, D., "System Identication of a Rotary Wing Micro Air Vehicle," *Journal of the American Helicopter Society*, Vol. 56, No. 2, April 2011, pp. 25001.

[83] Grauer J., Conroy J., Hubbard J. Jr., and Humbert J., "System Identification of a Miniature Helicopter," *Journal of Aircraft*, Vol. 46, No. 4, 2009, pp. 1260-1269.

[84] Tischler, M., and Remple, R., *Aircraft and Rotorcraft System Identification: Engineering Methods with Flight Test Examples.* AIAA Education Series, Reston, Virginia, 2012.

[85] Yeo, D., Sydney, N., and Paley, D., "Onboard Flow Sensing for Rotary-Wing UAV Pitch Control in Wind," AIAA Guidance, Navigation, and Control Conference, AIAA SciTech, Jan. 2016.

[86] Hoffmann, G., Huang, H., Waslander, S., and Tomlin, J., "Autonomous quadrotor helicopter testbed design, control, and experiments," AIAA Guidance, Navigation and Control Conference, AIAA SciTech, Aug. 2007.

[87] Manshadi, D M., "The Importance of Turbulence Reduction in Assessment of Wind Tunnel Flow Quality," Wind Tunnels and Experimental Fluid Dynamics Research, 2011.